Assessment of Seismic Protection Effectiveness of Unbonded Scrap Tire Rubber Pad Base Isolation Using Finite Element Analysis

Md Basir ZISAN

2021

Assessment of Seismic Protection Effectiveness of Unbonded Scrap Tire Rubber Pad Base Isolation Using Finite Element Analysis

By

Md Basir ZISAN

A Thesis Submitted to the Graduate School of Engineering in Partial Fulfilment of the Requirements for the Degree of

Doctor of Engineering

Kyoto University

This dissertation is devoted to my mother Mrs. Sadaner Nessa and my wife Dr. Afroja Sultana

Abstract

This research concentrated on the seismic protection effectiveness of unbonded scrap tire rubber pad (STRP) isolators indispensable for practical implementation. An STRP isolator differs from a conventional one due to the unidirectional flexible steel cord and installation method. Furthermore, its peculiar rollover deformation giving a distinct force-displacement response. These features should be included in analyzing and designing unbonded STRP isolators. In addition, the unbonded application is innovative and has no practical implementations or large-scale experimental validation. Therefore, investigation for seismic protection effectiveness of unbonded STRP isolation in real situations, including its general features, is essential. In addition, analytical solutions for force-displacement response, stiffness, and hysteresis behavior also necessary for practical design.

The vertical and lateral load performance and seismic capacity of strip-shaped STRP isolators with different length-to-width ratios and square isolators with different heights are investigated. The STRP isolators are anisotropic and display unsymmetric bulging in compression and a progressive rollover deformation. The restoring forces, stiffness, and damping ratios in a strip-shaped isolator are different in two orthogonal directions and are substantial in amount for a sizeable length-to-width ratio. A length-to-width ratio exceeding 4.0 is less significant for vertical stiffness. For a fixed aspect ratio, vertical stiffness increases with stack numbers while hysteretic properties and seismic capacity are insignificant. The displacement capacity and isolation period are different in the length and width directions of a strip-shaped isolator. The biaxial interaction increases the stiffness and effective damping of the unbonded STRP isolator, whereas its effect on the rollover deformation and hardening is less significant than the uniaxial loading. In addition, characteristics of input displacement path are essential for hysteresis behavior of unbonded STRP isolator.

The analytical models for horizontal force-displacement and lateral stiffness are helpful for the design of unboned STRP isolators is propsoed. The hysteresis force model, including the anisotropy and rollover displacement, is developed and validated by static and dynamic time history analysis.

The stress and strain in unbonded STRP isolators are analyzed for compressions, rotations, and lateral displacement. The pressure solution underestimates the elastomer stress. A large length-to-width ratio

quickens the lift-off initiation, and the growth of compression delays the same. Rotation increases the elastomer stress significantly at low compression and high length-to-width ratio. In contrast, lateral displacement reduces in-plane stresses but induces tension more substantial for a high length-to-width ratio. An effective length excluding the tension zone can avoid any fracture or damage at large displacement. Strain in the unbonded STRP isolator is lower than the design limits, and provided steel cord is sufficient.

Acknowledgment

All praise is due to Allah, who created us and kept us safe and healthy during the COVID-19 pandemic.

I am sincerely grateful to my supervisor, Prof. Akira IGARASHI, for his precious academic and mental supports and helpful feedback over the last three years. I express my most profound appreciation for his continuous support in challenging situations, critical thinking, and scientific writings.

I would like to express my appreciation to Prof. Yoshikazu Takahashi and Associate Prof. Yasuo Kitane for the reviews, critical comments, and invaluable suggestions that contribute to the improvement of this dissertation.

I would like to extend my gratitude to Associate Prof. Nozomu Yoneyama, the secretary Miho Mori and all other laboratory members to warm friendship and help during my studentships.

I would like to express my most heartfelt appreciation to the Ministry of Education, Culture, Sports, Science and Technology (MEXT), Japan, for granting the financial support "Monbugakakusho Scholarship" during my studentship at Kyoto University.

I would like to express my deepest love to my wife, Dr. Afroja Sultana, and daughter Zuharin Zisan Arshia who always supported me and sacrificed themselves for my Ph.D. study.

Table of Contents

List of Figures

List of Tables

Chapter 1

Introduction

This chapter aims to introduce the background and objectives of the dissertation. It also includes a brief description of the concept and historical development of seismic isolation and the different classes of isolation devices currently are being used, including the STRP isolator. In addition, it provides the outlines of the dissertation.

1.1 Background of the Research

The fast-growing urbanization is promoting infrastructure construction through a non-engineering practice due to a lack of code enforcement. Besides, a significant part of structures constructed before introducing seismic codes is vulnerable to severe devastation and high death tolls. The losses due to the earthquakes have increased significantly within the past decades especially pronounced in developing countries. Typical examples are the Wenchuan earthquake in 2008, and Sichuan Lushan Earthquake in 2013 in China (Yang et al., 2014), the Haiti earthquake in 2010 (Haiti PDNA, 2010), and the 2015 earthquake in Nepal (Nepal Earthquake, 2015). These earthquakes caused thousands of buildings to collapse entirely, including residential, educational facilities, hospitals, public and administrative buildings, and historical buildings, as shown in Fig. 1.1. A survey (Shah, 1983) between 1947 and 1980 indicates a total death of 358,980 in Asia compared to 94,569 in the rest of the world. The main reason is the inferior construction methods, lack of seismic design strategies, and unavailability of technology.

Various aseismic technologies are being practiced, including (i) increasing the capacity by providing large sections and superior materials, ii) implementation of bracing, iii) addition of damper, and iv) use of base isolation. Among these, base isolation is widely practiced due to its high effectiveness in reducing seismic demand as well as the damage level of a structure (Chimamphant and Kasai, 2016; Huang *et al*., 2013; Cardone and Flora, 2013). In seismic isolation, the natural period of a structure is shifted to the long period range by placing a horizontally flexible device at the base level. The steel-reinforced elastomeric isolators (SREIs) including the laminated rubber bearing (LRB), high damping rubber bearing (HDRB), natural

(a) School in Yingxiu, Sichuan province after 2008 Wenchuan earthquake (Kenneth Pletcher, 2008)

(b) Buildings damaged by 2001 Gujarat earthquake (Backhaus et al., 2010)

Figure 1.1 Typical damage in low-to-medium rise building in different earthquake

rubber bearing (NRB), and the friction pendulum bearing are mainly practiced today. However, a disadvantage of these systems is the high cost and weight (Kelly, 2002; Cutfield and Ma, 2014), making them uneconomical for less important structures (Pan et al., 2005; May, 2002). Therefore, to extend the earthquake-resistant design strategies for ordinary buildings and affordable to the middle-income group, the cost reduction and simplification of the design principle are of great concern.

In order to overcome the cost barrier, the scrap automobile tire is foreseen as an innovative material. At present, about 1.5 billion scrap tires weighing 17 million tons (RMA, 2009; JATMA, 2010; ETRMA, 2011; WBCSD, 2010) are produced worldwide. This abandoned tire causes accidental firing, or tire-derived fuel (TDF) emits toxic pollutants to the environment (Reisman, 1997; Richard et al., 2008). Figure 1.2 shows the stockpile of tires and their impact on the environment. The recovery rate of scrap tires increased to 80-90% in Europe, Japan, USA (ETRMA, 2011) when a prohibition is imposed on disposal in landfills. As a result, it has become a potential recycling material (ETRMA, 2011). However, only 7.4% of scrap tires in the European Union (ETRMA, 2011) and only 7.8% of those in the USA (RMA, 2011) were used in engineering applications.

(a) Stockpile

(b) Firing in stockpile

(c) Creating pollution

Figure 1.2 Scrap tire and its environmental impacts

The automobile tires are made by vulcanization of natural or synthetic rubber with interleaved steel cords and are expected to have similar functions to the conventional elastomeric isolator. The primary difference is the reinforcement type and virginity of the elastomers. In the elastomeric isolator, rubber is vulcanized with rigid steel shims where a layer of unidirectional steel cords in a scrap tire. Therefore, scrap tires can be a potential material for earthquake protection of buildings and bridges that reduces environmental pollutions. Since the cost of recycling tires is nearly zero and making an isolator using scrap tires needs only sizing and adhesive costs, therefore, this innovative idea can cut the cost barrier to practical seismic isolation strategies in developing countries. Some researchers (Turer and Özden, 2007; Tsang et al., 2012 and Mishra *et* al., 2013a, Hadad et al., 2017, Morales et al., 2018) pointed out the feasibility of the scrap tire as low-cost earthquake protection in the developing countries.

1.2 Existing Tools for Seismic Isolation

Elastomeric bearings that are composed of alternating rubber layers vulcanized with steel shims, as shown in Fig. 1.3, are widely used. The low-damping natural or synthetic rubber and high-damping rubber are two classes of elastomeric bearings. The stress-strain relationship of the low-damping natural rubber is nearly linear up to 150% shear and has an equivalent damping ratio of 2%~3% at 100% shear strain. In contrast, the high-damping rubber bearing is nonlinear at shear strain less than 20% (Naem and Kelly, 1999) and has a damping ratio of 10%~20% at 100% shear strain. Over the 20-100% shear strain, the shear modulus is approximately constant and increases at a large shear strain due to crystallization. It is beneficial to limit the displacement under the anticipated input of earthquake load.

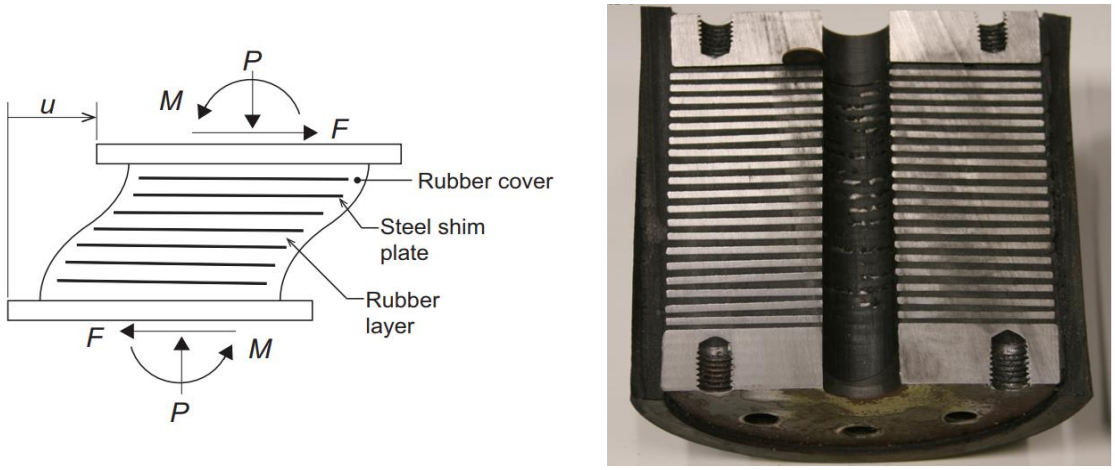

Figure 1.3 Elastomeric rubber bearing (Warn and Ryan, 2012)

Lead-rubber bearings were first introduced and used in New Zealand in the late 1970s (Robinson and Tucker, 1977). It differs from elastomeric rubber bearings by adding a lead-plug that is press-fit into a central hole in the bearing, as shown in Fig. 1.4. Under shear deformation, the lead plug's plastic deformation enhances the energy dissipation compared to the low-damping natural rubber bearing. The energy dissipation provided by the lead core, through its yielding, allows achieving an equivalent viscous damping coefficient up to about 30%, which is two times that of high damping elastomeric isolators (FIP Industriale, 2002).

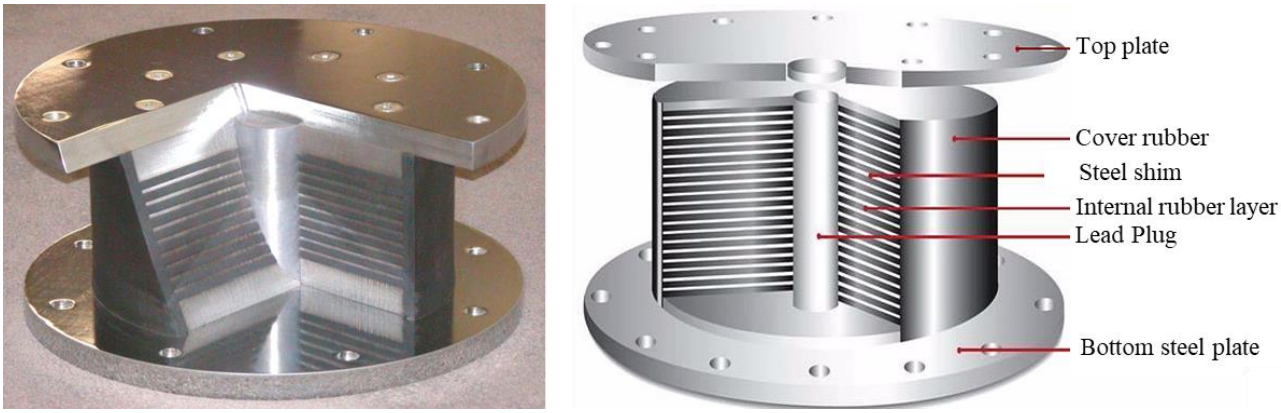

Figure 1.4 Lead-plug rubber bearing.

Calantrients proposed sliding isolation in 1909 using talc layer, as shown in Fig. 1.5. The Italian government first considered this isolation after the great Messina-Reggio earthquake of 1908. The Italian government commission recommended isolation using either a sand layer in its foundation or rollers under the column to allow a building to move horizontally (Naem and Kelly, 1999). The roller approach was accepted, and sliding isolation was not used. During the Indian earthquakes of Dhubai (1930) and Bihar (1934), the masonry building that slides on their foundation survived where similar adjacent fixed-base buildings were destroyed. The most commonly used materials for sliding bearings are unfilled or filled polytetrafluoroethylene (PTFE or Teflon) on stainless steel.

The friction pendulum isolation system combines a sliding isolation system and a restoring force system provided by the geometry. A single friction pendulum bearing consists of a baseplate, an articulated slider, and a spherical concave disc, as shown in Fig. 1.6. The slider is placed between the spherical sliding plate of stainless steel and that of the base plate. The side of the articulated slider is coated with low-friction polytetrafluoroethylene (PTFE) fabric impregnated with a lubricant. The lubricant is a silicone oil that shows almost no aging degradation. The slider's movement over the spherical surface causes the mass to

generate the system's restoring force. The friction between the articulated slider and the spherical surface generates the damping in the isolator. The effective stiffness and period of the isolation are controlled by the curvature of the concave surface. The multi-spherical Friction Pendulum bearings (Fenz and Constantinou, 2006) are among the most widely used seismic isolation bearings in the United States.

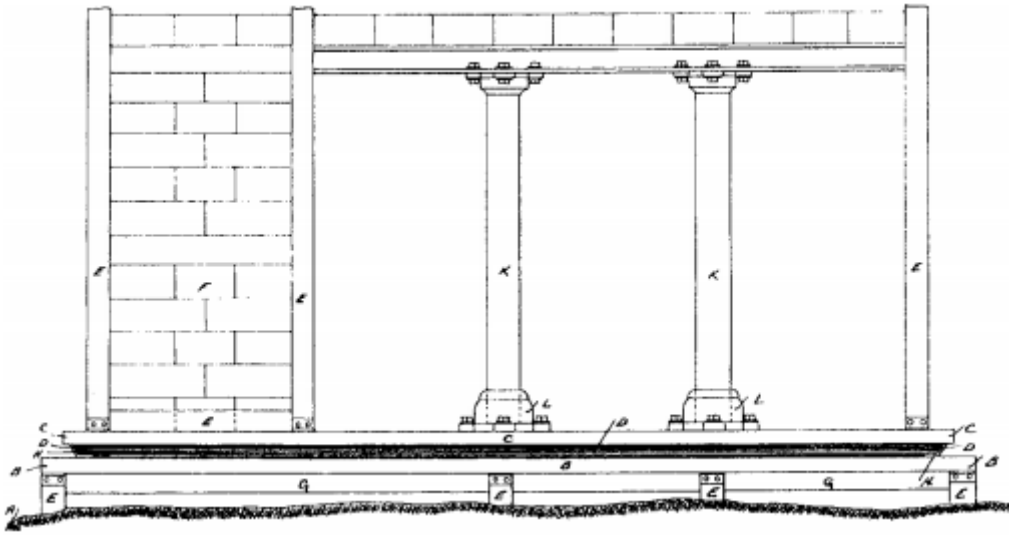

Figure 1.5 Calantrients's base isolation system (Naeim and Kelly, 1999)

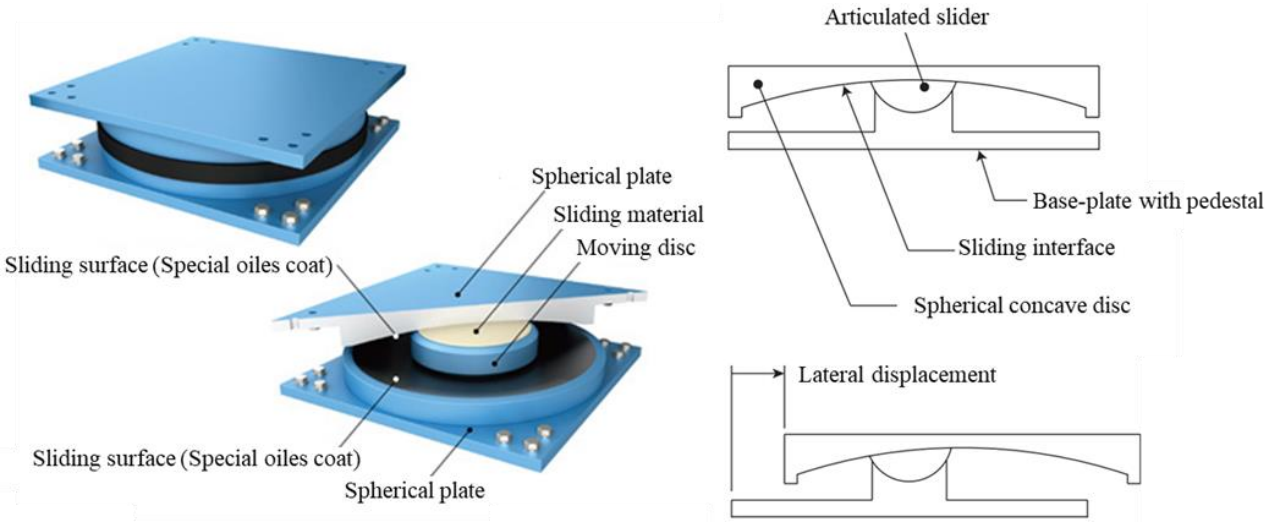

Figure 1.6 Friction pendulum sliding isolation.

1.3 Principle of Seismic Isolation

The basic structural design is based on the theory that the capacity of the structure should be higher than the demand.

$$\text{Capacity} > \text{Demand} \tag{1.1}$$

The seismic capacity is increased by providing a large section, high-strength material in the conventional design method or adding bracing. It limits the seismic demand depending on the ductility of the material. In a capacity design approach, a longer period is obtained by yielding materials. This yielding is designed to occur, especially in the beams adjacent to beam-column joints. In the conventional approach, acceptable earthquake forces and energy transfer to the structure from the ground is allowed. The structural design provides sufficient capacity for the structure to withstand these substantial forces. Earthquake registrant design based on the abovementioned philosophies increases the overall cost of the structure.

The use of base isolation reduces the seismic demand of a structure. It decouples the superstructure from substructure parts by shifting the fundamental period of structures beyond the dominant period of ground acceleration. As a result, earthquake forces and energy transfer to the structure significantly reduces. It is achieved by installing a horizontally flexible but vertically stiff element called a seismic isolator between the superstructure and substructure.

Figure 1.7 shows the change of seismic demand of fixed base and base-isolated structures in terms of fundamental period T and damping characteristics. The top red curve shows the 5% damped acceleration response spectrum used to design a non-isolated building. A more extended period reduces the spectral acceleration as well as the inertia force during an earthquake. But it results in a large displacement of the base-isolator, and this displacement is inverse to the damping properties of the structure and the isolator. During an earthquake, the isolator undergoes large lateral displacement while the entire superstructure remains elastic. As a result, the floor acceleration and inter-story drifts are significantly reduced. The performance of base-isolated buildings during the 1994 Northridge earthquake (Kelly, 1997) and the 1995 Kobe earthquake (Pan et al., 2005) are the best practical examples to describe the seismic performance of base-isolated buildings.

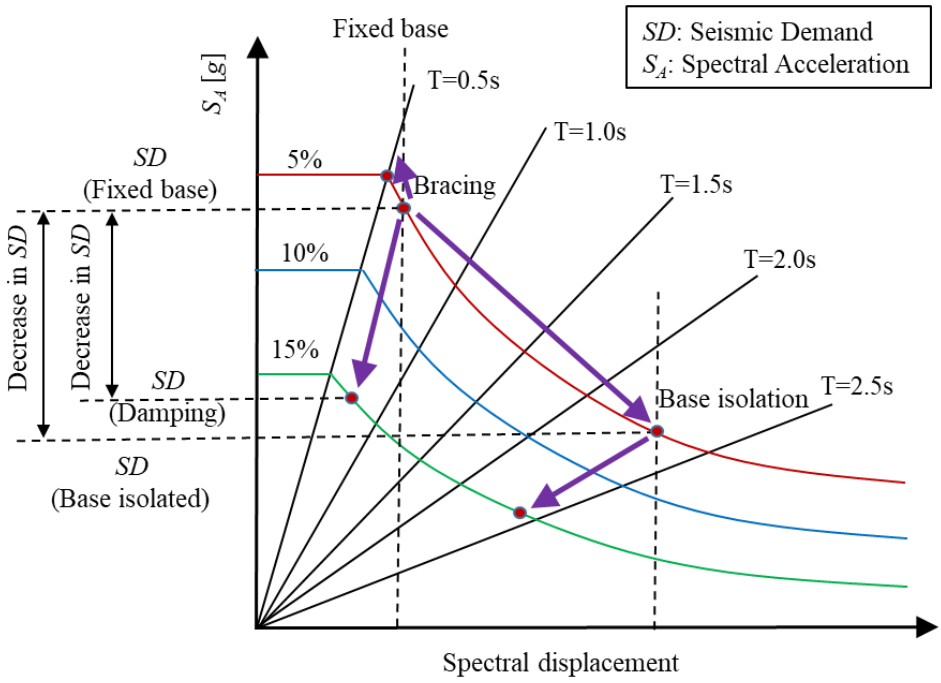

Figure 1.7 Response spectrum for different aseismic approaches and its effect on seismic demand (Mishra, 2012)

1.4 STRP Base Isolation

Turer and Özden (2008) first made an isolation device using scrap tire pads by stacking one above another without any adhesive. It was described as an innovative low-cost isolation method. However, unbonded layers of STP are impractical. Therefore, Mishra (2012) fabricated layer bonded and layer unbonded STRP isolators using scrap tire pads to study the feasibility of scrap tires in making seismic isolators. The preparation procedure of an STRP isolator from an automobile tire is briefly discussed by Mishra (2012). Figure 1.8a shows the preparation of a long rectangular specimen by removing the uneven tread part and sidewall. Then, the rectangular sample is cut into the required size. Figure 1.8b shows a single STRP specimen derived from Bridgestone 385/65R22.5 tire, 12 mm thick and typically has five steel-cord layers oriented by ±70° carcass steel. Large size isolator production is possible by stacking multiple strip-shaped specimens in alternating directions.

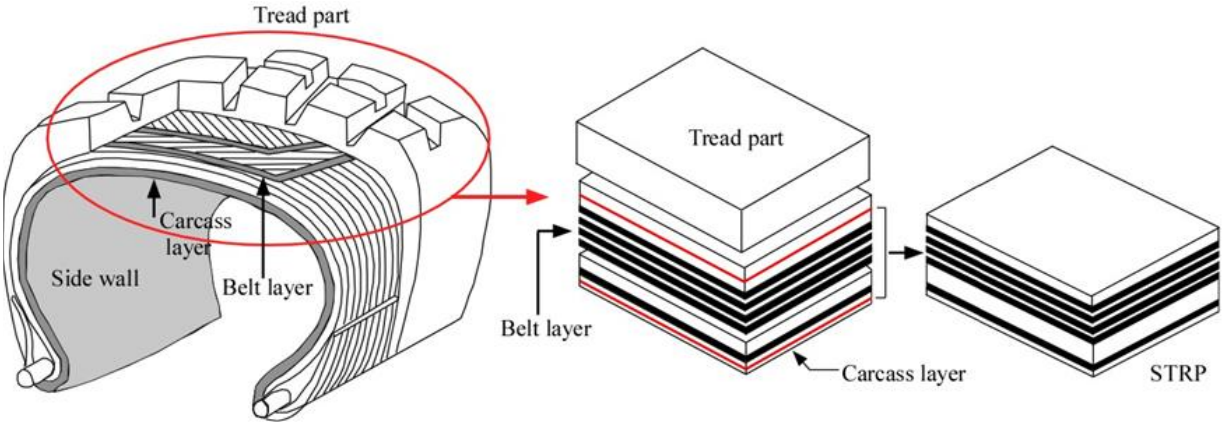

(a) Schematic presentation of STRP specimen preparation from tread part of an automobile tire

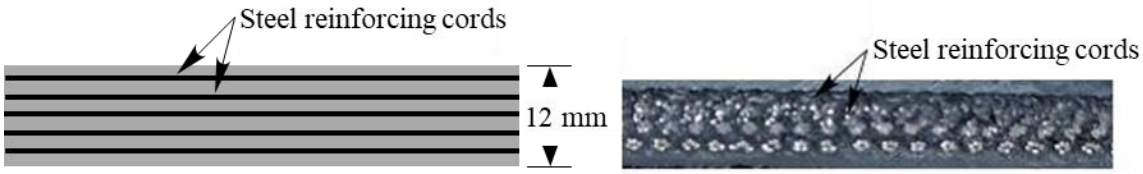

(b) Cross section of a single layer of STRP sketch and photograph

Figure 1.8 A schematic diagram of preparation procedure of a single layer STRP specimen from an automobile tire (Mishra, 2012)

Figure 1.9 shows the basic steps, and Fig. 1.10 describes a flowchart of preparation of the STRP isolator. First, the surface is made smooth using a belt sanding machine. Then, before applying adhesive, surface treatment was done using Chemlok 7701 primer to improve the bond receptibility. Finally, fusor 320/322 (Lord Corp.) epoxy adhesive material was used for bonding. Figure 1.9d shows the complete STRP isolators prepared and tested by Mishra (2012).

The experimental study shows bonding between layers of STRP improves its performance under vertical and horizontal load. Therefore, it was described that the STRP isolator is feasible for seismic isolation. However, several issues on STRP isolators remain unsloved and need to be investigated for practical implementation.

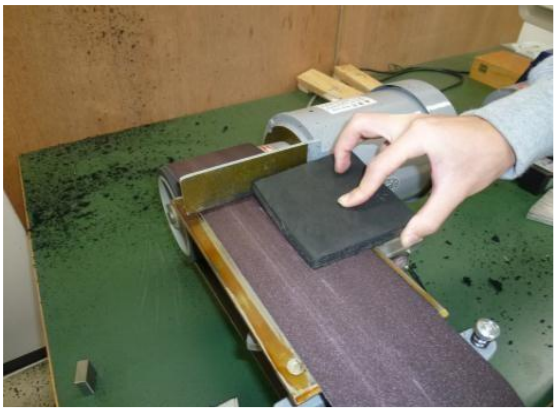

(a) Sanding of layer is in progress

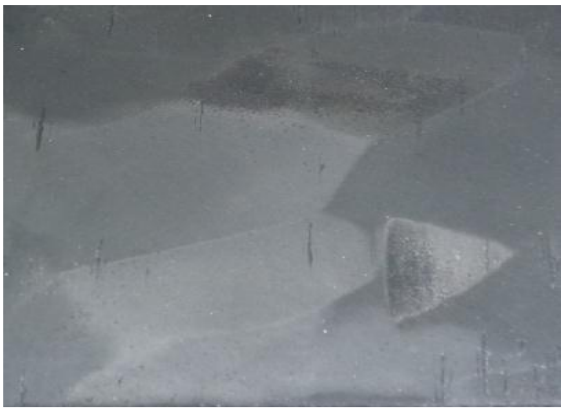

(b) Surface treatment by primer

(c) Adhesive on surface

(d) STRP isolator of 4-stacked STRPs

Figure 1.9 Procedure of manufacturing STRP isolator by stacking several STRP specimens (Mishra, 2012)

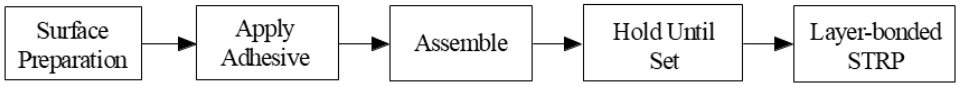

Figure 1.10 Basic steps involved in adhesive bonding of STRP layers.

1.5 General Features of STRP Isolators

An STRP isolator has some unique features that are different from a conventional elastomeric bearing. For example, an STRP isolator is fabricated from degraded automobile tires. In addition, reinforcement of STRP

isolator consists of steel cords placed in a layer and orientated in a specific direction, as shown in Fig. 1.11 and Table 1.1. In Bridgestone 385/65R22.5 tire, these cords are oriented by ±72° with the radial direction of the tires. These cords can resist the deformation of elastomer in the cord direction only, whereas bulging resistance of uniform in all directions in an elastomeric bearing. That is why an STRP isolator experiences unsymmetrical lateral expansion of elastomer.

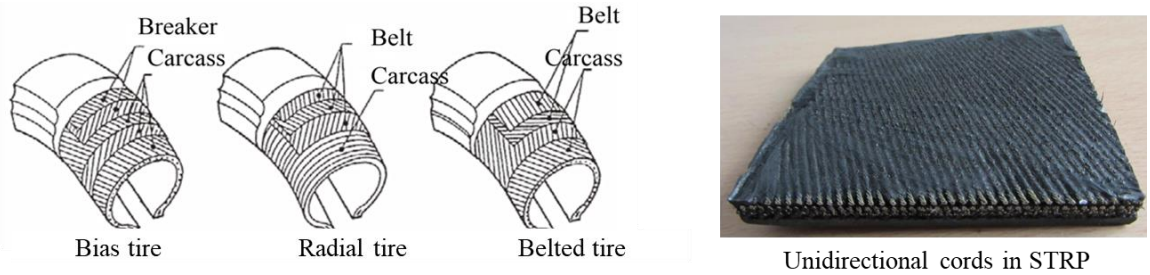

Figure 1.11 Orientation and arrangement of steel cord in different automobiles tire

Table 1.1 Orientation of steel cord in different automobiles tire

Tire Type	Ply angle	Belt angle
Radial Ply	70°~90°	10°~60°
Bias Ply	30°~40°	30°~40°
Belted Bias Ply	30°~40°	20°~30°

Besides, an STRP isolator is assumed to be installed without any mechanical fastening with the structure. This installation is preferable because it avoids significant tension generated within the elastomer in a bonded isolator. Because of unbonded application, the force-displacement behavior and deformation of the STRP isolator are different than that of the conventional isolator as shown in Fig. 1.12. It shows that an unbonded isolator rolls-off its surface from the support faces. As a result, the force-displacement relation is highly nonlinear, and the magnitude of lateral force at intermediate displacement decreases and then increases in large displacement. In contrast, the conventional bonded isolator does not display any rollover deformation.

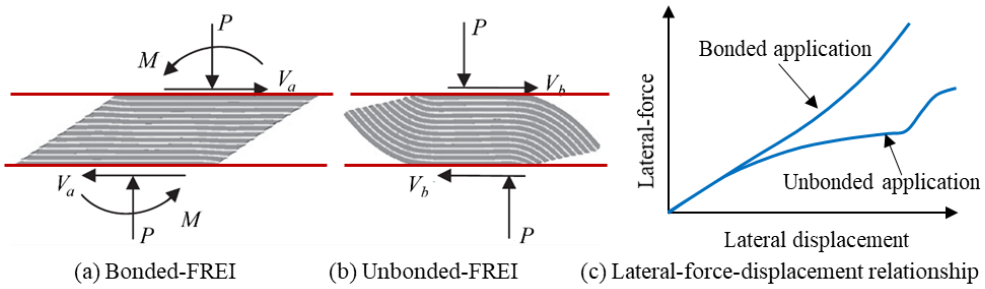

Figure 1.12 Typical deformation of unbonded STRP isolator and force-displacement curve

Considering the abovementioned unique features of the unbonded STRP isolator, the following issues should be carefully studied.

i. The STRP isolator is advantageous without any mechanical fastening with structure; however, a definite guideline or analytical solution to predicting the force-displacement response of the unbonded STRP isolator is still unknown.
ii. The reinforcement mechanism of the STRP isolators differs from that of the conventional isolator. Therefore, it might provide a different behavior and capacity of the STRP isolator, which raises the question of whether the STRP isolation performs equally with traditional isolation or not?
iii. The unbonded application has no established documentation on practical application. If an unbonded STRP isolator is utilized in a building, what would be the performance of the building and isolation system in natural earthquake conditions? Does unbonded application practical?
iv. Strip-shaped form of STRP isolator is economical for building with a non-rigid foundation. However, the lateral performance of strip-shaped isolators is still unknown. Therefore, it is appealing to investigate the beneficial aspect of strip-shaped isolators over a square-shaped isolator.
v. The strain-strain behavior of the STRP isolator is unknown and essential in the prediction of in-service loads on the STRP isolator.

Therefore, for a practical justification of an unbonded STRP isolator, a proper investigation of the abovementioned features is essential. In this dissertation, these issues are critically analyzed to reach a concrete conclusion.

1.6 Objectives of the Research

The STRP isolation system was proposed to overcome the cost barrier of the conventional systems and to facilitate the seismic design strategies and their implementation, especially in developing countries. For practical implementation of the STRP isolator, understanding of the design philosophy, nonlinear behavior under static and dynamic loading environments are necessary. Some recommendations left by the previous research for further improvement of the STRP isolation system are included in the current study.

An STRP isolator and its application method to actual structures without mechanical fastening are entirely different from conventional isolators. However, no documented method and design specifications for unbonded application of the STRP isolator are available. In addition, the STRP isolators and unbonded applications in an actual situation are unknown since no practical implementation, nor full-scale experimental studies are available. Therefore, it is essential to investigate the performance of the STRP isolator under lateral and vertical loads and seismic performance of STRP base-isolated buildings, including the unique features of the unbonded isolator to conclude whether an unbonded application is possible or not. Hence, the current study concentrated on the analytical prediction of the horizontal force-displacement relation, the lateral and vertical stiffness of unbonded isolation, and a hysteresis force model for practical design. Furthermore, the finite element method is used to analyze the STRP isolator since it can efficiently capture the unbonded boundary and geometric features of the STRP isolator.

The objectives of this study include the assessment of the lateral load performance of strip-shaped unbonded STRP isolators for different length-to-width ratios and square-shaped isolators for different heights. Furthermore, the displacement capacity and isolation period of unbonded STRP isolators are investigated at varying levels of seismicity using the equivalent lateral force method of the ASCE/SEI-7-10 code. In addition, the effects of biaxial cyclic displacement on the lateral performance of unbonded STRP isolator are also taken into consideration. In addition, the stress-strain condition in an unbonded STRP isolator is taken into consideration to determine the practical design load: compression, displacement, and rotation at the isolator-to-structure interface based on available code specifications.

1.7 Scope and Outline of the Dissertation

The following describes the scope and outline of the dissertation.

Chapter 1 includes the background, objectives, and scope of the study. It also briefs the principle, types, and historical development of the base-isolation system.

Chapter 2 is the literature review that briefs different low-cost isolation systems. It describes the past research on STRP isolators and their recommendation. It also summaries innovative ideas using scrap tires.

Chapter 3 is the theoretical background of the finite element analysis using MSC Marc-Mentat and the description of the FE analysis procedure. It outlines the elements used for FE modeling, material modeling, contact modeling, and analysis procedures for the dynamic and static environment.

Chapter 4 describes the lateral and vertical load performance of strip-shaped and square-shaped STRP isolators. It also contains an analytical formulation for horizontal and vertical stiffness and the load-displacement relationships. The seismic displacement demand and isolation period investigated based on ASCE SEI 7-10 code specifications are also summarized.

Chapter 5 is the stress-strain assessment of the unbonded STRP isolators for determining allowable design load: lateral displacement, compression, and rotation at the isolator-to-structure interface, based on the existing design guidelines. It also investigates the adequacy of steel cords in the STRP isolator.

Chapter 6 This chapter summarises the cyclic loading performance of square and rectangular shaped unbonded STRP isolators for biaxial displacement trajectories: circular, square, hourglass, and 8-shaped. In addition, performance for each unidirectional component of biaxial trajectories is also included. Finally, the performance of the isolator is documented in terms of the force-displacement relationship, stiffness, and effective damping ratio.

Chapter 7 includes the hysteresis force model for the unbonded application of STRP isolators. In addition, the calibration of model parameters and validation of the model is summarized.

Chapter 8 includes the conclusions of the present study and recommendations for future works.

References

Backhaus, R., Czaran, L. & Epler, N. et al. (2010): Support from space: The United Nations platform for space-based information for disaster management and emergency response (UN-SPIDER). Geoinformation for Disaster and Risk Management: Examples and Best Practices, 103–113.

Cardone D. and Flora A. (2016). An Alternative Approach for the Seismic Rehabilitation of Existing RC Buildings Using Seismic Isolation. *Earthquake Engineering & Structural Dynamics*, **45**, pp. 91-111.

Chimamphant S. and Kasai K. (2013). Comparative Response and Performance of BaseIsolated and FixedBase Structures. *Earthquake Engineering & Structural Dynamics*, **45**, pp. 5-27.

Cutfield M.R., Ma QT, and Ryan K.L. (2014). Cost-benefit analysis of base isolated and conventional buildings: A case study, Towards Integrated Seismic Design, 2014 NZSEE Conference, New Zealand,

ETRMA – European Tyre & Rubber Manufacturers' Association (Belgium), 2011. The Annual Report 2010/2011, Report downloaded from <http://www.etrma.org/default.asp> (May 2011).

Fenz, D. and Constantinou, M.C. (2006). Behaviour of the double concave Friction Pendulum bearing. *Earthq. Eng. Struct. Dyn., 35*, pp. 1403–1424.

Hadad H. A, Calabrese A., Strano S. and Serino G. (2017). A Base Isolation System for Developing Countries Using Discarded Tyres Filled with Elastomeric Recycled Materials, *Journal of Earthquake Engineering*, Vol. 21(2), pp. 246-266.

Haiti PDNA (2010). Haiti Earthquake PDNA: Assessment of damage, losses, general and sectoral needs, Prepared by the Government of the Republic of Haiti with support from the International Community.

Huang Y. N., Whittaker A. S., Kennedy R. P., and Mayes R. L. (2013). Response of Base-Isolated Nuclear Structures for Design and Beyond-Design Basis Earthquake Shaking. *Earthquake Engineering & Structural Dynamics*, **42**, pp. 339-356.

JATMA – The Japan Automobile Tyre Manufacturers Association NC (Japan), 2010. Tyre Industry of Japan 2010, Report downloaded from <http://www.jatma.or.jp/english/media/> (May 2011).

Kelly J.M. (1997), "*Earthquake-resistant design with rubber,*" 2nd Ed., London, Springer-Verlag.

Kelly M. J. (2002). Seismic isolation systems for developing countries. *EERI Distinguished Lecture*, *Earthquake Spectra*, 18(3), pp. 385–406.

Kenneth Pletcher (2008), Geography and History for Encyclopedia Britannica report "Great Wenchuan Earthquake, Wenchuan Da Dizhen, Wenchuan Earthquake, Wenchuan dizhen."

May P. J. (2002). Barriers to adoption and implementation of PBEE innovations. *PEER Rep. 2002/20*, Pacific Earthquake Engineering Research Center, University of California, Berkeley.

Mishara, H. K. (2012. "Experimental and Analytical Studies on Scrap Tire Rubber Pads for Application to Seismic Isolation of Structures." *Ph.D. Thesis*, Kyoto University, Kyoto, Japan.

Mishra H. K., Igarashi A., and Matsushima H. (2013a). Finite element analysis and experimental verification of the scrap tire rubber pad isolator. *Bulletin Earthquake Engineering*, 11(2), pp. 687-707.

Morales E., Filiatrault A. and Aref A. (2018), Seismic floor isolation using recycled tires for essential buildings in developing countries, *Bulletin of Earthquake Engineering*, Vol. 16, pp.6299–6333

Naeim F. and Kelly J. M. (1999). *Design of Seismic Isolated Structures: From Theory to Practice*, 1st ed.; John Wiley and Sons: Hoboken, NJ, USA.

Nepal Earthquake(2015): Post Disaster Needs Assessment, Vol. B: Sector Report, Government of Nepal, National Planning Commission, Singha Durbar, Kathmandu.

Pan P., Zamfirescu D., Nakashima M., Nakayasu N., Kashiwa H. (2005). Base-isolation design practice in Japan: Introduction to the post-Kobe approach. *Journal of Earthquake Engineering*, 9(1), pp. 147-171

Reisman J. I. (1997). Air emissions from scrap tire combustion, EPA-600/R-97-115 October 1997.

RMA – Rubber Manufacturers Association (USA), 2009. Scrap Tire Markets in the United States 9th Biennial Report, Report downloaded from <*http://www.rma.org/scrap_tires/*> (May 2011)

RMA 2011. US Scrap Tire Market Summary, Feb 2013, Washington, DC 20005. (⟨*http://www.rma.org/publications/scrap-tire-publications/market-reports*⟩).

Robinson, W. H., and Tucker, A. G. (1977). A Lead-Rubber Shear Damper. Bull. *New Zealand Natl. Soc. Eathq. Eng*., 10(3), pp. 151-153.

Shah B. V. (1983). Is the environment becoming more hazardous? - A global survey 1947 to 1980. 7(3), pp. 202-209, https://doi.org/10.1111/j.1467-7717.1983.tb00822.x.

Touaillon J. (1870). Improvement in buildings. U.S. Patent No. 99. 973, 1870

Tsang, H-H., Lo S. H., Xu X., and Sheikh M. N. (2012). Seismic isolation for low-to-medium-rise buildings using granulated rubber–soil mixtures: numerical study. *Earthquake Engineering Structural Dynamics*, 41(14), pp. 2009-2024.

Turer A. and Özden B. (2007). Seismic base isolation using low-cost scrap tire pads (STP). *Materials and Structures*, 41(5), pp. 891-908.

Warn, GP; Ryan, K.L. (2012). A Review of Seismic Isolation for Buildings: Historical Development and Research Needs. *Buildings*, *2*, pp. 300-325.

WBCSD (2010) – World Business Council for Sustainable Development, (Switzerland), 2010. End-of-Life Tyres: A Framework for Effective Management Systems. Report downloaded from <*http://www.wbcsd.org/templates/TemplateWBCSD5/layout.asp?MenuID*=1> (May 2011)

Yang J., Chen J., Liu H. and Zheng J. (2014). Comparison of two large earthquakes in China: the 2008 Sichuan Wenchuan Earthquake and the 2013 Sichuan Lushan Earthquake, *Natural Hazards*, Vol. 73,1127–1136.

Chapter 2

Literature Review

2.1 Introduction

The previous chapter urged the need for low-cost seismic isolation for general structures that should be affordable within the purchasing capacity of low-income groups. This chapter includes the experimental, analytical and finite element analysis works on different low-cost base-isolation methods, including materials, fabrications, and operating principles. In addition, other innovative concepts using automobile scrap tires and the previous research and their recommendations for further study on the isolator made with scrap tires rubber pad (STRP) are briefly discussed.

2.2 Review of Research on Low-cost Seismic Isolation

2.2.1 Fiber-Reinforced Elastomeric Isolator

2.2.1.1 Experimental works

Kelly (1997) suggested replacing the steel shims of elastomeric isolators using the fiber reinforcement, and the isolator is termed fiber-reinforced elastomeric isolator (FREI). Kelly and Takhirov (2002) and Kelly and Konstantinidis (2011) investigated the mechanical characteristics of FREIs by experimental and theoretical works. They concluded that the performance of unbonded FREIs is comparable to that of the SREIs. Figure 2.1 shows a photograph of the unbonded FREIs they tested. Konstantinidis et al. (2008) and Konstantinidis and Kelly (2014) addressed the limitation of SREI for low-cost structures. They replaced the steel shim using flexible, thin steel plates and excluded the thick endplates for fastening. The tested unbonded bearings survived large shear strains comparable to the strains of the conventional isolators under seismic loading.

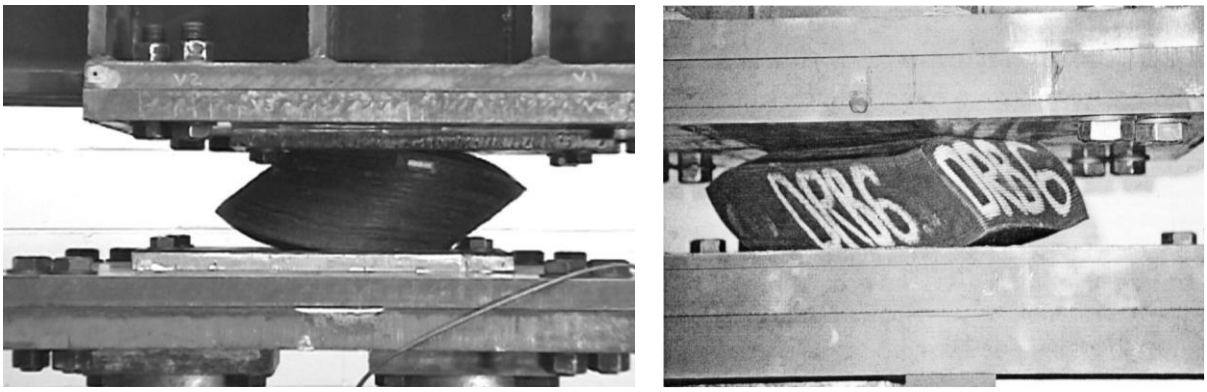

(a) (b)

Figure 2.1 Deformed state of unbonded FREI (a) Specimen J07 at 150% shear (Kelly and Takhirov (2001) (b) Specimen DRB6 at 100% shear (45°) (Kelly, 2001)

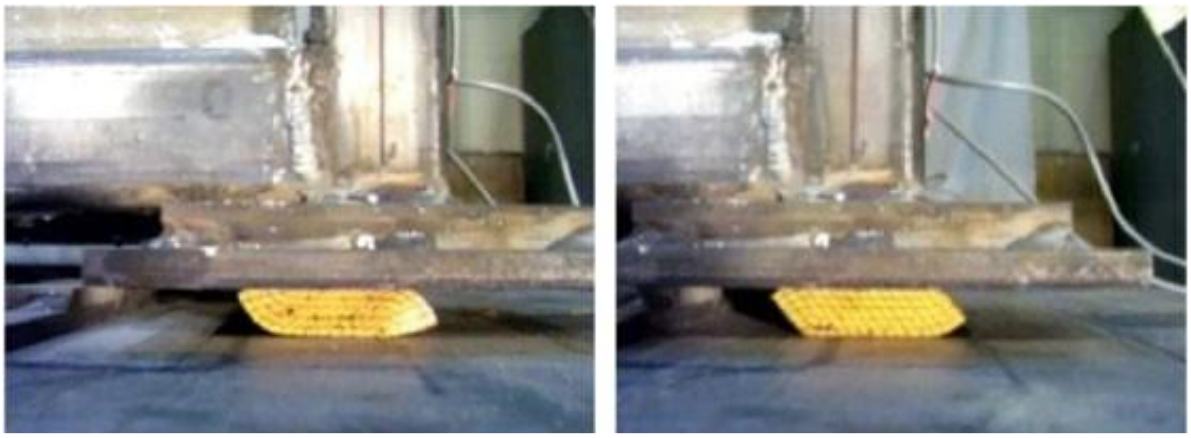

(a) (b)

Figure 2.2 Deformation of unbonded fiber-reinforced elastomeric isolator during shake table testing at the time instant of peak lateral displacement (Toopchi-Nezhad et al., 2009).

Toopchi-Nezhad et al. (2008a; 2008b; 2009a; 2009b) manufactured and tested FREIs made with carbon fiber. These studies investigated the lateral response characteristics and the role of the aspect ratio on the same, the sensitivity of stable-FREIs to lateral load and vertical pressure, and the seismic demand of unbonded FREIs. The findings indicate that FREIs may be effectively used in seismic mitigation of low-rise buildings with a fixed-base period of around 0.2 s and a 5% damped spectral acceleration at 1 s period up to 0.5 g. The effect of the vertical pressure on the lateral response can be neglected when the bearings are used in low-rise buildings. Authors addressed that FREIs are superior to SREIs in consideration of the

damping, cost-effectiveness, lightweight property, and the fabrication procedure. A shaking table test (Toopchi-Nezhad et al., 2009b; Huang et al., 2010; Losanno et al., 2019b) of base-isolated frames proved the stability and re-centering capability of unbonded FREIs. Figure 2.2 shows the photograph of isolators during the shaking table test (Toopchi-Nezhad et al., 2009b). Moon et al. (2002a, 2002b) compared the mechanical characteristics of the FREI made with different kinds of fiber with a similar SREI. They concluded that unbonded FREI is superior to that of the SREI in terms of vertical stiffness and effective damping. Strauss et al. (2014) identified the influence of the vertical stress, horizontal deflection, bearing height, the number of elastomer and reinforcement layers, reinforcement material, and types of bearing support on the effective shear modulus and damping ratio. It shows that the stiffness and damping ratio reduced in the shear deformation range between 10% to 100%. Al-Anany et al. (2017) described that the shape factor strongly influences the vertical response while the aspect ratio controls the stability of unbonded FREIs. The aspect ratio for a stable unbonded isolator should be larger than 2.50 (Van Engelen et al., 2015; Toopachi-Nehzad et al., 2008b; Osgooei et al., 2014).

An unbonded isolator cannot resist tension, making it unsuitable where overturning or vertical accelerations are anticipated. Besides, an unbonded isolator transfers the lateral load via friction and could potentially slip, resulting in permanent displacements. Van Engelen et al. (2014a) and Toopchi-Nezhad et al. (2019) proposed that a portion of FREI can be bonded without substantially altering the roll-over characteristics and the horizontal force-displacement relationship than that of a conventional unbonded stable-FREI. De Raaf et al. (2011) and Pauletta et al. (2015) investigated the conditions leading to instability of stable-FREIs using dynamic and monotonic lateral load tests. An unbonded FREIs exhibits superior buckling performance and no roll-out instability until 300% shear strain. The effect of the loading direction on unbonded FREIs was studied by Das et al. (2014; 2016) and Ngo et al. (2017). It indicated that the stiffness increases while the damping decreases for an orientation of the input displacement. Das et al. (2016) conducted a shaking table test for different loading directions on a 2-story building for a fixed base condition and then isolated with FREI, as shown in Fig. 2.3. The dynamic response of the base-isolated structure was compared with the same building's response without a base-isolation system. This study demonstrated that the seismic performance of the unreinforced masonry building is improved when unbonded FREIs are installed below the structure.

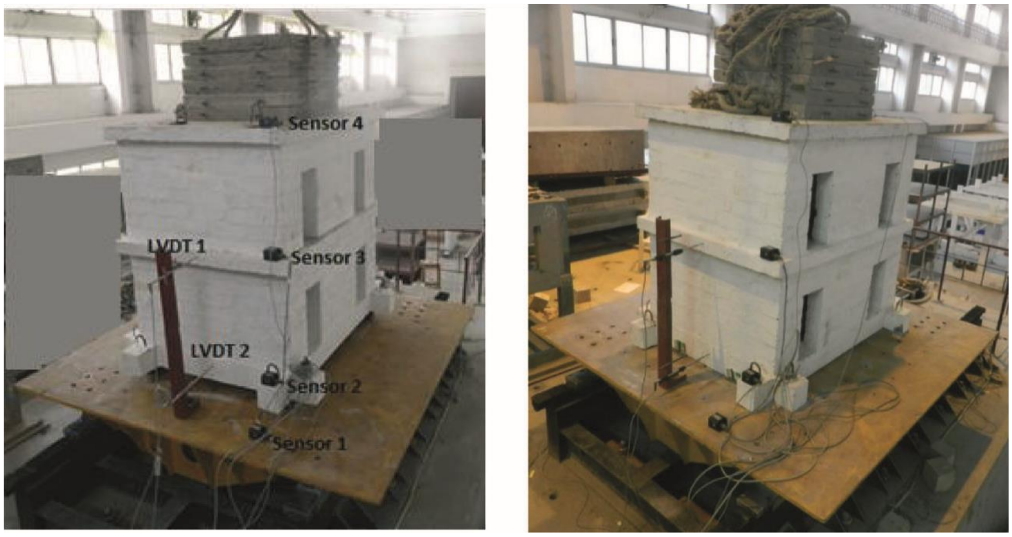

(a) Base isolated (BI) building (b) Fixed based (FB) building

Figure 2.3 shaking table test conducted by Das et al. (2016)

Tan et al. (2014) fabricated PFRI bearing with unsaturated polyester fiber made of polyester and glass fiber cloth, as shown in Fig.2.4. Its fabrication cost is 10% lower than that of the SREI. The damping ratio of PFRI is about 8~23%, and it can sustain 250% shear deformation without any damage. The compression modulus of PFRI is higher than that of the AASHTO LRFD guidelines for bonded isolators. The stress demand on rubber and reinforcement is low because of low horizontal stiffness and roll-over deformation.

Figure 2.4 PFRI isolator made and tested by Tan et al. (2014)

Xiao et al. (2004) proposed sliding-type isolation using sand, lighting ridge pebble, polypropylene and PVS sheet, and polythene membrane. Nanda et al. (2015) studied four friction isolation interfaces: marble–marble, marble–high-density polyethylene, marble–rubber sheet, and marble–geosynthetic. They also experimented a half-scale masonry building rested on marble–high-density polyethylene. Tsiavos et al.

(2020) conducted an experimental investigation of a low-cost PVC 'sandwich (PVC-s) seismic isolation. Figure 2.5 shows the schematic view of PVC sandwich seismic isolation, and Fig. 2.5a and 2.5b show the deposition of sandwiched sand and the bottom of PVC surface after sand deposition. Jampole et al. (2016) proposed a high-density polyethylene slider on a galvanized steel surface. The goal of these studies was the experimental assessment of low-cost seismic isolation using domestic material. The primary challenge is restoring capability. Besides, sliding of isolation affects the utilities even though flexible utilities are recommended. The isolations proposed by Xia, Nanda, and Tsiavos increase the construction cost because it requires two rigid slabs to install the isolation material. Besides, damage of sliding material and their replacement are additional problems.

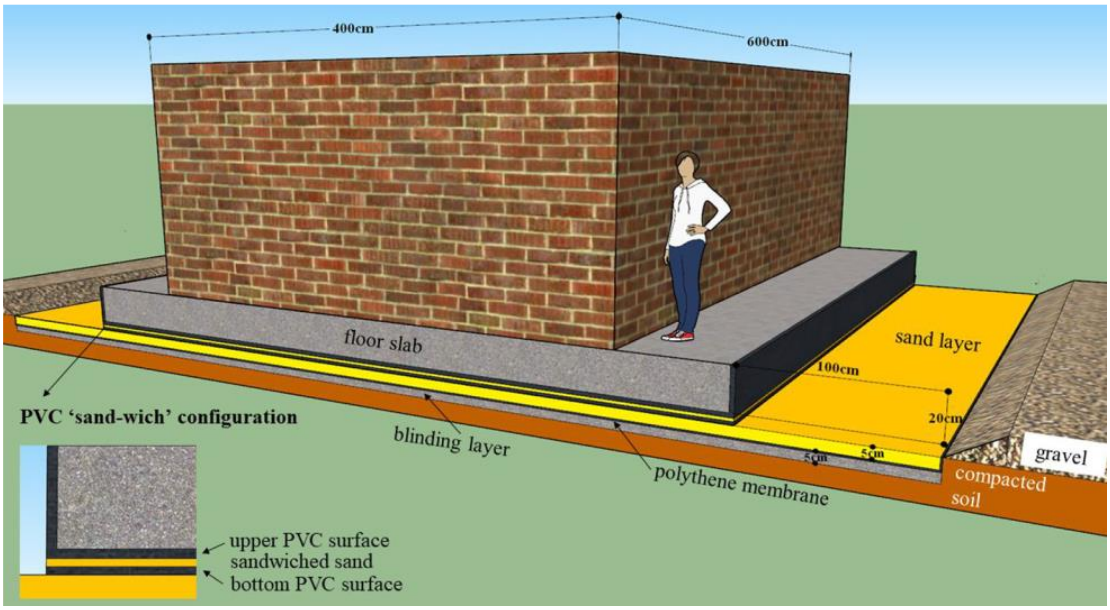

(a) Masonry school prototype structure located in Nepal (dimensions in cm).

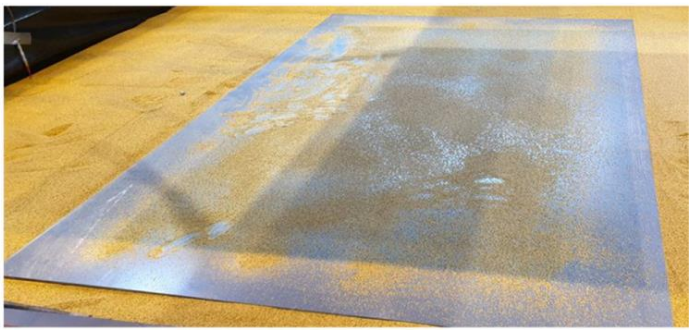

(b) Deposition of sandwiched sand and (c) bottom PVC surface after sand deposition

Figure 2.5 Schematic view for low-cost PVC sandwich seismic isolation (Tsiavos et al., 2020)

2.2.1.2 Analytical works

Tsai and Kelly (2001, 2002a, 2000b) derived the compression stiffness and tilting stiffness of fiber-reinforced bearings of infinite-strip, circular and rectangular shapes by assuming that the elastomeric layer is incompressible, and the reinforcement is flexible. Recently, bulk compressibility is included in the stiffness analysis of fiber-reinforced isolators of infinite-strip shape (Kelly, 2002; Kelly and Takhirov, 2002). Moon et al. (2003; 2004) experimentally and theoretically studied the compression and bending stiffness of strip-type FREIs with flexible fiber reinforcement. Toopchi-Nezhad et al. (2011) determined the horizontal stiffness of bonded FREI using a closed-form elastic solution (Tsai and Kelly, 2005). An unbonded FREI display peculiar roll-over deformation and force-displacement relationship, which are different from SERI, as shown in Fig. 2.6. Closed-form solutions for the lateral response of unbonded isolators were proposed based on the assumption that the roll-over surface is stress-free. Peng et al. (2007) derived a relationship assuming that the rubber is linear elastic. Konstantinidis et al. (2008) suggested a lower bound relation based on the assumption that the isolator's roll-over part is stress-free and has no resistance to the lateral load. Van Engelen et al. (2015) considered the combined action of bending and shear within the roll-over, whereas pure shear acts within the central elastomer. Toopchi-Nezhad (2014) proposed upper and lower bound values of the effective area of an unbonded isolator that has resistance to horizontal load. These approaches ignored the strain dependence of the shear modulus of elastomer (Gerharer, 2010; Gerharer et al., 2011) and the effect of vertical compression. Losanno et al. (2019a) derived an expression for the horizontal stiffness of unbonded FREIs considering the vertical compression. Osgooei et al. (2017) developed a Pivot-Elastic model that combines a bilinear pivot hysteretic model with a nonlinear elastic spring. Manzoori and Toopchi-Nezhad (2016) extended the Bouc-Wen model for the nonlinear hysteretic response of stable-unbonded FREIs. Toopchi-Nezhad et al. (2017) developed an algorithm for the design of structures supported by unbonded-FREIs. Chaghakaboodi and Toopchi-Nezhad (2020) studied the wind induced behavior of a stable-FREI system.

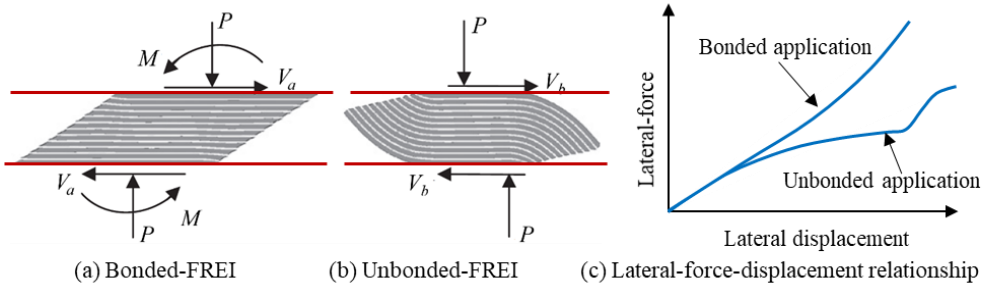

Figure 2.6 Free Body Diagram of Fiber-Reinforced Elastomeric Bearing

2.2.1.3 Finite element studies

Finite element analysis is a powerful method widely used for nonlinear elastomeric isolators simulations under a large displacement domain. It is furnished with different elements and material models for rubber-like material. The Mooney-Rivlin, Neo-Hokean, Odgen models are more rational and effective in predicting the large-strain behavior of elastomeric bearings. Mordini and Strauss (2008) and Osgooei et al. (2016) investigated the stiffness behavior of FREI using FE analysis. Osgooei *et al*. (2014a, 2014b, 2015), Ping et al. (2014) studied the stresses-strains relation in the FREIs for orientation of lateral load, the flexibility of reinforcement, and modified shape of rectangular FREIs, using FE analysis. These studies investigated the general circumstances of stress-strain demand in elastomer and reinforcement. Some research focused on the stress-strain relationship of unbonded FREIs. Toopchi-Nezhad *et al*. (2011; 2012) used the hyperelastic model to study the influence of shape factors on the response of unbonded FREI and stress-strain demand of elastomer fiber reinforcement. It was demonstrated that unbonded FREIs significantly lower the stress demand in elastomer, reinforcement, and bonding between fiber-reinforcement and elastomer. Toopchi-Nezhad (2014). Al-Anany and Tait (2017) mentioned that the isolator's low aspect ratio delays lift-off occurrence and reduces the stress-strain rate under rotational deformation. Van Engelen et al. (2014a; 2014b) used the FE method to study the stress-strain behavior of modified, bonded, and partially bonded FREIs. Ngo et al. (2017) studied the loading direction effect on the lateral response of the square-shaped FREI. It used the 3-terms Oden model to model the hyper - elastic behavior of the elastomer and Prony Viscoelastic Shear Response parameters model for the viscoelastic behavior. Dezfuli and Alam (2014) employed a hyper-viscoelastic model to simulate the nonlinear behavior of natural rubber under combined vertical pressure and cyclic lateral displacements. This parametric study investigated the effect of the thickness and the number of elastomer and fiber-reinforcement layers on the horizontal and vertical response of FREI. Habieb et al. (2017; 2018) adopted the Yeoh hyperelasticity model to study the FREI undergoing moderate and large deformations and masonry houses supported by FREI.

2.2.2 Seismic Isolation Using Automobile Tire

Geotechnical seismic isolation using rubber-soil mixtures (RSM) was introduced by Tsang (2008) and Tsang *et al*. (2012). It can significantly benefit ordinary buildings for which resources and technology are inadequate for earthquake mitigation with SREI or FREI system. Figure 2.7 shows a model of a 10-story building of width 40 m isolated with RSM. The effectiveness of RSM was studied by Madhusudhan et al.

(2019), Xiong and Li (2013) and Pistolas et al. (2020), and FE studies by Tsang et al. (2012) and Nanda et al. (2018) found that RSM isolation reduces the superstructure response by 40-60%. The potential problem is that the structure must be detached from the ground, particularly unfavorable even for small residential buildings. Besides, the cost of excavation and replacing soil for deep foundations may not be justifiable.

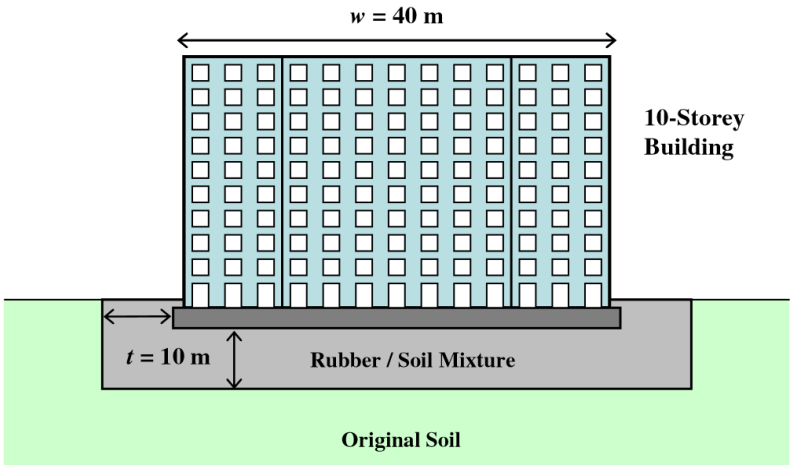

Figure 2.7 Schematic view of rubber-soil mixture isolation (Tsang et al., 2012)

Turer and Özden (2008) proposed a low-cost isolation system using scrap tire pads (STP) as described earlier. They performed compression and cyclic loading test on STP isolators made by stacking STP one above another without adhesive, as shown in Figure 2.8. The average compression that ruptured the steel-cords was 8.5 MPa, and the horizontal stiffness and damping ratio were reported 500~100 kN/m and 18~22%, respectively. Thus, it can be an innovative low-cost method of seismic isolation, but unbonded layers of STP are unsuitable for practical application.

(a) Stacked STP specimen (b) Inclined compression test setup

Figure 2.8 Stacked STP and inclined loading test on stacked STP isolator (Turer and Özden, 2008)

Hadad et al. (2017) used discarded Kart tires filled with recycled elastomeric materials and aggregates that proved sufficient vertical and horizontal stiffness and damping ratio of about 23~30%. A shaking table test of one-story and one-bay steel frames showed an excellent enhancement of the base-isolated structural response and no residual deformation within the isolator. The challenges arise from fire resistance, effects of ambient conditions, tire dimensions, the amount of filling material, and the size of the filling grains. The impact of these factors on the dynamic response of the isolators needs to be considered. Figure 2.9 shows the model and experiment done by Hadad et al. (2017).

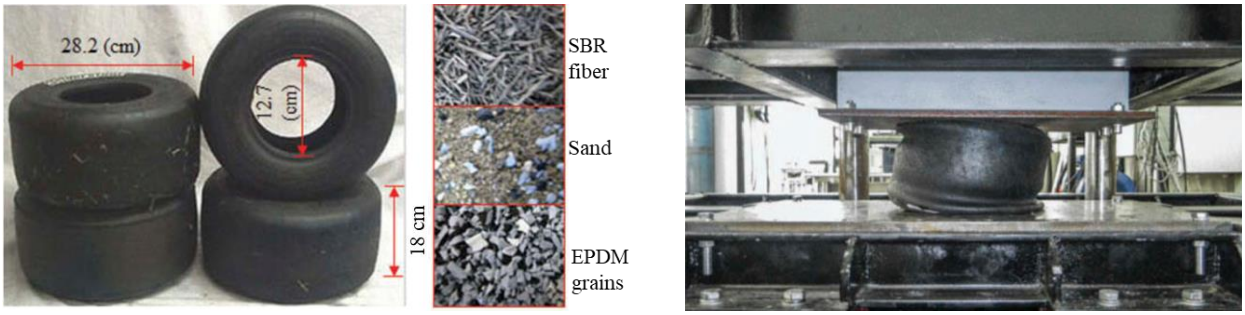

(a) Kart tires and the filler materials (b) Specimen filled with EPDM grains under shear testing

Figure 2.9 Discarded tire isolator filled with recycled elastomeric materials (Hadad et al., 2017)

Morales et al. (2018) proposed a recycled tire bearing (RTB) system consisting of tires cut through their diameter and then inserted between the structural slab of a designated room and a service floor surface, as shown in Fig.2.10. Figure 2.10b shows an RTB unit, and several units can be used for lateral and vertical stability of the supporting parts. The floor surface is locked with RTB, and the bottom part of each tire is inserted in a groove in the bottom plate. The base plate slides horizontally towards the opposite edge of the tire, whose sliding is prevented by a stopper under an in-plane horizontal load. The bottom parts of the tire are allowed to uplift from the base grooved plates that induces rocking motion of the tire under extreme out-of-plane seismic loads. The vertical vibration, rocking motion, and pre-compression force that affect the supporting structure's performance are the challenges in this system.

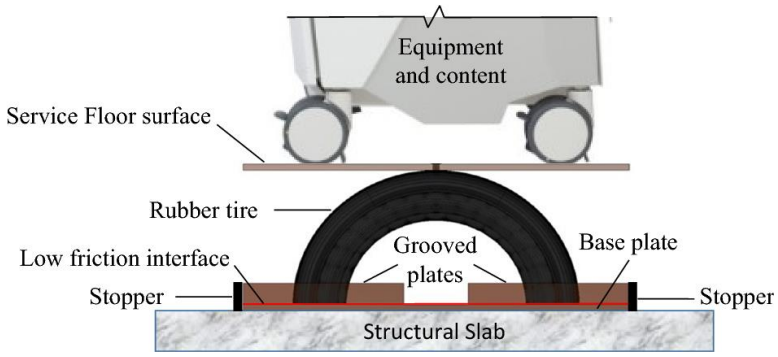

(a) Geometry of RTB floor isolation system

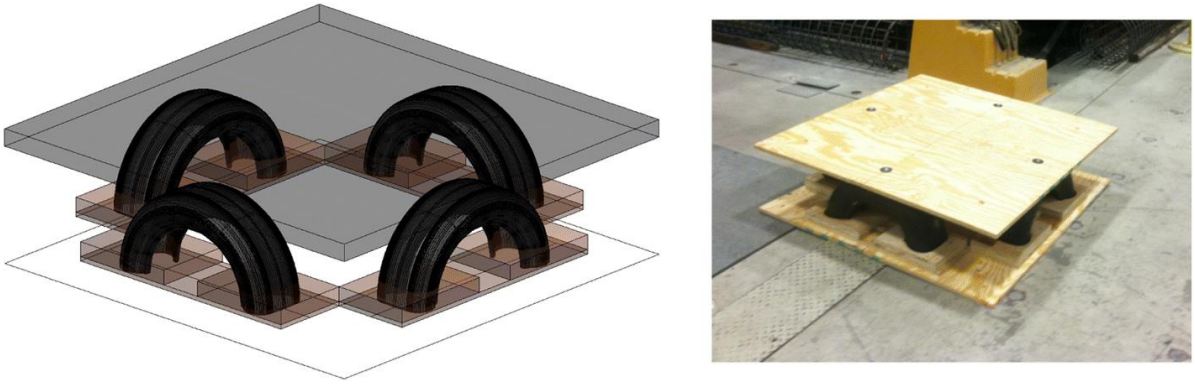

(b) RTB building block

Figure 2.10 recycled Tire Bearing (RTB) system (Morales et al., 2018)

Spizzuoco et al. (2014) proposed Recycle Rubber-Fiber Reinforced Bearing (RR-FRB) made with recycled-tire chips and carbon and polyester fibers. It is more advantageous than the SREI or FREI in dissipation capacity, manufacturing cost, and weight. The drawbacks are the low shear strain and tensile strength. Shaking table test results (Calabrese et al., 2015; Maddaloni et al., 2017) show that the roof acceleration and the story drift are substantially reduced than that of the fixed base structure. Figure 2.11 shows the RR-FRBs and shaking table test of an RR-FRB base-isolated frame.

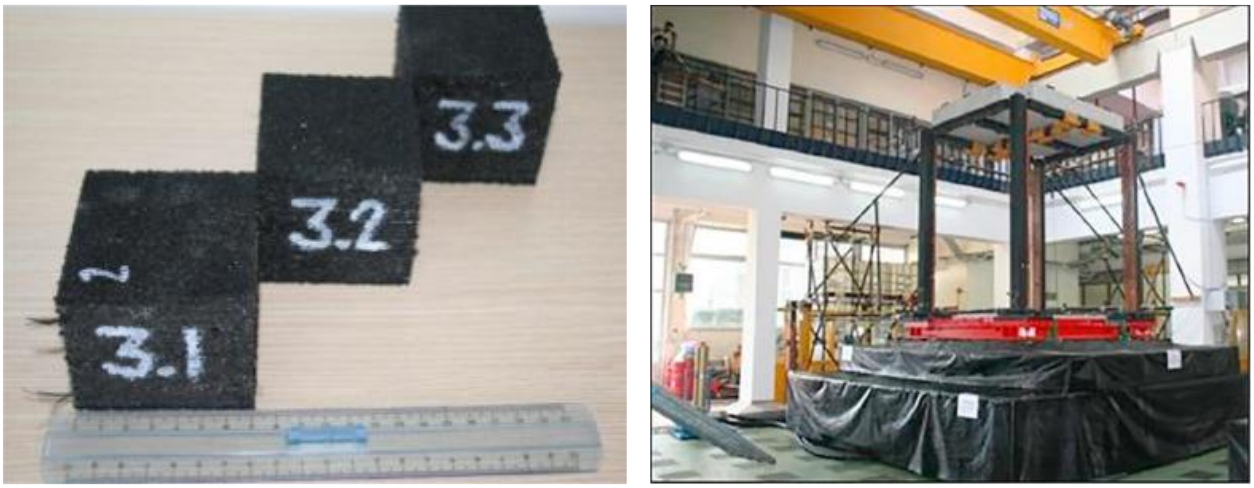

(a) RR-FRB (b) Shaking table test of RR-FRB isolated frame

Figure 2.11 RR-FRBs and shaking table test of RR-FRB isolated frame Calabrese et al. (2015)

Losanno et al. (2019a) derived an analytical expression of horizontal stiffness of an unbounded isolator, including the reinforcement characteristics, the effective area, and the shear modulus. A bidirectional shaking test (Losanno et al., 2019b) found the robust behavior and good re-centering capabilities of RR-FRBs and mentioned that RR-FRBs are viable seismic mitigation for structures. Finally, Losanno et al. (2020) reviewed recycled versus natural-rubber FREIs and claimed that the performance of natural-rubber FREIs is better than that of recycled rubber FREIs. However, recycled rubber devices are promising in protecting non-engineered constructions from moderate to high seismic inputs at a fraction of conventional technologies' cost.

2.3 Review of STRP Isolation System

Mishra et al. (2013b) conducted uniaxial tensile tests using a 2.0 mm thick dumbbell specimen derived from Bridgestone 385/65R22.5 tire. The objective of that test was to determine the hyperelastic parameters of scrap tire rubber. Figure 2.12 shows the experimental test data and three-term Mooney-Rivlin curve fitting for the same. The hyperelastic constants were then verified by performing FE analyses.

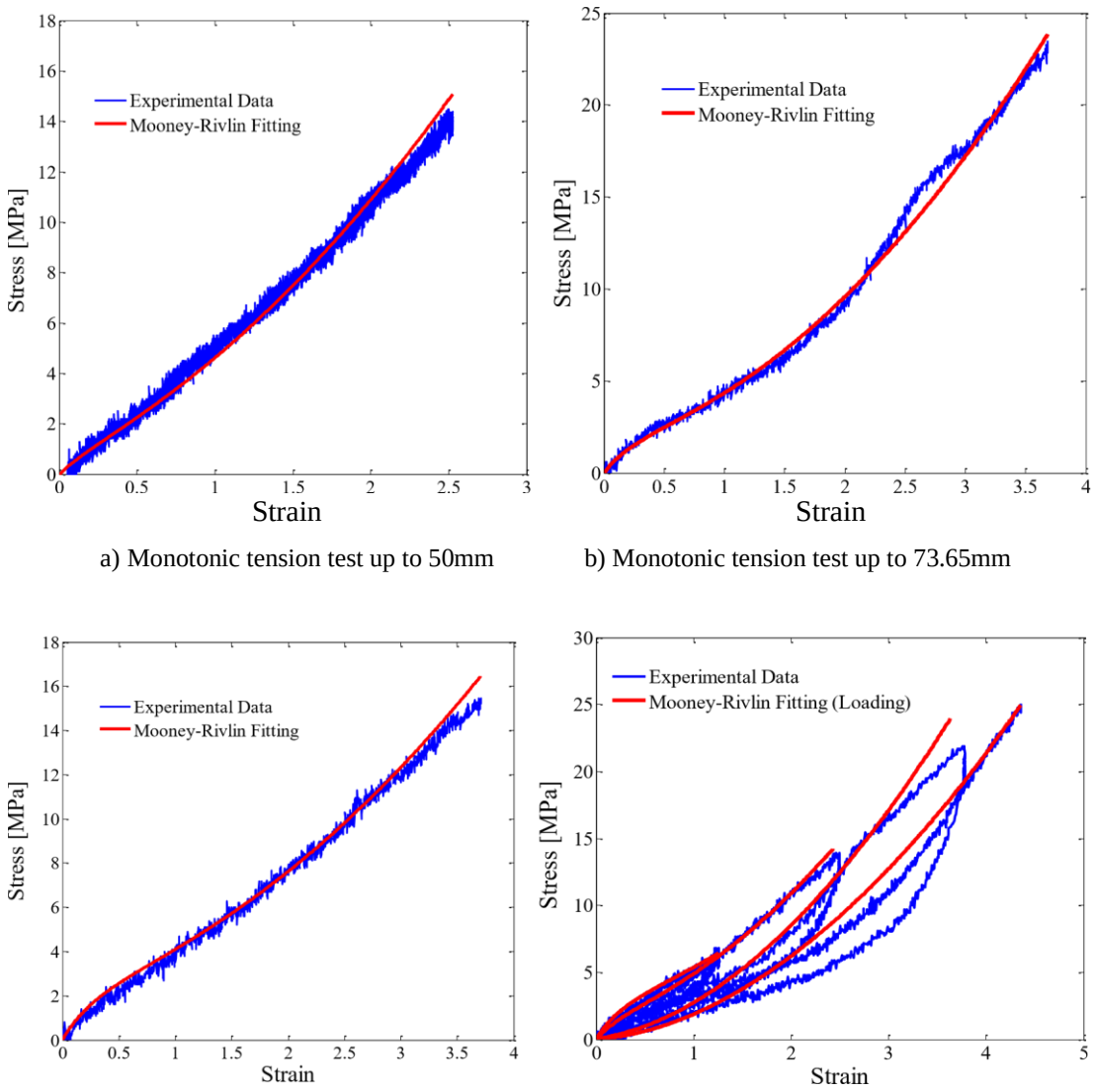

a) Monotonic tension test up to 50mm b) Monotonic tension test up to 73.65mm

c) Monotonic tension test up to 74.2mm d) cyclic tension test up to 87.2mm

Figure 2.12 Experimental test data and Mooney-Rivlin curve fitting (a)-(c) monotonic uniaxial tension test and (d): cyclic uniaxial tension test.

Layer bonded and layer unbonded STRP isolators were tested (Mishra et al., 2013a; Mishra et al., 2013b) under compression and combined compression and lateral load to determine the compression modulus and stiffness properties. Table 2.1 describes the experimental conditions and results of these tests. The deformation and stiffness properties of the layer bonded STRP isolator are found to be superior to that of the layer unbonded STRP isolator. These experiments were conducted under small lateral deformation (150%), and it is necessary to investigate the performance of these bearings for large lateral deformation (250%).

Table 2.1 Compressional and Cyclic shear test result (Mishra et al., 2013a; Mishra et al., 2013b)

Isolator	Compression test				Cyclic shear test			
	Vertical pressure (MPa)	K_v (MN/m)	E_c (MPa)	f_v (Hz)	Vertical pressure (MPa)	Max. lateral deformation	K_h (kN/m)	β%
Unbonded	9.19	21.6	155.5	11.4	5.0	80%	142.8	12%
STRP-6	11.66	20.7	149.0	11.2	5.0	103%	102.2	
Bonded	20.0	50.98	244.7	17.43	10.0	150%	85.3	18%
STRP-4	20 ∓ 4	56.41	270.8	18.34	5.0	150%	124.0	15%

A pseudo-dynamic test of a 1/3rd scale STRP isolator model is carried out STRPs (Mishra et al., 2014) using the 100% and 150% acceleration of the N-S component of the El-Centro record of the Imperial Valley 1940 earthquake. Figure 2.13 shows the test conditions, and Fig. 2.14 shows the photograph of the deformed shape of the unbonded STRP isolator. Under 150% acceleration input, deformation in the STRP isolator is found less than 100%. Both floor acceleration and story drift are reduced significantly. This test does not represent an unbonded STRP isolator's practical features during the service period. Since an unbonded isolator transfers lateral load via friction, overturning in an actual building is essential. Mishra (2012) performed a bidirectional analysis using SAP2000. The FE model of the unbonded isolator in that study was impractical since isolators are represented by bonded spring.

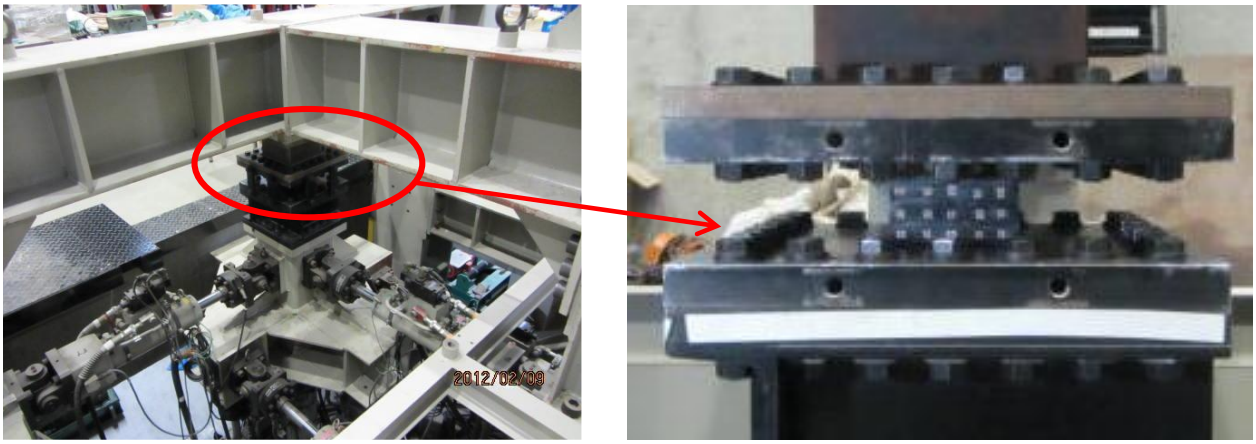

Figure 2.13 Overview of the pseudo-dynamic test (Mishra et al., 2014)

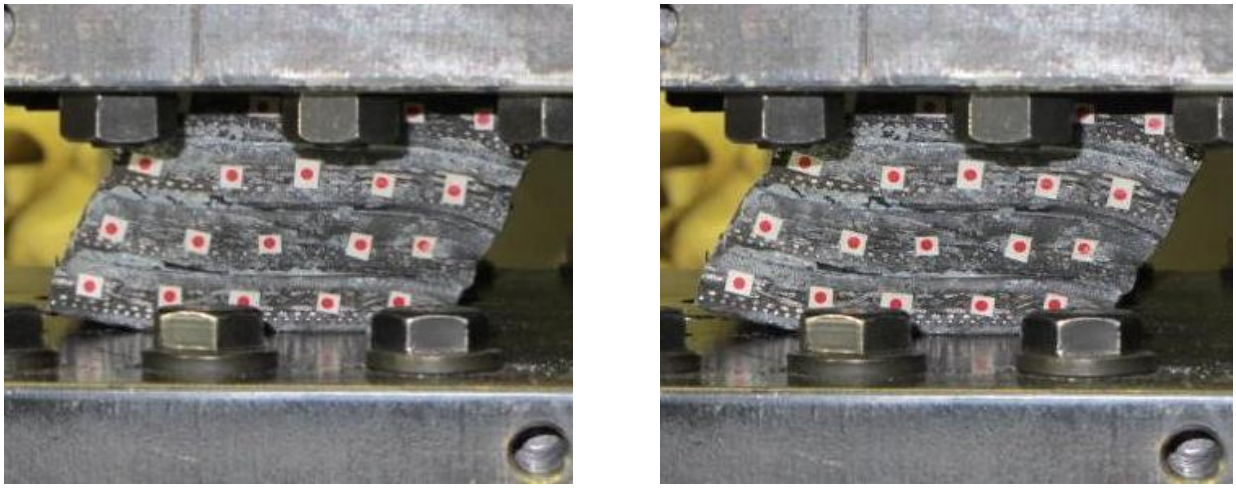

(a) 70% shear strain (b) 100% shear stain

Figure 2.14 Photographs showing lateral deformation of 1/3rd scale STRP model (Mishra et al., 2014)

The STRP isolator model used in the previous study had an aspect ratio of 1.39 (layer unbonded), and 2.08 (layer bonded) are impractical concerning buckling and lateral stability. Besides, the maximum horizontal displacement of STRP between 100% and 150% of shear strain is insufficient for evaluating isolators at large displacement when conventional elastomeric bearings are designed for 300% to 500% shear deformation. Therefore, only square-shaped isolators were investigated even though strip-shaped isolator is more economical for masonry or ordinary buildings without any rigid foundation.

The steel cords in a radial tire are orientated between 10° and 60° to the carcass steel (Ishikawa 2011). This steel cord resistance against elastomer bulging is negligible along its orthogonal direction. Twisted steel cords are more extensible and flexible than fiber material or steel shims and affect rubber-cord composite stiffness. The steel-cord orientation also affects the stiffness of cord-rubber composite (Shield and Costello, 1994). These features make STRP isolators different than that of the SREIs or FREIs.

2.4 Recommendations of the Previous Study

The previous study on the STRP isolator recommended further research on:

i) Bidirectional cyclic shear test and identification of the STRP isolator properties.

ii) Shaking table test of the STRP base-isolated structure to study the dynamic response of the isolation system and the base-isolated structure.

iii) An analytical model based on geometric and material properties of the STRP isolators to predict the vertical stiffness, horizontal stiffens, and force-displacement relationship.
iv) Long-term durability test of STRP bearings under vertical load and environmental loads such as temperature and moisture.

2.5 Conclusions

The works mentioned above are aiming to study the feasibility of low-cost seismic isolation applicable for ordinary buildings, especially in developing countries. Several promising methods, including replacing steel shims of SREIs using thinner flexible steel plates, carbon, glass, or polyester fiber, have been verified. Others encouraged domestic production of seismic isolators using automobile tires, rubber-soil mixture, sliding isolation using sand, lighting ridge pebble, polypropylene, PVS sheet, and polythene membrane. The scrap tire is a promising material with two-fold beneficial aspects: reducing environmental pollution and seismic mitigation for ordinary structures.

Research on the FREI system advances significantly through experimental tests, analytical approaches, and FE simulation. These include the design and manufacturing of FREIs, investigation of lateral stability and horizontal load performance of unbonded isolators, stiffness and damping properties for different shapes of isolators, aspect ratio, loading directions, and magnitude of the lateral and horizontal load. Some studies verified the effectiveness of unbonded applications using small-scale shaking table tests. Analytical approaches, including the horizontal load-displacement relationship and stiffness with flexible reinforcement, were proposed based on the simplified assumptions. The FE simulation is regarded as a robust and effective method for analyzing and predicting elastomeric isolators' performance in large displacement domains under different boundaries and parametric conditions.

Seismic isolation using automobile tires is an innovative method and is yet to be explored. The STP, STRP, RTB, and RR-FRB isolators made with scrap tires or RSM and tires filled with recycled elastomeric material can be an effective solution for earthquake mitigating low-rise buildings. The effectiveness of these systems is primarily investigated using reduced-scale testing facilities. Some studies focused on the isolator's square and circular shapes, but strip-shape is economical and cost-effective for ordinary and masonry structures with no rigid foundation. Although unidirectional loading was considered, extension to bidirectional loading is also required. The permissible value of compressive force, lateral displacement, and

rotation at the structure-to-isolator interface should be defined so that the stress-strain within the unbonded STRP isolator does not exceed the design guidelines. Large-scale testing of the unbonded isolator is necessary to understand the actual scenario of the unbonded application. The FE simulation can avoid the limitation of large-scale testing facilities. Besides, analytical formulation for vertical and lateral responses of STRP isolators is essential for design purposes. Therefore, this study focused on the analytical model for horizontal and vertical stiffness of STRP isolators and the effectiveness of STRP isolators in seismic protection of low-rise buildings.

References

Al-Anany, Y. M., Van Engelen, N. C., and Tait M. J. (2017). "Vertical and Lateral Behavior of Unbonded Fiber-Reinforced Elastomeric Isolators." *J of Composite for Construction*, ASCE, 21(5), 1-11.

Anne and Evans, R. (2006). The Composition of a Tyre: Typical Components, *The Waste & Resources Action Programme*, The Old Academy, 21 Horse Fair, Banbury, Oxon OX16 0AH

Calabesre, A., Spizzuoco, M., Serino, G., Corte, G. D. and Maddaloni, G. (2015). "Shaking table investigation of a novel, low-cost, base isolation technology using recycled rubber." *Struct. Control Health Monit*., 22(1), 107-122.

Chaghakaboodi, S. and Toopchi-Nezhad, H. (2020). On the wind-induced motion of unbonded fiber-reinforced elastomeric isolators: Designing for habitability, Struct Control Health Monit, 28(3), e2682

Das, A., Dutta, A. and Deb, S.K. (2014). Performance of fiber-reinforced elastomeric base isolators under cyclic excitation, Struct. Control Health Monit, 22, pp.197-220.

Das, A., Deb, S.K, and Dutta, A. (2016) Shake table testing of un-reinforced brick masonry building test model isolated by U-FREI, *Earthquake Engng Struct. Dyn*. 45, pp.253–272.

Dezfuli, F. H. and Alam M. S. (2014). Sensitivity analysis of carbon fiber-reinforced elastomeric isolators based on experimental tests and finite element simulations, Bull Earthquake Eng., 12, pp. 1025–1043.

De Raaf, G. P. M., Tait, M. J. and Toopchi-Nezhad, H. (2011). "Stability of fiber-reinforced elastomeric bearings in an unbonded application" *J. of Composite Mater.*, 45(18), 1873–1884

Gerhaher U. (2010). Faserverstärkte Elastomerlager – Konzeption und Bemessung. BOKU University;

Gerharer, U., Strauss, A., and Bergmeister, K. (2011). Verbesserte Bemessungsrichtlinien für Bewehrte Elastomerlager. Bautechnik, 88(7), pp. 451–8.

Jampole, E., Deierlein, G., Miranda, E., Fell, B., Swensen, S., & Acevedo, C. (2016). Full-Scale Dynamic Testing of a Sliding Seismically Isolated Unibody House. *Earthquake Spectra*, *32*(4), 2245–2270. https://doi.org/10.1193/010616EQS003M

Habieb, A. B., Milani G., and Tavio, T. (2018). Two-step advanced numerical approach for the design of low-cost unbonded fiber-reinforced elastomeric seismic isolation systems in new masonry buildings, Engineering Failure Analysis, 90, pp.380-396.

Habieb, A. B., Milani G., Tavio, T., and Milani F. (2017). Numerical Model of Low Cost Rubber Isolators for Masonry Housing in High Seismic Regions, International Journal of Civil and Environmental Engineering, 11(5), pp. 664-670

Hadad, H. A., Calabrese, A., Strano, S. & Serino, G. (2017). A Base Isolation System for Developing Countries Using Discarded Tyres Filled with Elastomeric Recycled Materials, Journal of Earthquake Engineering, 21, (2), pp. 246-266.

Huang, X. Y. and Zhou, F-l., Cao J-Y. Jian-yuan, Jin J-M,CAO Jing-yuan J. and Xian Q (2010). "Simulating earthquake shaking table of isolation structure with fiber-reinforced isolator and finite element analysis." *J. Guangzhou Univ. (Nat Sci Edtion)*, 5, 21–26.

Ishikawa, Y. (2011). "Systematic Review of Tyre Technology." National Museum of Nature and Science, Vol. 16, 1-137.

Kelly, J. M., (1997). *Earthquake-resistant design with rubber*, 2nd Ed., London, Springer-Verlag.

Kelly, J.M., (2001). "Seismic isolation systems for developing countries." EERI Distinguished Lecture 2001, *Earthq. Spectra.*, 18(3), 385–406.

Kelly, J.M. (2002). Seismic isolation systems for developing countries. Earthquake Spectra 18, 385–406.

Kelly M. J. and Takhirov, S. M., (2002). "Analytical and experimental study of fiber reinforced strip isolators." *PEER report 2002/11*, Dept. of Civil and Environ. Eng., University of California, Berkeley.

Kelly, J. M., and Konstantinidis, D.A., (2011). "Mechanics of rubber bearings for seismic and vibration isolation." John Willey and sons, Ltd.

Kirihara, K. (2011). "Production Technology of Wire Rod for High Tensile Strength Steel Cord". Kobelco Technology Review No. 30, 62-65.

Konstantinidis D., Kelly J. M., and Makris N. (2008). Experimental investigation on the seismic response of bridge bearings. Technical Rep. No. EERC 2008-02, Earthquake Engineering Research Center, Univ. of California, Berkeley, CA.

Konstantinidis, D. and Kelly,J. M. (2014). "Advances in Low-Cost Seismic Isolation with Rubber" *Proc., 10th US National Conf. on Earthq. Eng. Frontiers of Earthq. Eng.*, Anchorage, Alaska.

Konstantinidis, D. and Kelly,J. M. (2011). *Mechanics of Rubber Bearings for Seismic and Vibration Isolation*, 1st Ed., John Wiley & Sons, Ltd.

Losanno, D., Madera Sierra I. E., Spizzuoco M., Marulanda J., and Thomson P. (2019a). Experimental assessment and analytical modeling of novel fiber-reinforced isolators in unbounded configuration, Composite Structures, 212, pp. 66-82.

Losanno, D.. Spizzuoco, M. and Calabrese., A. (2019b). Bidirectional shaking-table tests of unbonded recycled-rubber fiber-reinforced bearings (RR-FRBs), Struct Control Health Monit. 26(9),e2386.

Losanno, D., Calabrese, A., Madera-Sierra, I. E., Spizzuoco, M., Marulanda, J., Thomson, P. & Serino, G. (2020). Recycled versus Natural-Rubber Fiber-Reinforced Bearings for Base Isolation: Review of the Experimental Findings, Journal of Earthquake Engineering, https://doi.org/10.1080/13632469.2020.1748764

Madhusudhan B.R., Boominathan A., Banerjee S. (2019) Properties of Sand–Rubber Tyre Shreds Mixtures for Seismic Isolation Applications. In: Adimoolam B., Banerjee S. (eds) Soil Dynamics and Earthquake Geotechnical Engineering. Lecture Notes in Civil Engineering, vol 15. Springer.

Maddaloni1,G., Caterino, N., and Occhiuzzi A. (2017). Shake table investigation of a structure isolated by recycled rubber devices and magnetorheological dampers, Struct. Control Health Monit., 24(5) :e1906.

Manzoori A. and Toopchi-Nezhad H. (2016). Application of an Extended Bouc-Wen Model in Seismic Response Prediction of Unbonded Fiber-Reinforced Isolators, Journal of Earthquake Engineering, 21(1).

Mishara, H. K. (2012. "Experimental and Analytical Studies on Scrap Tire Rubber Pads for Application to Seismic Isolation of Structures." Ph.D. Thesis, Kyoto University, Kyoto, Japan.

Mishra HK, Igarashi A, Matsushima H (2013b), "Finite element analysis and experimental verification of the scrap tire rubber pad isolator" Bulletin Earthquake Engineering, 11(2), 687-707.

Mishra HK and Igarashi A (2013a), "Lateral deformation capacity and stability of layer-bonded scrap tire rubber pad isolators under combined compressive and shear loading", Structural Engineering and Mechanics, 48(4), 479-500.

Mishra HK, Igarashi A, Ji D and Matsushima H (2014). "Pseudo-Dynamic Testing for Seismic Performance Assessment of Buildings with Seismic Isolation System Using Scrap Tire Rubber Pad Isolators." Journal of Civil Engineering and Architecture, 8(1), 73-88.

Moon, B.-Y., Kang, G..-J., Kang, B.- S., and Kim K.-S. (2002a). "An experimental study on fiber reinforced bearing." *J. of Earthq. Eng. Soci. of Korea (JEESK),* 6(1), 1-6

Moon, B.-Y., Kang, G.-J., Kang, B.-S., Kelly, J.M. (2002b). "Design and manufacturing of fiber reinforced elastomeric isolator for seismic isolation." *J. Mater. Process. Technol*., 130–131, 145–150.

Moon, B.-Y., Kang, G..-J., Kang, B.- S., Kim K.-S., and Kelly J. M. (2003). Mechanical properties of seismic isolation system with fiber-reinforced bearing of strip type, *International Applied Mechanics*, 39(10), pp.1231-1239.

Moon, B-Y., Kang, G.-J., Kang, B.-S. and Chou D-S. (2004). Design of Elastomeric Bearing System and Analysis of it Mechanical Properties, *KSME International Journal*, 18(1), pp. 20~ 29.

Morales, E., Filiatrault, A., and Aref, A. (2018). Seismic floor isolation using recycled tires for essential buildings in developing countries, Bulletin of Earthquake Engineering, 16, pp. 6299–6333

Mordini, A., and Strauss, A. (2008). "An innovative earthquake isolation system using fibre reinforced rubber bearings." *Eng. Struct.*, ELSEVIER, 30(10), 2739–2751.

Nanda, R. P., Shrikhande, M., and Agarwal, P. (2015). Low-Cost Base-Isolation System for Seismic Protection of Rural Buildings, *Practice Periodical on Structural Design and Construction*, 21(1), pp. 1-18.

Nanda, R. P., Dutta, S., Khan, H.A. and Majumder, S. (2018). Seismic Protection of Buildings by Rubber-Soil Mixture as Foundation Isolation, International Journal of Geotechnical Earthquake Engineering, 9(1), pp. 99-109.

Ngo TV, Dutta A, and Deb SK (2017), "Evaluation of horizontal stiffness of fibre-reinforced elastomeric isolators", *Earthquake Engineering and Structural Dynamics*, 46, 1747-1767.

Osgooei, P. M., Tait, M. J., and Konstantinidis, D. (2014a). "Finite element analysis of unbonded square fiber-reinforced elastomeric isolators (FREIs) under lateral loading in different directions." Composite. Struct., 113, 164-173.

Osgooei, P. M., Tait, M. J., and Konstantinidis, D. (2014a). Three-dimensional finite element analysis of circular fiber-reinforced elastomeric bearings under compression, *Composite Structures*, 108, pp. 191–204.

Osgooei, P. M., Van Engelen, N. C., Konstantinidis, D., and Tait, M. J. (2015). Experimental and finite element study on the lateral response of modified rectangular fiber-reinforced elastomeric isolators (MR-FREIs), Engineering Structures 85 (2015) 293–303.

Osgooei, P. M., Tait, M. J., and Konstantinidis, D. (2016). "Variation of the vertical stiffness of strip-shaped fiber-reinforced elastomeric isolators under lateral loading." Composite. Struct., 144, 177-184.

Osgooei, P. M., Tait, M. J., and Konstantinidis, D. (2017). Non-iterative computational model for fiber-reinforced elastomeric isolators, Engineering Structures 137, pp. 245–255.

Pauletta, M., Cortesia, A., and Russo, G. (2015). "Roll-out instability of small size fiber-reinforced elastomeric isolators in unbonded applications." *Eng. Struct.*, ELSEVIER, 102, 358–368.

Peng T. B., Li J. Z., and Fan L. C. (2007). Pilot study on the horizontal shear behaviour of FRP rubber isolators. Asia-Pacific Conference on FRP in Structures (APFIS 2007), pp. 443-449.

Pistolas, G.A., Pitilakis, K. & Anastasiadis, A. (2020). A numerical investigation on the seismic isolation potential of rubber/soil mixtures. Earthq. Eng. Eng. Vib. 19, 683–704

Prevorsek, D. C., Sharma, R. K. (1981). "Role of adhesion in viscoelastic properties of rubber-tire cord composites." *Rubber Chem. and Technol.,* 54(1), 72-90.

Shield, C. K. and Costello, G. A. (1994). "The effect of wire rope mechanics on the mechanical response of cord composite laminates: An energy approach." *J. of Appl Mech.,* ASME, 61(1), 9-15

Spizzuoco, M., Calabrese, A. and Serino, G. (2014). "Innovative low-cost recycled rubber-fiber reinforced isolator: Experimental tests and Finite Element Analyses." *Eng. Struct*., ELSEVIER, 76(1), 99-111.

Strauss A., Apostolidi E., Zimmermann T., Gerhaher U. and Dritsos, S. (2014). Experimental investigations of fiber and steel-reinforced elastomeric bearings: Shear modulus and damping coefficient, Engineering Structures, 75, pp. 402–413.

Tan, P., Xu, K., Wang, B., ChiaMing, C., Han, L. and FuLin, Z. (2014). "Development and performance evaluation of an innovative low-cost seismic isolator". *Sci. China Technol. Sci.*, 57(10), 2050-2061.

Toopchi-Nezhad, H., Tait M. J., and Drysdale R. G., (2008a). "Lateral Response Evaluation of Fiber-Reinforced Neoprene Seismic Isolators Utilize in an Unbonded Application." *J. of Struct. Eng.*, ASCE, 134(10), 1627-1637.

Toopchi-Nezhad, H., Tait, M. J. and Drysdale, R. G., (2008b). "Testing and modeling of square fiber-reinforced elastomeric seismic isolators." *Struct. Control Health Monit.*, 15(6), 876-900.

Toopchi-Nezhad, H., Drysdale, R. G. and Tait, M. J. (2009a). "Parametric Study on the Response of Stable Unbonded-Fiber Reinforced Elastomeric Isolators (SU-FREIs)." *J. of Composite Mater.*, 43(15), 1569-1587.

Toopchi-Nezhad, H., Tait, M. J., and Drysdale R. G. (2009b). "Shake table study on an ordinary low-rise building seismically isolated with SU-FREIs (stable unbonded-fiber reinforced elastomeric isolators)." *Earthq. Eng. and Struct. Dyn.,* 38(11), 1335-1357.

Toopchi-Nezhad, H., Tait M. J., and Drysdale R. G., (2011). "Bonded versus unbonded strip fiber reinforced elastomeric isolators: Finite element analysis, *Composite Structures*, ELSEVIER, 93(2), 850-859.

Toopchi-Nezhad, H., Tait M. J., and Drysdale R. G., (2012). "Influence of thickness of individual elastomer layers (first shape factor) on the response of unbonded fiber-reinforced elastomeric bearing." *J. Composite Mater*, SAGE, 47(27), 3433-3450.

Toopchi-Nezhad H. (2014). Horizontal stiffness solutions for unbonded fiber reinforced elastomeric bearings. Structural Engineering and Mechanics, 49(3), pp. 395–410.

Toopchi-Nezhad, H. , Ghotb, M.R. Al-Anany Y. M., and Tait, M. J. (2019). Partially bonded fiber reinforced elastomeric bearings: Feasibility, effectiveness, aging effects, and low temperature response. *Engineering Structures*, 179, pp. 120–128

Tsai, H.-C., Kelly, J.M. (2001). Stiffness analysis of fiber-reinforced elastomeric isolators, PEER Report 2001/05, Pacific Earthquake Engineering Research Center, University of California, Berkeley.

Tsai, H.-C., Kelly, J.M. (2002a) Stiffness analysis of fiber-reinforced rectangular seismic isolators. Journal of Engineering Mechanics, ASCE 128, 462–470.

Tsai, H.-C., Kelly, J.M., (2002b). Bending stiffness of fiber-reinforced circular seismic isolators. Journal of Engineering Mechanics, ASCE 128, 1150–1157.

Tsai HC, Kelly JM. (2005). Buckling of short beams with warping effect included. Int J Solids Struct; 42(1):239–53

Tsang HH, Lo SH, Xu X and Sheikh MN (2012), "Seismic Isolation for Low-to-Medium-Rise Buildings Using Granulated Rubber-Soil Mixtures: Numerical Study," Earthquake Engineering and Structural Dynamics, 41: 2009–2024.

Tsang HH (2008), "Seismic Isolation by Rubber-Soil Mixtures for Developing Countries," Earthquake Engineering and Structural Dynamics, 37(2): 283–303.

Tsiavos, A., Sextos, A., Stavridis, A., Dietz, M., Dihoru, L., & Alexander, N. A. (2020). Large-scale experimental investigation of a low-cost PVC 'sand-wich' (PVC-s) seismic isolation for developing countries. *Earthquake Spectra*, *36*(4), 1886–1911. https://doi.org/10.1177/8755293020935149

Turer, A. and Özden, B, (2008). "Seismic base isolation using low-cost scrap tire pads (STP)." *Mater. and Struct.*, 41(5), 891-908.

Van Engelen, N. C., Osgooei, P. M., Tait, M. J., and Konstantinidis, D., (2014a). Partially bonded fiber-reinforced elastomeric isolators (PB-FREIs), Struct. Control Health Monit., 22, pp. 417–432.

Van Engelen, N. C., Osgooei, P. M., Tait, M. J., and Konstantinidis, D., (2014b). Experimental and finite element study on the compression properties of Modified Rectangular Fiber-Reinforced ElastomericIsolators (MR-FREIs), *Engineering Structures*, 74, pp. 52–64

Van Engelen, N. C., Tait, M. J., and Konstantinidis, D., (2015). "Model of the shear behavior of unbondedfiber-reinforced elastomeric isolators." J. Struct. Eng., ASCE, 141 (7), 1-11.

Wong, J. Y. (2001). *Theory of ground vehicle*. 3rd Ed., John Wiley and Sons, Inc.

Xiong, W. and Li, Y. (2013), Seismic isolation using granulated tire–soil mixtures for less-developed regions: experimental validation. Earthquake Engng Struct. Dyn., 42: 2187-2193.

Xiao, H., Butterworth, J.W. & Larkin, T. (2014). Low-technology techniques for seismic isolation, Paper No. 36, 2004 NZSEE Conference, Auckland, New Zealand.

Chapter 3

Finite Element Modeling and Model Verification

3.1. Introduction

The finite element (FE) simulation is a robust and powerful method used to analyze rubber and rubberlike incompressible materials. This chapter describes the finite element (FE) modeling and model verification procedures for STRP isolators and STRP base-isolated structures using Marc-Mentat Software. It also includes the analytical approach for the material model, contact model, and modeling procedure.

3.2. Element Used to Discretize STRP Isolator

The rubber of the STRP isolator is modeled using element 84. It is an eight-node, first-order iso-parametric element with an extra node for a pressure degree of freedom. The pressure throughout the element is assumed constant by the ninth node. The first eight-node numbered from 1 to 8, as shown in Fig. 3.1a, each node has three displacement degrees of freedom. The mean pressure variable:
For an isotropic case,

$$H = \sigma_{kk}/E = -p \tag{3.1}$$

For an orthotropic case,

$$H = \left[\frac{\frac{\nu_{12}\nu_{31}}{E_1E_3}}{\frac{\nu_{12}\nu_{31}}{E_1E_3}+\frac{\nu_{12}\nu_{23}}{E_1E_2}+\frac{\nu_{31}\nu_{23}}{E_3E_2}}\sigma_1 + \frac{\frac{\nu_{12}\nu_{23}}{E_1E_2}}{\frac{\nu_{12}\nu_{31}}{E_1E_3}+\frac{\nu_{12}\nu_{23}}{E_1E_2}+\frac{\nu_{31}\nu_{23}}{E_3E_2}}\sigma_2 + \frac{\frac{\nu_{31}\nu_{23}}{E_3E_2}}{\frac{\nu_{12}\nu_{31}}{E_1E_3}+\frac{\nu_{12}\nu_{23}}{E_1E_2}+\frac{\nu_{31}\nu_{23}}{E_3E_2}}\sigma_3 \right] \frac{9}{E_1+E_2+E_3} = -p \tag{3.2}$$

where p is the negative hydrostatic pressure. Element outputs are six strains and six stresses, and the mean pressure. Element 84 supports the updated Lagrange procedure and finite strain plasticity with Mooney or Ogden material model.

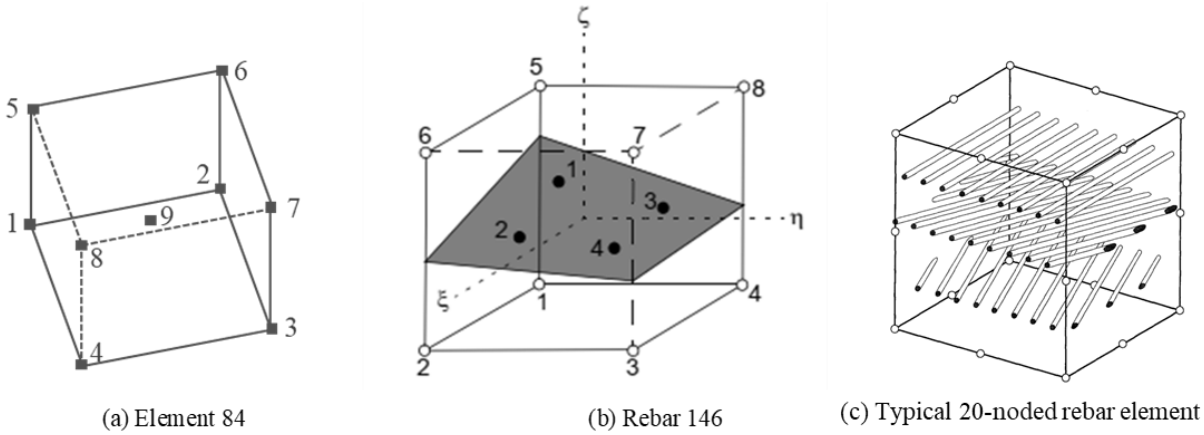

(a) Element 84 (b) Rebar 146 (c) Typical 20-noded rebar element

Figure 3.1 Element used for rubber and steel-cord modeling (Marc-Mentat, 2020E).

Numerical representation of reinforcing cords with spatial orientation is based upon the so-called "rebar layer concept" that is efficient in the context of geometrically and physically nonlinear analyses of cord-rubber composite (Helnwein et al., 1993; Meschke and Helnwein, 1994). Several steel-cord layers can be considered within a single overlay element without increasing the number of degrees of freedom. Meschke et al. (1997) and Helnwein et al. (1993) describe the rebar concept used for comprehensive FE models of automobile tires embedded with steel cords. Rebar 146, a hollow, iso-parametric, and 8-noded empty brick element containing single-strain steel cords, as shown in Fig. 3.1, is used. It is used in conjunction with element 84 used for elastomers. The rebar 146 element is integrated based on Gauss quadrature, and each rebar layer contains four integration points, as shown in Fig. 3.1b. It is necessary to define the steel-cord position, size, number of layers, and orientation at each integration point. It has three degrees of freedom in each node. The output is the second Piola-Kirchhoff stress and the Green strain.

3.3. Material Modeling

3.3.1. Hyperelasticity Model

Rubber is an incompressible and hyperelastic material that can return to the initial stage from a 500% strain level (Mars, 2002). Its stress-strain relationship is highly nonlinear. The hyperelasticity of rubber material is derived from strain energy function *W*, the energy stored within per unit volume as a function of strain (Ali et al., 2010), using the following equation.

$$W = f(I_1, I_2, I_3) \tag{3.3}$$

where I_1, I_2, and I_3 are invariants of the Green deformation tensor given by principle stretch ratios λ_1, λ_2, and λ_3 in the respective directions and can be found from uniaxial or biaxial tension test.

$$I_1 = \lambda_1^2 + \lambda_2^2 + \lambda_3^2 \tag{3.4}$$

$$I_2 = \lambda_1^2\lambda_2^2 + \lambda_2^2\lambda_3^2 + \lambda_3^2\lambda_1^2 \tag{3.5}$$

$$I_3 = \lambda_1^2\lambda_2^2\lambda_3^2 \tag{3.6}$$

The stretch ratios are expressed in terms of the uniaxial stretch ratio (Vahapoglu et al., 2011).

$$\lambda_1 = \lambda \tag{3.7}$$

$$\lambda_2 = \lambda_3 = \frac{1}{\sqrt{\lambda}} \tag{3.8}$$

For incompressibility condition,

$$\lambda_1\lambda_2\lambda_3 = 1 \tag{3.9}$$

A mathematical definition of stretch ratio is given as below:

$$\lambda_i = \frac{L_i + \Delta L_i}{L_i} = 1 + \varepsilon_i \text{ and } \varepsilon_i = \frac{\Delta L_i}{L_i} \tag{3.10}$$

where ε_i is called engineering strain. The most common hyperelastic models used in FE analysis are Neo-Hookean, Mooney, Mooney-Rivlin, Yeoh model, and Ogden material models. Several researchers used the Mooney-Rivlin material model for cord-rubber composite materials (Helnwein et al., 1993, Thein et al., 2016, Kongo-Kondé et al., 2013). Strain energy potential is expressed as:

$$W = \sum_{i,j=0}^{N} C_{ij}(I_1 - 3)^i (I_2 - 3)^j + \sum_{i=1}^{N} \frac{1}{D_i}(J_{el} - 1)^{2i} \tag{3.11}$$

where, C_{ij} and D_i are the material parameters determined from the test data and $C_{00} = 0$ (Markmann and Verron, 2006). J_{el} is the elastic volume ratio, N is the order of the polynomial. The first and second summation terms indicate the contribution from deviatoric and volumetric effects, respectively. The first order Mooney-Rivlin model is presented as follows:

$$W = C_{10}(I_1\text{-}3)+C_{01}(I_2\text{-}3) \tag{3.12}$$

The two-term model fits well with the test result for strain below 100% and is inadequate in predicting compression deformation mode and hardening at large strain (Marc Mentat, 2020A). Tschoegl (1971) suggests a three-term model for predicting the stress-strain upswing. The three-terms Mooney-Rivlin strain energy density function is:

$$W = C_{10}(I_1\text{-}3)+C_{01}(I_2\text{-}3)+C_{11}(I_1\text{-}3)(I_2\text{-}3) \tag{3.13}$$

where C_{10}, C_{01}, and C_{11} are known as Mooney-Rivlin material constant. Mishra and Igarashi (2012) employed the three-term model to determine the hyperelastic parameters of scrap tire rubber.

3.3.2. Viscoelasticity Model

The Prony series viscoelastic shear response parameters are used in the constitutive model to express the hysteretic force-displacement relationship observed in the test. The viscoelastic parameters are derived using a large strain viscoelasticity model (Simo, 1987; Marc-Mentat, 2020A). The following time-dependent elastic energy function characterizes a large strain viscoelastic material.

$$W(t)=W^{\infty}+\sum_{n=1}^{N} W^n exp(-t/\lambda^n) \tag{3.14}$$

where W^{∞} is the energy function for very slow processes, W^n is an extra amount of energy necessary for time-dependent processes. A characteristics time is associate with each amount of W^n. At time equal to zero (or for time processes: $t< \lambda^n$), the elastic energy reduces to:

$$W(0)=W^0 = W^{\infty}+\sum_{n=1}^{N} W^n \tag{3.15}$$

If energy function for each time-dependent part is assumed different only by a scalar constant, then:

$$W^n=\delta^n W^0 \tag{3.16}$$

The reduced equation is

$$W^0=W^{\infty} + W^0 \sum_{n=1}^{N} \delta^n \text{ or } W^{\infty} = (1 - \sum_{n=1}^{N} \delta^n)W^0 \tag{3.17}$$

The time-dependent energy is then given by Eq 3.19:

$$W(t)=W^0-W^0\sum_{n=1}^{N}\delta^n+\sum_{n=1}^{N}\delta^n exp(-t/\lambda^n) \quad (3.18)$$

$$W(t)=W^0\left[1-\sum_{n=1}^{N}\delta^n(1-exp(-t/\lambda^n)\right] \quad (3.19)$$

For simplicity of the discussion to the case N=1.0

$$W^{\infty}=(1-\delta)W^0 \quad (3.20)$$

$$W(t)=W^0[1-\delta(1-exp(-t/\lambda^n)] \quad (3.21)$$

In the Prony series form, δ^n is a time-dependent scalar multiplier, and λ^n is relaxation time.

3.3.3. Mullins Damage Parameters

Elastomers undergo damage by a mechanism in chain breakage, multi-chain damage, micro-void formation, and microstructural degradation due to detachment of filler particles from the network entanglement. Based on undamaged strain energy function, W^0, damage in the elastomer is obtained by multiplying the Kachanov factor as follows:

$$W=K(\alpha,\beta)W^0 \quad (3.22)$$

where $K(\alpha,\beta)$ is a factor accounting for damage. A unit value indicates full virgin condition and zero mean complete damage condition. Two methods are accounting for damage: the Miehe method and Ogden and Roxburgh method. The Miehe method can simulate two types of damage called discontinuous so-called Mullins' effect and continuous damage. These damages can be modeled within the additive or multiplicative decomposition using the Marc-Mentat program.

Additive decomposition:

$$K=d^{\infty}+\sum_{n=1}^{N}d_n^{\alpha}exp\left(-\frac{\alpha}{\eta_n}\right)+\sum_{n=1}^{N}d_n^{\beta}exp\left(-\frac{\beta}{\lambda_n}\right) \quad (N=1,2) \quad (3.23)$$

Multiplicative decomposition:

$$K=d^{\infty}+\sum_{n=1}^{N}d_n^{\alpha}exp\left(-\frac{\alpha+\delta_n\beta}{\eta_n}\right) \quad (N=1,2) \quad (3.24)$$

where d_n^{α}, d_n^{β}, η_n, λ_n, d_n and δ_n are the phenomenological parameters. If d^{∞} is not defined, the program calculates it such that at zero value of α and β, the Kachanov factor K is equal to unity.

3.4. Contact Modeling Between STRP and Structures

3.4.1. Contact Definition

Marc is designed with an efficient algorithm for contact searching among the contacting bodies. A contact table is used to define target contact and contact parameters between STRP and structure. These include friction, penetration tolerance, material hard-to-soft ratio, bias factor, initial gap, etc. Figure 3.2 shows a contact table indicating the contact interaction in the FE model. The rubber-to-rubber contact (Layer1 and Layer2) is glued (*G*), the rubber-to-rigid body contact (Layer1 and Top) is touch (*T*). The contact between the superstructure (here indicating MASS elements) and the top rigid body is glued (*GT*). There is no contact between MASS and rubber or MASS and bottom rigid body. Turning on the contact table is activating the specified contacts only. Without turning on, all bodies can contact, including the self-contact, and increase the computation cost. Touch contact triggers nonpenetration constrain through a tying boundary on the displacement components normal to the contact surfaces. The isolator separates from the rigid surface when contact stress turns on tension. A glue contact is used to tie all displacement degrees of freedom. The rotation can be constrained for a moment-carrying glue capability.

Contact Table Properties

Name: Contact_Table | View Mode: Entry List | Show Body Types

Entries

Show Visible Bodies Only

First Body	Second Body	Contact Interaction	Contact Type	Detection	
Layer1	Layer2	G	Glued	Automatic	Edit
Layer1	Top	T	Touching	N/A	Edit
Layer1	Bottom	T	Touching	N/A	Edit
Layer2	Layer3	G	Glued	Automatic	Edit
Layer2	Top	T	Touching	N/A	Edit
Layer2	Bottom	T	Touching	N/A	Edit
Mass	Top	GT	Glued	N/A	Edit
Layer3	Layer4	G	Glued	Automatic	Edit
Layer3	Top	T	Touching	N/A	Edit
Layer3	Bottom	T	Touching	N/A	Edit
Layer4	Top	T	Touching	N/A	Edit
Layer4	Bottom	T	Touching	N/A	Edit

Shown Entries | Activate | Deactivate | Remove | Detection | Remove Inactive

Populate / Manipulate | Full Default Contact | Touching | Glued

OK

Figure 3.2 Contact definition using contact table

3.4.2. Contact Occurring Criteria

The prediction of friction force and the contact position in an unbonded isolator is a complex process due to frequent changes of contact location and contact force with the lateral displacement. Therefore, the accuracy of finite element results depends on the precise prediction of contact position and contact force. Figure 3.3 shows a FE model and different contact components of the STRP isolator model. The top and bottom planes are called rigid bodies, whereas the rubber composite and MASS are called deformed bodies.

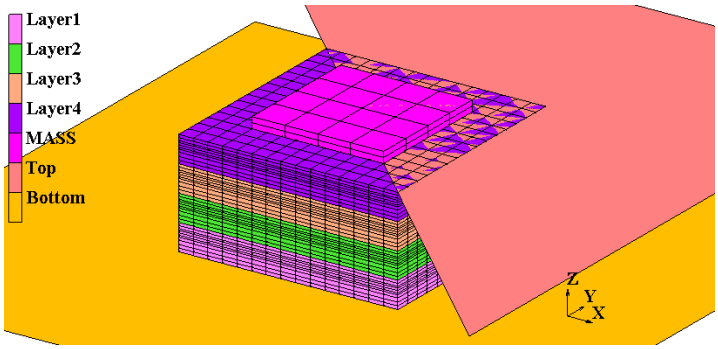

Figure 3.3 Contact modeling between bearing and structure

Figure 3.4 describes four cases relating to how and when contact takes place between deformed and rigid bodies.

Case 1: Contact not detected when $\Delta u_A \bullet n < \left| D-d \right|$

Case 2, 3: Contact detected when $\left| \Delta u_A \bullet n - d \right| < D$

Case 4: Penetration detected when $\Delta u_A \bullet n > \left| D+d \right|$

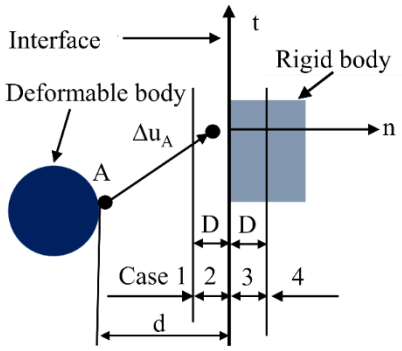

Figure 3.4 Contact interaction procedure between two bodies

Here, Δu_A is the incremental displacement vector of node *A*, *d* is the distance between two bodies approaching for contact, *n* is the normal unit vector with proper orientation. *D* is the contact detection distance, and the default value is *h*/20 or *t*/4, where *h* and *t* are the smallest dimension of element and shell thickness, respectively. In case 1, no constraint is applied since node *A* does not touch the rigid body. In case 2, node *A* is within the tolerance, and the contact constraint pulls the node to the contact surface if $F<F_s$, where F_s is the separation force equal to zero and *F* is the contact force. In case 3, node *A* penetrates contact tolerance, and contact constraint pushes the node to the contact surface. In case 4, node *A* penetrates out of contact tolerance, and increment gets split until penetration is within the tolerance limit. A contact tolerance is equally applied to both sides of the segment and can be changed by bias factor *B* ($0 \le B \le 1.0$). Once contact is detected, a constraint is imposed such that:

$$\nabla u_{normal} = V \cdot n \tag{3.25}$$

If the glue option is activated, an additional displacement constraint is formed as:

$$\nabla u_{tangential} = V \cdot t \tag{3.26}$$

Here *n* and *t* are normal and tangential vectors, and *V* is the prescribed velocity vector of the rigid surface.

3.4.3. Theory of Normal and Friction Contact

The standard set of equations to be solved within a nonlinear structural finite element analysis are based on the virtual works that can be written as:

$$G(u, \delta u)=0 \tag{3.27}$$

where u is the displacement field, and δu is the kinematically permissible variation of the displacement field. Contact conditions are included by adjusting the virtual work equation by two surface integrals:

$$G(u, \delta u)+\int_{\Gamma} \lambda_n \delta g_n d\Gamma+\int_{\Gamma} \lambda_t^T \delta g_T d\Gamma=0 \tag{3.28}$$

where Γ is the boundary of the bodies being in contact and subscript n and t indicates the normal and tangential contact. Function g_n is the gap function, $g_n>0$ indicates no contact, and $g_n=0$ means the point is on contact, whereas $g_n<0$ indicates the penetration. λ_n, g_t, and λ_t are the normal contact stress, the tangential gap vector, and the tangential stress vector.

The tangential friction is governed by Coulomb's friction law as follows:

$$\phi=\|\lambda_t\|-\mu\lambda_n \leq 0 \tag{3.29}$$

where μ is the friction coefficient, $\phi<0$ corresponds to sticking, and $\phi=0$ corresponds to slipping.

The contact part of Eq. 3.28 depends on the geometry of the bodies and displacement field u as follow:

$$G_c(u, \delta u)=\int_{\Gamma} \lambda_n \frac{\partial g_n}{\partial u} \delta u d\Gamma+\int_{\Gamma} \lambda_t^T \frac{\partial g_T}{\partial u} \delta u d\Gamma \tag{3.30}$$

Equation 3.28 is valid for all kinematically admissible variations of δu. Therefore, the contact contribution to the equilibrium equation is:

$$F_c^T(u, \delta u)=\int_{\Gamma} \lambda_n \frac{\partial g_n}{\partial u} d\Gamma+\int_{\Gamma} \lambda_t^T \frac{\partial g_T}{\partial u} \delta u d\Gamma \tag{3.31}$$

The solution procedure based on the augmented Lagrangian approach solved by Newton-Raphson iteration is described in Fig. 3.5 and Eq. 3.32.

$$\lambda_n^{trial}=P_n^{i\text{-}1}+E_n g_n^i;\ \lambda_t^{trial}=t_n^{i\text{-}1}+E_t g_t^i \tag{3.32}$$

where P_n and t_n are fixed estimations of λ_n and λ_t. E_n and E_t are normal and tangential penalty factors whose

values are estimated from the properties of contact bodies, $g_{n,}$ and g_t follow from the global iterative displacement solution. At contact, gap function, $g_n^i=0$ and $\lambda_n^{trial}=P_0^{i-1}$. The first displacement solution is obtained using $P_n=P_n^0$ which is employed to calculate the gap function g_n^1. Then the contact normal stress is updated by $P_n^1=P_n^0+E_n g_n^1$. This new contact normal stress is used in the subsequent iteration. Figure 3.5a shows the iteration procedure. The method is reduced to the penalty method with constant penalty factor E_n when augmentation is not performed. In the tangential direction, the augmentation procedure better approximates the sticking contact by adjusting the tangential stress, as shown in Fig. 3.5b. The Newton-Raphson solution procedure provides the contact contributions to the global force vector as given in Eq. 3.31 and the contributions to the global stiffness matrix as follows.

$$K_c=\frac{\partial}{\partial u}F_c \tag{3.33}$$

Evaluation of Eq. 3.32 and 3.33 depends on whether there is sticking or slipping. At the beginning of an analysis, typically sticking is assumed, but it is possible to check whether it is sticking or slipping after having the trial solution.

$$\phi^{trial}=\left\|\lambda_t^{trial}\right\|-\mu\lambda_n^{trial};\ \phi^{trial}<0\text{:sticking},\ \phi^{trial}>0\text{:slipping} \tag{3.34}$$

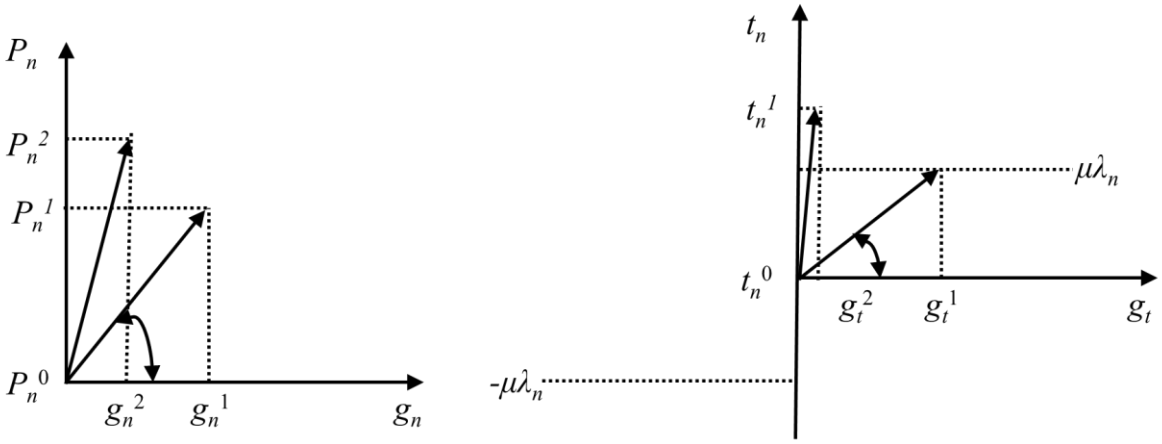

(a) (b)

Figure 3.5 Contact (a) normal and (b) friction stress updating by Augmented Lagrange Procedure

3.5. Bilinear Coulomb Friction Model

The bilinear Coulomb friction model based on nodal stress is:
For stick:

$$\|\sigma_t\| < \mu\sigma_n \tag{3.35}$$

For slip:

$$\sigma_t = -\mu\sigma_n . t \tag{3.36}$$

where σ_t is the tangential frictional stress, σ_n is the normal stress, μ is the friction coefficient, and t is the tangential vector given as below:

$$t = \frac{V_r}{\|V_r\|} \tag{3.37}$$

where V_r is the relative sliding velocity. When nodal force is used, the symbol σ is replaced by f. The friction stress or force is a step function for a load input depending on the relative sliding velocity V_r or incremental tangential displacement Δu_t, as shown in Fig 3.6a.

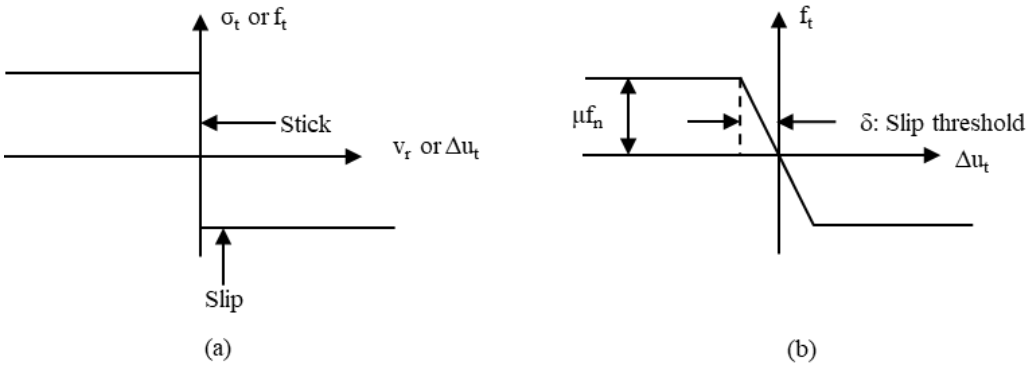

Figure 3.6 Coulomb friction model: (a) Step function (b) Bilinear model.

As shown in Fig. 3.6b, the bilinear assumption of Coulomb friction is considered to avoid the convergence difficulties that arise from the step function's discontinuity. It is based on the elastoplastic condition of the relative tangential displacement. The Coulomb law of friction in terms of slip surface is:

$$\phi = \|f_t\| - \mu f_n \tag{3.38}$$

For the stick or elastic domain, $\phi<0$, while $\phi>0$ is physically impossible. The rate of relative tangential displacement can be split into elastic and plastic parts as follows:

$$\dot{u}_t=\dot{u}_t^e+\dot{u}_t^p \tag{3.39}$$

The rate of change of friction force vector is related to the elastic tangential displacement by:

$$\dot{f}_t=D\dot{u}_t^e \tag{3.40}$$

$$D=\begin{bmatrix}\frac{\mu f_n}{\delta} & 0\\ 0 & \frac{\mu f_n}{\delta}\end{bmatrix} \tag{3.41}$$

where δ is the slip threshold or relative sliding displacement below which sticking is stimulated. The default value is 0.0025 times of average edge length of the element, and the friction force convergence ratio is 0.05. Attention is given to the case that, given a tangential displacement vector, the evolution of f_t would result in a physically impossible situation, so $\phi>0$. It implies that plastic or slip contribution must be determined.

$$\dot{f}_t = D(\dot{u}_t-\dot{u}_t^p) \tag{3.42}$$

The direction of slip displacement rate is given by the normal to the slip flow potential, ψ

$$\psi=\|f_t\| \tag{3.43}$$

$$\dot{u}_t^p=\dot{\lambda}\ \frac{\partial\psi}{\partial f_t} \tag{3.44}$$

where the slip displacement rate magnitude is $\dot{\lambda}$. With the slip surface, ϕ, different from the slip flow potential, ψ is an analogy to non-associative plasticity. Since a 'force point' can never be outside the slip surface, it is required that:

$$\dot{\phi}=\left(\frac{\partial\phi}{\partial f_t}\right)^T\dot{f}_t=0 \tag{3.45}$$

In this way, the magnitude of the slip rate can be determined. To this end, the equations above can be combined to:

$$\left(\frac{\partial \phi}{\partial f_t}\right)^T D\left(\dot{u}_t - \dot{\lambda}\frac{\partial \psi}{\partial f_t}\right) = 0 \qquad (3.46)$$

3.6. Solution Procedure

Newton-Rapson iterative procedure is used. The convergence is based on relative residual or relative displacement criteria. As a convergence criterion, the relative force and displacement tolerance is assumed to be 0.1. The constant load step method is considered. The contact among the bodies is specified using nonlinear node-to-segment contact. The bilinear Coulomb friction based on nodal force is utilized. The fraction force tolerance is assumed 0.05, whereases the slip threshold is given automatically choose by the program. A bias factor of 0.95 is used for contact detection in the case of touch contact. The rubber nodes separate from the rigid contact surface in an unbonded isolator. This separation is based on nodal stress, where the rubber node allows separation when contact stress is zero. In the case of dynamic analysis, the dynamic transient analysis is performed using the Single-Step-Houbolt implicit method. Marc-Mentat used it as a default method and recommended it for transient dynamic analysis. The Single-Step-Houbolt parameters, γ^1= 1.5 and γ= -0.5, are used. The large-strain analysis is performed, and the kinematic deformation is based on the Update Lagrange formulation. Figure 3.7 shows a flowchart of the overall FE analysis procedure.

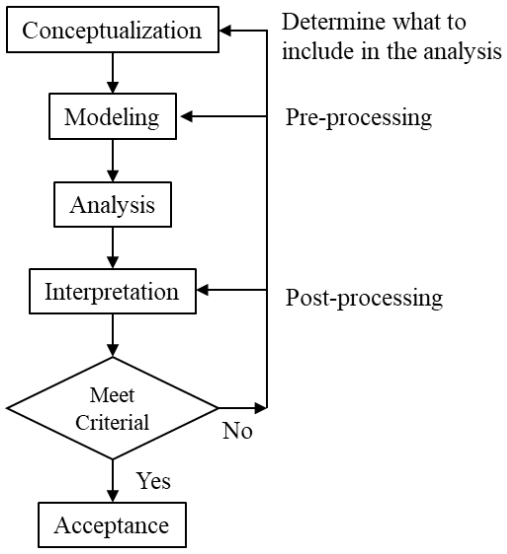

Figure 3.7 The flowchart of overall FE procedure

3.7. Finite Element Model Verification

3.7.1. STRP Isolator Description

An STRP of 12 mm thickness made from Bridgestone 385/65R22.5 tire has five reinforcement layers oriented by ±70° to carcass steel, as shown in Fig. 3.8.

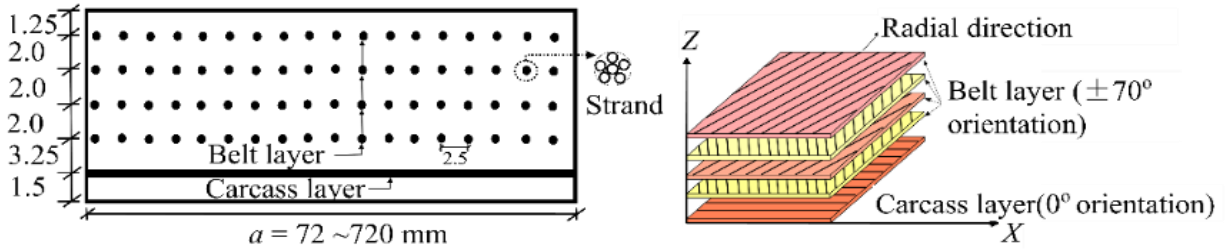

(a) 12-mm single layer STRP (b) Orientation and number of reinforcing layers

Figure 3.8 Reinforcing steel cords in single layer STRP (Bridgestone tire 385/65R22.5)

The experimented STRP isolator is made by stacking four individual STRP layers one above another which is called STRP-4. The size of the STRP-4 is 100×100×48 mm. The thickness of each rubber thickness and that of each steel-cord layer are 2.4 mm and 0.4 mm. The equivalent thickness for steel-cord thickness is assumed for analytical calculation. The primary and secondary shape factor of STRP is 10.4 and 2.08, respectively. Table 2 shows the properties of reinforcing steel cords of the scrap tire. The hyperelastic properties of tire rubber are obtained from Bridgestone 385/65*R*22.5 (Mishra and Igarashi, 2012) using the Mooney-Rivlin material model. The Prony series viscoelastic shear response parameters are employed in the constitutive model of the elastomer to express the hysteretic stress-strain relationship observed in the test. The viscoelastic parameters are derived using a large strain viscoelasticity model described in the previous section. Elastomer softening is introduced from the discontinuous phenomenological damage model, which represents the Mullins effect described in the last paragraph. A pair of multiplier and relaxation time parameters are assumed in each iteration. Then, FE analysis is carried out until the hysteresis loop from the experiment is matched with the FE analysis. The best-suited material parameters for Bridgestone 385/65*R*22.5 parameters are shown in Table 3.

Table 3.1 Properties of reinforcing cord (Bridgestone 385/65*R*22.5)

Layer	Layer No.	No. of Filaments	Filament dia (mm)	Single cord area (mm^2)	Orientation	Equivalent thickness t_f(mm)	Yield Strength (MPa)	Spacing (mm)	E (GPa)	v
Carcass	1	5	0.2	0.44	0°	0.40	2800	2.5	200	0.3
Belt	4	14	0.4	0.63	∓70°					

Table 3.2 Hyperelastic properties of elastomer (Bridgestone 385/65*R*22.5)

Mooney-Rivlin Constant			Shear Modulus (MPa)		
C_{10}	C_{01}	C_{11}	G_{25}	G_0	v
0.40	1.22315	0.18759	1.10	1.31	0.49995

Table 3.3 Viscoelastic and Mullin damage parameters (Bridgestone 385/65*R*22.5)

Prony Shear Responses				Mullin-Damage Parameters			
δ^1	λ^1	δ^2	λ^2	1st scalar	1st relaxation	2nd scalar	2nd relaxation
0.30	0.2	0.30	0.55	0.01	5.0	0.05	10.0

3.7.2. Finite Element Model

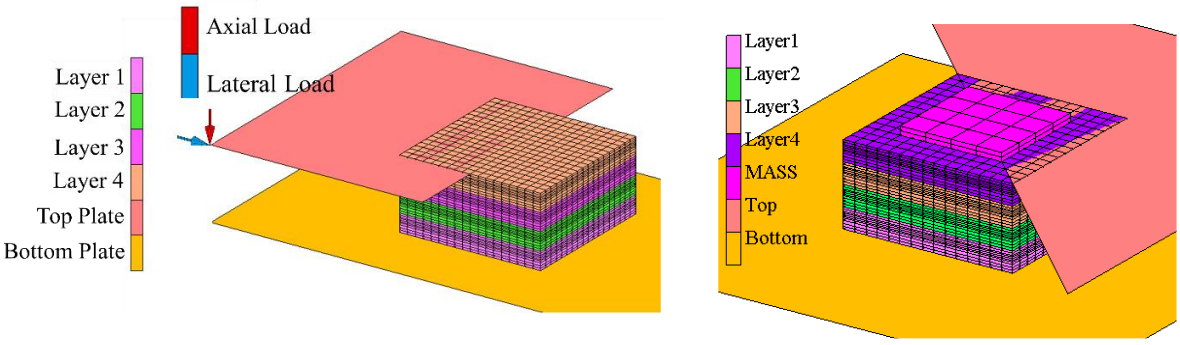

(a) FE model for quasi-static test (b) FE model for pseudo-dynamic test

Figure 3.9 Finite element models of STRP-4 isolator

Figure 3.9 shows the FE model of the STRP-4 isolator. The bottom and top contact surfaces are modeled as a rigid body. All degrees of freedom of the bottom surface and rotational degrees of freedom of the top surface are constrained. Axial force and lateral displacement are applied at the top surface. The contact between the adjacent layers of STRP is assumed as a glue contact so that any detachment or slip between the layers of STRP is not allowed. The friction coefficient used for tire-dry asphalt is 0.7, tire-concrete is

1.0, and rubber-rubber is 1.15 (Glenn, 2006; Walter Forensic Engineering, 2006). The contact surface between the rubber and rigid surfaces is specified as touch contact with the bilinear Coulomb friction model with a friction coefficient of 0.80. In touch contact, each rubber node is constrained along the direction normal to the contact surface, and detaching of the rubber node from the contact surface is allowed. For accurate simulation of the frictional behavior, the segment-to-segment contact algorithm is used. The so-called mixed-method based on Herrmann's formulation is used in large strain analysis for elastomer rubber, and the geometric nonlinearities are incorporated using the updated Lagrangian formulation

3.8. Model Verification

Table 3.4 describes the loading condition used in the experiment and FE analysis. The cyclic displacements consist of three full-reverse cycles for each magnitude of lateral displacements. Before application of lateral load, the isolator is compressed by 5.0 MPa pressure. The ground motion used for the dynamic loading test is the north-south component of the Imperial Valley 1940 earthquake.

Table 3.4 Loading conditions in Quasi-static and dynamic loading tests.

Test name	Loading conditions	
Compression	Step I: Loading to 13.7 MPa then unloading to zero	
	Step II: Loading 20.0 MPa ± (4.0 MPa of three fully reverse cycles) then unloading	
Cyclic Shear	Vertical compression	5.0 MPa
	Shear displacement in terms of rubber thickness	37.5%, 75%, 112.5% and 150%
Pseudo-dynamic	Rigid mass	1107.4 kg
	Input ground motion	N-S component of Imperial valley 1940
	PGA	$a_x = 0.313g$

3.8.1. Verification for Vertical Stiffness

The experimental procedure to determined the vertical stiffness of STRP-4 was described by Mishra (2012). The same conditions are used in the FE simulation. The specimen was loaded up to an equal pressure of 13.7 MPa and unloaded at the initial stage. Then the compressive load was increased to 20 MPa axial pressure on the STRP-4. Starting from 20 MPa, three fully reverse cycles with ±4.0 MPa amplitude were used, and then unloading is performed. The vertical stiffness is defined by the slope of the force-

displacement curve within the cyclic loading part, which is obtained by the least-square curve fitting. Figure 3.10 shows the vertical force-displacement relation for FE simulation and tested specimen, where figure 3.10b is taken from Mishra (2012). The displacement in the tested specimen is substantially high due to the curvature of the STRP pad. Hence, the vertical stiffness found from the experiment, 56.41 kN/mm, is about 29% lower than the FE analysis result, 79.725 kN/mm. Vertical stiffness of STRP specimen can be improved by surface smoothing and using precompression using the bonding process.

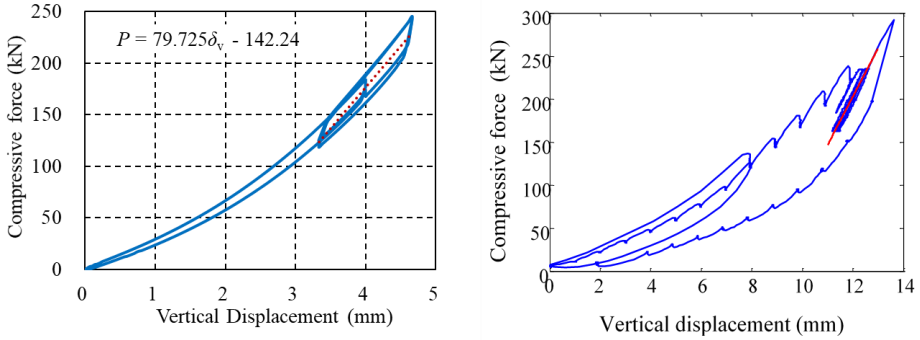

(a) FE analysis (b) Experiment

Figure 3.10 Experimental and FE simulation of the vertical load-displacement relationship

3.8.2. Verification for Cyclic Loading

Table 4 shows the comparison of stiffness values of STRP-4 isolator at four displacement levels, obtained by the past cyclic loading test (Mishra et al., 13a) and FE analysis. A good agreement can be seen among these stiffness values. The hysteresis curve obtained from FE analysis compared with the test result is shown in Fig. 3.11. It is shown that the accuracy of the FE model is acceptable. In particular, the average value of the effective stiffness for STRP-4, defined by the slope of the hysteresis curve and estimated by least-square fitting, is about 124.5 kN/m in both cases. The effective damping obtained by FE analysis is 16.9% higher than the experimental value.

Table 3.5 Horizontal stiffness and damping: Experimental and FEA

Shear strain	Horizontal Stiffness, K_h *(kN/m)*			Effective damping (%)		
(%)	Experiment	FEA	Experiment/FEA	Experiment	FEA	Experiment/FEA
37.5	262	258	1.02	13.2	15.3	0.86
75	206	190	1.08	12.2	16.5	0.74
112.5	163	163	1.00	14.2	15.8	0.90
150	133	137	0.97	15.0	16.4	0.91

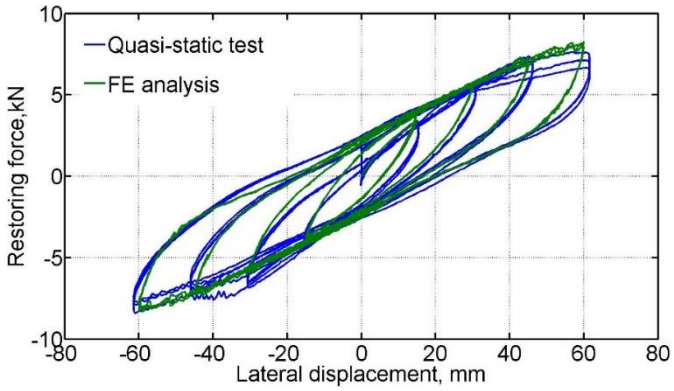

Figure 3.11 Comparison of hysteresis loop found from FE analysis and experiment.

3.8.3. Verification for Dynamic Loadings

Figure 3.12 shows the test condition used for the STRP-4 isolator (Mishra et al., 2014). A rigid mass is applied to the tested specimen through the upper loading block. The experimental loading system consists of one, three, and five actuators in *x*, *y*, and *z* directions. Three actuators have pin connections between the reaction frame and rigid loading block and provide reaction forces F_x, F_y, and F_z or displacements u_x, u_y, and u_z. Four actuators are used to restraint the rotation about the *x* and *y*-axis and the remaining two constraint rotations about the *z*-axis. The isolator is placed between two steel plates, as shown in Fig. 3.12b, without bonding between the plate and the specimen. The actuator F_z controls the vertical compression on STRP, and actuator F_x controls the horizontal displacement or lateral load. F_y restrained the out-of-plane movement. Figure 3.9b shows the FE model presenting the dynamic test conditions. The rigid bottom plane is allowed to move in the direction of ground acceleration only. The rigid top plane carries structural mass and allows it to move freely.

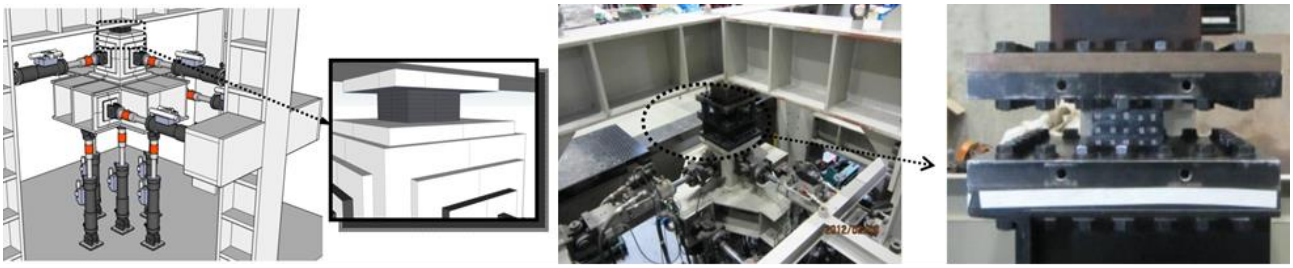

(a) Schematic view of loading system (b) Pseudo-dynamic test of STRP isolator

Figure 3.12 Pseudo-dynamic test conditions (Mishra et al., 2014)

Figure 3.13 compares restoring force-time history and hysteresis loop of STRP-obtained from pseudo-dynamic test and FE analysis result obtained by transient dynamic analysis. The FE analysis result matched well with the experimental test result. Besides, the restoring force peaks and the lateral displacement found from the FE analysis are very close to the experimental result. Figure 3.14 shows that the FE model is efficient in triggering the rollover deformation found from the experiment. Therefore, based on these comparative studies, it is concluded that the FE model of the STRP-4 isolator is acceptable and correctly represents the practical model.

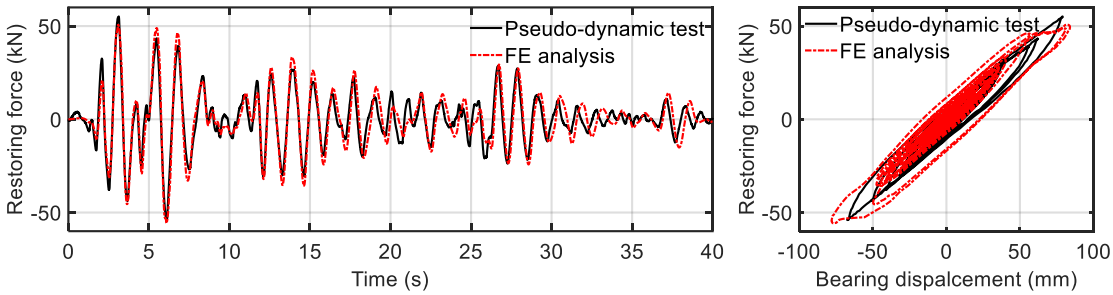

(a) Restoring force time history (b) Hysteresis curve

Figure 3.13 Restoring force-time history and hysteresis loop between FE analysis and experiment

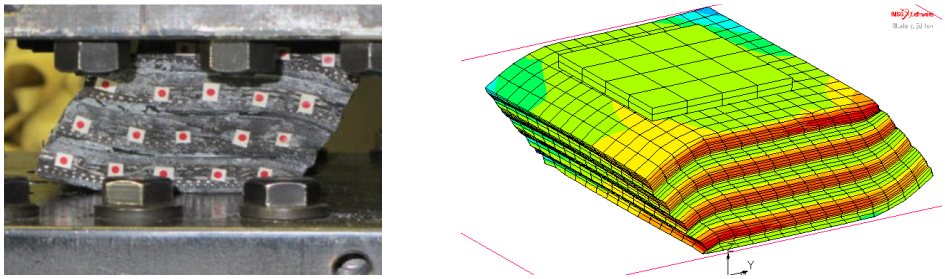

(a) Pseudo-dynamic test (b) FE analysis

Figure 3.14 Deformation of STRP-4 isolator at 100% shear strain

3.9. Conclusion

The finite element modeling and model verification for unbonded STRP isolators using the Marc-Mentat Software are presented. The FE model considered the viscoelastic and hyperelastic properties of elastomer, including the Mullins effect. The FE model is verified with the static and dynamic loading test results. It is found that the simulation results are matched well with the test results. Therefore, it implies that the developed model is acceptable for further simulation of the STRP isolator.

References

Ali A, Hosseini M and Sahari B. (2010). A review of constitutive models for rubberlike materials. *American Journal of Engineering and Applied Sciences*. 3(1), pp. 232-239.

Glenn Elert (1998–2006). *The Physics Hypertextbook, http://hypertextbook.com/physics/mechanics/friction/.* Cited 01 Dec 2006

Helnwein, P., Liu, C. H.M Meschke, G., and Mang, H.A.(1993). A new 3D-FE-Model for Cord Reinforced Composites, Application to Analyses of Automobiles Tires, *Finite Element in Analysis and Design.* 14, pp. 1-16.

Kongo-Kondé, A., Rosu, I., Lebon, F., Brardo, O., and Devésa. B. (2013). On the modeling of aircraft tire. Aerospace Science and Technology. 27 (1), pp.67-75.

Mars, W.V. (2002). Cracking energy density as a predictor of fatigue life under multiaxial conditions. *Rubber Chem. Technol*. 75, pp. 1-17.

Markmann, G. and E. Verron (2006). Comparison of hyperelastic models for rubber-like materials. *Rubber Chem. Technol*. 79 pp. 835-858.

Mishara, H. K. and Igarashi, A. (2012). Experimental and Analytical Study of Scrap Tire Rubber Pad for Seismic Isolation. *Int. J. of Civil and Environ. Eng.* 6(2), pp. 107-113.

Mishra, H. K., Igarashi, A., Matsushima, H. (2013a), Finite element analysis and experimental verification of the scrap tire rubber pad isolator, *Bulletin Earthquake Engineering*. 11(2), pp. 687-707.

Mishra, H. K., Igarashi, A, Ji, D., and Matsushima, H. (2014). Pseudo-Dynamic Testing for Seismic Performance Assessment of Buildings with Seismic Isolation System Using Scrap Tire Rubber Pad Isolators, *Journal of Civil Engineering and Architecture*. 8(1), pp.73-88.

MSC.Marc. (2020A). *Theory and user information*, Vol. A, Santa Ana, CA, MSC Software Corporation.

MSC.Marc. (2020E). *Theory and user information*, Vol. E, Santa Ana, CA, MSC Software Corporation.

Meschke, G. and Helnwein, P. (1994). Large-Strain 3D Analysis of Fiber-Reinforced Composite Using Rebar Element: Hyperelastic Formulation for Cords, *Computational Mechanics*. 13(4), pp. 241-254.

Meschke, G., Payer, H. J., and Mang H. A. (1997). 3D Simulations of Automobile Tires: Material Modeling, Mesh Generation, and Solution Strategies. *Tire Science and Technology*, 25(3), pp. 154-176.

Simo, J. C. (1987). On a Fully Three-dimensional Finite Strain Viscoelastic Damage Model: Formulation and Computational Aspects, *Computer Methods in Applied Mechanics and Engineering*. 60, 153-173.

Thein, C.K.M., Tan, H. M., and Lim, C. H, (2016). Numerical modelling and experimental inflation validation of a bias two-wheel tire, *Journal of Engineering Science and Technology,* 4th EURECA 2015 Special Issue February (2016) 70 - 81© School of Engineering, Taylor's University

Tschoegl N.W. (1971). Constitutive Equations for Elastomers, *Journal of Polymer Science: Part A-1*, 9, pp. 1959-1970.

Vahapoglu, V., Karadeniz, S. and Yazici, I. (2011). Uniaxial tensile testing of rubberlike materials. *Experimental Technique*. 35(1), pp. 24-27

Walters Forensic Engineering (2006), *Skidmark analysis & braking*,
http://www.waltersforensic.com/articles/accident_reconstruction/vol1-no8.htm. Cited 01 Dec 2006.

Chapter 4

Lateral and Vertical Performance of STRP and An Analytical Model for Horizontal Force-Displacement

This chapter focused on the finite element analysis and analytical modeling for vertical and horizontal stiffness of the STRP isolator. Analytical models are evaluated with FE analysis results and experimental results. Based on the FE analysis result, the lateral response and the displacement capacity of square-shaped isolator for different height and strip-shaped isolator with different length-to-width ratios are investigated using Equivalent Lateral Force (ELF) method specified in ASCE SEI 7-10 code.

4.1 Introduction

Automobile tires are made by vulcanization of natural or synthetic rubber material with embedded reinforcing steel cords. The steel cords are placed in the form of layers and orientated in some specific directions. Some researchers have focused on this particular feature of tire material and explored the possibility of the application of the scrap automobile tire material for seismic isolation of structures, and it has been suggested that the scrap tire is regarded as economical and environmentally friendly for the isolation of low to medium-rise buildings (Turer and Özden, 2007; Spizzuoco et al., 2014; Calabrese et al., 2015). The scrap tire rubber pad (STRP) has an equivalent damping ratio of approximately 10~22% and a vertical to horizontal stiffness ratio exceeding 150 (Mishra, 2012; Mishra et al., 2013a; Mishra and Igarashi, 2013b). Those properties of STRP satisfy the requirement as a suitable isolation material (Kelly, 1997; Eurocode 8, 2004). For structures made of masonry or concrete walls, the strip shape isolator is expected to be a cost-effective component of seismic isolation application since a strong base foundation layer is not required (Kelly, 1997; 2002; Tsai and Kelly, 2002) as opposed to the application of SREI. They derived an expression for the compression modulus of strip-shaped FREIs reinforced with flexible carbon fiber and experimented for the same. Their theoretical analyses and the test results confirm that it is possible to produce a fiber-reinforced strip isolator that matches the behavior of a steel-reinforced isolator. Although a strip shape isolator is more suitable to those types of structures, the previous studies on STRP isolators are limited to the types of slender shapes with an aspect ratio of 2.08, and such devices are considered to

be unstable even at low levels of lateral strain (Van Engelen et al., 2015). The force-displacement relation of STRP bearings (Mishra and Igarashi, 2013b; Igarashi et al., 2013) and the seismic response of a hypothetical building isolated with STRP bearings have been investigated through a pseudo-dynamic test (Mishra et al., 2014). Since the twisted reinforcing cords in STRP provide low flexural rigidity, STRP exhibits a unique rollover deformation such that the bearing surfaces initially remain in contact with supports and are separated from the support faces under lateral load (Mishra and Igarashi, 2013b). Such deformation causes a reduction followed by accretion in the lateral stiffness (Toopchi-Nezhad et al., 2008a; Osgooei et al., 2014).

In the present study, square and strip-shaped STRP isolators satisfying the geometric criteria for stability defined by ASSHTO-LRFD design guidelines are investigated by 3D finite element analysis to assess the vertical and lateral performance and the seismic capacity in the orthogonal directions and for different heights of STRP isolator. A modified analytical approach is proposed for the load-displacement relationship under lateral force. The vertical and lateral responses are evaluated using an analytical approach and FE analysis. A unidirectional cyclic lateral load is considered, and strip-shaped isolators are analyzed for loading in longitudinal and transverse directions. The lateral load performance of STRP isolators is evaluated by load-displacement characteristics, lateral stiffness, and effective damping ratio. The maximum bearing displacement of the STRP isolators induced by the design earthquakes is assessed using the method prescribed in AASHTO-LRFD design guidelines to verify the feasibility of the STRP isolator application.

4.2 Scrap Tire Rubber Pad Isolators

The geometric properties of square and strip-shaped STRP isolators considered for the present study are shown in Table 4.1. In the case of the strip-isolator, each bearing consists of two layers of STRP with a height of 24 mm and a width of 72 mm. The length of the strip-isolators is varied so that the shape factor is changed in the range between 7.5 and 13.6 and the length-to-width ratio between 1 and 10. The dimensions of strip bearings are maintained so that the aspect ratio in the longitudinal direction is that in the short direction multiplied with the length-to-width ratio. The aspect ratio in the longitudinal direction is changed from 3.0 to 30. As for square bearings, the aspect ratio is 3.0. The thickness and the shape factor of these isolators are varied from 12 mm to 72 mm and from 3.75 to 22.5, respectively. The equivalent thickness of the elastomer layers and that of the reinforcement layers are assumed to be 2.4 mm and 0.4 mm, respectively. An aspect ratio exceeding 2.50 (Toopchi-Nezhad et al., 2008b; 2009a; Van Engelen et al., 2015) is assumed for each specimen to meet the stability criteria. Notation of isolator shown in Table 4.1

in the form of 'STRP-X/Y' is used to designate the type of STRP isolator model, indicating the number of layers by X and the length-to-width ratio by Y. Loading test of the isolator denoted by STRP-4/1 was carried out. The test results are used for material modeling and model verification.

Table 4.1 Geometric properties of STRP isolator models

Group	Designation	Dimensions $l \times w \times h$ (mm)	l/w	Rubber thickness t_r (mm)	Equivalent thickness t_e (mm)	Shape factor S	Aspect ratio	
							R_x	R_y
Experiment	STRP-4/1	100× 00×48	1	40	2.4	10.4	2.1	2.1
Group-I: Strip shape	STRP-2/1	72×72×24	1	20	2.4	7.5	3	3
	STRP-2/2	144×72×24	2	20		10	6	3
	STRP-2/4	288×72× 24	4	20		12	12	3
	STRP-2/10	720×72×24	10	20		13.6	30	3
Group-II: Square shape	STRP-1/1	36×36×12	1	10	2.4	3.75	3	3
	STRP-2/1	72×72×24	1	20		7.5		
	STRP-3/1	108×108×36	1	30		11.3		
	STRP-4/1	144×144×48	1	40		15		
	STRP-5/1	180×180×60	1	50		18.8		
	STRP-6/1	216×216×72	1	60		22.5		

4.3 Analytical Approach for Vertical Stiffness

The vertical stiffness of a bonded elastomeric bearing under pure compression is determined using the following equation.

$$k_v = \frac{E_c A}{t_r} \tag{4.1}$$

where E_c is the compression modulus and k_v indicates the vertical stiffness at pure compression. A is the plan area of the isolator, and t_r is the total rubber thickness. Kelly and Calabrese (2012) derived an expression for compression modulus based on the pressure solution (PS) approach. For a strip-shaped fiber-reinforced elastomeric bearing, it can be expressed as

$$E_c = K\frac{\rho}{\rho+\gamma}\left(1-\frac{\tanh\beta}{\beta}\right) \tag{4.2}$$

where parameter β, γ, and ρ can be defined as follow.

$$\gamma=\frac{12Gt_eS^2}{E_ft_f} \tag{4.3}$$

$$\rho=\frac{12GS^2}{K} \tag{4.4}$$

$$\beta^2=\gamma+\rho \tag{4.5}$$

In these equations, G and t_e is the shear modulus and thickness of each layer of elastomer, S is the first shape factor, K is the bulk modulus of the elastomer, and E_f, t_f and υ_f are the young modulus, equivalent thickness and passion ratio of the steel cord, respectively. Using the assumption that all elastomer layers have the same compression modulus (neglecting the effect of boundary conditions) and equivalent thickness of steel-cords, the vertical stiffness of an isolator with n layers of elastomer can be calculated by

$$k_v=\frac{E_cA}{n\,t} \tag{4.6}$$

Tsai (2004) derived the effective compression modulus of the i^{th} elastomer layer $E_c^{(i)}$ in an FREI bonded to rigid endplates using the Pressure Approach (PA) method. The compression modulus calculated by the pressure approach is:

$$E_c^{(i)}=2\mu+\lambda\left\{1-\frac{\lambda}{\lambda+2\mu}\left[\left(\frac{\beta_{3i}{}^2-\alpha_0{}^2}{\beta_{3i}{}^2-\beta_{2i}{}^2}\right)\frac{tanh\beta_{2i}b}{\beta_{2i}b}+\left(\frac{\beta_{2i}{}^2-\alpha_0{}^2}{\beta_{2i}{}^2-\beta_{3i}{}^2}\right)\frac{tanh\beta_{3i}b}{\beta_{3i}b}\right]\right\} \tag{4.7}$$

where μ and λ are Lamé's constants and

$$\beta_{2i}{}^2=\frac{1}{2}\left[\alpha_0{}^2+\alpha_{2i}{}^2+\alpha_{3i}{}^2-\sqrt{(\alpha_0{}^2+\alpha_{2i}{}^2+\alpha_{3i}{}^2)^2-4\alpha_0{}^2\alpha_{2i}{}^2}\right] \tag{4.8}$$

$$\beta_{3i}{}^2=\frac{1}{2}\left[\alpha_0{}^2+\alpha_{2i}{}^2+\alpha_{3i}{}^2+\sqrt{(\alpha_0{}^2+\alpha_{2i}{}^2+\alpha_{3i}{}^2)^2-4\alpha_0{}^2\alpha_{2i}{}^2}\right] \tag{4.9}$$

$$\alpha_0=\frac{1}{t_e}\sqrt{\frac{12\mu}{\lambda+2\mu}} \tag{4.10}$$

$$\alpha_1=\sqrt{\frac{12\mu\,(1-\upsilon_f{}^2)}{E_ft_ft_e}} \tag{4.11}$$

$$\alpha_{2i}{}^2=\frac{\alpha_1{}^2(-f_{i+1}+2f_i-f_{i-1})}{12f_i} \tag{4.12}$$

$$\alpha_{3i}{}^2=\frac{\alpha_1{}^2(f_i+f_{i\text{-}1})}{2f_i} \tag{4.13}$$

$$f_i=4\frac{i}{n}\left(1-\frac{i}{n}\right) \tag{4.14}$$

$$\lambda=3\mathrm{K}\frac{\upsilon}{1+\upsilon} \tag{4.15}$$

$$\mu=3\mathrm{K}\frac{\upsilon-2\upsilon}{2+2\upsilon} \tag{4.16}$$

$$\frac{K}{G}=\frac{2}{3}\frac{1+\upsilon}{1-2\upsilon} \tag{4.17}$$

In these equations, υ is the Poisson's ratio for elastomer, and n is the number of elastomer layers. The total vertical stiffness of the isolator can be calculated using the following equation.

$$k_v=\frac{A}{t\sum_{i=n}^{n}\frac{1}{E_c^{(i)}}} \tag{4.18}$$

4.3.1 Vertical Stiffness of STRP Isolators

Mishra (2012) described the experimental procedure to determine the vertical stiffness employed in the FE analysis. First, the isolator is loaded by vertical displacement equal to 10% of the original height of the isolator. Then three fully reverse cycles with ±20% of the previous displacement were imposed. The vertical stiffness is calculated from the slope of the force-displacement curve within the cyclic loading part. Both square-shaped and strip-shaped isolators were taken into consideration. The shear modulus at 25% strain is estimated to be 1.1 MPa from the experimental test under 5.0 MPa compression. The bulk modulus K is 950 MPa, calculated using Eq. 4.17, and Poisson's ratio is 0.4998. The elastic modulus of steel-cord and Poisson's ratio is 200 GPa and 0.20, respectively.

Figure 4.1 shows the vertical force-displacement relationship at pure compression in different strip-shape. Figure 4.2 shows the same for square-shaped STRP isolators have an aspect ratio of 3.0 and for a different number of stacks. The equation of the slope of the force-displacement curve under the cyclic loading part is shown in each figure and is determined using the least square method. Table 4.2 and Table 4.3 show the comparison of vertical stiffness found from two closed-form solutions with the FE analysis result in the strip-shaped and square-shaped isolator. It shows that the pressure solution highly underestimating the vertical stiffness, which is high for a high value of the length-to-width ratio. The prediction of the pressure approach is somewhat overestimating and acceptable. The normalized value of vertical stiffness (K_v/A) is

large for a high length-to-width ratio of the isolator, although the vertical pressure is the same. This is due to the more significant influence of free ends in an isolator with a high length-to-width ratio.

Figure 4.3 shows the effect of the length-to-width ratio and number of stacks on the compression modulus ($E_c=k_v t_r/A$). For a length-to-width ratio below 4.0, the compression modulus is changed abruptly, beyond which the influence of the length-to-width ratio decreases with an increase of length-to-width ratio. Similarly, for a fixed aspect ratio, the compression modulus increases with a rise in the number of stacks.

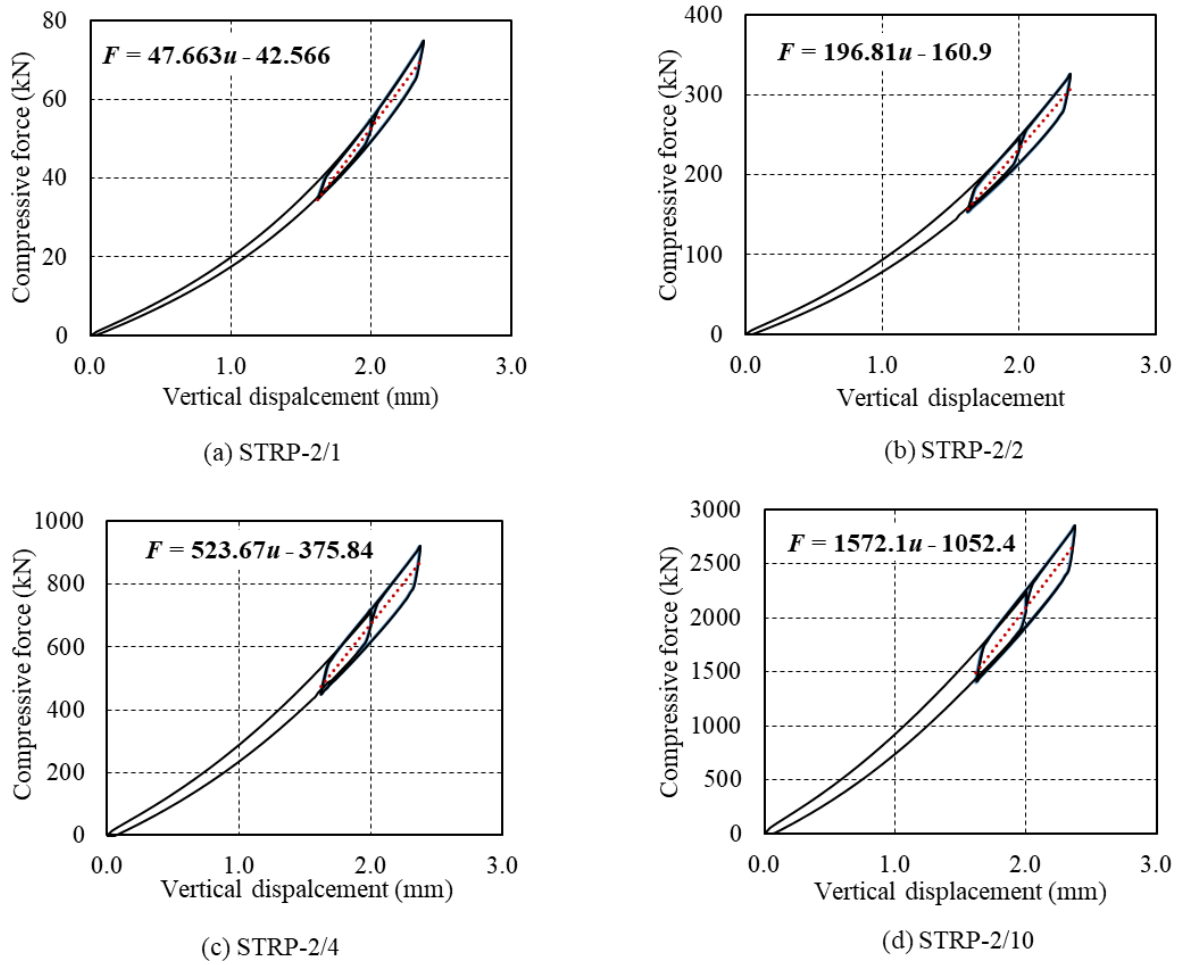

(a) STRP-2/1 (b) STRP-2/2

(c) STRP-2/4 (d) STRP-2/10

Figure 4.1 Vertical force-displacement curves for STRP isolators

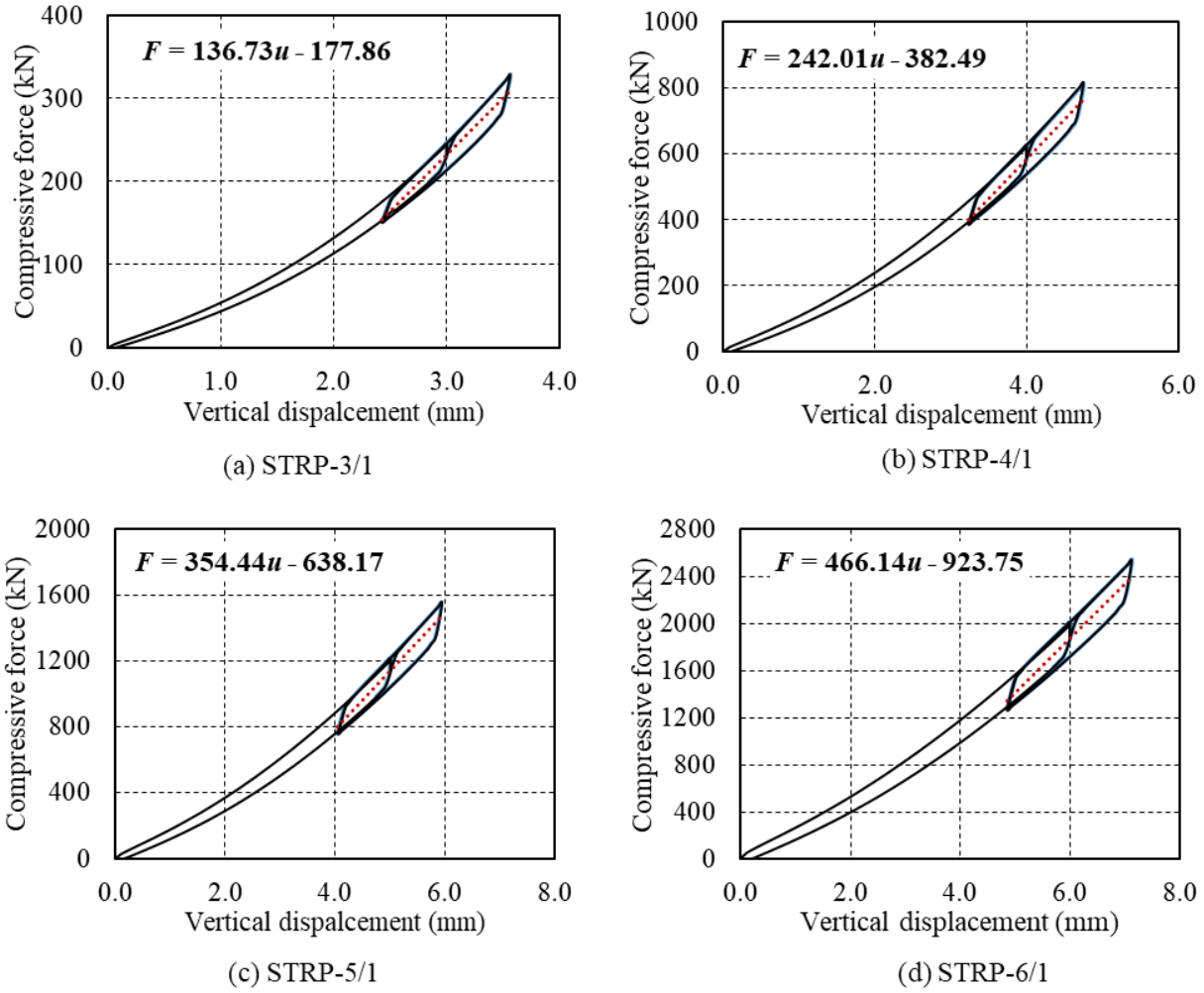

Figure 4.2 Vertical force-displacement curves for different stack number and aspect ratio of 3.0 of STRP isolator: (a) 3-stacks, (b) 4-stacks, (c) 5-stacks and (6) 6-stacks

Table 4.2 Vertical Stiffness for strip-shaped isolator (*kv*) kN/mm

Isolator	FEA	PS	Difference(%)	PA	Difference (%)
STRP-4/1	68.6	60.9	-11.2	73.7	+6.7
STRP-2/1	47.7	41.0	-15.1	51	+7.4
STRP-2/2	196.8	121	-38.4	212	+7.6
STRP-2/4	523.7	301.5	-42.4	597	+12.4
STRP-2/10	1572.1	861.7	-45.2	1767	+12.4

Table 4.3 Vertical Stiffness for square-shaped isolator (k_v) kN/mm

Isolator	FEA	PS	Difference(%)	PA	Difference (%)
STRP-3/1	136.7	103.9	-24.0	124.1	-9.2
STRP-4/1	242.0	185.7	-23.3	212.4	-12.2
STRP-5/1	354.4	276.2	-22.1	306.3	-13.6
STRP-6/1	466.1	370.7	-20.5	402.5	-13.6

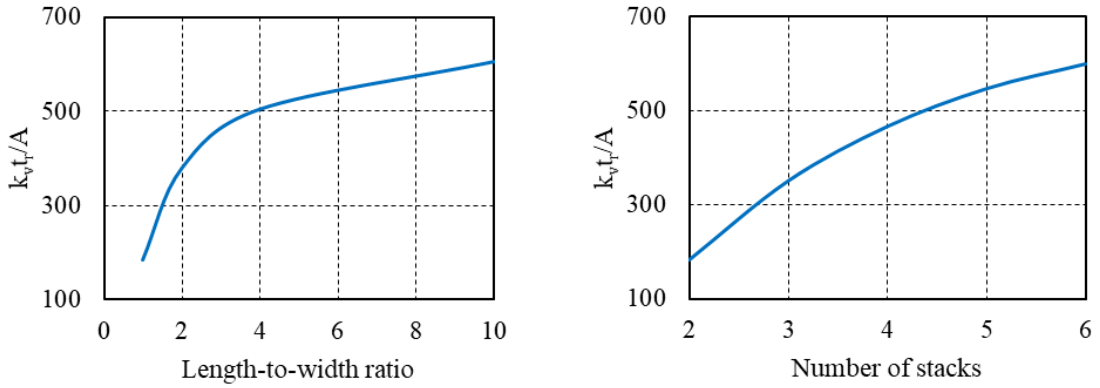

Figure 4.3 Vertical stiffness for different length-to-width ratios and heights for a fixed aspect ratio.

4.4 Horizontal Stiffness

The horizontal stiffness of a bonded type bearing is given by the following equation (Kelly, 1997):

$$K_b = \frac{GA}{t_r} \tag{4.19}$$

in which G is the shear modulus, and A is the plan area of the isolator. The shear modulus is found to decrease as the lateral strain increases (Ashkezari *et al.*, 2008; Strauss *et al.*, 2014; Das *et al.*, 2014), and in the case of unbonded type bearing, a significant reduction of the shear modulus occurs within the intermediate strain levels (Strauss *et al.*, 2014) followed by a rise after the full rollover. In order to express such strain dependence of the shear modulus, the effective modulus, G_{eff}^{ub} was proposed by Gerharer (Gerharer *et al.*, 2011; Ngo *et al.*, 2017) as given by

$$G_{eff}^{ub}=\begin{cases} G\left\langle 1-\left[\dfrac{p}{p_{crit,0}\left\{1-\left(\frac{u}{a}\right)^2\right\}}\right]^2\right\rangle\left(1-\dfrac{u}{a}\right) & \text{for } 0\le u<t_r \\ G\left\langle 1-\left[\dfrac{p}{p_{crit,0}\left\{1-\left(\frac{t_r}{a}\right)^2\right\}}\right]^2\right\rangle\left(1-\dfrac{t_r}{a}\right) & \text{for } t_r\le u<1.5t_r \end{cases} \tag{4.20}$$

Garharer assumed shear modulus is constant between 100% and 150% shear deformation. For deformation exceeding 150%, no prediction for shear modulus is available. However, some studies show that the horizontal stiffness of the unbonded isolator increases due to rollover deformation. Besides, deformation beyond the full rollover causes the rubber molecules more interactive and come close together. Therefore, it is assumed that the shear modulus is going to be restored beyond the rollover deformation. Hence, it is proposed that for displacement exceeding 150% shear, elastomer modulus increases according to the following equation.

$$G_{eff}^{ub}=\begin{cases} G\left\langle 1-\left[\dfrac{p}{p_{crit,0}\left\{1-\left(\frac{u}{a}\right)^2\right\}}\right]^2\right\rangle\left(1-\dfrac{u}{a}\right) & \text{for } 0\le u<t_r \\ G\left\langle 1-\left[\dfrac{p}{p_{crit,0}\left\{1-\left(\frac{t_r}{a}\right)^2\right\}}\right]^2\right\rangle\left(1-\dfrac{t_r}{a}\right) & \text{for } t_r\le u<1.5t_r \\ G\left\langle 1-\left[\dfrac{p}{p_{crit,0}\left\{1-\left(\frac{2.5t_r-u}{a}\right)^2\right\}}\right]^2\right\rangle\left(1-\dfrac{2.5t_r}{a}+\dfrac{u}{a}\right) & \text{for } 1.5t_r\le u<2.5t_r \end{cases} \tag{4.21}$$

where p is vertical pressure on the isolator, u is lateral displacement, a is the isolator dimension parallel to the lateral load, and t_r is the total rubber thickness. $P_{\text{crit},0}$ is called the critical load capacity of the bearing at zero lateral strain and is given by the following expressions:

$$p_{crit,0}=\frac{p_{crit}}{a^2}, \qquad p_{crit}=\frac{\sqrt{2}\pi GASr}{t_r}, \qquad r=\frac{a}{2\sqrt{3}} \tag{4.22}$$

where r is the radius of gyration and S is the shape factor (Kelly, 2003). Although the shear modulus is assumed to be constant for a nominal shear strain of rubber between 100% and 150% in the previous studies by Gerharer and Ngo, the shear modulus has been shown to reduce, and some literature identified nonlinear reduction (Mishra *et al*., 2014; Strauss *et al*., 2014; Tsai and Hsueh, 2001) and is observed to increase for

shear strain exceeding 150% (Strauss *et al*., 2014; Russo *et al*., 2013). In the unbonded application, both friction force and friction area change as the lateral deformation increases, as shown in Fig. 4.4. These effects are expressed by the following expression (Toopachi-Nezhad, 2014):

$$A_{eff}=b(a-d) \quad \text{where} \quad d=\frac{25}{16}\gamma h \tag{4.23}$$

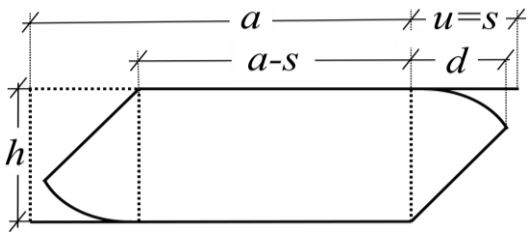

Figure 4.4 Lateral deformation of unbonded STRP isolator

in which A_{eff} is the effective bearing area that remains in contact with supports, d is the projected length of the rollover region, h is the height of the isolator, as described in Fig. 4.4. The geometric parameter γ is defined by

$$u=s=\frac{25}{64}\,h\left[2\gamma\sqrt{1+4\gamma^2}+ln\left(2\gamma+\sqrt{1+4\gamma^2}\right)\right] \tag{4.24}$$

Although the axial load affects the displacement corresponding to the initiation of the bearing's separation from the support faces (Russo *et al*., 2013; Pauletta *et al*., 2015), this effect is ignored in the study of Topchi-Nezhad. Moreover, the deformed shape of the stress-free side rubber surfaces tends to change from a parabolic one to a flat plane normal to the layer when the bearing displacement exceeds the rollover displacement, resulting in a reduction of shear strain and apparent stiffening of the bearing. In the current study, both rollover deformation and the effect of axial load are considered through a modified effective area, A_{effm} given by

$$A_{effm}=b\{a-(d-d_0)\} \qquad \text{where} \quad d_0=H\sqrt{1-\left(1-\frac{p}{E_c}\right)^2} \tag{4.25}$$

and d used in Eq. (4.25) is replaced with $d-(u-1.67t_r)$ for displacement such that $u\geq 1.67t_r$. Therefore, the restoring force and lateral stiffness of an unbonded STRP isolator is given by

$$F_u = \frac{G_{eff} A_{effm}}{t_r} u \tag{4.26}$$

$$K_u = \frac{G_{eff} A_{effm}}{t_r} \tag{4.27}$$

4.4.1 Restoring Force and Horizontal Stiffness of STRP Isolators

Figures 4.5 and 4.6 show the comparison of restoring force obtained from analytical solution and FE simulation results for strip and square shape isolators, respectively. Both constant and user-modified shear modulus for shear strain exceeding 150% is considered. In the case of a square-shaped isolator, as shown in Figs. 4.5a and 4.6, the analytical solutions matched well until 167% shear strain. For displacement exceeding 167% shear, the analytical solutions underestimating the restoring force. A modification in shear

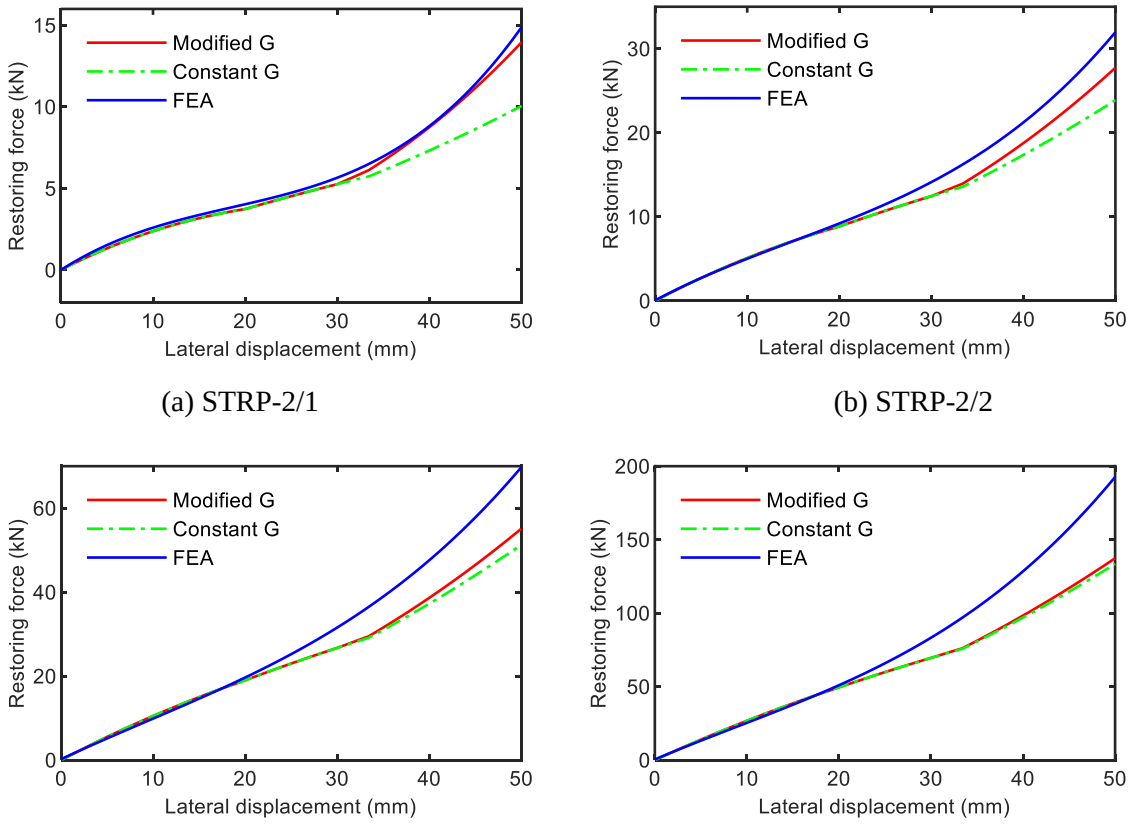

(a) STRP-2/1 (b) STRP-2/2

(c) STRP-2/4 (d) STRP-2/10

Figure 4.5 Force-displacement relationship of strip-shaped isolator: comparison between FE analysis and analytical model.

modulus, as proposed in Eq. 4.21 for displacement exceeding 150% shear, shows a better approximation of the restoring force. In the case of the strip-shaped isolator, the underestimation of restoring force increases with an increase of length-to-width ratio because the isolator becomes self-restraint. In addition, restoring force for constant and modified shear modulus are comparable for a high length-to-width ratio of the isolator.

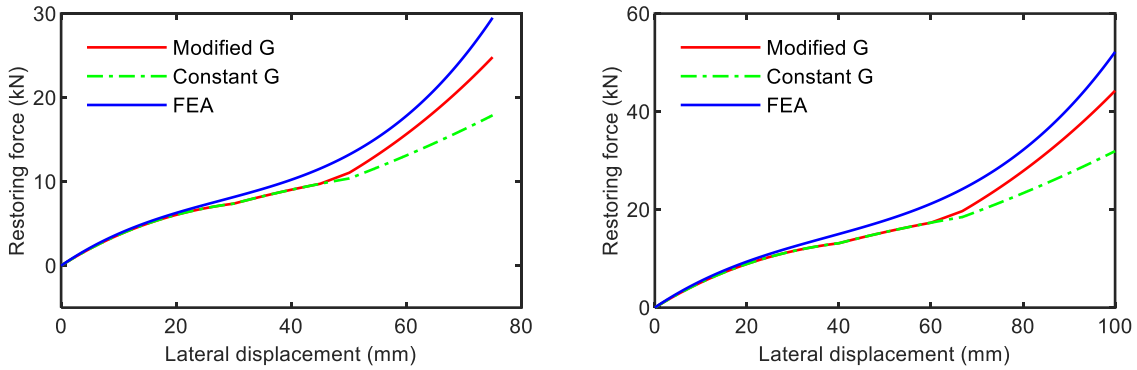

(a) STRP-3/1

(b) STRP-4/1

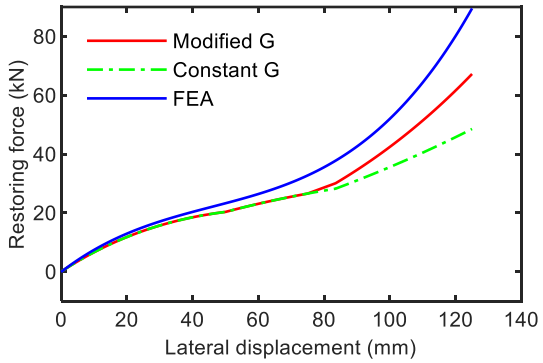

(c) STRP-5/1

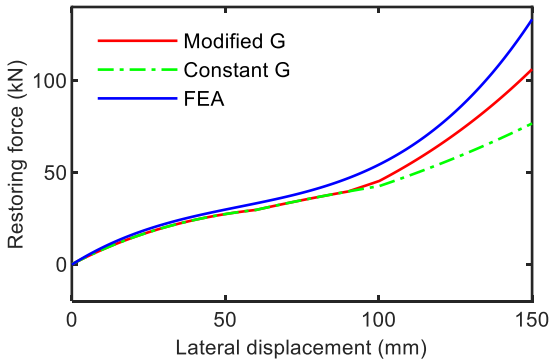

(d) STRP-6/1

Figure 4.6 Force-displacement relationship of square-shaped isolator: comparison between FE analysis and analytical model.

In order to check the validity of the proposed method to STRP isolators, lateral stiffness estimated by the modified method (with constant *G*) is compared with the data obtained in different experimental studies by Toopchi-Nezhad (2008a), Al-Anany (2017), and Mishra (2013a). Comparison of lateral stiffness shown in Fig. 4.7, in which notation "EX," "EM," and "MM" indicate experiment, the existing method, and the modified method, respectively. In a lower shear strain range of less than 150%, stiffness found from the existing solution is comparable with the experimental result, and the modified solution provided a slightly

higher value than the existing method because of the compression effect. However, for displacements exceeding 150%, the existing method significantly underestimates the stiffness obtained by the experimental results. The reason is that bearing rollover deformation is ignored in the existing method when deformation exceeds the limit shear strain of 167% at which the vertical rubber surfaces of the isolator touch the support faces (Toopchi-Nezhad, 2014; Konstantinidis and Kelly, 2014). Figures 4.7a and 4.7b show that the modified method provides a considerably close prediction of the experimental result at all displacement ranges.

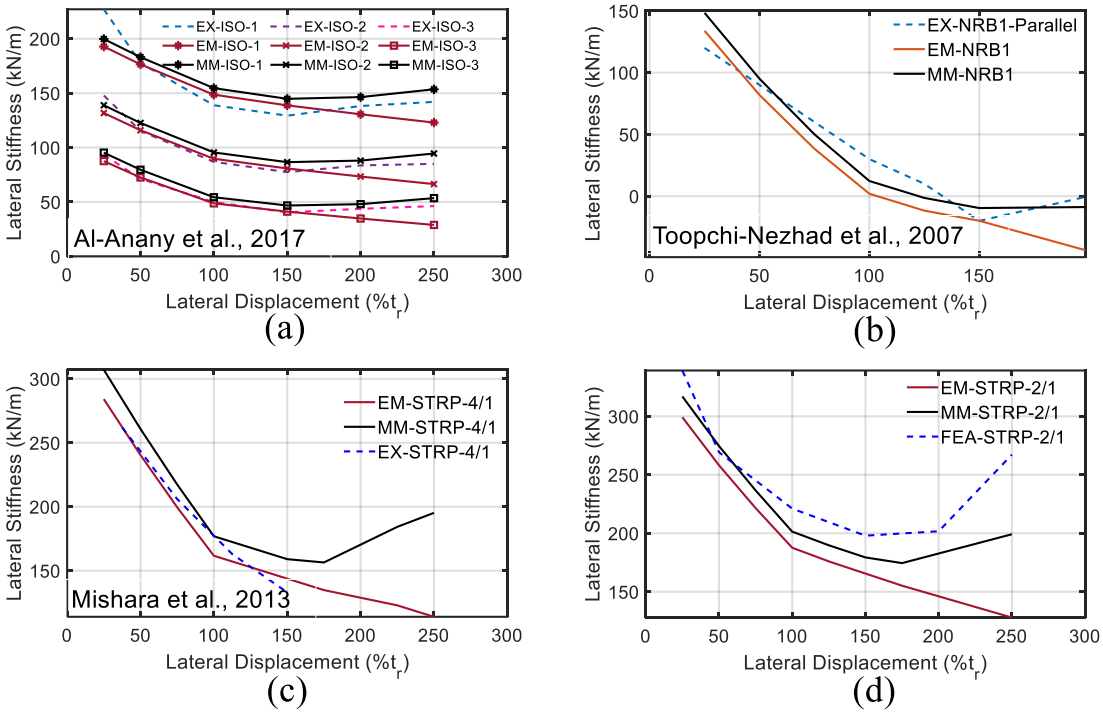

Figure 4.7 Comparison lateral stiffness estimated by the proposed method, existing analytical approach with experimental studies.

4.5 Lateral Load Performance of STRP Isolator

4.5.1 Load-Displacement Relationships

Figures 4.8 and 4.9 show the normalized force-displacement curves of the STRP-2/1, 2/2, 2/4, and 2/10 strip-shaped isolators. The hysteresis curves indicate that each isolator subjected to a compressive load of 5.0 MPa exhibits a stable rollover behavior and displays no slippage within the lateral displacement corresponding to 250% shear strain. Therefore, the minimum aspect ratio of 3.0 recommended in

AASHTO-LRFD method A (AASHOT-LRFD, 2014) for bonded type isolators can also be used for the unbonded case as a stability requirement at 5.0 MPa compression. According to Figs. 4.8 and 4.9, a large value of length-to-width ratio induces the onset of hardening at a lower strain level and subsequent rapid increase of the restoring force, which is highly noticeable in the longitudinal direction. For example, the hardening in STRP-2/2, 2/4, and 2/10 initiates from a displacement exceeding 100% shear strain in the longitudinal direction, as shown in Figs. 4.8b to 4.8d, whereas the hardening in the transverse direction starts from a 150% shear strain, which is shown in Figure 4.9. In both directions, STRP-2/1 shows hardening initiates from 150% shear strain. Comparing these hysteresis curves, the contribution of the rollover in the restoring force is increased for bearing with a low aspect ratio as STRP-2/1 in Fig. 4.8a. In contrast, the contribution becomes negligible for aspect ratios greater than 5.0 as STRP-2/10 in Fig. 4.8d.

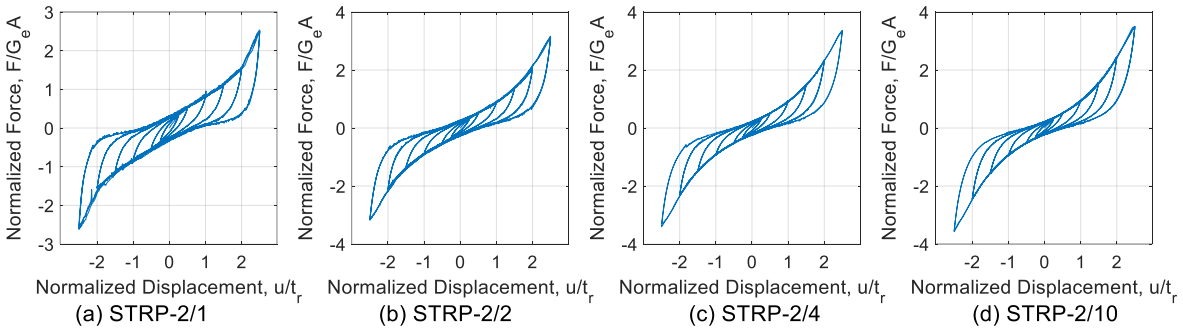

Figure 4.8 Hysteresis curve for longitudinal loading

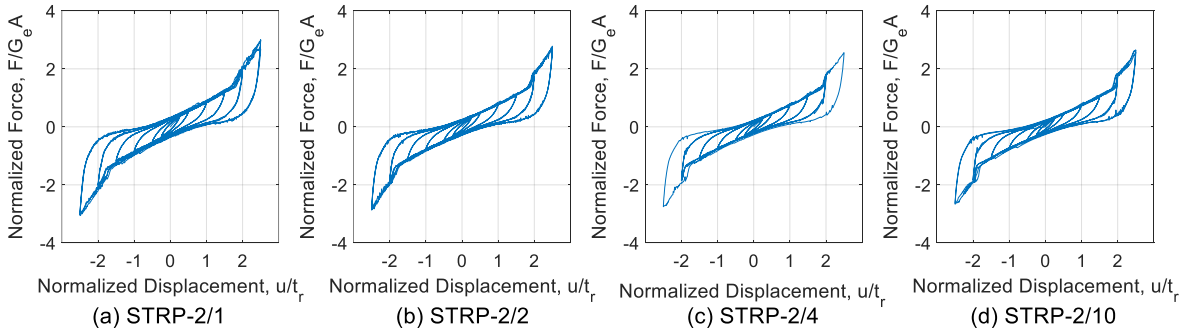

Figure 4.9 Hysteresis curve for transverse loading

Figure 4.10a shows the computed deformed shapes of the STRP-2/1 isolator at different levels of longitudinal displacements. The top and bottom surfaces of the isolator roll-off from the contact surfaces, resulting in a reduction of the shear area on the contact surface. The shear area reduction continues until the vertical side surfaces of the bearing come in touch with the contact surface, as shown in Fig. 4.10b. This

result conforms with the deformed shape of the STRP isolator models observed during loading tests (Mishra and Igarashi, 2103b).

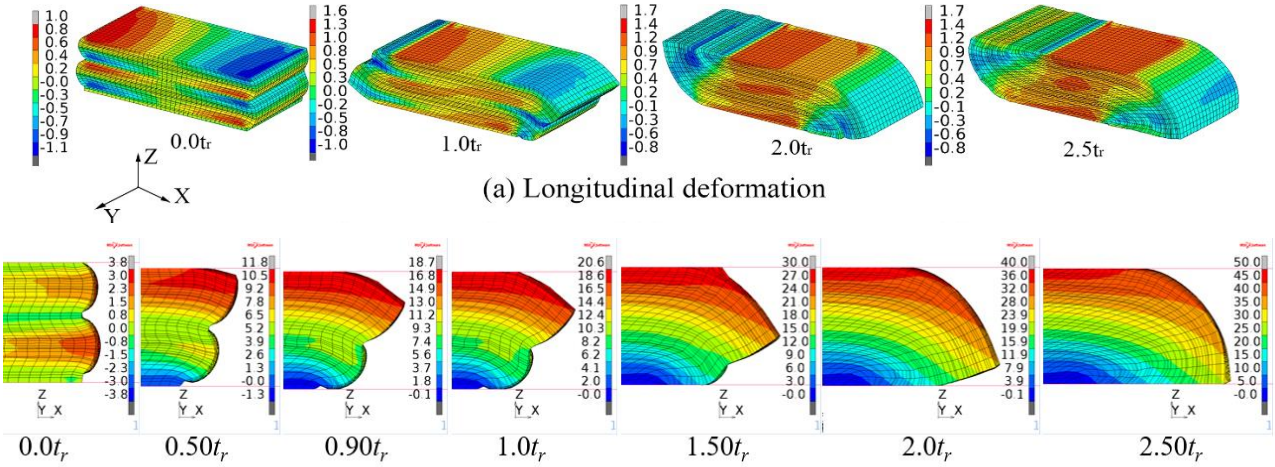

(a) Longitudinal deformation

(b) Progressive contact of STRP isolator with support face

Figure 4.10 Lateral deformation of un-bonded STRP isolator

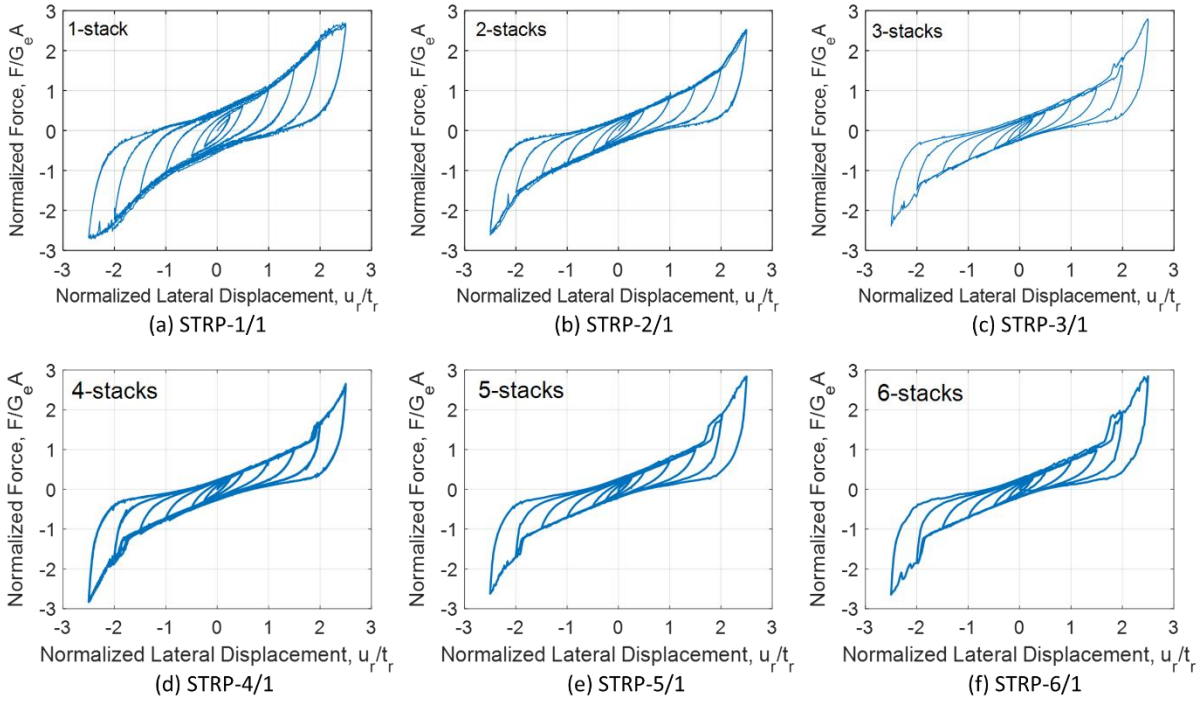

Figure 4.11 Normalized force-displacement relations for different numbers of stacked STRPs

The normalized force-displacement curves of square-shaped isolators for different numbers of stacked STRPs are shown in Fig. 4.11. Each bearing has an aspect ratio equal to 3.0 and is subjected to shear loading up to 250% shear strain under an axial compression of 5.0 MPa. These figures indicate that each bearing displays a positive increment of lateral force and no slippage up to 250% shear strain. It implies that the number of stacks does not affect the lateral stability if the aspect ratio is maintained to 3.0. Therefore, an aspect ratio of 3.0 is suitable against instability without regarding the height of an un-bonded STRP isolator. The normalized value of the maximum restoring force of stacked STRPs at 250% shear strain is almost unaffected by the number of STRP stacks. The area of the hysteresis loop for any number of STRP stacks exceeding 3.0 is nearly the same.

6.2 Horizontal Stiffness and Effective Damping Ratio

The values of stiffness and damping ratio of the strip-STRP isolators obtained from FE analysis are shown in Tables 4.4 and 4.5. Figure 4.12 shows the plots of normalized lateral stiffness and the longitudinal-to-transverse stiffness ratio at different levels of lateral strains and length-to-width ratios. The dashed line indicates the stiffness obtained from the modified stiffness solution (with constant G), while the solid line indicates the stiffness found from the FE analysis result. The stiffness of square-shaped STRP-2/1 obtained by the modified method shows good agreement with the FE analysis result for displacements up to 150% shear strain. However, the FE analysis result for displacement exceeding 150% shear strain is higher than the values obtained by the modified method. For the other isolators, the transverse stiffness is comparable with that from the modified method for displacements up to 100% shear strain, and the modified method provides good estimates of the longitudinal stiffness only for a displacement of 25% shear strain. In summary, the modified method results in higher stiffness in the intermediate displacement range and lower stiffness in the higher displacement range. The

Table 4.4 Horizontal stiffness and damping of STRP-2 isolator under longitudinal loading.

Normalized displacement (u/t_r)	STRP-2/1		STRP-2/2		STRP-2/4		STRP-2/10	
	K_h (kN/m)	Damping β (%)	K_h (kN/m)	Damping β (%)	K_h (kN/m)	Damping β (%)	K_h (kN/m)	Damping β (%)
$0.25t_r$	339.2	14.31	658.6	12.04	1296.4	11.76	3229.3	11.7
$0.5t_r$	269.3	16.63	528.6	14.59	1071.4	13.69	2699.3	13.5
$1.0t_r$	221.1	15.45	461.8	12.91	970.0	11.93	2500.7	11.6
$1.5t_r$	198.0	14.66	477.3	11.04	1045.4	9.95	2720.8	9.6
$2.0t_r$	201.7	13.39	549.6	9.50	1211.6	8.74	3182.5	8.4
$2.5t_r$	267.3	11.00	657.6	8.85	1404.0	8.40	3670.7	8.2

probable reasons for this discrepancy are the following two factors: the effect of the length-to-width ratio as described in Fig. 4.5 and distinctive rollover peculiar to the STRP isolator, as shown in Fig. 4.10. The STRP isolator displays a progressive rollover deformation leading to touching of the vertical side face on the support face at a displacement of 90% shear strain. The touching area keeps growing until a 250% shear strain displacement, as shown in Fig. 4.10b, instead of 167% shear strain generally observed for FREI (Konstantinidis and Kelly, 2014). The feature of STRP isolators regarding this progressive contact makes the device more restrained and stable. This property becomes more visible with the increase of the length-to-width ratio.

Table 4.5 Horizontal stiffness and damping of STRP-2 isolator under transverse loading.

Normalized displacement (u/t_r)	STRP-2/1		STRP-2/2		STRP-2/4		STRP-2/10	
	K_h (kN/m)	Damping β (%)	K_h (kN/m)	Damping β (%)	K_h (kN/m)	Damping β (%)	K_h (kN/m)	Damping β (%)
$0.25t_r$	350.9	12.95	630.1	12.44	1203.0	10.97	2928.3	12.3
$0.5t_r$	274.2	16.10	493.5	15.11	949.5	14.63	2345.0	14.4
$1.0t_r$	222.1	15.09	406.1	14.13	794.5	13.48	1970.8	13.2
$1.5t_r$	205.9	13.85	386.7	12.74	759.6	12.26	1867.4	12.1
$2.0t_r$	268.0	10.66	490.4	9.89	941.5	9.76	2371.5	9.5
$2.5t_r$	314.2	10.77	586.2	9.88	1101.3	10.08	2755.8	9.8

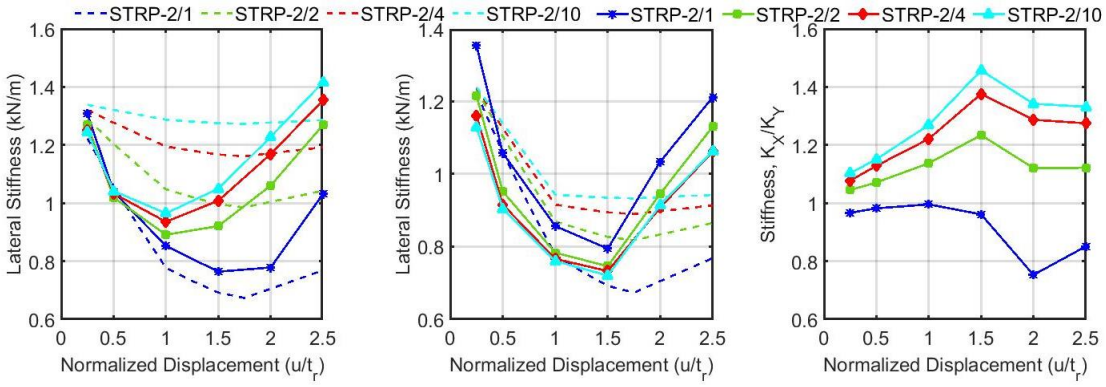

(a) Longitudinal direction (b) Transverse direction (c) Longitudinal-to-transverse ratio of stiffness

Figure 4.12 Relationship between horizontal stiffness and lateral displacement

Figure 4.12 shows that as the length-to-width ratio increases, the longitudinal stiffness increases, whereas the transverse stiffness shows a minor decrease. For example, comparing STRP-2/1 and STRP-2/10, longitudinal stiffness increased by 37.4%, 57.8% and 37.5% at displacement of 150%, 200% and 250% shear

strain, respectively. On the other hand, the transverse stiffness decreased by 12% on average at each level of lateral displacement. Therefore, a high value of length-to-width ratio reduces the efficiency of isolation of a strip size isolator in the longitudinal direction. Figure 4.9c shows the relationship of the longitudinal-to-transverse stiffness ratio and the lateral displacement. As the length-to-width ratio increases, stiffness in the longitudinal direction increases by 1.15~1.40 times.

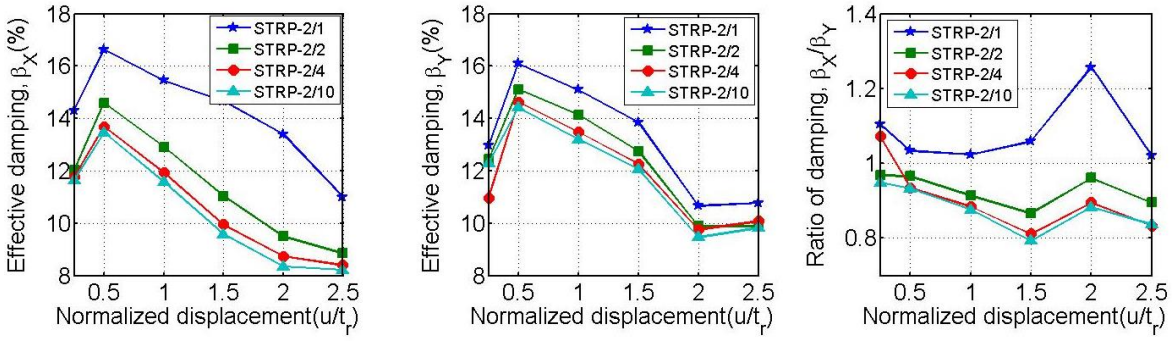

(a) Longitudinal direction (b) Transverse direction (c) Longitudinal-to-transverse ratio of damping

Figure 4.13 Effective damping vs. lateral displacement obtained by FE analysis.

Figure 4.13 shows the effective damping ratios obtained from the FE analysis results. This result indicates that the minimum effective damping ratio of the strip STRP isolator is approximately 8% for the longitudinal direction and 10% for the transverse direction. The effective damping ratio tends to be lower for a high value of the length-to-width ratio. The length-to-width ratio as high as 10 causes an average damping reduction of about 26.5% and 10.3% at each level of lateral displacement in the longitudinal and transverse directions, respectively. For displacement at 250% shear strain, the effective damping ratio decreased by 38% and 33% for the longitudinal and transverse directions, respectively. The damping of the strip bearing is higher in the transverse direction than in the longitudinal direction, as given in Fig. 4.13c. The specified minimum damping in the design recommendation should be selected considering these properties of the STRP isolator.

Table 4.6 shows the stiffness and damping values of the square-shaped bearing with a different number of stacks of STRP. The number of stacks increases from 1 to 6, and each stack is 12 mm thick. The aspect ratio is assumed to equal 3.0 for all isolators. Each isolator is compressed by 5.0 MPa pressure first and then subjected to shear loading up to 250% shear strain in the carcass direction. Figure 4.14 shows the normalized stiffness and damping ratio for different numbers of stacks. Although the normalized stiffness decreases with the number of stack increases, the variation of the values is within ±10% of the average value. Therefore, horizontal stiffness increases approximately in proportion with the number of stacks, provided that the aspect ratio is maintained to 3.0. The damping ratio decrease by 10~20% as the number of stacks increases from 2 to 6, and the minimum damping is 10% for the 6-stacked STRP isolator.

Table 4.6 Horizontal stiffness and damping of square STRP isolator for loading in the carcass direction.

Normalized displacement (u/t_r)	STRP-1/1		STRP-2/1		STRP-3/1		STRP-4/1		STRP-5/1		STRP-6/1	
	1-stack		2-stacks		3-stacks		4-stacks		5-stacks		6-stacks	
	K_h (kN/m)	Damping β (%)	K_h (kN/m)	Damping β (%)	K_h (kN/m)	Damping β (%)	K_h (kN/m)	Damping β (%)	K_h (kN/m)	Damping β (%)	K_h (kN/m)	Damping β (%)
$0.25t_r$	213.9	14.8	350.9	12.95	458.6	13.4	585.1	12.3	712.4	10.9	832.5	10.96
$0.5t_r$	168.1	19.4	274.2	16.10	354.6	15.3	483.7	14.8	551.8	14.8	654.3	14.54
$1.0t_r$	136.2	19.1	222.1	15.09	293.5	14.6	381.2	14.2	451.4	14.1	550.1	13.44
$1.5t_r$	136.6	16.9	205.9	13.85	271.4	13.9	362.0	12.9	429.0	13.1	505.9	12.81
$2.0t_r$	146.9	14.8	268.0	10.66	304.2	12.0	442.1	10.3	557.0	9.9	721.8	10.91
$2.5t_r$	140.2	12.8	314.2	10.77	402.9	10.2	569.0	9.4	707.7	9.4	853.9	9.72

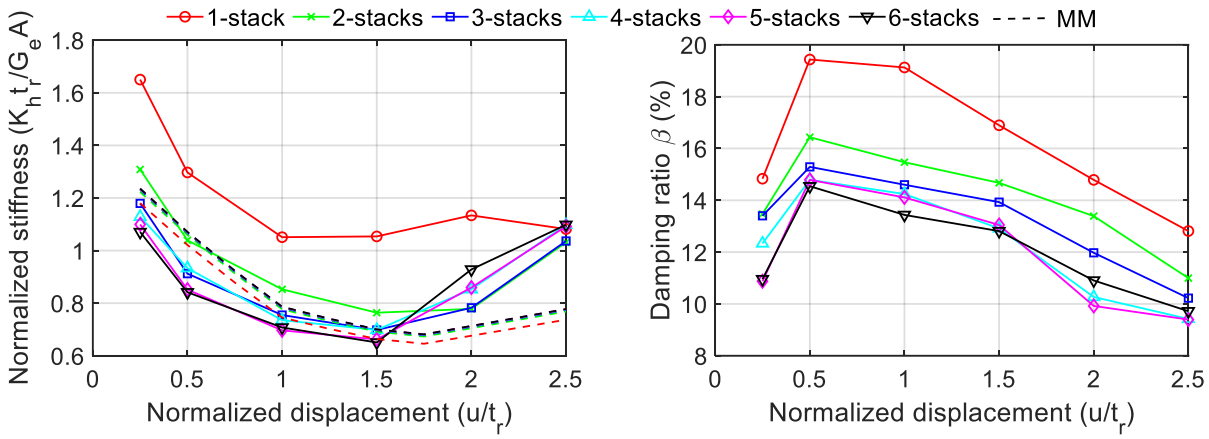

Figure 4.14 Normalized stiffness and damping ratio for different number of stacks of STRP

4.6 Maximum Displacement and Period of STRP Isolator

In this section, the seismic capacity of the strip-STRP isolators is assessed to check the feasibility of the STRP isolators under an example of building design conditions that can be encountered in application practice. The equivalent lateral force (ELF) procedure is considered for the seismic design of low-rise buildings with a regular plan. ELF method is advantageous in the analysis of low-rise buildings is due to the fact that the displacement in the first mode is mainly concentrated at the isolator. The assessment is carried out for two levels of design earthquakes: DBE and MCE. The maximum design lateral displacement (D_D) and the effective period (T_D) of an STRP isolator are determined by

$$D_D = \frac{gS_{D1}T_D}{4\pi^2 B_D} \quad \text{and} \quad T_D = 2\pi\sqrt{\frac{W}{k_{hmin}\,g}} \tag{4.28}$$

where g is the gravitational acceleration (mm/s^2), T_D is the isolation period (s), W is the effective seismic weight (5.0 MPa), k_{hmin} is the minimum effective stiffness (kN/mm), B_D is the damping coefficient, and S_{D1} is 5% damped DBE spectral acceleration at a period of 1s and is given by

$$S_{M1} = F_v\,S_1 \quad \text{and} \quad S_{D1} = 2/3\,S_{M1} \tag{4.29}$$

in which S_1 is risk-targeted MCE spectral acceleration for a period of 1s, and F_v is the site class coefficient obtained from ASCE/SEI 7-10. For the MCE level, displacement, D_M, and period, T_M is obtained by substituting the suffix D by M in Eq. (4.28). Both the displacement and the period are satisfying Eq. (4.28) can be found through an iterative procedure (Toopchi-Nezhad *et al*., 2008a) shown in Fig. 4.15.

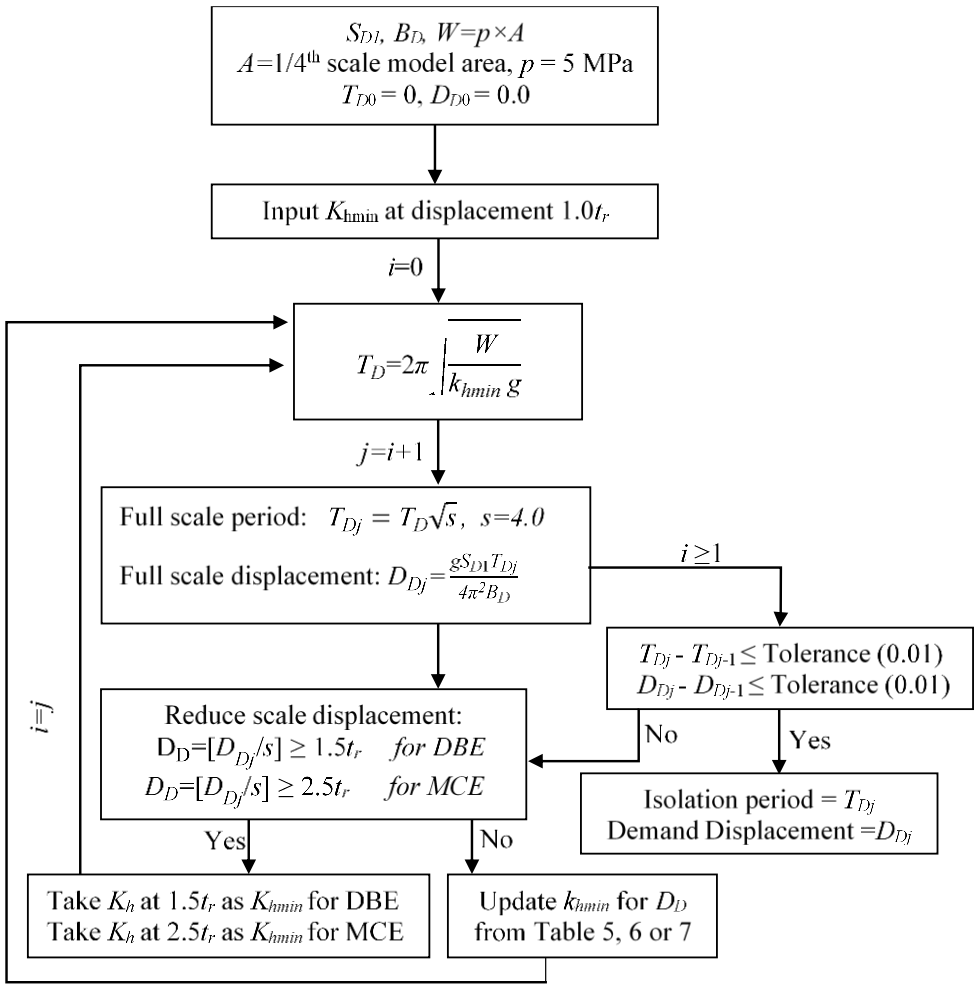

Figure 4.15 Flowchart for seismic capacity calculation

4.6.1 Performance of Strip-STRP isolator

The isolation period and displacement capacity at DBE and MCE spectral accelerations are estimated based on the stiffness and damping listed in Tables 4.4 and 4.5 of the 1/4th scale prototype models (Group-I). The displacement, period, and stiffness of the full-scale model are four, two, and four times, respectively, of the 1/4th scale model, following the similitude law (Kim *et al*., 2009). Therefore, the plan areas of the full-scale models are determined to be 288×288 mm, 576×288 mm, 1152×288 mm, and 2880×288 mm, and the height is 96 mm. Each isolator carries a seismic weight that produces a pressure equal to 5.0 MPa. It is assumed that allowable shear strains at DBE and MCE levels should be within 100%~150% and 200%~250%, respectively. The minimum effective damping ratio and the corresponding damping coefficient, B_D and B_M for the DBE and MCE levels displacement, chosen to be 100% and 250% shear strain, are listed in Tables 4.7, 4.8, and 4.9. Each iteration begins with an initial stiffness, K_{hmin} taken at 100% shear strain. The seismic performance describes here is applicable only for lateral load acting along with one of the principal axes of the isolator. The assessment procedure is carried out for the following three cases with different levels of seismicity:

- Case 1: Ground condition: class C site, S_1=0.40, S_{D1}=0.373g, and S_{M1}=0.56g
- Case 2: Ground condition: class D site, S_1=0.40, S_{D1}=0.43g, and S_{M1}=0.64g
- Case 3: Ground condition: class D site, S_1=0.50, S_{D1}=0.5g, and S_{M1}=0.75g

The assessment results for Cases 1, 2, and 3 are summarized in Tables 4.7, 4.8, and 4.9, respectively. The isolation periods at DBE and MCE levels ($T_D \approx$ 1.23~1.45s and $T_M \approx$ 1.11~1.40s) for each level of seismicity are

Table 4.7 Performance for case-1 (Class C site, S_1=0.40)

1/4th scale model	Full-scale model dimension (mm)	Damping β		Damping Coefficient		Spectral Acceleration		Isolation Periods (s)		Max. Shear strain	
		DBE	MCE	B_D	B_M	S_{D1}	S_{M1}	DBE	MCE	DBE	MCE
Longitudinal direction											
STRP-2/1	STRP-8/1: 288×288×96	12%	9%	1.26	1.16	0.373g	0.56g	1.42	1.40	1.31	2.09
STRP-2/2	STRP-8/2: 576×288×96							1.33	1.25	1.23	1.88
STRP-2/4	STRP-8/4:1152×288×96							1.29	1.21	1.19	1.81
STRP-2/10	STRP-8/10: 2880×288×96							1.27	1.18	1.17	1.78
Transverse direction											
STRP-2/1	STRP-8/1: 288×288×96	13%	10%	1.29	1.20	0.373g	0.56g	1.42	1.22	1.25	1.86
STRP-2/2	STRP-8/2: 576×288×96							1.47	1.26	1.31	1.92
STRP-2/4	STRP-8/4:1152×288×96							1.48	1.28	1.32	1.95
STRP-2/10	STRP-8/10: 2880×288×96							1.50	1.28	1.33	1.95

Table 4.8 Performance for case-2 (Class D site, S_1=0.40)

1/4th scale model	Full-scale model dimension (mm)	Damping, β		Damping Coefficient		Spectral Acceleration		Isolation Periods (s)		Max. Shear strain	
		DBE	MCE	B_D	B_M	S_{D1}	S_{M1}	DBE	MCE	DBE	MCE
Longitudinal direction											
STRP-2/1	STRP-8/1:288×288×96	12%	9%	1.26	1.16	0.43g	0.64g	1.45	1.33	1.50	2.27
STRP-2/2	STRP-8/2:576×288×96							1.33	1.21	1.41	2.08
STRP-2/4	STRP-8/4:1152×288×96							1.28	1.17	1.35	2.01
STRP-2/10	STRP-8/10:2880×288×96							1.26	1.15	1.33	1.97
Transverse direction											
STRP-2/1	STRP-8/1:288×288×96	13%	10%	1.29	1.20	0.43g	0.64g	1.42	1.24	1.47	2.05
STRP-2/2	STRP-8/2:576×288×96							1.46	1.28	1.52	2.11
STRP-2/4	STRP-8/4:1152×288×96							1.47	1.30	1.53	2.15
STRP-2/10	STRP-8/10:2880×288×96							1.48	1.30	1.53	2.15

Table 4.9 Performance for case-3 (Class D site, S_1=0.50)

1/4thscale model	Full-scale model dimension	Damping β		Damping Coefficient		Spectral Acceleration		Isolation Periods (s)		Max. Shear strain	
		DBE	MCE	B_D	B_M	S_{D1}	S_{M1}	DBE	MCE	DBE	MCE
Longitudinal direction											
STRP-2/1	STRP-8/1:288×288×96	12%	9%	1.26	1.16	0.5g	0.75g	1.44	1.25	1.83	2.51
STRP-2/2	STRP-8/2:576×288×96							1.30	1.16	1.60	2.33
STRP-2/4	STRP-8/4:1152×288×96							1.25	1.13	1.54	2.26
STRP-2/10	STRP-8/10:2880×288×96							1.23	1.11	1.52	2.22
Transverse direction											
STRP-2/1	STRP-8/1:288×288×96	13%	10%	1.29	1.20	0.5g	0.75g	1.37	1.26	1.64	2.45
STRP-2/2	STRP-8/2:576×288×96							1.40	1.22	1.69	2.37
STRP-2/4	STRP-8/4:1152×288×96							1.41	1.25	1.70	2.42
STRP-2/10	STRP-8/10:2880×288×96							1.42	1.24	1.71	2.42

substantially longer than 1.0s at which an earthquake contains maximum energy (Skinner *et al.*, 1993). Tables 4.7, 4.8, and 4.9 show that the maximum shear strain of the STRP isolators almost satisfies the allowable limit of 150% (DBE) and 250% (MCE) in all three cases.

Figure 4.16 shows the relationship between the equivalent natural period and the length-to-width ratio. It is observed that the natural period decreased by 12~15% in the longitudinal direction (X) as the length-to-width ratio increase from unity to 10. In contrast, the tendency of the natural period in the transverse direction (Y) is the opposite. Figure 4.17 shows the relationship between the maximum shear strain vs. the length-to-width ratio. The transverse displacement increases both at DBE and MCE levels as the value of the length-to-width ratio increases while the longitudinal displacement reduces. The effect of the length-to-width ratio on the displacement conforms to the change of isolation period as shown in Fig. 4.16.

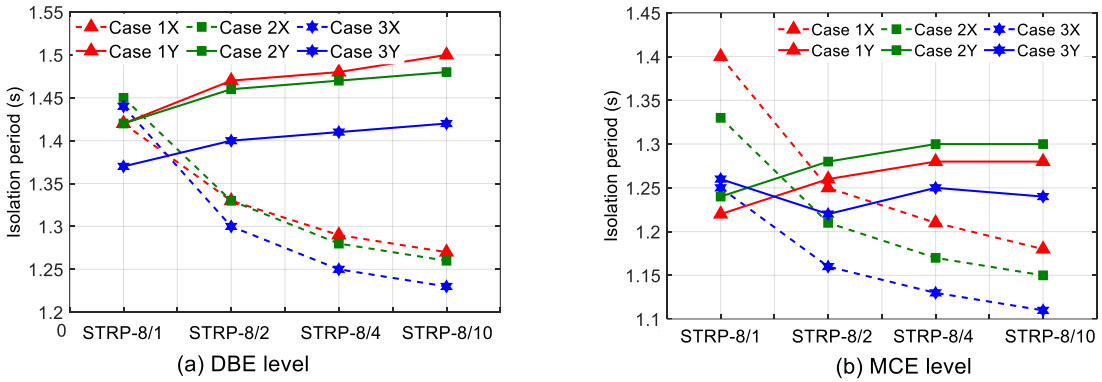

Figure 4.16 Isolation period of 96 mm Strip-STRP isolator (X: Longitudinal, Y: Transverse)

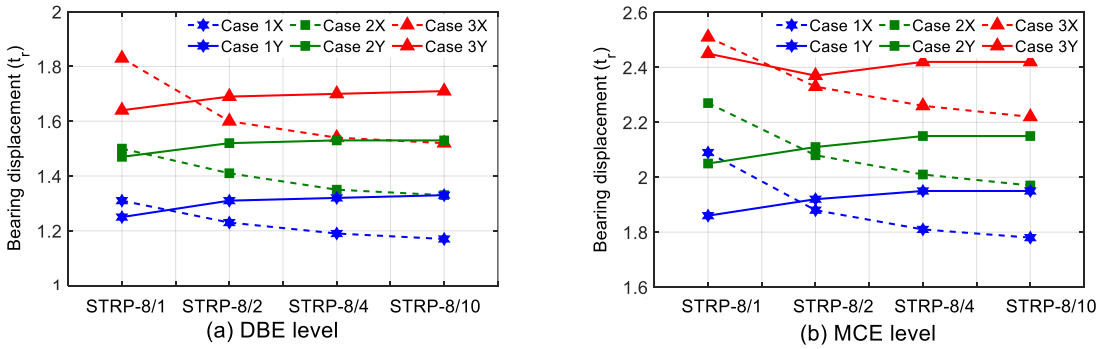

Figure 4.17 Maximum displacement of 96 mm Strip-STRP isolator (X: Longitudinal, Y: Transverse)

Figure 4.18 shows the relationship between the seismic response coefficient (C_s) and the length-to-width ratio. The seismic response coefficient is defined by the ratio of total base shear to the weight of the structure. The base shear is calculated by the bearing displacement at DBE and MCE multiplied by the corresponding stiffness obtained from Tables 4.4 and 4.5. It shows that in each seismic case, the seismic response coefficient is the same for any values of the length-to-width ratio in the transverse direction. On the other hand, the coefficient increases around 16% both in DBE and MCE levels for the length-to-width ratio increase from unity to 10 in the longitudinal direction. The seismic response coefficient increases with the seismicity of the site class.

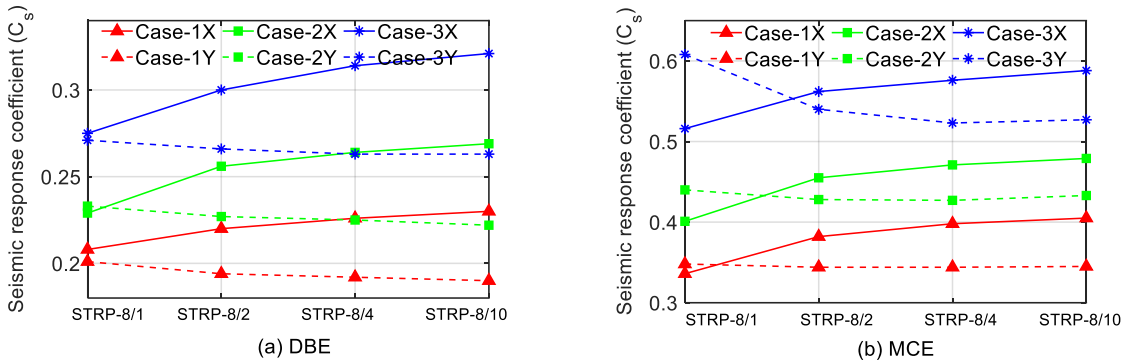

Figure 4.18 Seismic response coefficient (Cs) of 96 mm Strip-STRP isolator (X: Longitudinal, Y: Transverse)

4.6.2 Minimum Height for Effective Isolation

A typical earthquake ground motion record contains a substantial amount of energy within a period range of 0.1s~1.0s and a maximum in the range of 0.2s~0.6s (Skinner *et al.*, 1993). Therefore, the height of an isolator that provides a period longer than 1.0 s is defined as the minimum height for effective isolation and preferable for seismic mitigation of a low-medium-rise building with a fixed base period in the range of 0.1s-0.5s. It is expected that the period elongation results in a reduction of seismic load capacity to the building and of the excitation of higher modes. For a fixed magnitude of static load, the isolation period primarily depends on the lateral stiffness determined by shear modulus, thickness, and plan dimensions of the elastomer. This section discusses the relationship between the STRP isolator height and isolation period based on the design spectral acceleration. For this purpose, the prototype STRP-2/4 with aspect ratios 12 and 3.0 in the length and width direction is considered. The relationship between the horizontal stiffness and the isolator height is obtained from the numerical analysis results of STRP-2/4 as shown in Tables 4.4 and 4.5 and the similitude law with different scale factors. A rigid mass that produces 5.0 MPa axial compression is considered in all bearing heights.

The isolator heights and respective isolation periods are checked for a target level of spectral acceleration by the iterative method such that the nominal shear strain of the isolators remains within the allowable limits. The damping coefficients B_D and BM in the longitudinal direction are taken as 1.29 and 1.20, corresponding to 12% and 9% effective damping. The respective values in the transverse direction are taken as 1.26 and 1.16 for 13% and 10% effective damping. These damping values correspond to 100% and 250% shear strain at which STRP-2/4 has the minimum and maximum lateral stiffness within the DBE and MCE displacement limits.

Figure 4.19 shows the relationship between spectral acceleration, isolator height, isolation period, and maximum bearing displacement. The horizontal axis of these plots is the required isolator height for the DBE level spectral acceleration shown in Fig. 4.19a. It indicates that the needed isolator height increases with an increase of spectral acceleration. An increase in elastomer height causes lengthening the isolation period, as shown in Fig. 4.19b. It shows that 72 mm is the height of the isolator (864×216 mm) at 0.4g DBE level acceleration that offers isolation periods of 1.10s and 1.25s in the longitudinal and transverse directions, respectively. At the MCE level, the respective periods for the same isolator are also longer than 1.0s. Therefore, 72 mm can be regarded as the minimum height of the STRP isolator for effective isolation up to DBE level acceleration 0.4*g*. At 0.65*g* DBE acceleration, the required height is 180 mm that provides an isolation period around 1.5s and 2.0s in the longitudinal and transverse direction, respectively. Figure 4.19c shows the maximum bearing displacement for DBE and MCE level spectral acceleration up to 0.65*g* and 0.975*g*, respectively. The maximum shear strain of the isolator is confirmed to be well within the allowable limits of 150% (DBE) and 250% (MCE). In particular, the maximum shear strain is substantially lower than 250%, implying that the isolator shows no slippage or instability under 5.0 MPa compression, even in the case of MCE. Therefore, the assumed strip-STRP isolators subjected to 5.0 MPa compression can satisfactorily be used at DBE level spectral acceleration up to 0.65*g* by utilizing an appropriate height up to 180 mm.

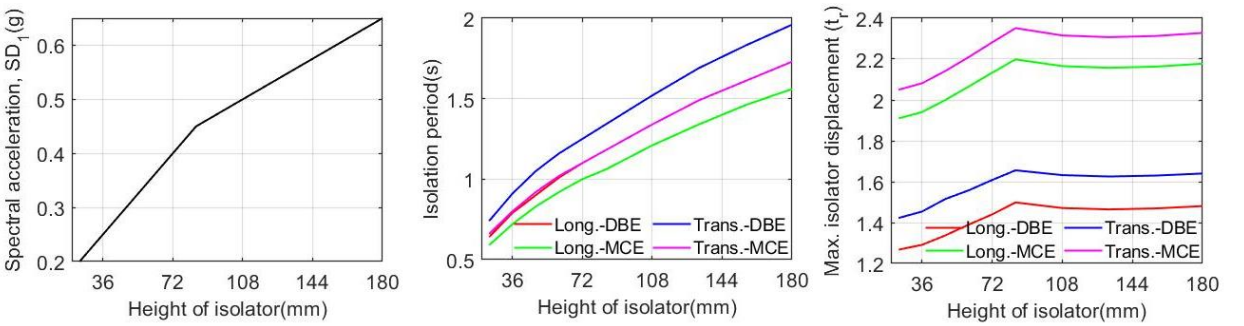

Figure 4.19 Relation between spectral acceleration, height, period, and displacement capacity in strip-shaped isolator

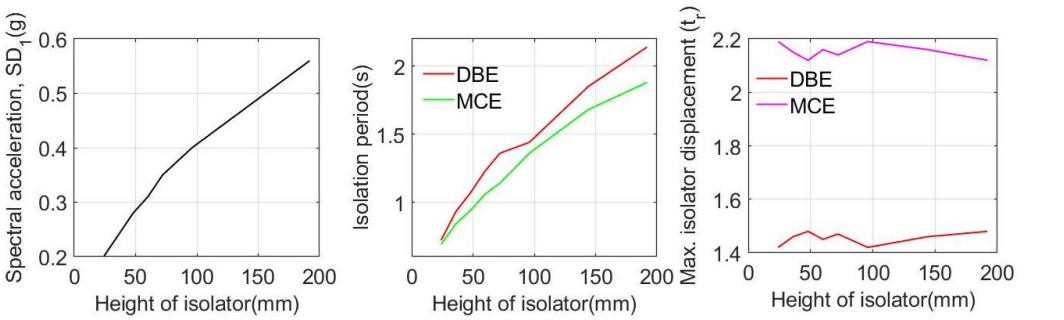

(a) Height vs spectral acceleration (b) Height vs isolation period (c) Height vs. Max. isolator displacement

Figure 4.20 Relation between spectral acceleration, height, period, and displacement capacity in square isolator

A similar set of plots for a square-shaped isolator (Group-II in Table 1) with different heights is shown in Fig. 4.20. An aspect ratio equal to 3.0 and a vertical that produces 5.0 MPa pressure is considered for all heights. From Table 4.6, minimum damping of 13% and 10% corresponding to the minimum and maximum stiffness are assumed for each isolator. Figure 4.20b indicates that for an isolator of 6 STRP stacks (216×216 mm), the height of 72 mm is required for 0.35*g* DBE level spectral acceleration that offers a period of 1.36s and 1.14s at DBE and MCE levels. At 0.56*g* DBE acceleration, the required height is 192 mm that provides an isolation period of around 2.14s. The maximum shear strain for all height and respective acceleration shown in Fig. 4.20c remains within the allowable limits for DBE and MCE levels.

The plots are helpful in the preliminary design of strip-STRP isolator of aspect ratios of 12 and 3.0 in the length and width directions, respectively, or a square bearing with aspect ratio 3.0, for a vertical load equivalent to 5.0 MPa. The total plan area of the isolator can be distributed based on column force such that pressure on individual bearing becomes nearly 5.0 MPa and an aspect ratio exceeding 3.0. This change in aspect ratio does not change the period or maximum nominal shear more than 10-15%, as seen in the previous section. However, if the average pressure within the isolators maintains 5.0 MPa, then the global isolation period remains unchanged. It should be noted that a higher aspect ratio is preferable because it enhances the stability and safety margin. The orientation of bearing and the direction of loading can also affect these results.

4.7 Conclusion

A series of 3-D FE analyses of STRP isolator models with various length-to-width ratios are conducted to investigate the influences of the STRP isolator shape on the cyclic load performance. A friction-based

model of unbonded isolators is developed with a material model as well as a contact model to express the unbonded condition. The FE model is validated by comparing the analytical solution and experimental test results, showing sufficient accuracy of the FE model for the preliminary design of the unbonded STRP isolator. The isolators are analyzed under the condition of 250% lateral shear under 5.0 MPa static compression. The findings from the FE analysis can be summarized as follows:

- The pressure approach is more accurate in the prediction of vertical stiffness of the STRP isolator. The effect of the length-to-width ratio on vertical stiffness is significant for a small value and gradually decreases for a high value. For a fixed aspect ratio of the isolator, increasing the stack number increases the vertical stiffness.
- A modified stiffness solution is used to represent the horizontal stiffness of square STRP within the range of 150% shear. The progressive rollover of the STRP beyond that range results in an increase of lateral stiffness.
- The minimum normalized stiffness of the strip-STRP isolator in the transverse and longitudinal directions is in the range of 0.65~0.75 and 0.90~1.0 times that calculated by the effective shear modulus, and the minimum equivalent damping ratio is 10% within the shear strain range of 1.0~1.5. Therefore, the normalized stiffness of the square bearing of 3 or more stacks at the same displacement is 0.68~0.72.
- The dependence of stiffness on the length-width ratio is significant in the longitudinal direction and minor in the transverse direction. On average, stiffness increases by 37~58% and decreases by 12% in the longitudinal and transverse directions, respectively, as the length-to-width ratio increases from 1 to 10. The stiffness of the strip-shaped isolator in the longitudinal direction is 1.15~1.40 times higher than in the transverse direction. The square bearing exhibits equal stiffness in both directions until 150% shear strain then substantially falls in the carcass direction. For an aspect ratio of 3.0, the dependence of stiffness on the height of the isolator is negligible.
- At 250% shear strain, the equivalent damping ratio of the strip-STRP isolator decreases by 38% and 33% in the longitudinal and transverse directions, respectively, whereas the square bearing shows a 52% reduction. The dependence of damping on the length-to-width ratio and height is insignificant for a value larger than 4.0 and 3 or more layers of STRP, respectively.
- For site conditions of both class C and D of the ASCE/SEI 7-10, the isolated period of the structure with a strip-isolator at DBE and MCE levels is found to be longer than 1.11s. The maximum bearing displacement of a 96 mm strip-isolator in the longitudinal direction at class C site with the spectral value of S_1= 0.4 and at class D site with S_1 = 0.40 and 0.50 are found to be within the allowable limit.

On the other hand, at the class D site with S_1= 0.50, the maximum bearing displacement exceeds the permissible limit at the DBE level. In contrast, the capacity at the MCE level for each seismicity is lower than the upper limit (shear strain of 2.50). In the transverse direction, the average period and maximum displacements are about 12~15 % and 10~15% larger than that of longitudinal value. The maximum bearing displacement for a length-to-width ratio of 10 decreases by 10~15% compared with the case of a length-to-width ratio of unity.

- For a 6-stacks STRP of an aspect ratio of 12 and 3 in the length and width direction, respectively, 72 mm is the minimum height that provides an isolation period longer than 1.0s. At DBE level with acceleration of 0.4*g*, the same isolator experiences a lateral shear of 2.28 and 2.13 at MCE-level in the transverse and longitudinal directions, respectively.

Reference

AASHTO-LRFD (2014), "*LRFD Bridge Design Specifications*", 7th Ed., Washington, D. C.

Al-Anany YM, Van Engelen NC and Tait MJ (2017), "Vertical and Lateral Behavior of Unbonded Fiber-Reinforced Elastomeric Isolators", *Journal of Composite for Construction*, 21(5), 1-11.

ASCE/SEI 7-10 (2010): *Minimum Design Loads for Buildings and Other Structures*, ASCE, 1801 Alexander Bell Drive, Reston, Virginia.

Ashkezari GD, Aghakouchak AA, Kokabi M (2008), "Design, manufacturing and evaluation of the performance of steel like fiber reinforced elastomeric seismic isolators", *Journal of Material Processing Technology*, 197, 140–150.

Calabrese A, Spizzuoco M, Serino G, Corte GD and Maddaloni G (2015), "Shaking table investigation of a novel, low-cost, base isolation technology using recycled rubber", *Structural Control Health Monitoring*, 22(1), 107-122.

Das A, Dutta A and Deb SK (2014), "Performance of fiber-reinforced elastomeric base isolators under cyclic excitation", *Structural Control Health Monitoring*, 22, 197-220.

Eurocode 8 (2004), "*Design of structures for earthquake resistance"*, BS EN 1998-1:2004.

Gerharer U, Strauss A and Bergmeister K (2011), "Verbesserte Bemessungsrichtlinien für Bewehrte Elastomerlager. *Bautechnik*, 88(7), 451–458 (in German).

Igarashi A, Matsushima H and Dang J (2013), "Influence of Loading Direction on the Seismic Performance of Rectangular STRP Isolators", *Journal of Applied Mechanics*, JSCE, 16(2), 425-434.

Kelly JM (1997), "*Earthquake-resistant design with rubber"*, 2nd Ed., London, Springer-Verlag.

Kelly MJ (2002), "Seismic isolation systems for developing countries", *EERI Distinguished Lecture, Earthquake Spectra*, 18(3), 385–406.

Kelly JM (2003), "Tension buckling multilayer elastomeric bearings", *Journal of Engineering Mechanics*, 129 (12), 1363–1368.

Kelly, J.M. Calabrese, A. (2012). Mechanics of fiber reinforced bearings. PEER Report 2012/101, Pacific Earthquake Engineering Research Center, University of California, Berkeley; 2012

Kim NS, Lee J-H and Chang SP (2009), "Equivalent multi-phase similitude law for pseudodynamic test on small scale reinforced concrete models", Engineering Structures, 31 (4), 834-846.

Konstantinidis and Kelly JM (2014), "Advances in low-cost seismic isolation with rubber", *10th US National Conference on Earthquake Engineering Frontiers of Earthquake Engineering*, July 21-25, 2014, Anchorage, Alaska

Mishra HK (2012), "Experimental and Analytical Studies on Scrap Tire Rubber Pads for Application to Seismic Isolation of Structures" *Ph.D. Thesis*, Kyoto University, Japan.

Mishra HK, Igarashi A, Matsushima H (2013a), "Finite element analysis and experimental verification of the scrap tire rubber pad isolator" *Bulletin Earthquake Engineering*, 11(2), 687-707.

Mishra HK and Igarashi A (2013b), "Lateral deformation capacity and stability of layer-bonded scrap tire rubber pad isolators under combined compressive and shear loading", *Structural Engineering and Mechanics*, 48(4), 479-500.

Mishra HK, Igarashi A, Ji D and Matsushima H (2014). "Pseudo-Dynamic Testing for Seismic Performance Assessment of Buildings with Seismic Isolation System Using Scrap Tire Rubber Pad Isolators." *Journal of Civil Engineering and Architecture*, 8(1), 73-88.

Ngo TV, Dutta A, and Deb SK (2017), "Evaluation of horizontal stiffness of fibre-reinforced elastomeric isolators", *Earthquake Engineering and Structural Dynamics*, 46, 1747-1767.

Osgooei PM, Tait MJ, and Konstantinidis D (2014), "Finite element analysis of unbonded square fiber-reinforced elastomeric isolators (FREIs) under lateral loading in different directions", *Composite Structure*, 113, 164-173.

Pauletta M, Cortesia A, and Russo G (2015): Roll-out instability of small size fiber-reinforced elastomeric isolators in unbonded applications. Engineering Structures, 102, 358–368.

Russo G, Pauletta M and Cortesia A (2013), "A study on experimental shear behavior of fiber-reinforced elastomeric isolators with various fiber layouts, elastomers and aging conditions", *Engineering Structure*, 52, 422 433.

Skinner RI, Robinson WH and McVerry GH (1993), "*An introduction to seismic isolation"* Wiley, Chichester, U.K.

Spizzuoco M, Calabrese A and Serino G (2014), "Innovative low-cost recycled rubber-fiber reinforced isolator: Experimental tests and Finite Element Analyses", *Engineering Structure*, 76(1), 99-111.

Strauss A, Apostolidi E, Zimmermann T, Gerhaher U and Dritsos S (2014), "Experimental investigations of fiber and steel reinforced elastomeric bearings: shear modulus and damping coefficient", *Engineering Structures*, 75, 402–413.

Toopchi-Nezhad H, Tait MJ, Drysdale RG (2008a), "Lateral Response Evaluation of Fiber-Reinforced Neoprene Seismic Isolators Utilized in an Unbonded Application" *Journal of Structural Engineering, ASCE,* 134(10), 1627–1637.

Toopchi-Nezhad H, Tait MJ and Drysdale RG (2008b), "Testing and modeling of square fiber-reinforced elastomeric seismic isolators", *Structural Control Health Monitoring,* 15(6), 876-900.

Toopchi-Nezhad H, Drysdale RG and Tait MJ (2009a), "Parametric Study on the Response of Stable Unbonded-Fiber Reinforced Elastomeric Isolators (SU-FREIs)" *Journal of Composite Materials,* 43(15), 1569-1587.

Toopchi-Nezhad H (2014), "Horizontal stiffness solutions for unbonded fiber reinforced elastomeric bearings" *Structural Engineering and Mechanics*, 49(3), 395–410.

Tsai H-C, Hsueh SJ (2001), "Mechanical properties of isolation bearings identified by a viscoelastic model", International *Journal of Solids and Structures*, 38, 53–74.

Tsai H-C and Kelly JM (2002), "Stiffness analysis of fiber-reinforced rectangular seismic isolators" *Journal of Engineering Mechanics,* ASCE, 128(4), 462–470.

Tsai, H.C. (2004). Compression stiffness of infinite-strip bearings of laminated elastic material interleaving with flexible reinforcements. *Int J Solids Struct.,*41, pp. 6647–6660.

Turer A and Özden B (2007), "Seismic base isolation using low-cost scrap tire pads (STP)", *Materials and Structures*, 41(5), 891-908.

Van Engelen, N. C., Tait, M. J., and Konstantinidis, D., (2015), "Model of the shear behavior of unbonded fiber-reinforced elastomeric isolators", *Journal of Structural Engineering,* ASCE, 141 (7), 1-11.

Chapter 5

Evaluation of Unbonded STRP Isolators Based on the Existing Design Guidelines

This chapter reports the stress-strain in unbonded STRP isolators to investigate the stability and limit forces required for a practical design following the existing code specifications. It includes a brief description of stress and strain of elastomer specified in different codes. The unbonded STRP isolators with different length-to-width ratios are analyzed for compression of 2.5, 5.0, 7.5, and 10.0 MPa, including the upper and lower limits of the compression force defined by the AASHTO-LRFD specification, and bearing-to-structure interface rotation and shear displacement of 0.05-radian and 250%, respectively.

5.1 Introduction

Reinforcement of STRP isolators consists of unidirectional steel cords that are vulcanized with rubber and have elastomer bulging resistance in the cord direction only, unlike the conventional isolator. Besides, the flexible steel cords allow rollover deformation of an unbonded isolator. Hence, the stress-strain behavior of the STRP isolator could be different than that of the conventional bonded elastomeric isolator. However, there is an inadequate justification of stress-strain of an unbonded STRP isolator based on the design guidelines. The previous study (Mishra et al., 2012; 2013a, 2013b) focused on the hyperelastic properties and the stiffnesses and damping ratios of STRP isolators through experimental research. It is recommended that STRP isolator is potential for low-to-medium rise buildings, but no definition for allowable loads and working stress-strain is mentioned. Since the STRP isolator is made from inferior material, the stress-strain needs proper diagnosis to define the limiting operational forces requires for practical design. Though AASHTO-LRFD, BS EN 15129, and JRA define the allowable compression and tension in a conventional isolator, no specification for unbonded isolators is given.

The stress-strain of an unbonded isolator is affected by the overturning of overlaying structure and the rotation at the bearing-to-structure interface. It is also affected by the absence of a rigid diaphragm or due to planar irregularity of a building (Ohsaki et al.,2015; Moghadam and Konstantinidis, 2015; Crowder and Becker, 2015). Moghadam and Konstantinidis (2015) mentioned that rotations affect the stress-strain and the critical shear capacity of an isolator. Some researchers focused on the stress-strain in unbonded FREIs. Toopchi-Nezhad et al. (2011) demonstrated that an unbonded connection lowers the stress demand of the elastomer, reinforcement, and the bonding between them. Al-Anany and Tait (2015) mentioned that the isolator's low aspect ratio delays lift-off occurrence and reduces the stress-strains rate under rotational deformation. Osgooei et al. (2014a, 2014b, 2015) studied the stresses-strains for the orientation of lateral load, reinforcement flexibility, and modified shape of the rectangular FREIs. These studies considered the general circumstances of stress-strain, which is needed to be investigated based on the design guidelines. Besides, the stress-strain for a combination of compression, bearing-to-structure interface rotation, and lateral displacement is still unknown. Therefore, this study focused on the in-service stress-strain in unbonded STRP isolators to predict the permissible lateral displacement, compression, and the bearing-to-structure interface rotation required for a practical design. Strip-shaped isolators with different length-to-width ratios are analyzed for the following combination loads.

Case-1: compression and bearing-to-structure interface rotation.

Case-2: compression, bearing-to-structure interface rotation, and lateral displacement.

Case-3: compression and lateral displacement

In the following sections, the bearing-to-structure interface rotation and the length-to-width ratio are termed as rotation and *l/w* ratio, respectively. The vertical pressures on bearing are assumed to be 2.5, 5.0, 7.5, and 10.0 MPa, including the upper and lower limits of the compressive force defined by the AASHTO-LRFD specification. A maximum rotation of 0.05-radian and a displacement of 250% shear are considered.

5.2 Specification for Elastomeric Bearings

To prevent the instabilities of a bonded type bearing, AASHTO LRFD Method A (AASHTO-LRFD, 2012) suggests a minimum aspect ratio of 3.0. Similarly, an unbonded isolator is called a stable one for an aspect ratio exceeding 2.60 (Toopchi 2008b; Van Engelen et al., 2015). In this study, an aspect ratio exceeding 3.0 is assumed for unbonded isolators. According to Method B, a bonded bearing is stable if

$$2A<B \tag{5.1}$$

$$A=\frac{1.95\frac{t_r}{L}}{\sqrt{1+\frac{2L}{W}}} \text{ and } B=\frac{2.67}{(S+2)\,(1+\frac{L}{4W})} \tag{5.2}$$

where S, W, L, and t_r are the shape factor, width, length, and total elastomer thickness of the isolator, respectively, or if the compressive stress σ_s within the elastomer satisfies

$$\sigma_s \leq \frac{GS}{(2A\text{-}B)} \tag{5.3}$$

The shear modulus G should be between 0.55 MPa and 1.72 MPa, and the elastomer in STRP isolator satisfies this criterion. In Method A, the compressive stress, σ_s within the elastomer should satisfy,

$$\sigma_s \leq 1.25GS \text{ and } \sigma_s \leq 1.25 \text{ ksi} \tag{5.4}$$

The stress limit in Eq. 5.4 is allowed to increase by 25% for laminated steel bearing. Some design codes allow tensile stresses up to 2G by BS EN 15129 and EN 1337-3, up to 2G–3G by AASHTO, up to 2.0 MPa by JRA. In China's seismic design code, the tensile stress is limited to 1.0 MPa. The Eurocode 8 Part 2 restricts the development of tensile stresses.

AASHTO defined the allowable shear strain equal to 0.5t_r due to the lateral displacement only to avoid the lift-off and delamination. An unbonded isolator is free from such restrictions since rollover deformation is allowed. AASHTO-LRFD eliminated the limit against lift-off due to rotation by imposing the maximum shear strain, more appropriate than preventing lift-off. At the service limit state, the shear strain due to the combined action of axial load, rotation, and shear displacement should satisfy

$$(\gamma_{a,st}+\gamma_{r,st}+\gamma_{s,st})+1.75(\gamma_{a,cy}+\gamma_{r,cy}+\gamma_{s,cy}) \leq 5.0 \tag{5.5}$$

where γ_a, γ_r and, γ_s are the shear strain due to the axial load, rotation, and shear displacement, respectively, and subscripts "*st*" and "*cy*" indicate the static and cyclic loadings, respectively. Shear strain in rectangular bearing due to rotation is given by

$$\gamma_r=D_r\left(\frac{L}{t_{ri}}\right)^2\frac{\theta}{n} \tag{5.6}$$

where D_r is 0.5, L is the bearing's length perpendicular to the axis of rotation, θ is the rotation in radian, t_{ri} is the thickness of individual elastomer layer, n is the number of interior layers of the elastomer. The shear strain due to the statical axial load should satisfy

$$\gamma_{a,st} = D_a \frac{\sigma_s}{GS} \leq 3.0 \tag{5.7}$$

in which D_a is 1.40 for a rectangular type bearing. The minimum thickness of the steel layer, h_s should be 1.60 mm, and at the service limit state should satisfy

$$h_s \geq \frac{3 t_{ri} \sigma_s}{F_y} \tag{5.8}$$

where σ_s is the in-service elastomer stress and F_y is the yield strength of reinforcing material. In all cases, the shear strain is defined by Eq. 5.9, where u and t_r are the horizontal displacement and total rubber thickness of the bearing.

$$\gamma = \frac{u}{t_r} \tag{5.9}$$

5.3 STRP Isolators and Model Verifications

Table 5.1 shows the geometric properties of the square and strip-shaped STRP isolators considered in this study. The geometric and material properties were reported in Chapter 3. The FE element modeling is the same as described in Chapter 3. In the case of bearing-to-structure interface rotation, the top rigid-plane is allowed to rotate to the centroid of the bearing, as shown in Fig. 5.1. Axial force and lateral displacement are applied at the top surface.

Table 5.1 Geometric properties of STRP isolator models

Bearing	Designation	Dimension $l \times w \times h$ (mm)	l/w	Rubber thickness t_r (mm)	Equivalent thickness t_{ri} (mm)	Shape factor, S	Aspect ratio	
							R_x	R_y
Experiment	STRP-4/1	100 × 100 × 48	1	40	2.4	10.4	2.1	2.1
FE analysis	STRP-2/1	72 × 72 × 24	1	20	2.4	7.5	3.0	3.0
	STRP-2/2	144 × 72 × 24	2			10	6.0	
	STRP-2/3	216 × 72 × 24	3			11.3	9.0	
	STRP-2/4	288 × 72 × 24	4			12	12.0	
	STRP-2/10	720 × 72 × 24	10			13.6	*30.0*	

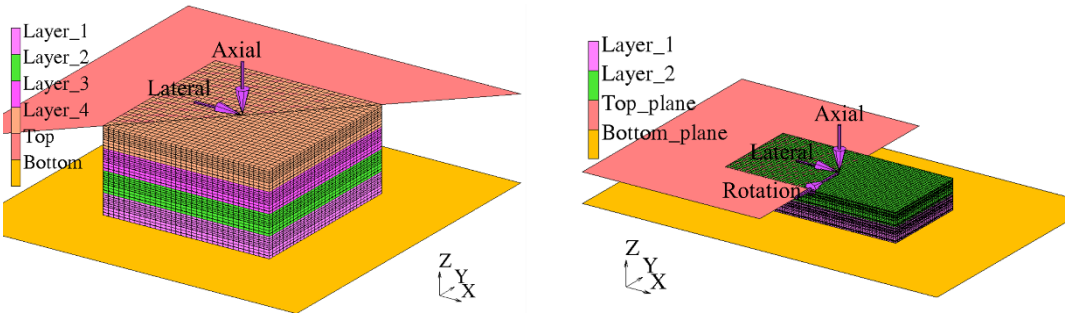

a) STRP-4/1 isolator model b) STRP-2/2 isolator model

Figure 5.1 FE model indicating contact element and boundary conditions.

5.4 Deformed Shape of Isolators

Figures 5.2 and 5.3 show the lateral bulging in the longitudinal and transverse directions, respectively, in STRP-2/1, 2/2, 2/4, and 2/10 isolators subjected to 5.0 MPa compression. The elastomer within the belt and carcass zones in the longitudinal and transverse directions shows high bulging with a maximum in the belt zone. This unsymmetrical bulging is due to the steel cords' orientation, which is ±70° and 0° in the belt and carcass layers, respectively, with the longitudinal direction. Figure 5.4 quantifies the lateral expansion for different *l/w* ratios. For an *l/w* ratio equal to 1.0, lateral bulging in the length direction is 71% higher than

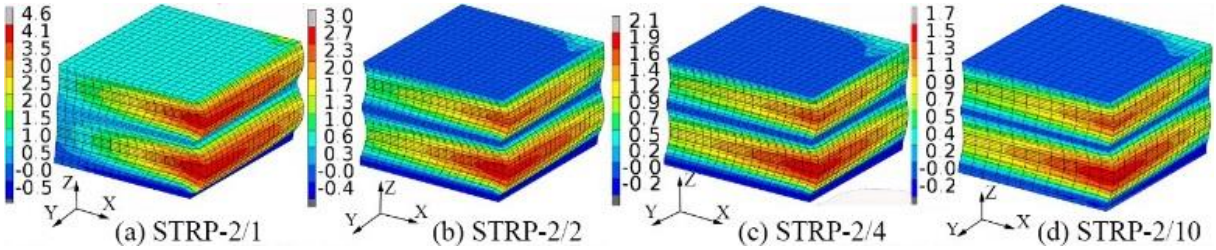

Figure 5.2 Bulging in the longitudinal direction (carcass direction)

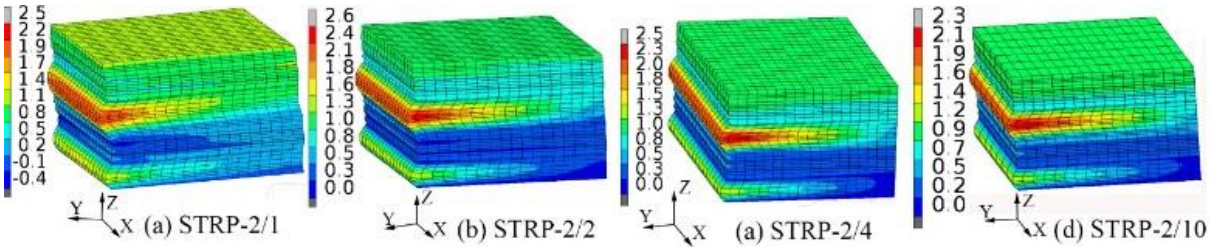

Figure 5.3 Bulging in the transverse direction (orthogonal to carcass direction)

that in the width direction. Lateral bulging decreases with the *l/w* ratio increases and is approximately equal in both directions for *l/w* equal between 2 and 4. Therefore, a low aspect ratio that induces unsymmetrical bulging in the STRP isolator can be minimized by selecting an *l/w* ratio between 2 and 4 or an aspect ratio between 6 and 12.

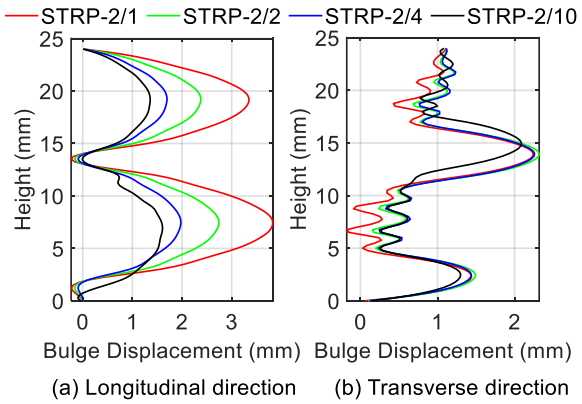

Figure 5.4 Bulging displacement of STRP isolator

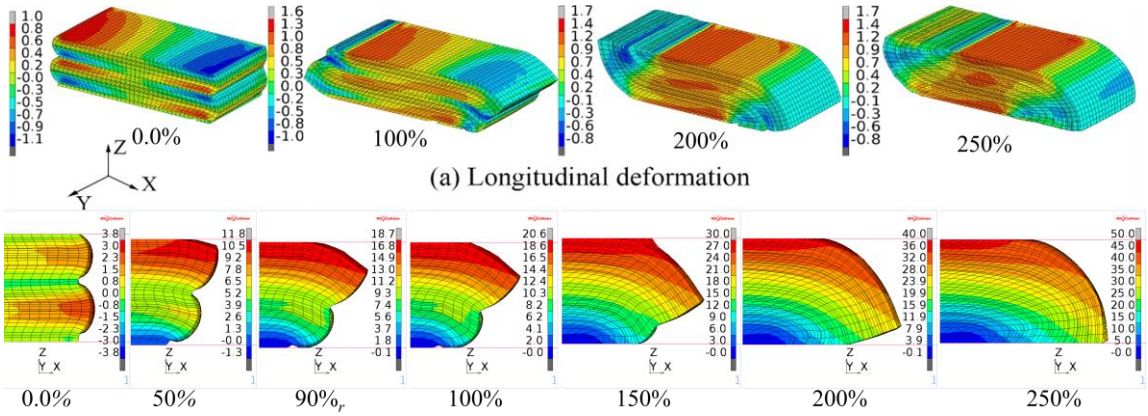

(b) Progressive contact of STRP isolator with support face at different level of shear strain

Figure 5.5 Lateral deformation of un-bonded STRP-2/1 isolator

Figure 5.5 shows the lateral deformation at different levels of shear displacement of the STRP-2/1 isolator in the longitudinal direction. Both top and bottom surfaces of the isolator roll-off from the contact surfaces reduce the net friction area. As a result, the isolator displays a progressive rollover deformation, and the vertical side face starts touching the support face at 90% shear level. The touching area keeps growing until 250% shear strain, as shown in Fig. 5.5b, instead of 167% generally observed in FREI (Konstantinidis and Kelly, 2014). The bearing's deformed shape displays a peculiar one observed in the loading experiment

(Mishra et al., 2013a; 2013b). The progressive contact makes the STRP isolator more restrained and stable, which is more noticeable for a high *l/w* ratio.

5.5 In-Service Stress Within Elastomer

An unbonded STRP isolator displays large displacements and rotations, which need to define the local coordinates to quantify the stresses and strains. Figure 5.6 shows the notations for triaxial stress-strain components S_{11}, S_{22}, and S_{33}, in an undeformed and deformed isolator. In a pure compression, the stress-strain components are parallel to the global *X*, *Y,* and *Z*-axis of the element, as shown in Fig. 5.6a. The stress-strain components are updated when the bearing undergoes any displacement or rotation, as shown in Fig. 5.6b. In the load Case-1 and Case-2, bearing displacement in the longitudinal direction is only considered, whereas displacement in both orthogonal directions is considered for Case-3. Hence, in Case-1 and Case-2, stresses-strains are measured at the mid-height, and the centroidal axis parallels the longitudinal direction. In Case-3, it is at mid-height and along both centroidal axes.

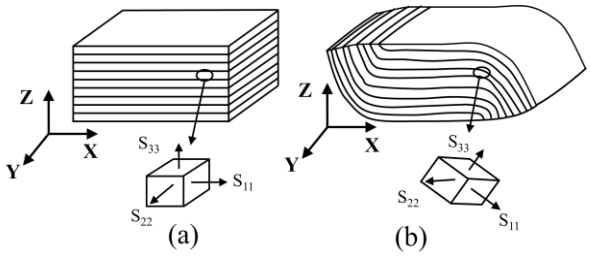

Figure 5.6 Local stress-strain in the undeformed and deformed stage

Along with the FE analysis, the stress magnitude and its distribution are estimated using the "pressure solution" approach proposed by Tsai and Kelly (2001), as given in Eq. 5.10.

$$\frac{S(x)}{p} = \frac{\alpha b(\cosh \alpha b - \cosh \alpha x)}{\alpha b \cosh \alpha b - \sinh \alpha b} \tag{5.10}$$

where, $S(x)$ is the elastomer stress, x is the location, p is the applied vertical compression, a and b is the dimension of the isolator in the longitudinal and transverse direction, respectively.

5.5.1 Elastomer Stress in Case-1

Figure 5.7 shows the contours of stress S_{11} and S_{33} in STRP-2/2 isolator under a 5.0 MPa compression plus rotations at 0.0, 0.01, 0.03, and 0.05-radians. The lift-off is visible for 0.03 and 0.05-radian rotations near the left-end. An increase in the rotation increases the compression zone and shifts the peak stress toward the bearing's end. Figure 5.8 shows the distribution of normalized stresses (S_{11}/p, S_{22}/p, and S_{33}/p) along the length of the STRP-2/1, 2/2, 2/3, 2/4 isolators under a 5.0 MPa compression plus a rotation of 0.0, 0.01, 0.03, and 0.05-radians.

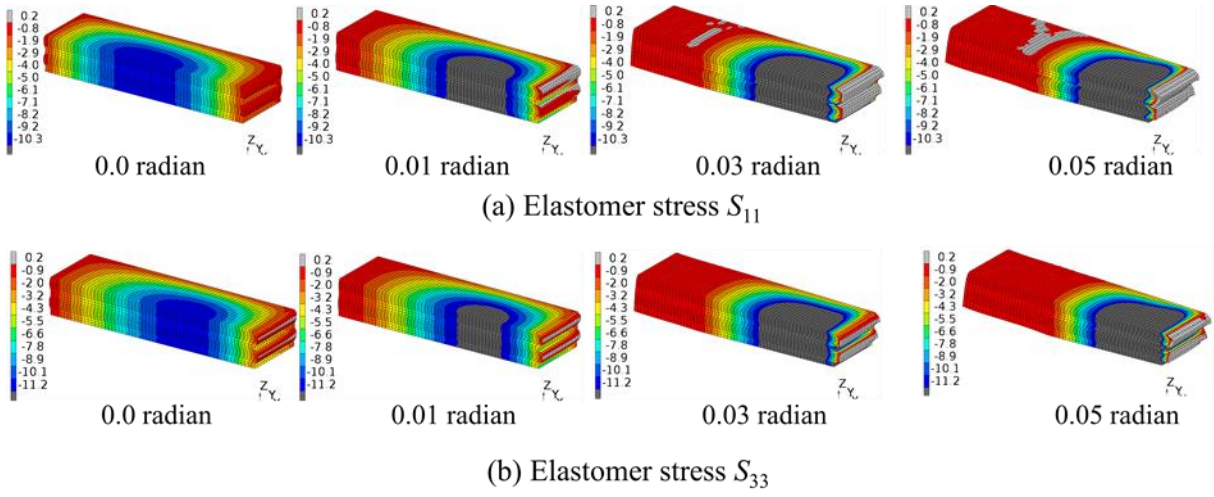

Figure 5.7 Elastomer stress in STRP-2/2 at 5.0 MPa compression and different rotation

A comparison with the FE analysis results shows that the analytical solution (S_{33}) underestimates the elastomer stress by about 16% for the *l/w* ratio 1.0 and 26% for the *l/w* ratio exceeding 1.0. The analytical solution overlooks the steel cords' orientation that affects the local stress in the FE model. Figure 5.8 shows the triaxial stress components (S_{11}/p, S_{22}/p, and S_{33}/p) at different rotations levels. In the notation, for example, S_{11}/p-0.05, the numeric value 0.05 indicates the rotation in radian. It shows that the triaxial stresses are approximately the same for a fixed rotation. It confirms the hydrostatic pressure rule within the STRP isolator, which is the basis of the "pressure solution" approach.

Figure 5.9 shows a relationship between peak stresses' normalized values for different rotations and a vertical compression of 2.5, 5.0, 7.5, and 10.0 MPa. In a simple compression, normalized stress, 1.75 for STRP-2/1 and 1.90 for other bearings, is independent of the *l/w* ratio and bearing pressure. Stresses increase with an increase of rotation while decrease with an addition of compressive force. The effect of rotation is

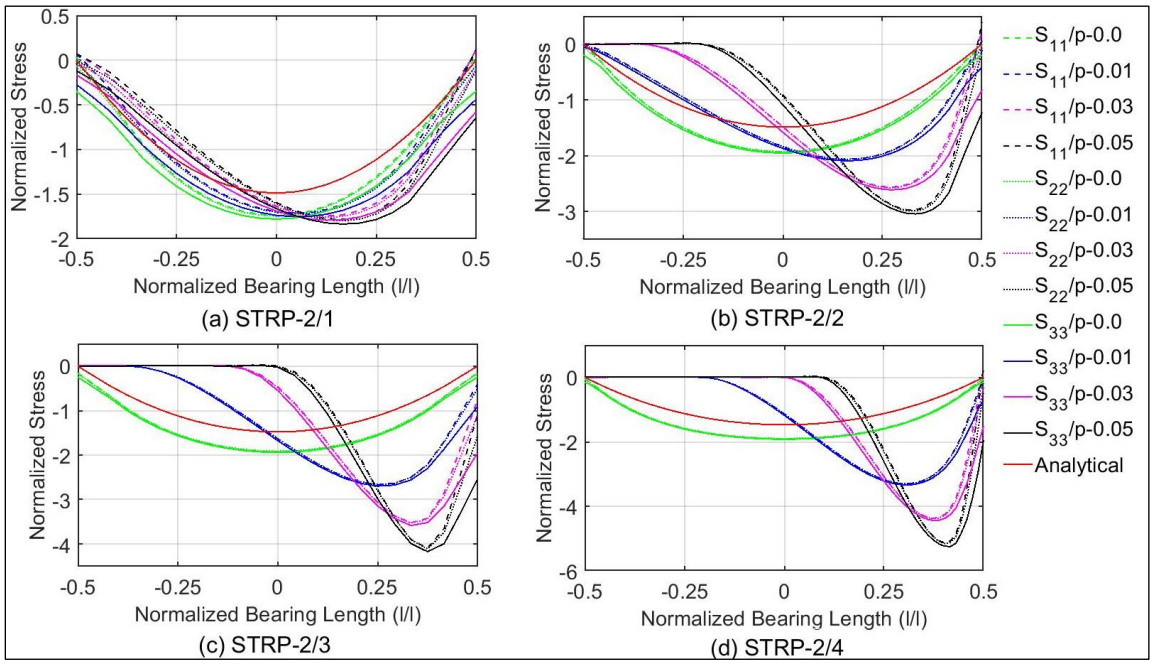

Figure 5.8 Profile of normalized stresses (S_{11}/p, S_{22}/p, and S_{33}/p) due to axial (5.0 MPa) and rotation

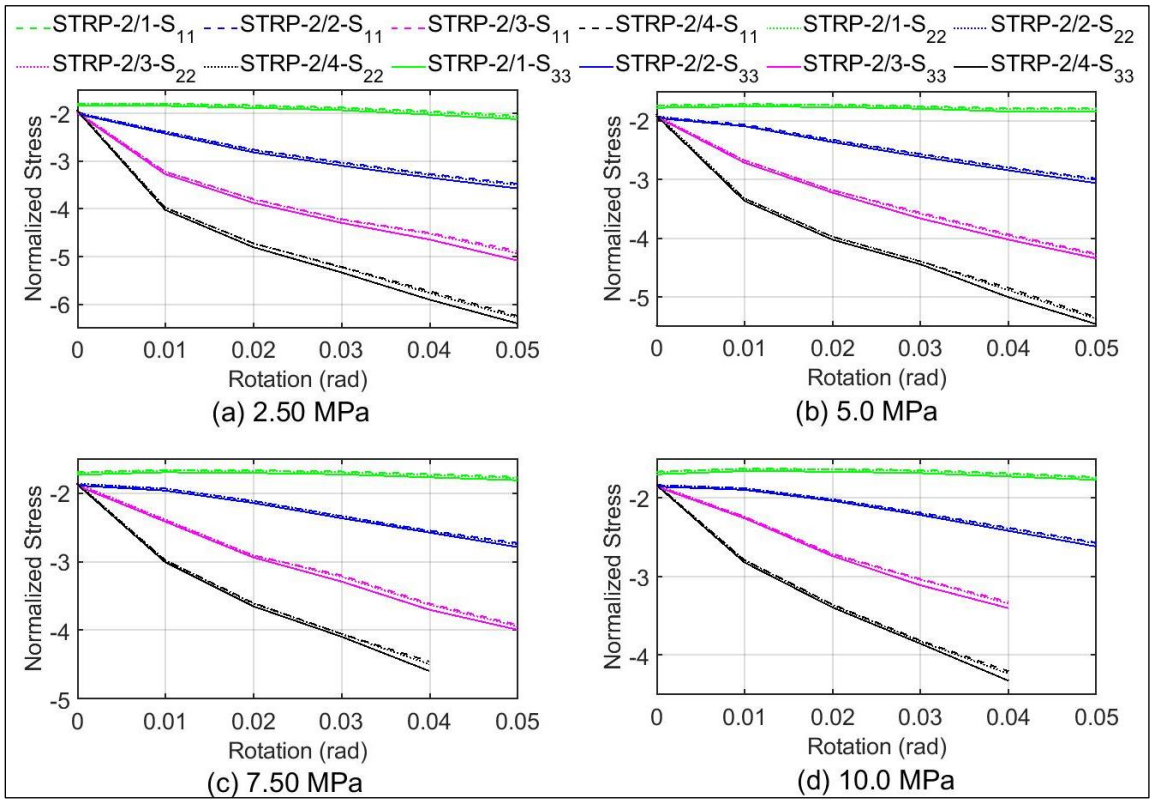

Figure 5.9 Peak value of normalized elastomer stress (S_{11}/p, S_{22}/p, and S_{33}/p)

significant for a high *l/w* ratio. For example, the average of the triaxial stress components in STRP-2/1 for 2.5 and 10.0 MPa pressures ranges between 1.82~2.09 and 1.68~1.75, respectively. In this range, the first and second values stand for 0.0 and 0.05-radian rotations, respectively. Similarly, the average for the triaxial stress components in STRP-2/4 is 1.94~6.31 and 1.83~4.25, respectively, due to 2.5 and 10.0 MPa compression. It implies that the rotation is less meaningful for an *l/w* equal to 1.0 (STRP-2/1) but significant for 4.0 (STRP-2/4) in which stresses increase by 225% and 132%, respectively, at 2.5 MPa and 10.0 MPa pressure due to the rotation changes from 0.0 to 0.05-radian. At 0.05 radian, the *l/w* ratio increase from 1.0 to 4.0 increases the stresses by 202% under 2.50 MPa and 143% under 10.0 MPa. Therefore, the rotation effect is more significant at a low compression and a high *l/w* ratio.

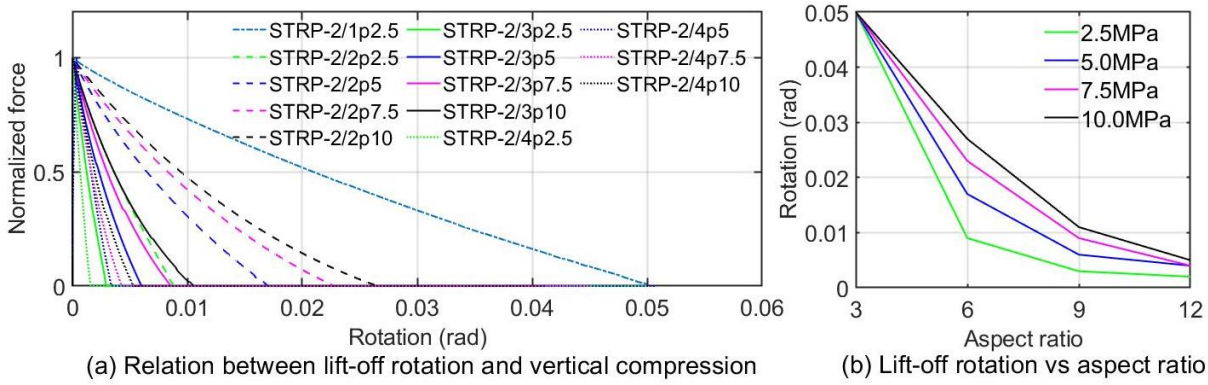

(a) Relation between lift-off rotation and vertical compression (b) Lift-off rotation vs aspect ratio

Figure 5.10 Lift-off rotation for different aspect ratio (3-times of l/w ratio)

Figure 5.10a shows the normalized contact force vs. lift-off rotation for *l/w* ratios and compression force. In a notation like "STRP-2/1p2.5," p2.5 indicates 2.5MPa pressure on the STRP-2/1 isolator. When compression is unchanged, the lift-off zone's reaction force decreases as rotation progresses, and the rotation corresponding to the zero reaction force is called lift-off rotation. Figure 5.10b shows that a high *l/w* ratio causes the lift-off at a small rotation, and an increase in compression force delays the lift-off occurrence. The STRP-2/1 exhibits no lift-off until 0.05-radian rotation, even under the lowest compressive force. That is why stresses in the STRP-2/1 isolator are less sensitive to rotation. Therefore, the aspect ratio of 3.0 suggested by AASHTO-LRFD is useful in preventing the lift-off of unbonded isolators. Moreover, the rotation that initiates the nonlinear behavior caused by the lift-off initiation (MTO. OPSS 1202, 2008) can be 0.05-radian for an aspect ratio of 3.0. This criterion will check the instabilities and failures due to the rotation. According to Fig. 5.10b, the lift-off rotation in STRP-2/2 is 0.01 and 0.027-radians for 2.5 MPa and 10.0 MPa compressions, respectively. Figure 5.9 indicates that the rotation effect on the stresses

of the same isolator is less until the lift-off initiation. The lift-off rotation in STRP-2/3 and STRP-2/4 is 0.003 and 0.002-radians, respectively, under 2.50 MPa. The corresponding rotation for the same isolators is 0.011 and 0.005-at 10.0 MPa.

5.5.2 Elastomer Stress in Case-2

In load Case-2, isolators are analyzed for a 5.0 MPa compression plus different rotation and lateral displacement combinations. Figure 5.11 shows the stress contour (S_{11} and S_{33}) in the STRP-2/2 isolator at various rotation and lateral displacement combinations. The stress-contour S_{33} with or without lateral displacement is nearly the same as shown in Figs. 5.7b and 5.11b. However, the in-plane stress, S_{11}, as shown in Figs. 5.7a and 5.11a differ substantially due to the lateral displacement. Besides, Fig. 5.11a shows that the isolator experiences enough tension between the compressed and lift-off zone for a combination of 0.05-radian rotation and 250% shear displacement (0.05rad- 250%).

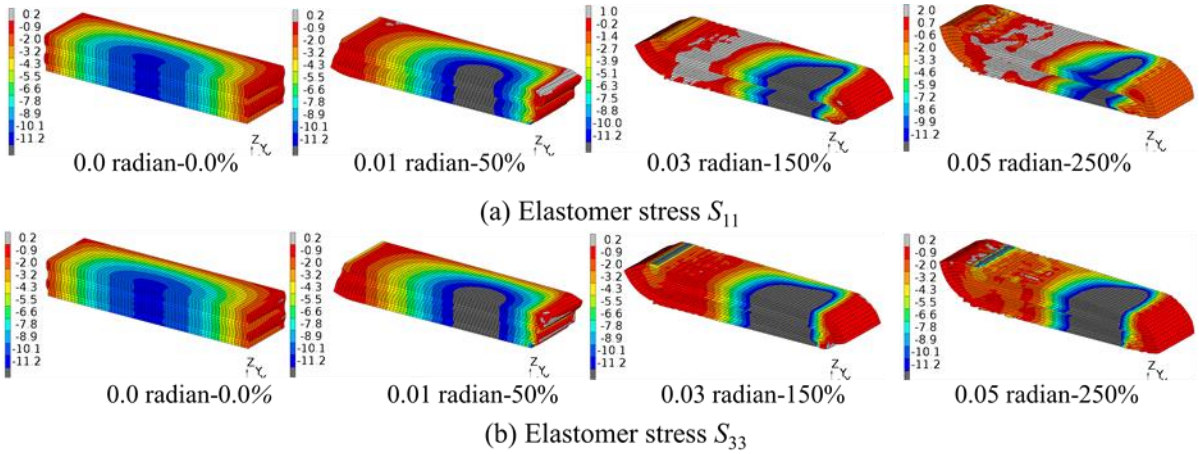

Figure 5.11 Contour of elastomer stress due to axial (5.0 MPa), rotation, and shear deformation (%)

Figure 5.12 presents the profile of normalized stresses along the bearing's length for 5.0 MPa compression in load Case-2. The notation like "S_{33}/p-0.01-150%" indicates the normalized stress component S_{33} for a combination of 0.01-radian rotation and 150% shear displacement. It shows that the hydrostatic pressure rule exists until a combination of 0.01-radian rotation and 50% shear strain (0.01rad-50%). Beyond this limit, the triaxial stress components show significant inequality between the lift-off and compressed zones.

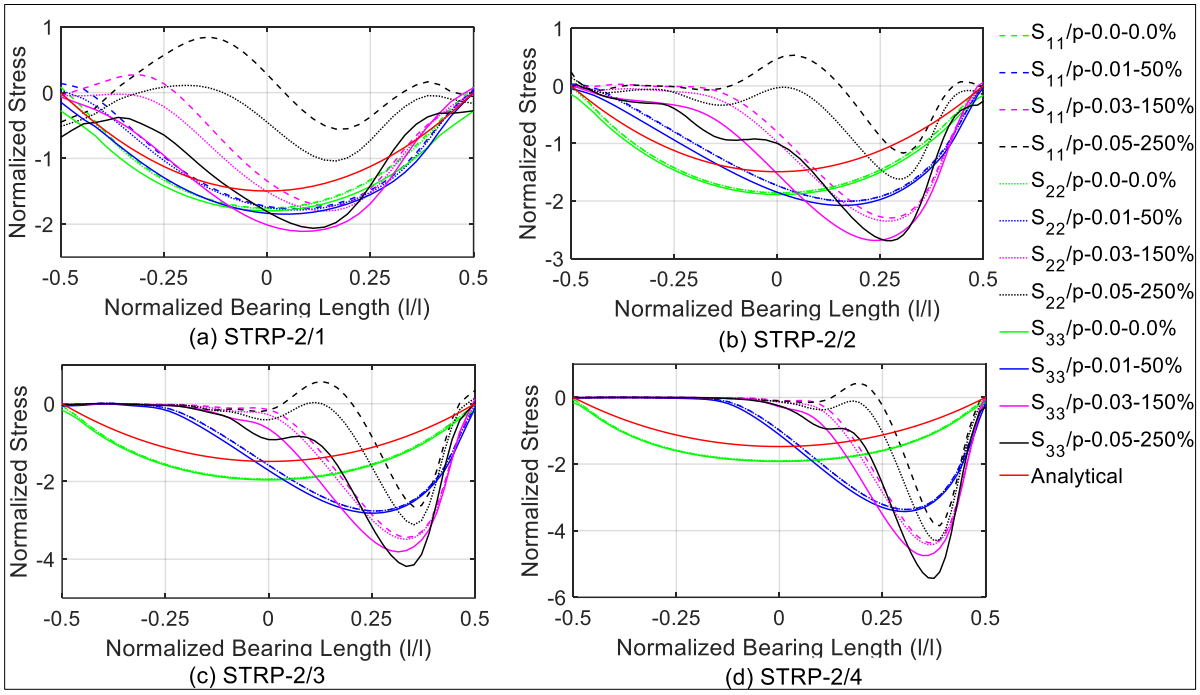

Figure 5.12 Profile of normalized stresses (S_{11}/p, S_{22}/p, and S_{33}/p) due to axial (5.0 MPa), rotation, and displacement (%)

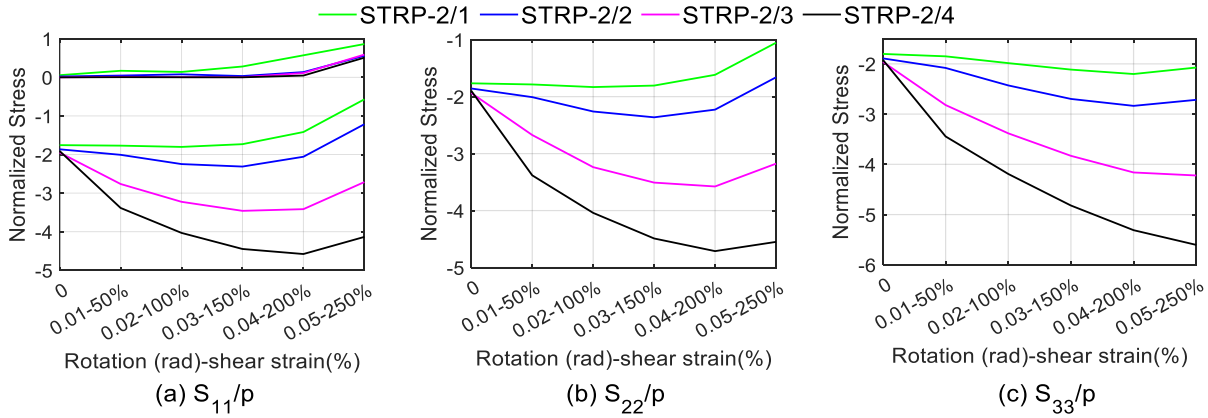

Figure 5.13 Normalized peak stress (S_{11}/p, S_{22}/p, and S_{33}/p) due to axial (5.0 MPa), rotation, and lateral displacement.

Figure 5.13 shows the peak of normalized stresses in load Case-2. The in-plane tension (S_{11}/p) is insignificant until 0.03-radian rotation plus 150% shear displacement (0.03rad-150%), which then reaches to 0.86 at 0.05-radian plus 250% shear (0.05rad-250%). This tension is larger than $2G$-$3G$, the limiting negative pressure for the onset of cavitation or debonding (AASHTO-LRFD, Naeim, and Kelly, 1999). The

vertical stress, S_{33}/p with or without a lateral displacement is nearly equal, as seen from Figs. 5.9b and 5.13c. On the other hand, the in-plane stresses (S_{11}/p and S_{22}/p) are substantially reduced when the force on isolators exceeding 0.03-radian plus 150% shear. For example, stress S_{11}/p at 0.05-radian plus 250% shear (0.05rad-250%) reduces by 68%, 59%, 36%, and 23% in STRP-2/1, 2/2, 2/3, and 2/4, respectively, in comparison with pure compression. The same reduction for S_{22}/p is 42%, 45%, 26%, and 15%, respectively. Therefore, the inclusion of lateral displacement substantially reduces the in-plane stresses, which is prominent for a low *l/w* ratio.

5.5.3 Elastomer Stress in Case-3

The stresses and strains in the load Case-3 are analyzed for a displacement up to 250% shear strain under 5.0 MPa compression. Figures 5.14 and 5.15 show the in-plane stresses contour in STRP-2/1 and 2/2,

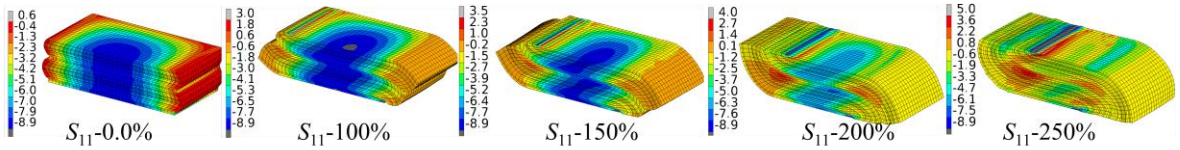

(a) Stress at different level of shear displacement(%) in the longitudinal direction

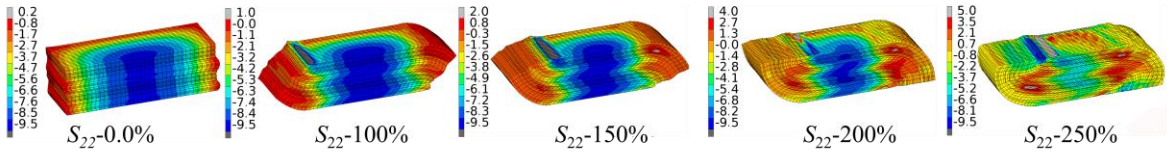

(b) Stress at different level of shear displacement(%) in the transverse direction

Figure 5.14 Stress contour in STRP-2/1 at different level displacement (%) under 5.0 MPa compression

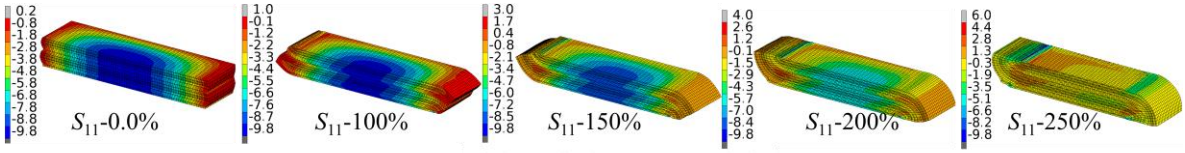

(a) Stress at different level of shear displacement (%) in longitudinal direction

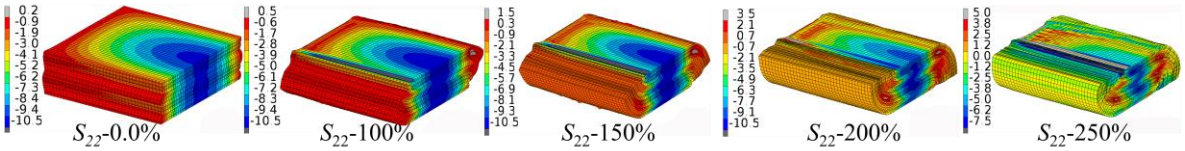

(b) Stress at different level of shear displacement (%) in transverse direction

Figure 5.15 Stress contour in STRP-2/2 at a different level of shear displacement (%) under 5.0 MPa compression

respectively, at different displacement levels in the longitudinal and transverse directions. It shows that the length of the compression zone and the magnitude of the in-plane stress decrease with the lateral displacement. Bearings experience a considerable in-plane tension for a displacement exceeding 200% shear. The rollover deformation causes stress concentration at the top-left or bottom-right edge of the isolator, and the rollover surfaces are stress-free.

Figures 5.16 and 5.17 quantify the profile of normalized stresses S_{11}/p, S_{22}/p, and S_{33}/p in the longitudinal and transverse directions, respectively, at a shear displacement of 0.0%, 100%, 200%, and 250%. It shows that the in-plane tension near the bearing's surface initiates for displacement exceeding 200% shear. At 250% shear displacement, almost the entire isolator undergoes in-plane tensile stress (S_{11}/p) due to longitudinal loading, as shown in Fig. 5.16a(iv). Contrarily in the transverse loading, Figs. 5.17a and 5.17b show that tension arises only near the bearing's end. The maximum normalized tension S_{11}/p is 0.89 in the longitudinal direction (Fig. 5.16), and S_{22}/p is 1.0 in the transverse direction (Fig. 5.17b) in STRP-2/1. These peak tensions are larger than the $2G$-$3G$ and locating between $0.022l$ and $0.25l$ or $0.039l$ and $0.33l$ from the bearing's two free ends.

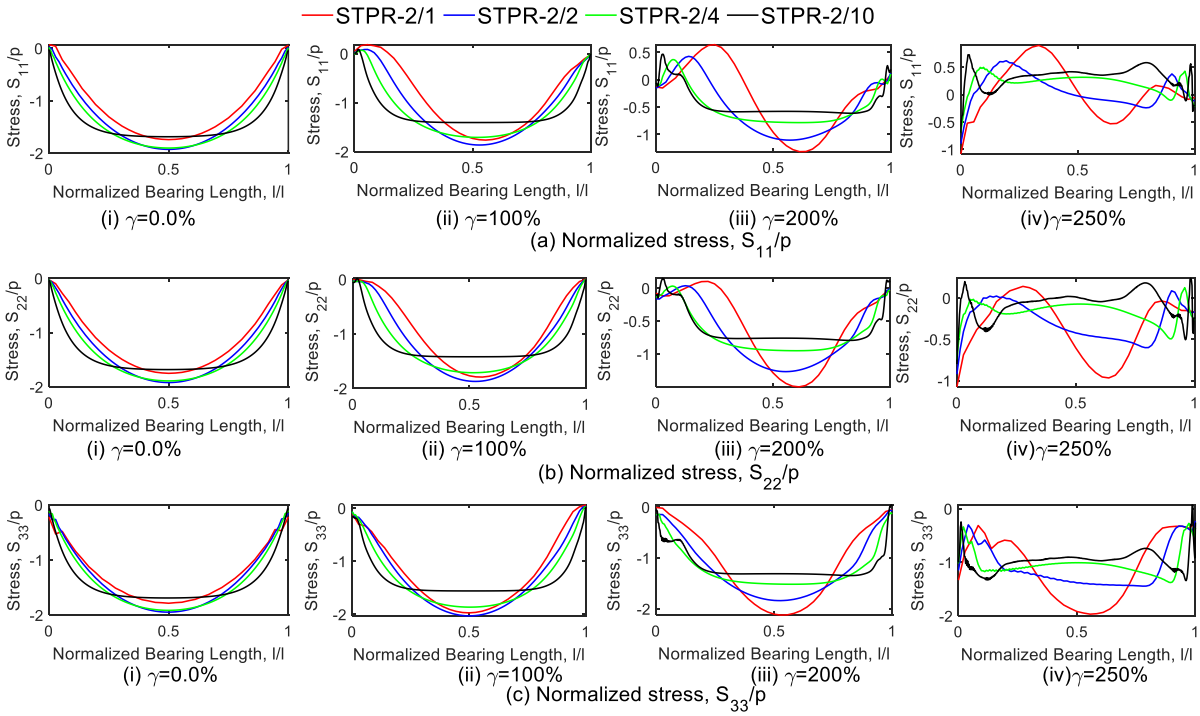

Figure 5.16 Normalized stress components for longitudinal loading.

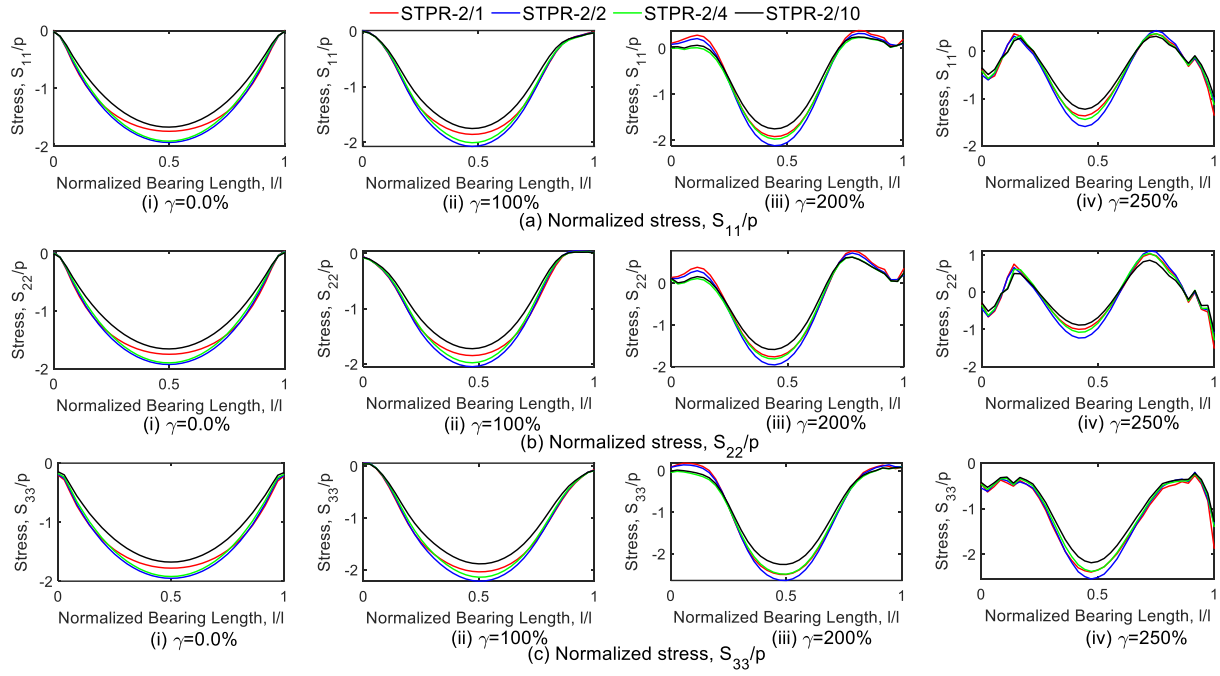

Figure 5.17 Normalized stress components for transverse loading.

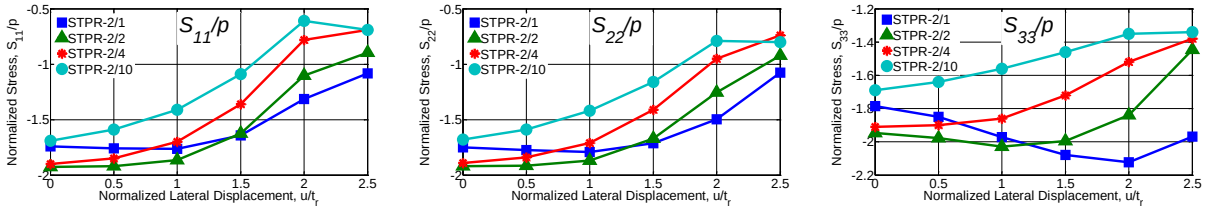

Figure 5.18 Maximum normalized stress S_{11}/p, S_{22}/p, and S_{33}/p in the longitudinal direction

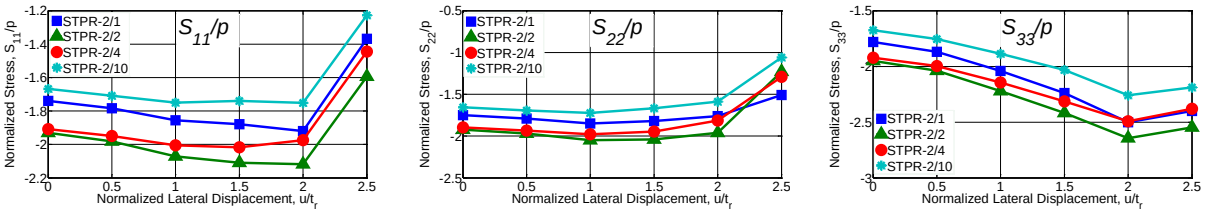

Figure 5.19 Maximum normalized stress S_{11}/p, S_{22}/p, and S_{33}/p in the transverse direction

Figures 5.18 and 5.19 show the peak of normalized stress in load Case-3, in which the in-plane stresses at 250% shear displacement are the stresses at the compressed rollover zone. Figure 5.18 shows that the in-plane stresses (S_{11}/p and S_{22}/p) and the vertical stress (S_{33}/p) reduce by 14~64% and 20%, respectively, for shear displacement increase to 200% in the longitudinal direction. In contrast, Fig. 5.19 shows that the vertical stress increases by 23-30% and the in-plane stresses are nearly the same for the same displacement

in the transverse direction. As the *l/w* ratio increases from 2 to 10, the triaxial stresses decrease by 15-25% for lateral displacement in the transverse direction. In contrast, an average 15-50% reduction occurs due to displacement in the longitudinal direction.

5.6 Strain in Elastomer

5.6.1 Elastomer Strain in Case-1 and Case-2

Figure 5.20 shows the elastomer strain contour (ε_{31}) for load combinations Case-1 and Case-2. Figure 5.21 shows the strain distribution along the bearings' length for the same combinations under 5.0 MPa compression. Both figures indicate that the outermost elastomer strain occurs close to the free ends due to compression only. When rotation or rotation plus lateral displacement progresses, the peak strain shifts toward the compressed zone in load Case-1 and the center in load Case-2. In both cases, strain at the transition zone between the compressed and lift-off zones is highly increased by the rotation.

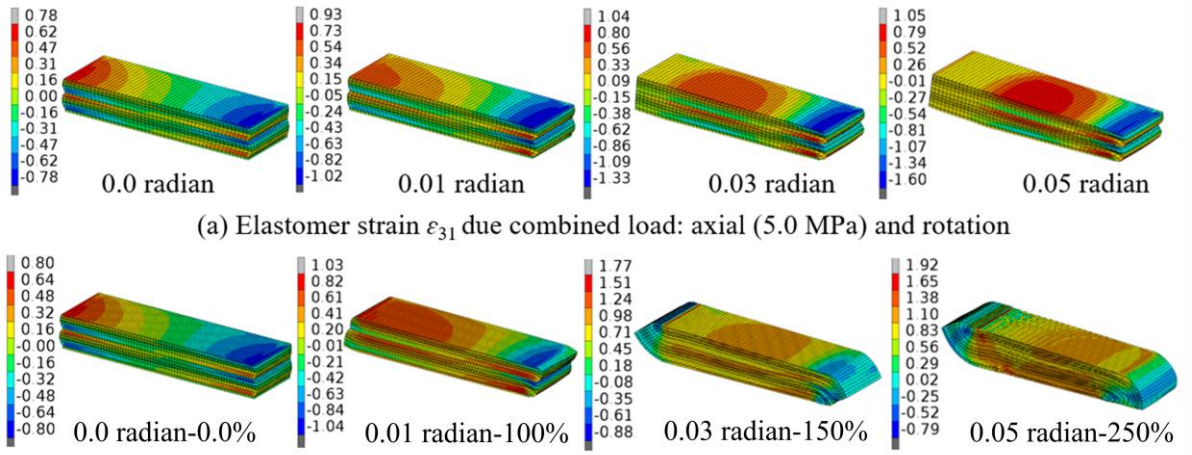

(a) Elastomer strain ε_{31} due combined load: axial (5.0 MPa) and rotation

(b) Elastomer strain ε_{31} due combined load: axial (5.0 MPa), rotation and lateral displacement

Figure 5.20 Elastomer strain (ε_{31}): (a) Case-1 and (b) Case-2

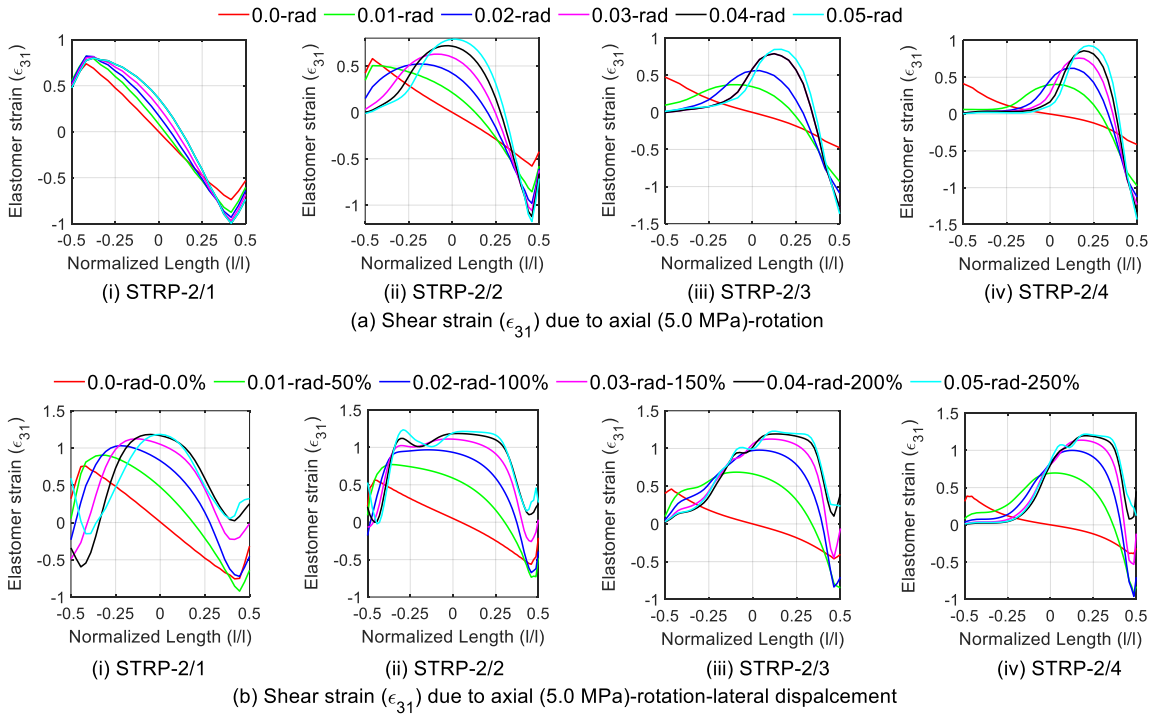

Figure 5.21 Elastomer strain along the length of the bearing (a) Case-1 and (b) Case-2

Figure 5.22 shows a relationship between elastomer peak strains and rotations at different compressions under load Case-1. Elastomer strains increase both for rotation and pressure on the bearing. In the absence of rotation, the elastomer strain of 0.70 in STRP-2/1 under 2.5MPa compression raises to 1.10 at 10.0 MPa. At 0.05-radian rotation, the same isolator's strain increases by around 71% and 33% at 2.5 and 10.0 MPa, respectively. The rotation effect is large for a high *l/w* ratio. The maximum elastomer strain is 1.47 and 1.51 in STRP-2/1 and 2/2, respectively, substantially lower than the imposed shear strain.

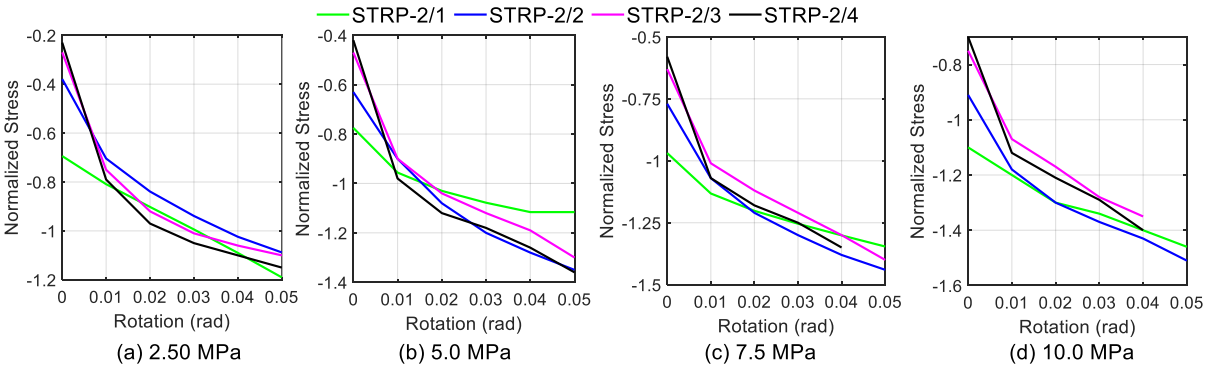

Figure 5.22 Peak of elastomer strain (ε31) due to compression and rotation

Figure 5.23 shows the peaks of elastomer strain for the load Case-2 consisting of 5.0 MPa compression and rotation and shear displacement up to 0.05-radian and 250%, respectively. Elastomer strains within the isolators are equal beyond the combination of 0.02-radian rotation plus 100% shear displacement (0.02rad-100%). It implies that the displacement effect is superlative than the rotation. The maximum elastomer strain is 1.25 for the combination of 0.05-radian rotation plus 250% shear displacement (0.05rad-250%), also much lower than the imposed strain.

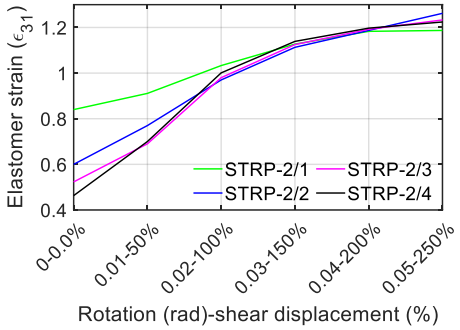

Figure 5.23 Peak of elastomer strain (ε_{31}) due to compression, rotation, and lateral displacement

5.6.2 Elastomer Strain in Case-3

Figure 5.24 shows the contour of elastomer strain in STRP-2/2 for load Case-3 under 5.0 MPa compression plus displacement up to 250% shear. Figure 5.25 shows the strain distributions along the length of the bearings. These figures show that the peak strain at compression-only moves from the end to the center of bearing for bearing's displacement. Such movement assimilates imposed displacement without increasing elastomer strain. The elastomer strain changes with *l/w* ratios for displacement in the longitudinal direction only, although the peak strains are the same for displacement exceeding 150%. The effect of *l/w* ratios is negligible for displacement in the transverse direction. Figure 5.26 shows the peak strains at different displacement levels. A comparison between Figs. 5.26a and 5.26 indicate that the rotation effect is insignificant in the presence of lateral displacement. In both cases, the maximum elastomer strain within the isolators is about 1.25, substantially lower than the applied shear of 2.50.

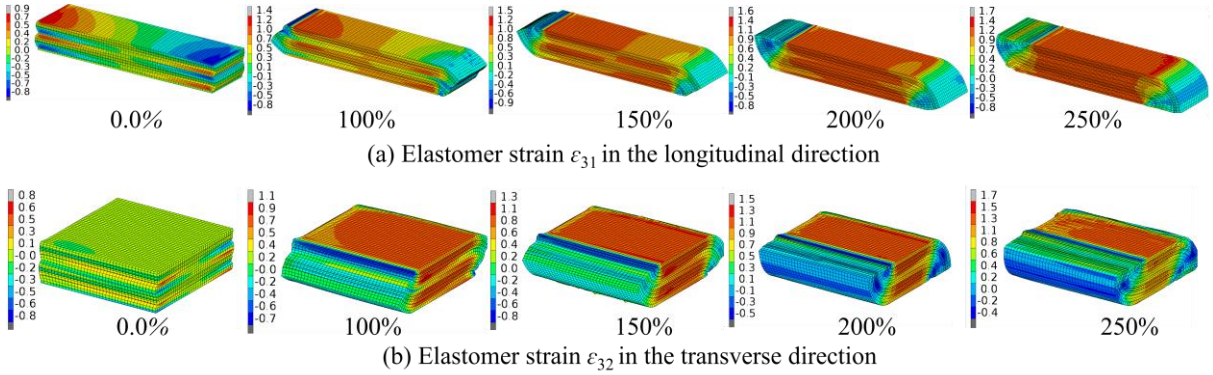

Figure 5.24 Elastomer strain (ε_{31} and ε_{32}) at different levels of shear displacement (%) for 5.0 MPa compression

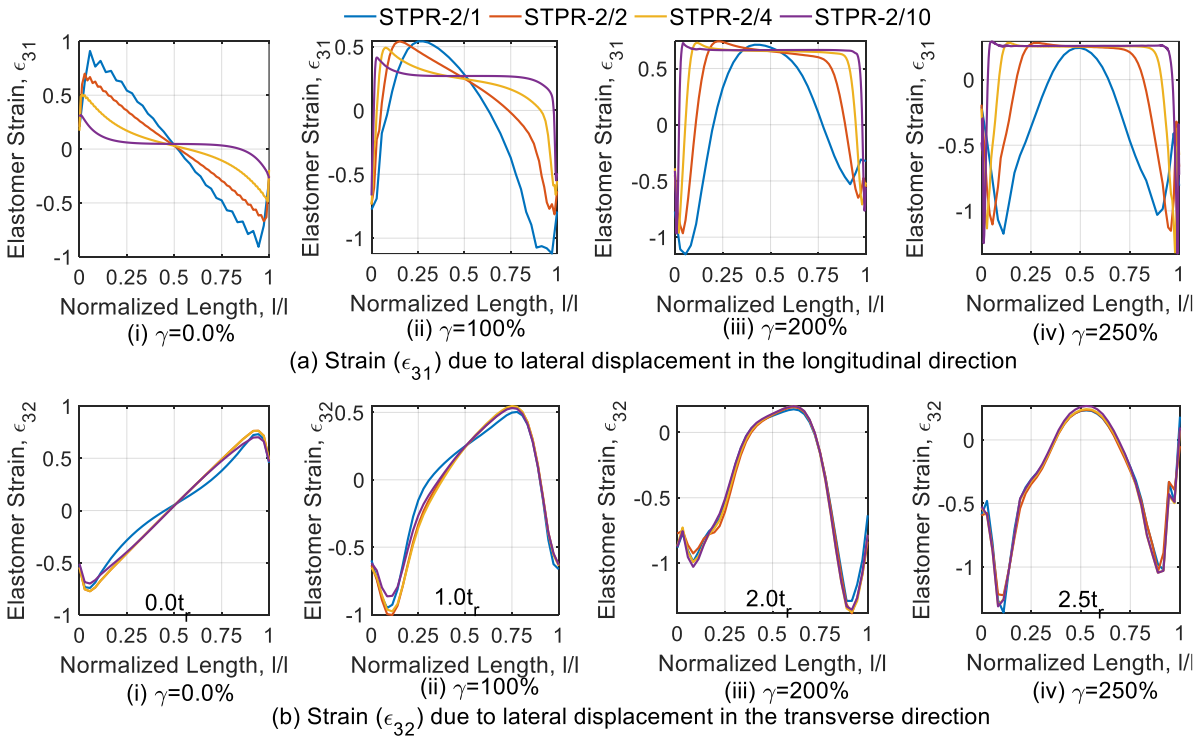

Figure 5.25 Elastomer strains in longitudinal and transverse directions for 5.0 MPa compression and lateral displacement

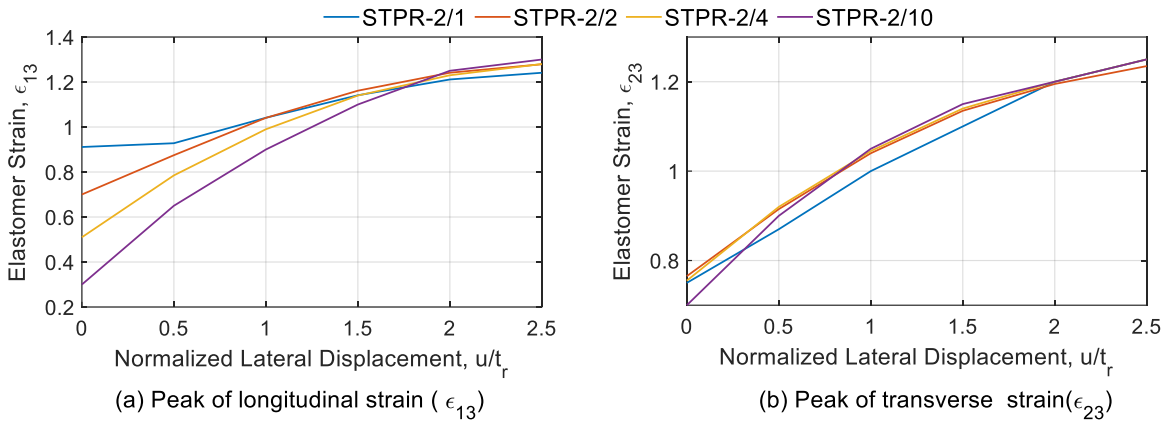

Figure 5.26 Peak value of elastomer due to compression plus lateral displacement

5.7 Stress in Steel-Cord

5.7.1 Steel-Cord Stress in Case-1 and Case-2

The rebar stress means the stress in the carcass steel (6th layer from bottom) except for the belt steel stress (5th layer) in the case of bearing's displacement in the transverse direction. The steel cords in the belt layer have a minimum angular distance with transverse direction. Figure 5.27 shows the normalized stress (S/p) pattern along the bearings' length for 5.0 MPa compression in the load Case-1 and Case-2. In load Case-1 (Fig. 5.27a), the rebar exhibits only tension for any rotation. However, an inclusion of lateral displacement in Case-2 (Fig. 5.27b), steel cord suffers compression at 0.05-radian rotation plus 250% shear displacement (0.05radian-250%). This compression possibly buckles the steel cords and expects the steel chord to return to its original form without any permanent failure during the unloading. Like the elastomer, streel cords are stress-free in the lift-off zone, and the peak stress shifts towards the bearing's end.

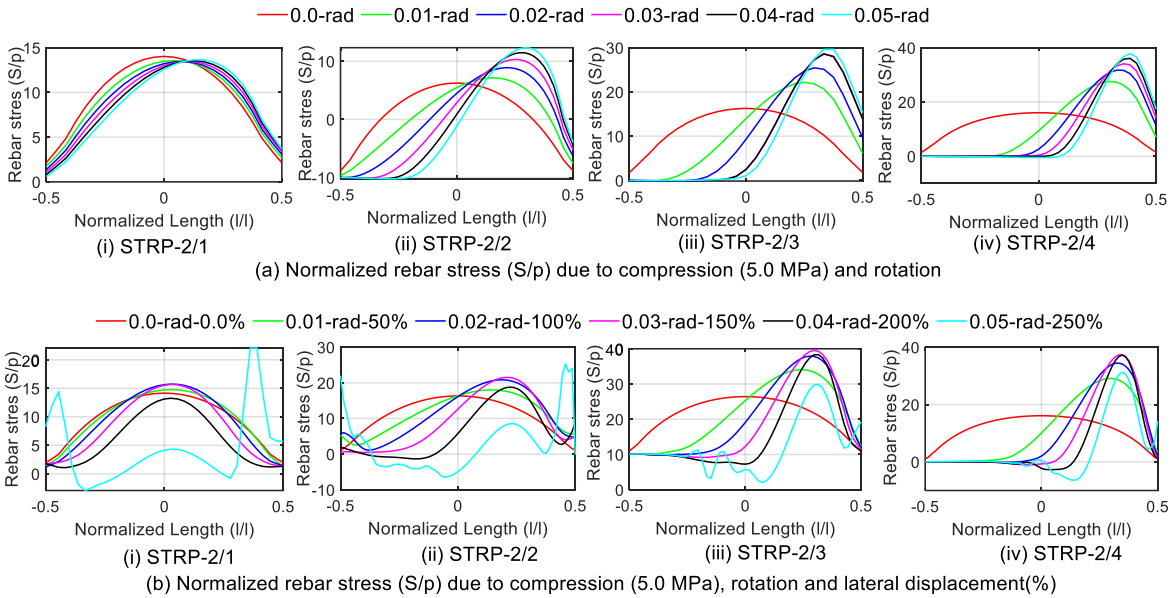

Figure 5.27 Profile of rebar stress (S/p) along the length of the bearing (a) Cas-1 and (b) Case-2

Figure 5.28 shows the normalized peak rebar stress (*S/p*) in load Case-1. In simple compression, stress is independent of the *l/w* ratio and vertical pressure. The rebar stress increases with an increase of rotation and is significant for a high *l/w* ratio and low compression. Moreover, the normalized stress decreases with an increase of pressure on the bearing. For example, rebar stress in STRP-2/1 is less sensitive to the rotation until 0.05-radian, and it is about 14.9 and 12.5 at 2.5 and 10.0 MPa, respectively. At 2.5 MPa and 0.01-radian, the stress in STRP-2/2, 2/3, and 2/4 is 36%, 84%, and 127% higher than that of STRP-2/1. Similarly, at 0.05-radian and 2.5 MPa compression, rebar stress in the respective isolators is 76%, 140%, and 200% higher than that of STRP-2/1. These percentages reduce when the compressive force on the bearing increases.

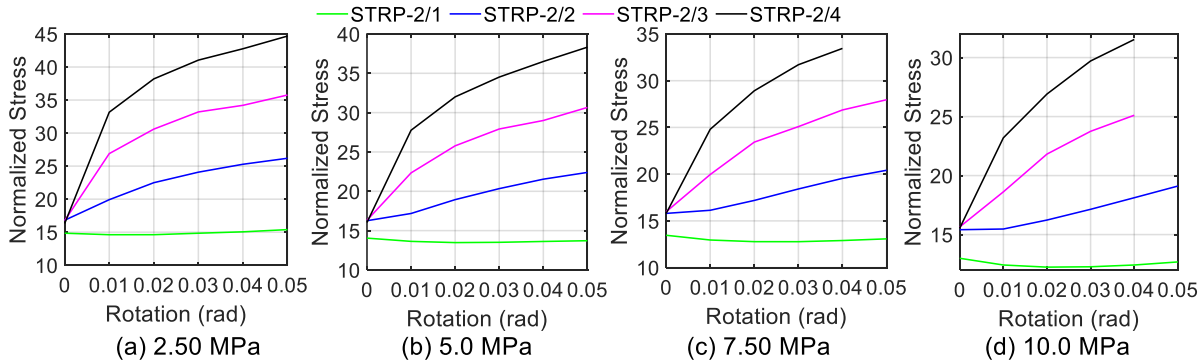

Figure 5.28 Peak of normalized rebar stress (S/p) in load Case-1

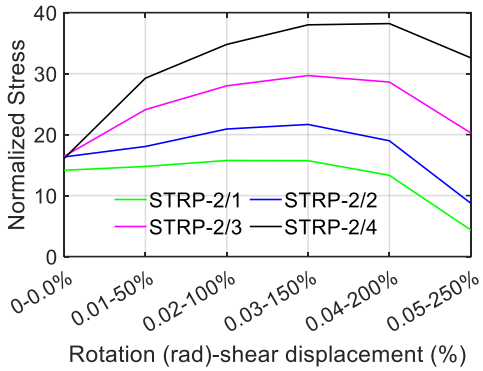

Figure 5.29 Peak of normalized rebar stress (S/p) in load Case-2

Figure 5.29 shows a similar plot for rebar stress in load Case-2 under 5.0 MPa compression. The rebar stress increases until a combination of 0.03-radian rotation plus 150% shear displacement (0.03rad-150%) and then decreases. For 0.05-radian rotation plus 250% shear (0.05rad-250%), stress reduces by 68%, 54%, 30% and 15% in STRP-2/1, 2/2, 2/3 and 2/4, respectively, compare with the rebar stress for 0.04 radian plus 200% shear displacement (0.04rad-200%).

5.7.2 Steel-Cord Stress in Case-3

Figure 5.30 shows the normalized rebar stress profiles in the two orthogonal directions of the bearing under the load Case-3. The rebar stress is compression for a displacement exceeding 200% shear, especially for bearing displacement in the longitudinal direction. Figure 5.31 shows the peak of normalized rebar stress at different lateral displacement levels. The rebar stress reduces as the lateral displacement progresses, and the maximum reduction is about 20-40% and 10-15% in the longitudinal and transverse direction, respectively. Besides, an increase of *l/w* ratio from 2 to 10 reduces the stress by 20-32% on average in both directions. The maximum normalized rebar stresses in the longitudinal and transverse directions are 16.2 and 17.7, equal to 81 MPa and 88.5 MPa, respectively. These are appreciably insignificant than the steel cords' yield strength, 2800 MPa (Kirihara, 2011; Tashiro and Tarui, 2003; Ishiwaka, 2011).

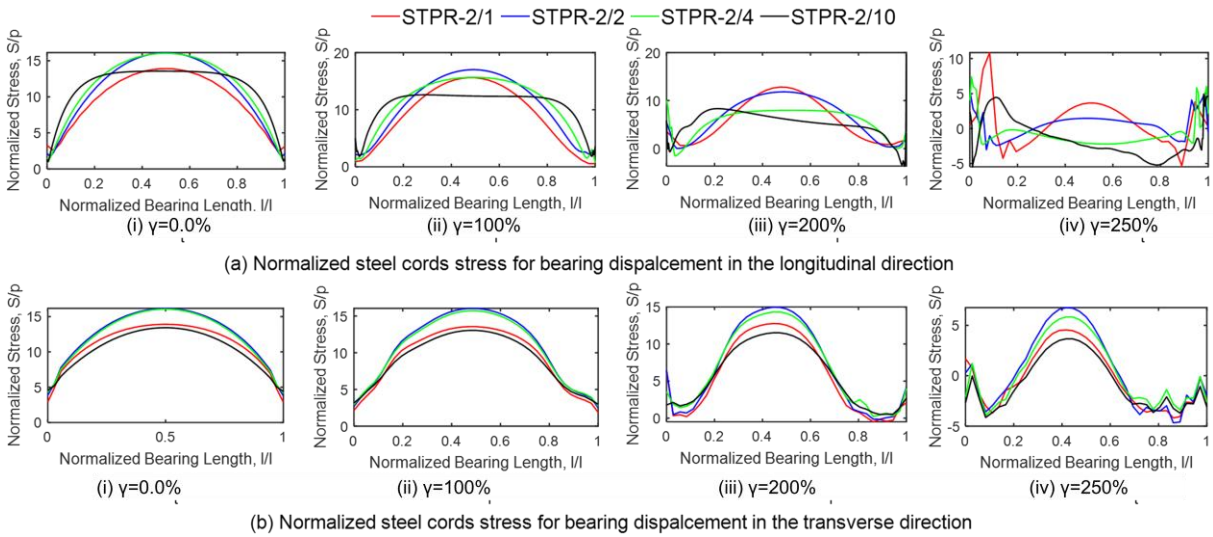

Figure 5.30 Profiles of normalized rebar stress (*S*/*p*) in load Case-3

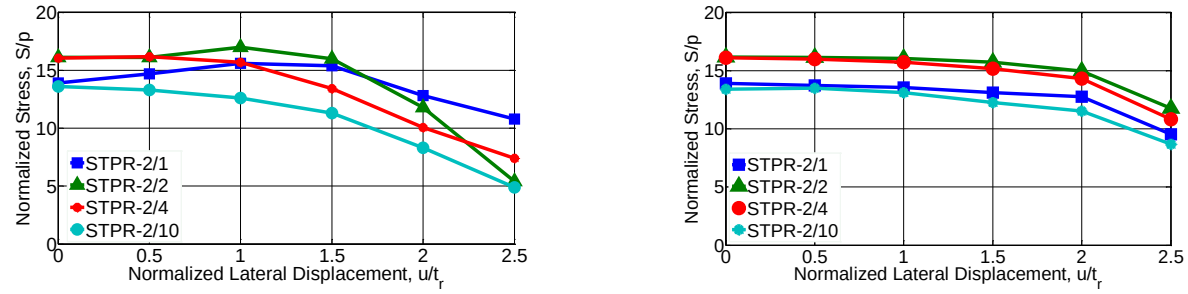

(a) Steel cord stress for longitudinal loading (b) Steel cord stress for transverse loading

Figure 5.31 Peak normalized stress in steel cords, S/p

5.8 Evaluation of STRP Isolator Using Code Specification

5.8.1 In-service Elastomer Stress and Stability

The limits of normalized compressive stress (σ_s/p) for the STRP isolators as per AASHTO-LRFD method A and at 2.5, 5.0, 7.5, and 10.0 MPa compressions is 4.3, 2.2, 1.4, and 1.1, respectively. For a shear modulus of 1.31 MPa, the upper limit of the normalized tensile stress is 1.60, 0.79, 0.52, and 0.39, respectively, under the same compression. The in-service stress should be lower than these limiting values. In load Case-1, as shown in Fig. 5.9, the STRP-2/1 satisfies these limits for any combination of compression and rotation up to 5.0 MPa and 0.05-radian, respectively. Similarly, the STRP-2/2 complies with a combination of 0.05-

radian plus 2.5 MPa and 0.02-radians plus 5.0 MPa. STRP-2/3 and 2/4 comply up to 0.03 and 0.01-radians, respectively, under 2.50 MPa compression.

In load Case-2, as seen from Fig. 5.13, the working stress in STRP-2/1 also satisfies the limiting stress, 2.20 under 5.0 MPa compression plus any combination of rotation and displacement within 0.05-radian and 250% shear, respectively. However, elastomer tension exceeds for displacement higher than 200% shear. The STRP-2/2 follows STRP-2/1 except for the vertical stress that exceeds the compressive stress limit at 5.0 MPa plus any combination of rotation and displacement exceeding 0.02-radian and 100% shear, respectively. The STRP-2/3 and 2/4 disagree with the design limits even under the lowest rotation 0.01-radian and compression 2.5 MPa. However, for a zero rotation in load Case-3, as shown in Figs. 5.18 and 5.19, all isolators comply with the design guidelines for any combination of compression within 5.0 MPa and displacement within 250% shear. However, the in-plane tension, as shown in Figs. (5.16a and 5.16b) and (5.17a and 5.17b) cross the limit for displacement exceeding 200% shear.

In general, the STRP isolators have a unit value of *l/w* ratio fit for any combination of compression, rotation, and within 5.0 MPa, 0.05-radian, and 200% shear, respectively. Similarly, the *l/w* ratio of 2.0 complies with the design limits within 5.0 MPa compression plus rotation and displacement up to 0.02-radian and 100% shear. The *l/w* ratio exceeding 2.0 opposes the design limit even under the lowest rotation and compression. In the absence of rotation, STRP isolators with an *l/w* ratio of 10 are suitable until 200% shear displacement under 5.0 MPa compression.

Table 5.2 Stability and stress evaluation of STRP isolators by AASHTO-LRFD method B

	Longitudinal direction					Transverse direction				
Bearing	STRP-2/1	STRP-2/2	STRP-2/3	STRP-2/4	STRP-2/10	STRP-2/1	STRP-2/2	STRP-2/3	STRP-2/4	STRP-2/10
A	0.31	0.12	0.07	0.04	0.01	0.31	0.38	0.41	0.44	0.49
B	0.25	0.18	0.15	0.13	0.09	0.25	0.21	0.19	0.19	0.17
$2A<B$	*NS*	*NS*	*S*	*S*	*S*	*NS*	*NS*	*NS*	*NS*	*NS*
σ_s/p (Eq.7.3)	4.53	38.7	-137	-57.4	-43.8	4.53	4.04	3.91	3.85	3.72
$\sigma_s/p \geq (\sigma_s/p)_{FEA}$	*S*	*S*	-	-	-	*S*	*S*	*S*	*S*	*S*
Remarks	*SS*	*SS*	*ST*	*SS*	*SS*	*SS*	*SS*	*S*	*SS*	*SS*

S: Satisfactory, *NS*: Not satisfactory, *SS*: Satisfactory and stable, (-)ve: Stable and independent of σ_s

Table 5.2 summarizes the stability as per method B for load Case-3 for combinations of compression and displacement within 5.0 MPa and 250% shear, respectively. It also shows the normalized stress σ_s/p from Eq.5.3, and a negative value means the bearing is stable and independent of σ_s. The normalized value of working stress $(\sigma_s/p)_{FEA}$ is taken from the FE analysis results shown in Figs. 5.18 and 5.19. Isolators with an *l/w* ratio exceeding 3.0 satisfy 2A < B in the longitudinal direction only. Contrarily, bearings that opposed 2A<B agreed with $\sigma_s/p \geq (\sigma_s/p)_{FEA}$. Therefore, as per the AASHTO-LRFD specification, bearings are stable under 5.0 MPa compression plus 250% shear displacement.

In the load Case-1 and Case-2, the elastomer stresses are calculated in the longitudinal direction only. In STRP-2/1, the normalized stress, σ_s/p at 2.5 and 5.0 MPa and calculated using Eq.5.3, is 9.1 and 4.53, respectively. The respective value for STRP-2/2 is 77.4 and 38.7. These are substantially higher than the working stress, $(\sigma_s/p)_{FEA}$ in STRP-2/1 and 2/2 presented in Figs. 5.9 and 5.13 for any combination of compression, rotation, and displacement within 5.0 MPa, 0.05-radian, and 250% shear. Therefore, STRP-2/1 and 2/2 are stable for rotation up to 0.05-radian plus 5.0 MPa compression and 250% shear displacement.

5.8.2 In-service Elastomer Strain

The unbonded isolator is beneficial because the elastomer strain is substantially low due to the rollover deformation. Figure 5.22 gives the maximum strain in the STRP-2/1 isolator is 0.80 and 1.10 at a simple compression of 5.0 and 10.0 MPa, which is less than the code specified limit 3.0 as defined in Eq. 5.7. Figures 5.22 and 5.23 give the upper limit of elastomer strain within the isolators is 1.51 for any combination of compression, rotation, and displacement within compression 10.0 MPa, 0.05-radian, and 250% shear, respectively. Moreover, Fig. 5.26 shows that the elastomer strain along with two orthogonal directions is around 1.30 for any combination of shear displacement until 250% under 5.0 MPa compression. These strains are substantially lower than the AASHTO-LRFD specified limit 5.0 as defined in Eq. 5.5 and applied shear strain 2.50.

5.9 Stress and Equivalent Thickness of Steel Cord

In load Case-1, as shown in Fig. 5.28, the highest normalized rebar stress in STRP-2/1 is 13.7 (68.5 MPa) and 22.5 (112.5 MPa) in STRP-2/2 within the acceptable limit of 5.0 compression and 0.05-radian rotation. For STRP-2/3 and STRP-2/4, these are 30.5 (152.5 MPa) and 38.0 (190 MPa), respectively, those are disregarded because elastomer stresses in these bearings exceed the allowable limit. In load Case-2, the maximum rebar stress in STRP-2/1 and STRP-2/2 is 12.8 (64.0 MPa) and 21.5 (107.5 MPa), respectively, found from Fig. 5.29. In load Case-3, the peak of normalized stress within the bearings group is 16.2 (81.0 MPa) in the longitudinal direction and 16.2 (81.0 MPa) in the transverse direction, seen from Fig. 5.31. The stresses mentioned above are appreciably insignificant to the steel cord's yield strength.

AASHTO-LRFD recommends a minimum thickness of 1.6 mm for the steel layer. The equivalent thickness of steel in the STRP isolator is 0.4 mm, sufficiently below 1.6 mm. The elastomer layer thickness ranges between 2.0 mm and 3.25 mm is also smaller than that of the SREI. Figures 5.9 and 5.13 give the maximum in-plane normalized stress in STRP-2/1 and 2/2 within allowable compression, and rotation is 1.82 and 2.35. Figures 5.18 and 5.19 indicate that the acceptable stresses are 2.15 and 2.0 in the orthogonal directions under the same conditions. Thus, the maximum normalized elastomer stress is 2.35, equal to 11.75 MPa. For a 3.25 mm thick elastomer layer, the required thickness of steel from Eq. 5.8 is 0.041 mm, substantially below the provided thickness of 0.4 mm.

5.10 Effective Length and Allowable Displacement

Tension is a critical parameter for an unbonded STRP isolator and develops due to the lateral displacement. In load Case-2, the highest normalized tension is 0.86 (Fig. 5.13a), located at the transition zone under a compression, rotation, and displacement of 5.0 MPa, 0.05-radian, and 250% shear, respectively. In load

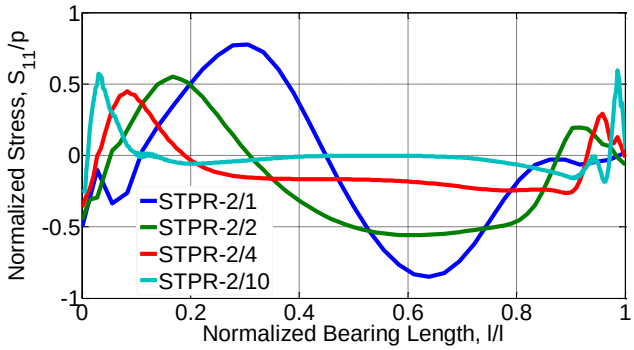

Figure 5.32 S_{11}/p at 231% shear displacement in the longitudinal direction

Case-3, the highest normalized tension stresses in the longitudinal and transverse directions are 0.89 (Fig. 5.16a) and 1.0 (Fig. 5.17b), respectively, for displacement exceeding 200% shear. These tensions are larger than 3*G*, limiting negative pressure for the onset of fracture-related problems (Naeim and Kelly, 1999). Figure 5.32 shows the in-plane stress S_{11}/p at 5.0 MPa compression and 231% shear displacement; the maximum displacement at which the STRP isolator has the largest *l*/*w* ratio is less than 3*G*. Here, the tension peaks are located within 0.022*l*~0.039*l* and 0.25*l*~0.33*l* from the free surface of STRP-2/10 and STRP-2/1, respectively. On average, these critical distances are about $1.0t_r$ ~ $1.30t_r$. Therefore, the "effective length" of a strip-STRP isolator is the bearing's length, excluding the critical distance, and can be considered shear displacement exceeding 200%.

5.11 Conclusions

The stress-strain relationship in STRP isolators of different *l*/*w* ratios is analyzed to determine the allowable forces following the design guidelines for various combinations of compression, rotation, and lateral displacement. For this purpose, an FE-model efficient in simulating incompressible behavior and large deformation of rubber is modeled, including the hyperelastic and viscoelastic properties of rubber, and verified with an analytical solution and past loading test results. The unbonded condition is modeled as a touch contact using the bilinear Coulomb friction model. The *l*/*w* ratios are taken between 1.0 and 10.0, and isolator dimensions are selected so that the aspect ratio in the length direction is *l*/*w* times that in the width direction. An aspect ratio of 3.0 is chosen for all isolators in the width direction. A vertical pressure of 2.5, 5.0, 7.5, and 10.0 MPa includes the upper and lower limits in AASHTO-LRFD specification, and a rotation and shear displacement up to 0.05-radian 250%, respectively, are considered. The findings of the FE analysis are summarized below.

- STRP isolators exhibit unsymmetrical lateral bulging, which is minimum for an *l/w* ratio between 2.0 and 4.0. Besides, a progressive rollover deformation initiates at 90% shear displacement and continues until 250% shear. Thus, the full-contact occurs at 250% shear instead of 167% observed in FREI.
- Pressure solution can be exercised considering 16% and 26% underestimation in elastomer stress for l/w ratios of 1.0 and exceeding 1.0, respectively. The steel cords' orientation affects the FE analysis results overlooked by an equivalent thickness in pressure solution.
- The aspect ratio 3.0 is suitable against lift-off and instability of an unbonded STRP isolator at 250% shear displacement, 0.05-radian rotation, and 2.5 MPa compression. An increase in *l/w* quickens the lift-off initiation that delays with an increase of compression.
- Rotation increases the in-service stress, and its effect is more significant at low compression and for a high *l/w* ratio. Lateral displacement reduces the in-service compression stresses and induces tension, which is more profound for high *l/w* ratios.
- STRP isolator has an *l/w* ratio of 1.0 meets design specification within any combination of 5.0 MPa compression, 0.05-radian rotation, and 200% shear. The *l/w* ratio 2.0 complies within 5.0 MPa compression plus rotation and displacement up to 0.02-radian and 100% shear. The *l/w* ratio exceeding 2.0 opposes the design limit even under the lowest rotation and compression. In the absence of rotation, STRP isolators with an *l/w* ratio of 10 are suitable until 200% shear displacement under 5.0 MPa compression.
- An effective length excluding the tension zone ($1.0t_r$~$1.30t_r$) might be suitable to avoid any occurrence for shear displacement exceeding 200%.
- The maximum elastomer strain for any values of *l/w* ratios is much lower than the design limits due to static compression or any combinations of compression, rotation, and lateral displacement.
- Stress in steel cord is appreciably insignificant compare with the steel cord's yield strength. The equivalent thickness of steel cords in STRP is sufficient to resist elastomer bulging and meets the design limits.

References

AASHTO. LRFD bridge design specifications. Washington, DC: American Association of State Highway and Transportation Officials; 2012.

Al-Anany Y. Tait MJ.A (2015). Numerical study on the compressive and rotational behaviour of fiber reinforced elastomeric isolators (FREI). Compos Struct, Vol.133, pp.1249–66

BS EN 15129: 2009. Anti-seismic devices. BSI British Standards; 2010.

Crowder AP, Becker TC. (2015). Preliminary study on the behaviour of a column-top isolation system. Proc. 11th Canadian Conference on Earthquake Engineering, July 21 – 24, 2015M Victoria, BC.

CAN/CSA-S6-06. Canadian highway bridge design code. Ontario: Canadian Standard Association; 2006.

EN 1998–2. Eurocode 8: design of structures for earthquake resistance, Part 2: bridges. Brussels, Belgium: European Committee for Standardization; 2005.

EN 1337-3: 2005. Structural bearings – Part 3: elastomeric bearings. Brussels: European Committee for Standardization; 2005.

Ishiwaka Y. (2011), Systematic Review of Tyre Technology. National Museum of Nature of Science. 2011); 16: 1-137

Japan Road Association, JRA. Bearing support design for highway bridges, Tokyo, Japan; 2011.

Kirihara, K. (2011). "Production Technology of Wire Rod for High Tensile Strength Steel Cord". Kobelco Technology Review No. 30, 62-

Konstantinidis and Kelly (2014). Advances in low-cost seismic isolation with rubber, 10th U.S. National Conference on Earthquake Engineering Frontiers of Earthquake Engineering July 21-25, 2014, Anchorage, Alaska

Mishra, H. K. (2012). "Experimental and Analytical Studies on Scrap Tire Rubber Pads for Application to Seismic Isolation of Structures." Ph.D. Thesis, Kyoto University, Japan.

Mishra, H. K., Igarashi, A., Matsushima, H. (2013a). "Finite element analysis and experimental verification of the scrap tire rubber pad isolator." Bul Earthquake Eng., Springer, 11(2), 687-707.

Mishra, H. K., Igarashi, A. (2013b). "Lateral deformation capacity and stability of layer-bonded scrap tire rubber pad isolators under combined compressive and shear loading." Struct. Eng and Mech., Techno Press, 48(4), 479-500.

Moghadam, S.R. Konstantinidis, D. (2015). Effect of Rotation on the Horizontal Behavior of Rubber Isolators, 11th Canadian Conf. on Earthquake Engineering, Victoria, BC, Canada.

MTO. OPSS 1202. Material specification for bearings – elastomeric plain and steel laminated. Toronto, Ontario: Ontario Ministry of Transportation; 2008.

Naeim F., Kelly J. M. (1999). Design of seismically isolated structures: from theory to practice. New York, NY: John Wiley & Sons.

Osgooei, P. M., Tait, M. J., and Konstantinidis, D. (2014a). Three-dimensional finite element analysis of circular fiber-reinforced elastomeric bearings under compression, *Composite Structures*, 108, pp. 191–204.

Osgooei PM, Tait MJ, Konstantinidis D. (2014b). Finite element analysis of unbonded square fiber-reinforced elastomeric isolators (FREIs) under lateral loading in different directions. Compos Struct 2014; 113:164–73

Osgooei, P. M., Van Engelen, N. C., Konstantinidis, D., and Tait, M. J. (2015). Experimental and finite element study on the lateral response of modified rectangular fiber-reinforced elastomeric isolators (MR-FREIs), Engineering Structures 85 (2015) 293–303.

Ohsaki, M., Miyamura, T., Kohiyama, M., Yamashita, T., Yamamoto, M., Nakamura, N. (2015). "Finite-Element Analysis of Laminated Rubber Bearing of Building Frame under Seismic Excitation", *Earthquake Engineering and Structural Dynamics*, 44(11), 1881-1898.

Toopchi-Nezhad, H., Tait, M. J. and Drysdale, R. G., (2008b). "Testing and modeling of square fiber-reinforced elastomeric seismic isolators." Struct. Control Health Monit., 15(6), 876-900.

Toopchi-Nezhad H, Tait MJ, Drysdale RG (2011). Bonded versus unbonded strip fiber reinforced elastomeric isolators finite element analysis. Composite Structures, 93:850–859.

Toopchi-Nezhad H. Horizontal stiffness solutions for unbonded fiber reinforced elastomeric bearings. Structural Engineering and Mechanics 2014, 49(3):395–410.

Tashiro, H. and Tarui, T. (2003). State of the Art for High Tensile Strength Steel Cord, NIPPON STEEL TECHNICAL REPORT No. 88, pp. 87-91

Tsai HC, Kelly JM (2001). Stiffness analysis of fiber-reinforced elastomeric isolators. Berkeley, California: Pacific Earthquake Engineering Research Center, PEER; 2001/5.

Van Engelen, N. C., Tait, M. J., and Konstantinidis, D., (2015): "Model of the shear behavior of unbondedfiber-reinforced elastomeric isolators." J. Struct. Eng., ASCE, 141 (7), 1-11

Chapter 6

Biaxial Performance of Unbonded Scrap Tire Rubber Pad Isolator

This chapter focused on the cyclic loading performance of unbonded STRP isolators for a biaxial lateral load. Both square and strip-shaped unbonded STRP isolators are analyzed under circular, square, hourglass, and 8-shaped biaxial displacement trajectories. The lateral load performance was also investigated for the unidirectional component of each biaxial trajectory in order to conclude the effect of biaxial loading. Finally, the performance of the isolator is documented in terms of force-displacement relationship, stiffness, and effective damping ratio.

6.1 Introduction

The base-isolation technique is used in buildings, bridges, nuclear power plants, and so forth due to its high effectiveness in reducing seismic demand and the level of the collapse of structures (Chimamphant and Kasai, 2016; Huang et al., 2013; Cardone and Flora, 2016) during an earthquake. The STRP isolator is expected to have functions similar to steel-reinforced elastomeric isolators to be used for the isolation of lightweight structures. An experimental study shows that an STRP isolator subjected to unidirectional cyclic loading provides an effective damping ratio of 10~22% and a vertical-to-horizontal stiffness ratio within 450~600 (Mishra, 2012), exceeding 150, indispensable for isolation material (Eurocode 8). The shear modulus of tire rubber is around 1.0 MPa (Mishra et al., 2013a; Turer and Özden, 2007) within the range of natural rubber, 0.55~1.20 MPa specified by AASHTO-LRFD for seismic isolator. The beneficiary aspects are that an STRP isolator without any mechanical bonding with the structural elements bypasses a large amount of tension within the elastomer and improves the isolation's efficiency through roll-over deformation. They concluded that STRP isolators are suitable for application to low-to-medium-rise buildings.

A practical implementation of unbonded STRP isolators requires considering its nonlinear hysteretic response under uni- and bi-directional horizontal loads. The bidirectional loading is essential because the effectiveness of unbonded isolators depends on friction, which differs from the bonded isolator. The previous studies (Mishra et al., 2013a, 2013b) on unbonded STRP isolators were conducted using unidirectional cyclic loading only, and they recommended further investigation under bidirectional load. Mishra et al. (2014) performed a pseudo-dynamic test on a 1/3rd scale unbonded STRP isolator and a numerical simulation of a hypothetical three-story base-isolated building based on bilinear idealization force-displacement relationship of unbonded STRP isolators (Mishra, 2012). This simulation considered the unidirectional lateral load while ignored the friction-dependent contact of the STRP isolator. Zisan and Igarashi (2020, 2021) studied the horizontal stiffness of unbonded strip-shaped STRP isolators for different length-to-width ratios and unidirectional loading. Since there is no appropriate documentation on the bidirectional performance of unbonded STRP isolators, it is essential to investigate the STRP isolators subjected to the bidirectional cyclic load for practical design and implementation.

Although the existing design specifications provide well-defined methodologies and design principles for conventional elastomeric isolators (AASHTO-LRFD, ASCE-SEI-7/10, Eurocode 8), unbonded application of a base isolator is yet to be explored in detail to be used in practice. Because of friction-dependent and unbonded contact conditions, the existing design specifications are incompatible for the application of unbonded STRP isolators. These codes also recommend investigating a base-isolated structure under bidirectional loading conditions. Therefore, the objective of this study is to assess the effect of bidirectional loading on the lateral load performance of an unbonded STRP isolator. Table 6.1 shows the geometric properties of the STRP isolators. Both geometric and material properties of these isolators were described in Chapter 3. The FE modeling and model verification are also described in Chapter 3.

Table 6.1 Geometric properties of STRP isolator models

Group	Designation	Dimensions $l \times w \times h$ (mm)	Length-to-width ratio	Rubber thickness t_r (mm)	Equivalent thickness t_e (mm)	Shape factor S	Aspect ratio	
							R_x	R_y
STRP isolator	STRP-2/1	72 × 72 × 24	1	20	2.4	7.5	3	3
	STRP-2/2	144 × 72 × 24	2	20		10	6	3

6.2 Bidirectional Displacement Trajectories

Figure 6.1 shows the displacement trajectories that are used to evaluate the bidirectional performance of unbonded STRP isolators. These trajectories are suggested for the bidirectional performance of SREIs, and high damping rubber bearing (HDRB) in some previous studies (Grant et al., 2008; and Huang et al., 2000). The restoring force of rubber-isolators is amplitude-dependent (Fujita et al. 1989a); hence the shear strain of 25%, 50%, 100%, 150%, 200%, and 250% of total rubber thickness is assumed in the unidirectional displacement cases. The maximum of resulting radial displacements under the bidirectional loading is 1, $\sqrt{2}$, $\sqrt{2}$ and 1.39 times of *X* and *Y*-components of the circular, square, hourglass, and 8-shaped trajectory, respectively. The frequency and the velocity of the *Y*-component of the hourglass and 8-shaped trajectories are 1.5 and 2.0 times that of the *X*-component. Each isolator is compressed by 5.0 MPa pressure before the application of lateral force. In the unidirectional loading case, displacement in the *X* and *Y*-directions (u_x and u_y) are applied separately, whereas simultaneously applied in the case of bidirectional loading. In the linear displacement trajectory (Zisan and Igarashi, 2021), the strain rate is constant. In contrast, the rate of strain changes from a maximum to zero and vice-versa in other trajectories shown in Fig. 6.1.

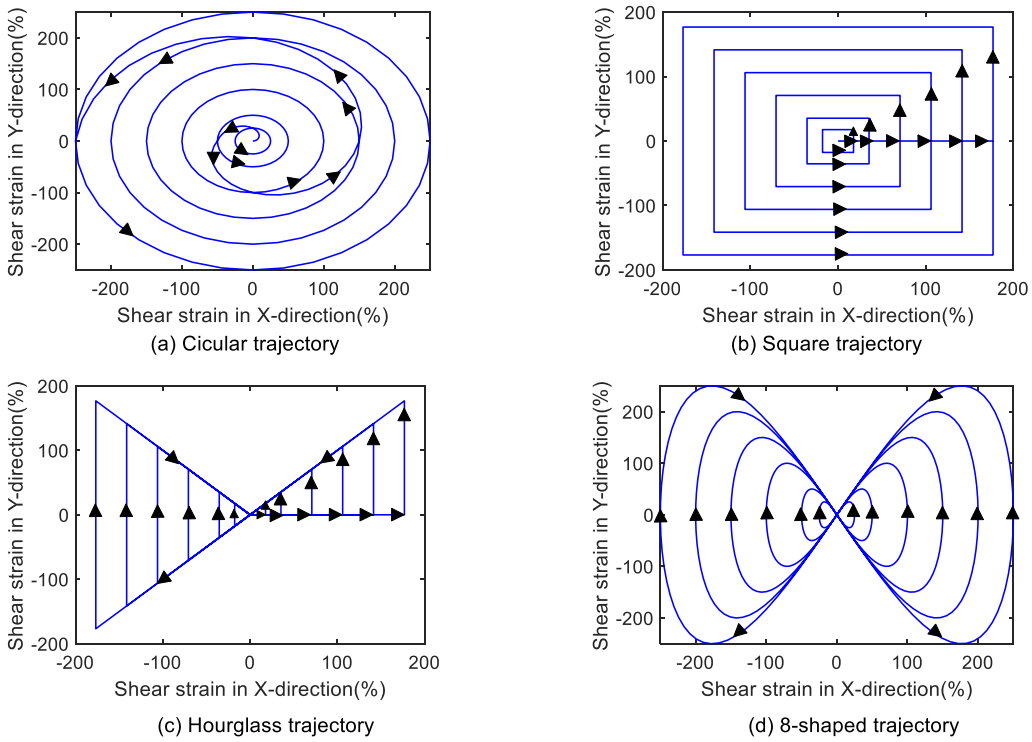

Figure 6.1 Bidirectional displacement trajectories

6.3 Lateral Load Performance

6.3.1 Deformed Shape of Isolators

Figures 6.2 and 6.3 show the deformed shape of the unbonded STRP isolators at different levels of bilateral strains (ε_x and ε_y). The deformation of isolators under the unilateral strain is presented in Chapter 4. It shows that the location and area under the roll-over part are changing with the orientation of the radial displacement. The progressive contact between the roll-over section and rigid planes observed in the

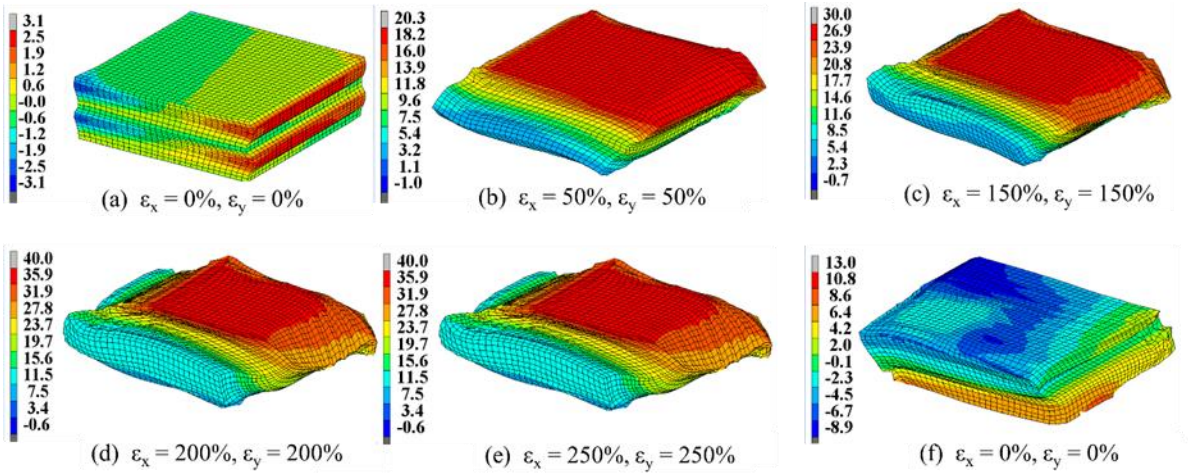

Figure 6.2 Isolator deformations in X and Y-directions under the square trajectory

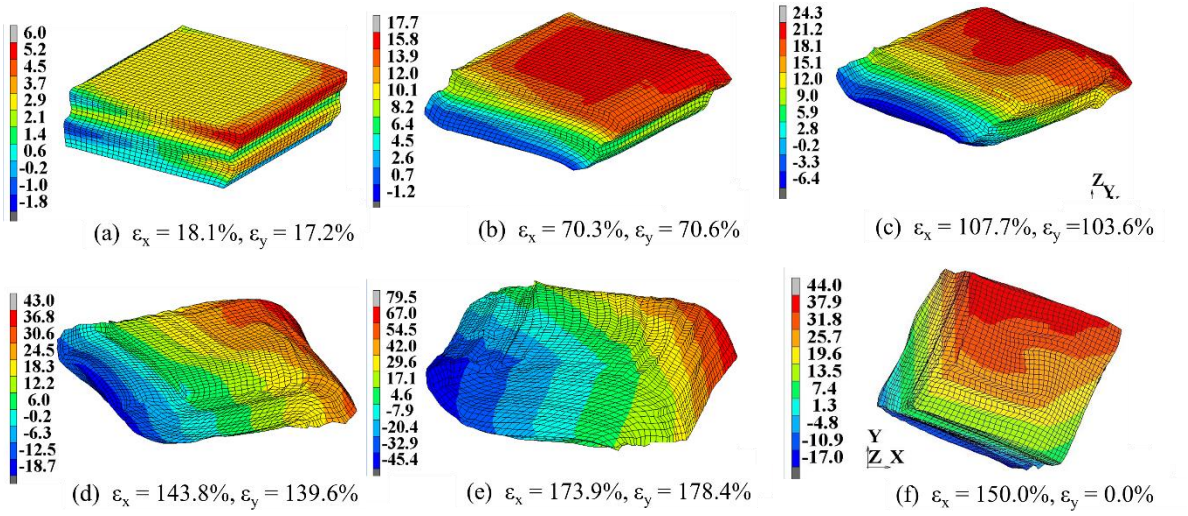

Figure 6.3 Isolator deformations in X and Y-directions under the circular trajectory

unidirectional loading is insignificant in bidirectional loading. Although the corner of the bearings is subjected to full contact under the maximum radial strain, as shown in Fig. 6.2b and 6.2e, it does not increase the contact area due to the square or rectangular geometry of the bearings. Figure 6.2f shows that the STRP isolator sustains residual deformation after complete unloading, and Fig.6.3f shows that isolators experience deformation in the *Y*-direction even external strain ε_y is zero. Therefore, the bidirectional components are coupled, and bidirectional interaction influences the orthogonal components of elastomer strain.

6.3.2 Hysteresis Behaviour

Figures 6.4-6.7 show the restoring force of STRP-2/1 (square-shaped) and STRP-2/2 (strip-shaped) isolators subjected to the displacement trajectories shown in Fig. 6.1. In the plots, the combined result from individual unidirectional analyses in *X* and *Y*-components is also shown to compare the unidirectional analysis with the bidirectional counterpart. The restoring forces are comparable up to 50% radial shear, beyond which restoring force in bidirectional loading becomes more significant than the unidirectional loading, except for 250% radial shear. The interaction between the two horizontal force components is visible in terms of the increment of restoring force. The comparison indicates that the isolator displacement in one direction affects the restoring force in the other orthogonal direction even though the displacement in the orthogonal direction remains unchanged.

The hardening effect appearing in the uniaxial loading case becomes less significant in the bidirectional loading case, as shown in Figs. 6.4-6.7 since the restoring force contribution from the roll-over area is relatively high when the isolator is displaced along the principal axis. The hysteresis loops for unidirectional cyclic loading are narrower than those for the bidirectional horizontal displacement. It is possibly due to the strain rate dependency of the rubber and velocity dependency of the contact friction force. The strain rate and velocity of the isolator are constant in the linear trajectory while gradually changing from the maximum to zero and vice-versa in the other trajectories. Besides, the interaction between the friction force components in the bidirectional loading case affects the hysteresis force. In both loading cases, the hysteresis loops are stable and do not return to the shapes of a smaller amplitude except for the 250% shear level in bidirectional loading. Therefore, the hysteretic force at each strain level depends on the experienced elastomer strain. The characteristic strength defined by the restoring force intercept at zero strain increases with the imposed shear level, and also the bidirectional interaction increases the characteristic strength.

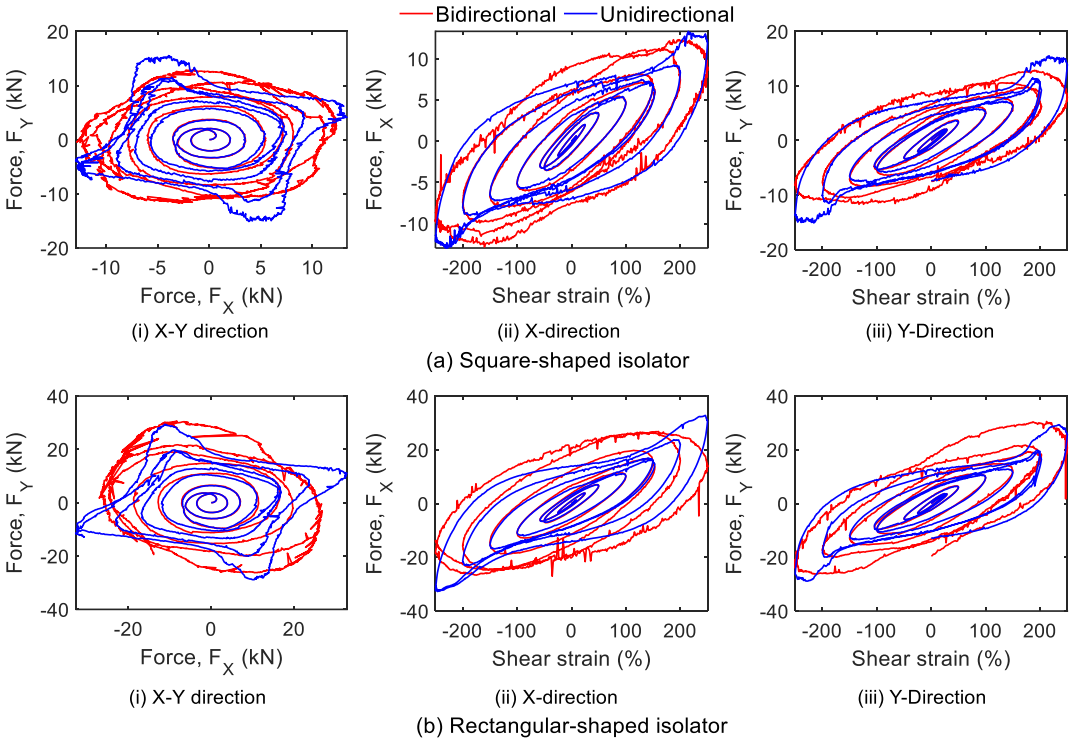

Figure 6.4 Hysteresis loops: loading with a circular trajectory of horizontal displacement.

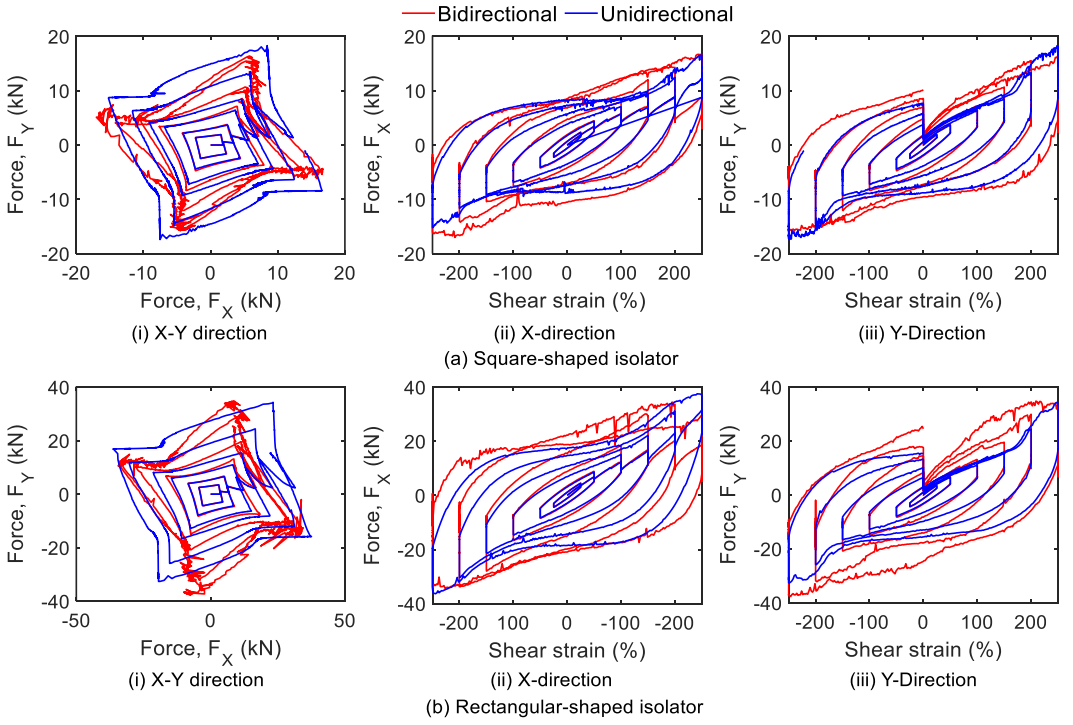

Figure 6.5 Hysteresis loops: loading with a square trajectory of horizontal displacement.

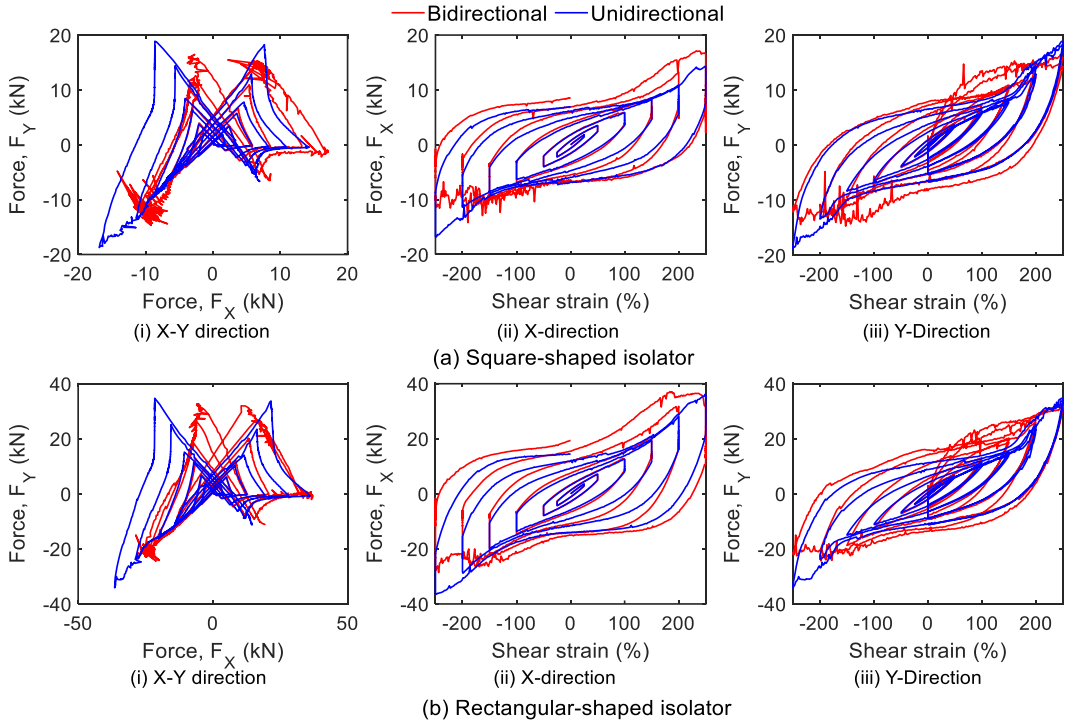

Figure 6.6 Hysteresis loops: loading with hourglass trajectory of horizontal displacement.

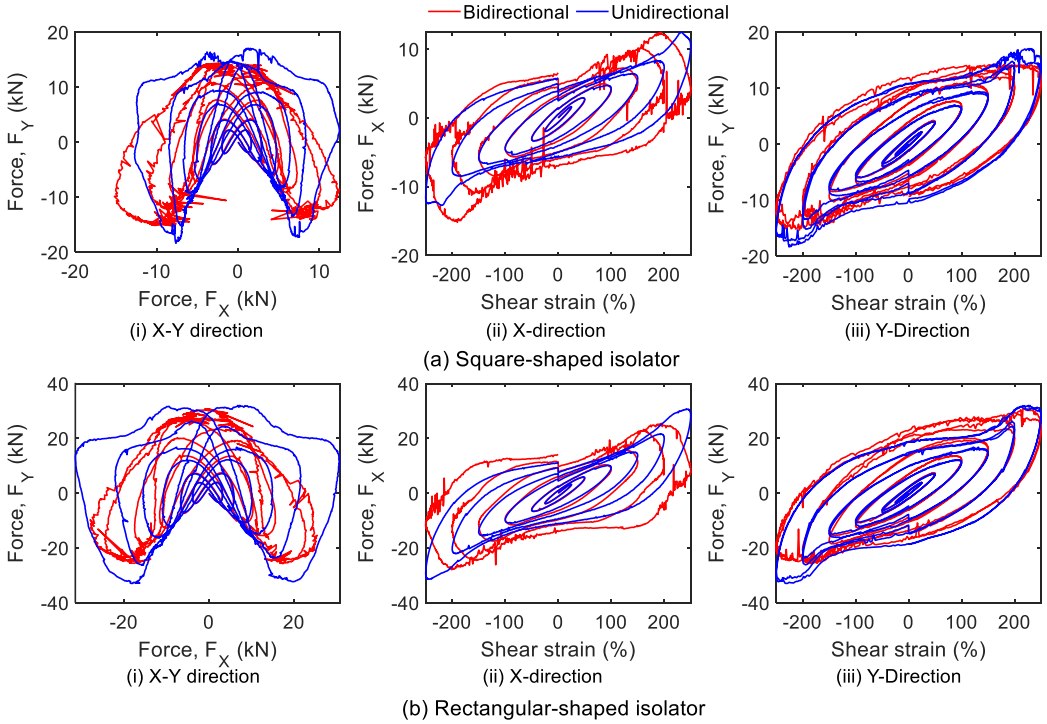

Figure 6.7 Hysteresis loops: loading with the 8-shaped trajectory of horizontal displacement.

Figure 6.8 shows the hysteretic response of the strip-shaped STRP isolators in the *X*-direction (longitudinal direction along the longer side in plan) and *Y*-direction (width direction along the shorter side) under the unidirectional linear displacement. The magnitude of the restoring force in the *X*-direction and that in the *Y*-direction of strip-shaped STRP isolators are different because of their anisotropy. Even in the square-shaped STRP-2/1 isolator, the restoring force in the *Y*-direction is higher than in the *X*-direction because of steel cord orientation. In strip-shaped isolators (STRP-2/2, 2/4, and 2/10), the restoring force in the *X*-direction is higher than that in the *Y*-direction, and the difference between the *X* and *Y* components of restoring force increases with an increase of the length-to-width ratio. It confirms that the STRP isolators are anisotropic. The previous study (Zisan and Igarashi, 2021) indicates that the anisotropic behavior causes the average stiffness to increase by 37~58% in the longitudinal direction and decreases by 12% in the transverse direction, as the length-to-width ratio increases from 1 to 10. Besides, the horizontal stiffness of the strip-shaped isolator in the longitudinal direction is 1.15~1.40 times higher than that in the transverse

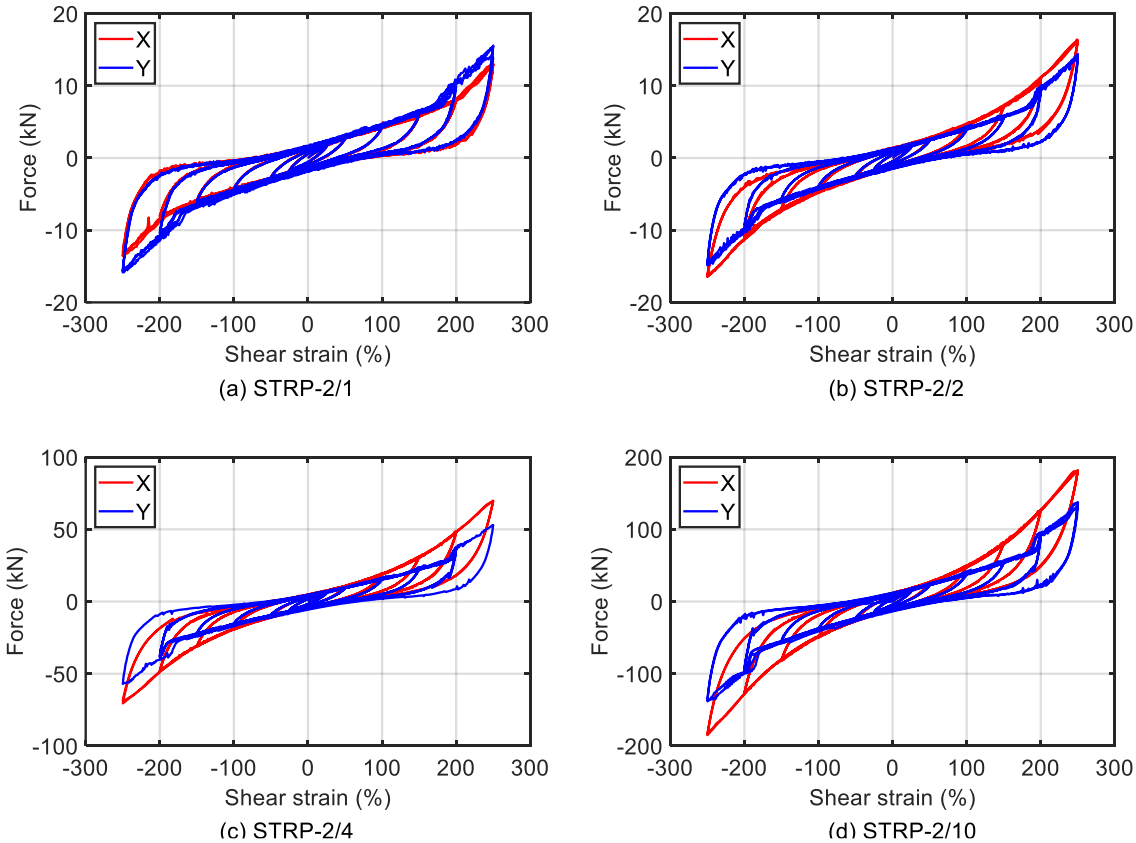

Figure 6.8 Hysteresis loops for the linear trajectory of horizontal displacement

direction. The orientation of steel cords and the length-to-width ratio is considered for such anisotropic behavior.

Figures 6.7-6.8 clearly show the influence of the characteristics of displacement trajectories on the shape of the hysteresis loop and its magnitude. The hysteresis loops under circular and 8-shaped displacement trajectories, as shown in Figs. 6.4 and 6.7 are rounder than that of the hysteresis loop for square and hourglass trajectories, as shown in Figs. 6.5 and 6.6. For hourglass and 8-shape displacement trajectories, the *Y*-component of restoring force is more significant than that of the *X*-component due to the high frequency and high velocity of the *Y*-component. Figure 6.8 shows that the hysteretic loop exhibits higher hardening in the linear type cyclic displacement than that of the *X* or *Y*-component of bidirectional trajectories under unidirectional loading case.

6.3.3 Horizontal Stiffness

Figure 6.9 shows horizontal stiffness in square and strip-shaped isolators at different uni- and bi-directional horizontal displacement levels. In figures, the captions *SQ* and *REC* stand for square and strip-shaped isolators, respectively, *BX*, *BY*, and *UX*, *UY*, indicate the bidirectional and unidirectional displacement case, respectively, in *X*, *Y*-directions. It shows that the bidirectional loading effect on the horizontal stiffness is insignificant for displacement below 50% shear and significant between 100% and 200% shear. Horizontal stiffness in the bidirectional loading is higher than that of the unidirectional loading except for the 250% shear level. Stiffness decreases with an increase of lateral shear except for unidirectional loading, in which stiffness increases for shear displacement exceeding 150%. Horizontal stiffness for linear displacement trajectory shows the same trend (Zisan and Igarashi, 2020). In the unidirectional loading case, stiffness increases for a displacement exceeding 150% shear due to the roll-over deformation and hardening effect. Therefore, designing of base-isolated structure based on uniaxial hysteretic parameters overestimate the structural responses. The square-shaped isolator is stiffer in the *Y*-direction than that in the X-direction due to steel-cords orientation, whereas a high length of strip-shaped isolator makes it more restrained in the longitudinal direction (*X*-direction).

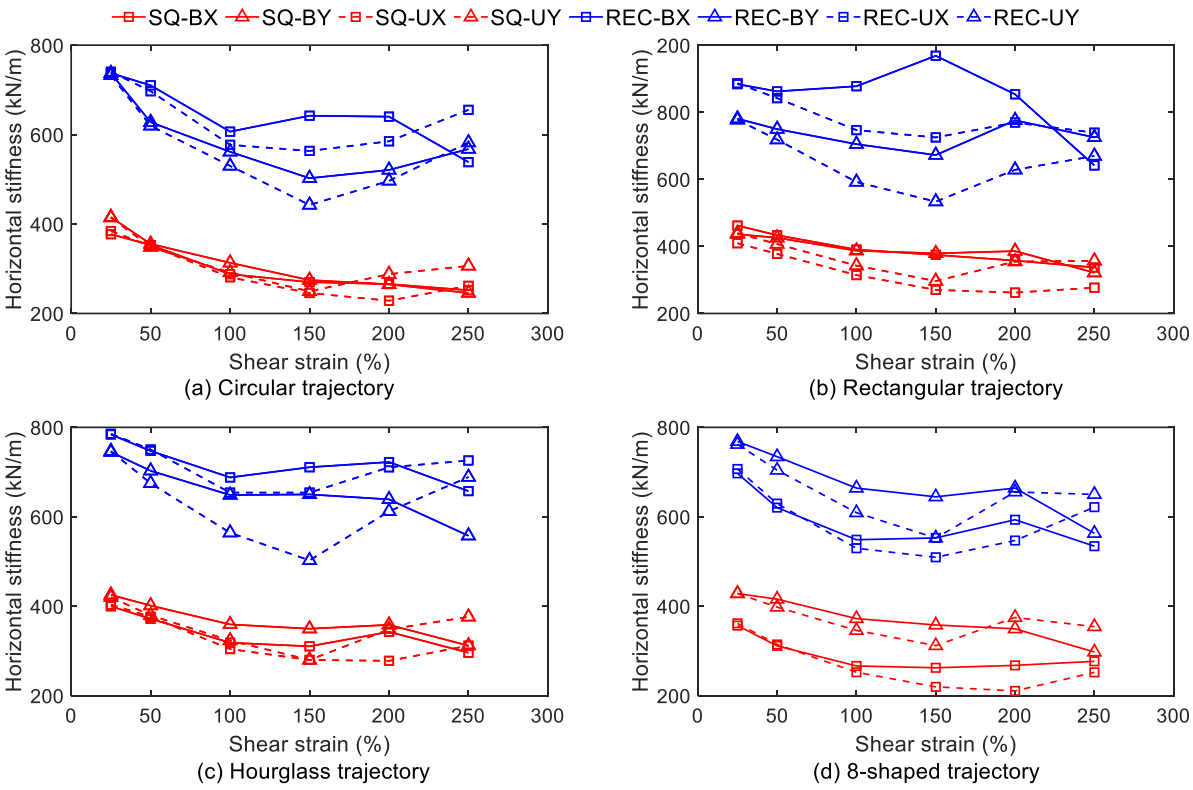

Figure 6.9 Horizontal stiffness in square and strip-shaped isolators

Figure 6.9 is reorganized into Fig.6.10 to study the effect of inputs displacement characteristics on the stiffness. The captions "*C*," "*S*," "*H*," and "*8*" stand for circular, square, hourglass, and 8-shaped trajectories, respectively. It indicates that stiffness at the same displacement level is varied among the displacement trajectories. For example, Fig.6.10a shows that the stiffness at 150% shear under the unidirectional displacement of *X*-component of 8-shaped, circular, square, and hourglass trajectories is 220, 245, 270, and 280 kN/m, respectively. The same stiffness in the *Y*-direction is 331, 250, 296, and 280 kN/m. Figure 6.10b shows a similar trend in the bidirectional loading case. The strip-shaped isolator also offers different stiffness at the same magnitude of the input displacement in different trajectories. These differences are substantial in the longitudinal direction, as shown in Fig. 6.10c and 6.10d. The current design code AASHTO-LRFD, ASCE/SEI 7-10, suggests the minimum horizontal stiffness found from the cyclic loading test to be used for design purposes. But no specification is given regarding the nature of the cyclic load. Therefore, the horizontal stiffness should be defined for different displacement trajectories for a practical design.

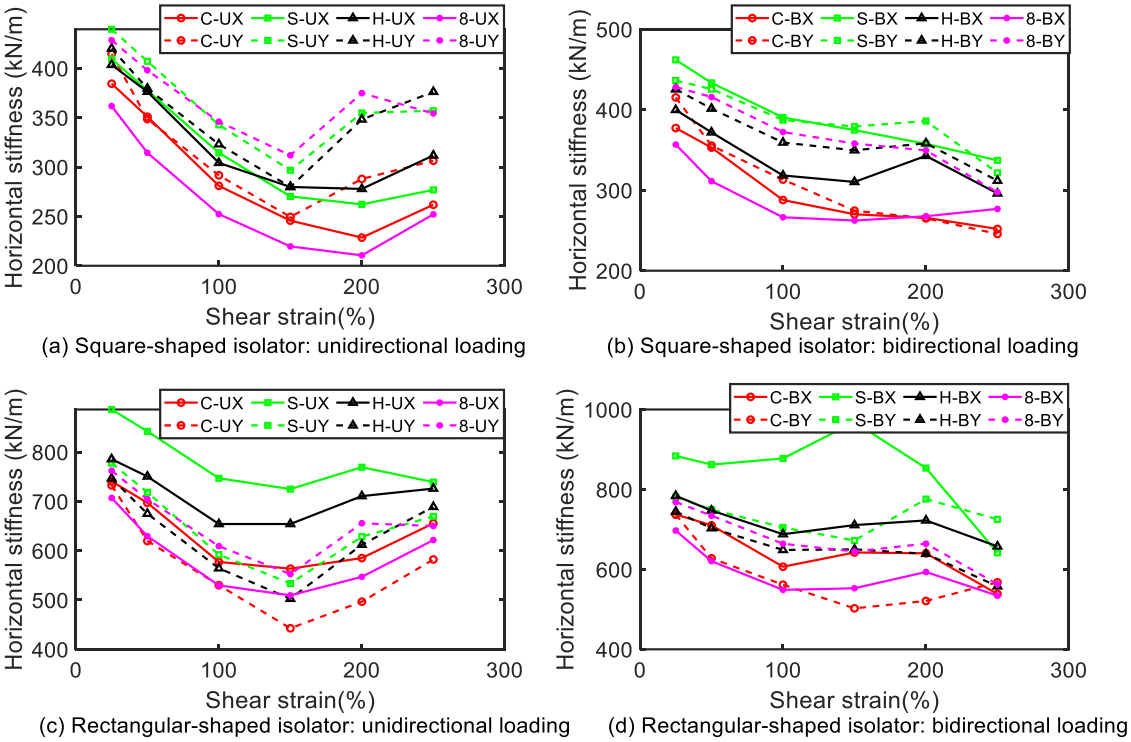

Figure 6.10 Influence of displacement characteristics on horizontal stiffness

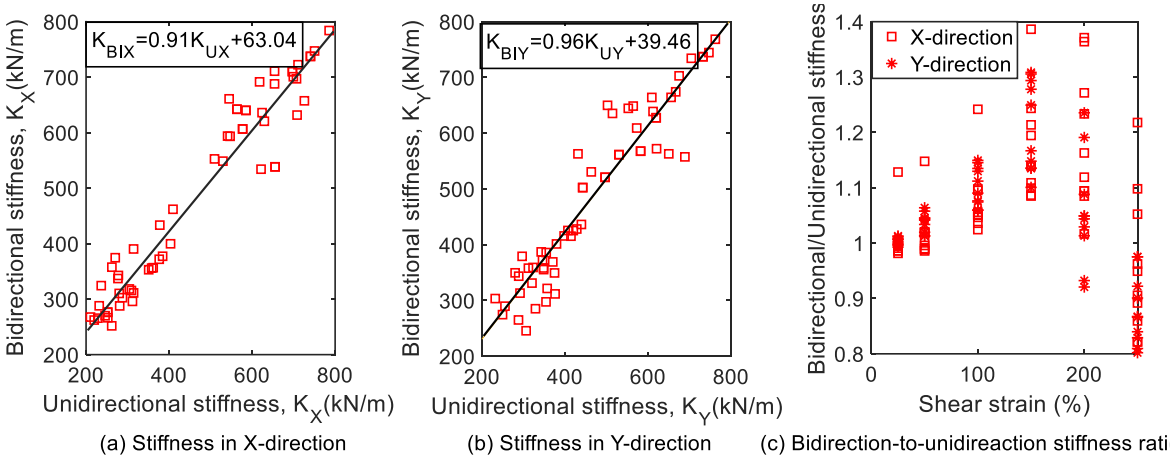

Figure 6.11 Relation between stiffness under unidirectional and bidirectional loading

Figure 6.11 provides a relation between uni- and bi-directional horizontal stiffness in *X* and *Y*-directions obtained using linear regression. These relations are helpful in calculating the stiffness and period in bidirectional loading from unidirectional loading test data in the preliminary design stage. The upper and lower bound stiffness in the bidirectional loading is 1.25 and 0.8 times that of the stiffness obtained from

the relations shown in the figures. The lower bound of the stiffness corresponds to 250% shear displacement, as shown in Fig. 6.11c. It indicates that stiffness in bidirectional loading increases until 200% shear deformation, which can be about 1.40 times of unidirectional horizontal stiffness.

6.3.4 Effective Damping Ratio

Figure 6.12 shows that the effective damping ratios increase with an increase of horizontal displacements except for the unidirectional loading case where it slightly decreases for displacement exceeding 150% shear. The damping ratios in bidirectional loading are higher than that of unidirectional loading. The minimum damping ratio is around 10% at 25% shear displacement, and the maximum is approximately 35% at 200% shear. High damping is expected from the flexibility and internal friction within the steel cord and the elastomer's inherent properties. A change in the strain rate or velocity influences the interaction between two

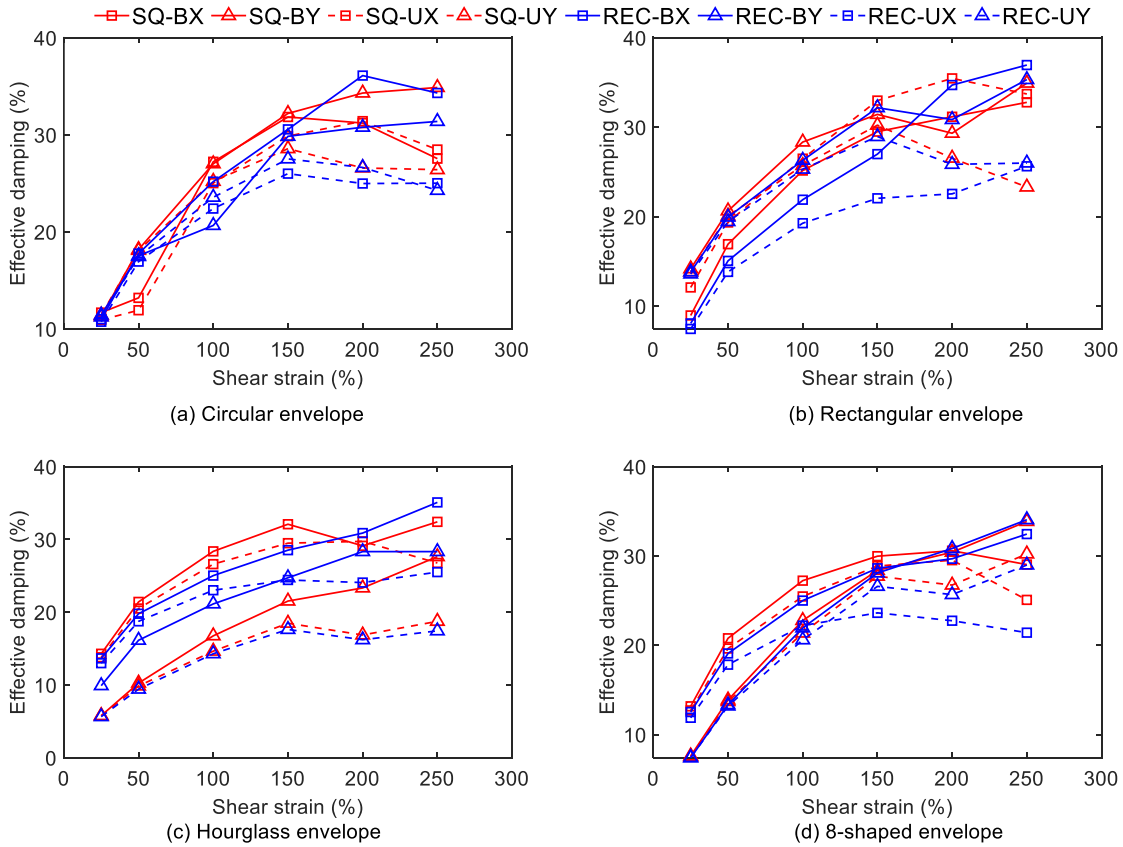

Figure 6.12 Effective damping ratio in square and strip-shaped isolators

components of the contact friction that contributes to the damping of the system. The damping ratios are about 10%~16% in the linear displacement trajectory (Zisan and Igarashi, 2021). In uni and bi-directional displacement components of the circular, square, hourglass, and 8-shaped trajectories, damping ratios are higher than those of the unidirectional linear trajectory.

Figure 6.13 shows a relation for effective damping ratios between uni- and bi-directional loading. The upper and lower bound of the effective damping ratios in the bidirectional loading is 1.35 and 0.85 times, respectively, that of the unidirectional loading. Figure 6.13c shows the quotient of the bidirectional-to-unidirectional effective damping ratio. It shows that the damping ratio in the bidirectional loading is higher than that of the unidirectional loading. It is about 10~20% until 150% shear strain and can be more than 60% for a displacement exceeding 150% shear.

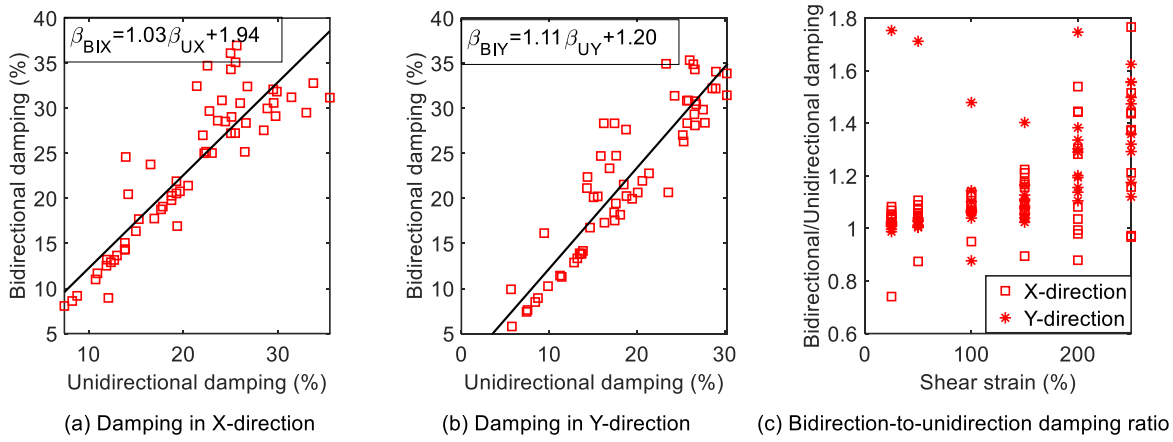

Figure 6.13 Relation between damping due to unidirectional and bidirectional loadings

6.4 Conclusions

This study focused on the lateral load performance and the force-displacement relationship of unbonded STRP isolators for different trajectories under uni- and bi-directional horizontal displacements. In addition, this study aims to assess the effect of bidirectional loading on the performance of an unbonded STRP isolator. Based on the FE analyses and analytical results, the findings are summarized as follows:

- The effect of bidirectional loading on the lateral performance and force-displacement relation is significant for displacement exceeding 50% shear. The roll-over deformation and hardening are more pronounced in the unidirectional loading than that of the bidirectional loading. In bidirectional loading,

isolator displacement at a fixed direction affects the restoring force and elastomer strain to its orthogonal direction.

- The shape of the hysteresis loop and its magnitude depending on the characteristics of the input displacement path. Existing codes do not specify the nature of cyclic displacement. Therefore, the hysteretic parameter must be evaluated under the different displacement paths for an efficient isolation system design.
- Both horizontal stiffness and effective damping ratio in the bidirectional loading are higher than those of the unidirectional loading, indicating that designing a base-isolated structure based on the hysteretic parameter that is determined from the unidirectional loading test overestimates the structural response. The horizontal stiffness increases until 200% shear deformation and becomes about 1.40 times that of the unidirectional stiffness. In bidirectional loading, the minimum effective damping ratio is about 10% at 25% shear displacement, reaching nearly 35% at 200% shear. In linear and unidirectional displacement, the effective damping ratio is 10%~16%. Within 150% shear deformation, the damping ratio is 10~20% higher than that of the unidirectional loading case, and it is higher than 60% at an extensive displacement range.
- A relationship for bidirectional stiffness and effective damping ratio applicable for preliminary design is proposed. For any stiffness or damping from the unidirectional loading test, the upper and lower value of bidirectional stiffness is 1.25 and 0.8 times of stiffness calculated using these relations. The lower bound stiffness stands for 250% shear. Similarly, effective damping is 1.35 and 0.85 times.

References

AASHTO-LRFD (2014). LRFD Bridge Design Specifications. 7th Ed., Washington, D. C.

ASCE/SEI 7-10 (2010). Minimum Design Loads for Buildings and Other Structures, ASCE, 1801 Alexander Bell Drive, Reston, Virginia.

Cardone D. and Flora A. (2016). An Alternative Approach for the Seismic Rehabilitation of Existing RC Buildings Using Seismic Isolation. *Earthquake Engineering & Structural Dynamics*, **45**, pp. 91-111.

Chimamphant S. and Kasai K. (2016). Comparative Response and Performance of BaseIsolated and FixedBase Structures. *Earthquake Engineering & Structural Dynamics*, **45**, pp. 5-27.

Eurocode 8 (2004). Design of structures for earthquake resistance. BS EN 1998-1:2004.

Grant D. N., Fenves G. L. and Whittaker A. S. (2008). Bidirectional Modelling of High-Damping Rubber Bearings, Journal of Earthquake Engineering, 8:S1, pp. 161-185.

Huang Y. N., Whittaker A. S., Kennedy R. P., and Mayes R. L. (2013). Response of Base-Isolated Nuclear Structures for Design and Beyond-Design Basis Earthquake Shaking. *Earthquake Engineering & Structural Dynamics*, **42**, pp. 339-356.

Huang W.-H., Fenves, G. L., Whittaker A. S., and Mahin S. A. (2000). Characterization of seismic isolation bearings for bridges from bi-directional testing, 12 WCEE, Auckland, New Zeland, Sunday 30 January - Friday 4 February 2000.

Mishra H. K. (2012). Experimental and Analytical Studies on Scrap Tire Rubber Pads for Application to Seismic Isolation of Structures. Ph.D. Thesis, Kyoto University, Japan.

Mishra H. K., Igarashi A., and Matsushima H. (2013a). Finite element analysis and experimental verification of the scrap tire rubber pad isolator. Bulletin Earthquake Engineering, 11(2), pp. 687-707.

Mishra H. K. and Igarashi A. (2013b). Lateral deformation capacity and stability of layer-bonded scrap tire rubber pad isolators under combined compressive and shear loading. Structural Engineering and Mechanics, 48(4), pp. 479-500.

Mishra H. K., Igarashi A., Ji D., and Matsushima H. (2014). Pseudo-Dynamic Testing for Seismic Performance Assessment of Buildings with Seismic Isolation System Using Scrap Tire Rubber Pad Isolators. Journal of Civil Engineering and Architecture, 8(1), pp. 73-88.

Turer A. and Özden B. (2007). Seismic base isolation using low-cost scrap tire pads (STP). Materials and Structures, 41(5), pp. 891-908.

Zisan M. B. and Iarashi A. (2020). Lateral Load Performance Evaluation of Unbonded Strip-STRP Base Isolator, 17th World Conference on Earthquake Engineering (17WCEE), September 13th to 18th, 2020, Sendai, Japan.

Zisan M. B. and Iarashi A. (2021). Lateral Load Performance and Seismic Demand of Unbonded STRP Base Isolator, Earthquake Engineering and Engineering Vibration (Accepted).

Chapter 7

Hysteresis Force Model for Unbonded Application of Scrap Tire Rubber Pad Isolator

This chapter focused on the hysteresis force model for the unbonded application of STRP isolators. A simplified force model is proposed for dynamic-time history analysis and structural design purposes of the unbonded STRP isolator. Calibration of model parameters and validation of the proposed model is carried out using FE analysis results.

7.1 Introduction

The STRP isolator, referring to the seismic isolator made with an automobile scrap tire pad, is expected to functions similarly to steel-reinforced elastomeric isolators or fiber-reinforced elastomeric isolators. It provides an effective damping ratio of 10~22% and a vertical-to-horizontal stiffness ratio of 450~600 (Mishra, 2012), exceeding 150, which is indispensable for isolation material (Eurocode 8). The shear modulus of tire rubber is around 1.0 MPa (Mishra et al., 2013a; Turer and Özden, 2007) within the range of natural rubber, 0.55~1.20 MPa specified by AASHTO-LRFD for seismic isolator. The previous studies (Mishra et al., 2013a, 2013b) reported the damping and stiffness of unbonded STRP isolators in addition to a pseudo-dynamic test on a 1/3rd scale unbonded STRP isolator (Mishra et al., 2014). The beneficiary aspects of the STRP isolator are that it can be utilized without mechanical fastening with the structural elements that bypass a large amount of tension within the elastomer and improve the efficiency of the isolation system through a roll-over deformation. This feature provides a unique force-displacement relation of the unbonded STRP isolator different from that of the conventional isolator.

Although the existing design specifications provide well-defined methodologies and design principles for conventional elastomeric isolators (AASHTO-LRFD, ASCE-SEI-7/10, EURO CODE), unbonded implementation of base isolators is yet to be explored in detail to be used in practice. Because of friction-

dependent and unbonded contact conditions, the existing design specifications are incompatible for the application of unbonded STRP isolators. Some researchers proposed horizontal force-displacement relationships of unbonded isolators based on the hyperelasticity of rubber material. Peng et al. (2007) derived a relationship assuming that the rubber is linear elastic. Konstantinidis et al. (2008) suggested a lower bound relation based on the assumption that the isolator's roll-over part is stress-free and has no resistance to the lateral load. Van Engelen et al. (2015) considered combined bending and shear within the roll-over, whereas pure shear acts within the central elastomer. Toopchi-Nezhad (2014) proposed upper and lower bound values of the effective area of an unbonded isolator that has resistance to horizontal load. Zisan and Igarashi (2020) proposed an analytical solution for the horizontal stiffness of unbonded STRP isolators for a unidirectional lateral load. These studies are suitable for unidirectional horizontal displacement only and considered the hyper-elasticity of rubber material without rate dependency. Besides, these models are not valuable for the computation of the hysteresis behavior under unbonded conditions.

The existing design codes offer a bilinear force-displacement model for conventional isolators, and model parameters are evaluated from horizontal shear tests (Naeim and Kelly, 1999). Toopchi-Nezhad et al. (2009) used the bilinear model to analyze stable-unbonded FREIs. This evaluation is reasonably appropriate for moderate lateral displacements because unbonded isolators exhibit significant softening behavior at large displacement, which needs a trilinear model suggested by De Raaf et al. (2011). Manzoori and Toopchi-Nezhad (2017) proposed an extended version of the Bouc-Wen model for the nonlinear hysteretic response of stable-unbonded FREIs using fifth-order polynomial. This model considered the deformation of the isolator in one direction only. Since the deformation and friction of an unbonded isolator in bidirectional horizontal load are different from those of unidirectional loads, it is inevitable to include the bidirectional interacting in the hysteresis force model.

In this chapter, the approximated representation of the hysteretic behavior of unbonded STRP isolators by a modified version of the Park-Wen model is proposed. A variant of the modified Park-Wen model has originally been proposed to express the bidirectional behavior of high-damping rubber isolators in past research (Dang et al., 2016). In this study, the modified Park-Wen model is extended for the STRP isolator so that (1) the hysteretic component is further modified to achieve a superior representation of the STRP isolator under the unbonded condition (2) the elastic component accommodates anisotropy of the STRP isolator in terms of stiffness when strip-shaped geometry is utilized in the application.

7.2 Hysteresis Force Model

The Bouc-Wen hysteretic model is expressed by Eq. 7.1 and 7.2 are widely used in mechanical and structural engineering applications such as reinforced concrete and steel structures, magneto-rheological dampers, and seismic isolators (Sireteanu et al. 2010, Domaneschi 2012).

$$F = \alpha k u + (1-\alpha) k Z \tag{7.1}$$

$$\dot{Z} = A\dot{u} - \gamma|\dot{u}|Z|Z|^{n-1} - \beta\dot{u}|Z|^{n} \tag{7.2}$$

where F is the restoring force, k is the initial stiffness, α is the post-yield stiffness ratio, u is the displacement, and Z is the dimensionless hysteretic component variable that depends on the time history of u provided as the input. The parameters A, β, γ, and n control the size and shape of the hysteresis loop. The versatility of the Bouc-Wen model is that the hardening or softening of the hysteretic behavior can be represented with a smoothly varying or nearly bilinear relationship. Later, Park et al. (1986) extended the Bouc-Wen model to express the bidirectional hysteretic force-displacement relationship, including the bidirectional components' coupling effect. The Park-Wen model for the bidirectional horizontal restoring force represented by the x and y components, F_x and F_y, is given by Eq.7.3.

$$\begin{bmatrix} F_x \\ F_y \end{bmatrix} = \alpha k \begin{bmatrix} u_x \\ u_y \end{bmatrix} + (1-\alpha) k \begin{bmatrix} Z_x \\ Z_y \end{bmatrix} \tag{7.3}$$

$$\dot{Z}_x = A\dot{u}_x - \beta|\dot{u}_x Z_x|Z_x - \gamma\dot{u}_x Z_x^{\,2} - \beta\left|\dot{u}_y Z_y\right|Z_x - \gamma\dot{u}_y Z_x Z_y \tag{7.4}$$

$$\dot{Z}_y = A\dot{u}_y - \beta\left|\dot{u}_y Z_y\right|Z_y - \gamma\dot{u}_y Z_y^{\,2} - \beta|\dot{u}_x Z_x|Z_y - \gamma\dot{u}_x Z_x Z_y \tag{7.5}$$

where Z_x, Z_y as given by Eqs. 7.4 and 7.5 are the hysteretic component variables, u_x, u_y are the displacements, and the subscripts x and y denote that the variable is for x and y components, respectively. The Park-Wen model is relatively simple and has been utilized to analyze elastomeric isolators' hysteretic behavior (Özdemir, 2010; Zhou et al., 2017; Dang et al., 2016). A shortcoming is an inadequacy in describing the interaction between the elastomer strain components when the isolator experiences displacement in one direction and is fixed in another perpendicular direction (Dang et al., 2016). It is also pointed out that the

Park-Wen model cannot represent the hardening effect (Abe *et* al., 2004a; Grant et al., 2008; Dang et al., 2016). Grant et al. (2008) and Dang et al. (2016) considered the strain dependency of hysteresis force in a high damping rubber bearing by introducing a quadratic function of the shear strain ε as the amplitude of the hysteretic component in the restoring force. The model proposed by Dang et al. (2016) is referred to as the Modified Park-Wen model. Figure 7.1 shows the physical interpretation of strain dependency of the hysteretic component of the original Park-Wen and Modified Park-Wen models.

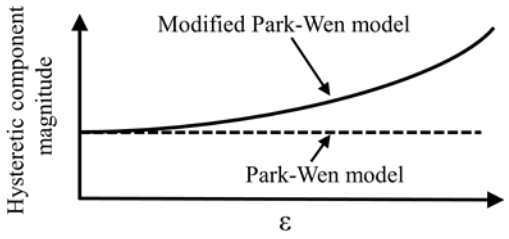

Figure 7.1 Hysteretic force component under unidirectional loading (Dang et al., 2016)

An unbonded isolator shows a hysteretic behavior that can be reasonably approximated by a bilinear model for moderate lateral displacements (Toopchi-Nezhad et al., 2009), while it involves softening of the force-displacement curve at large displacements caused by roll-over deformation (De Raaf et al., 2011). Manzoori and Toopchi-Nezhad (2016) considered a fifth-order trinomial to represent the softening of the load-displacement curve of unbonded FREIs. Observation of Fig.6.8 shown in Chapter 6 reveals that a fourth or higher degree polynomial is suitable for an appropriate representation of softening of the backbone curve of unbonded STRP isolators.

In the present study, strain dependence of the hysteretic component is implemented to the Park-Wen model using a fourth-order binomial. Furthermore, the anisotropic nature of the strip-shaped isolator is included in the elastic component of the Park-Wen model. The bidirectional hysteretic displacement-force model for strip-shaped STRP isolators obtained by these two types of modifications is expressed by Eq. 7.6.

$$\begin{bmatrix} F_x \\ F_y \end{bmatrix} = \alpha \begin{bmatrix} ck_0 & 0 \\ 0 & k_0 \end{bmatrix} \begin{bmatrix} u_x \\ u_y \end{bmatrix} + (b_1 + b_2|\varepsilon|^4)(1-\alpha) \begin{bmatrix} ck_0 & 0 \\ 0 & k_0 \end{bmatrix} \begin{bmatrix} Z_x \\ Z_y \end{bmatrix} \tag{7.6}$$

where

$$k_0 = \frac{G_e A_0}{t_r} \tag{7.7}$$

$$|\varepsilon| = \frac{\sqrt{u_x{}^2 + u_y{}^2}}{t_r} \tag{7.8}$$

in which k_0 is the horizontal stiffness defined by Eq. 5.7, G_e is the shear modulus of elastomer, A_0 is the isolator's plan area, t_r is the total rubber thickness, b_1 and b_2 are constants to specify the strain-dependence of the hysteretic component amplitude illustrated in Fig. 7.1, and c is a parameter to express the stiffness difference along with the two orthogonal directions due to anisotropy of the strip-shaped isolators. The stiffness difference increases with the level of shear displacement and the length-to-width ratio. The radial component of elastomer strain ε is given by Eq. 7.8.

The dimensionless intercept of hysteretic force at zero strain in x and y directions is $b_1(1-\alpha)ck_0$ and $b_1(1-\alpha)k_0$, respectively. It is proposed to use Eq. 7.9 to approximate the parameter b_1 accounting for the length-to-width ratio.

$$b_1 = \frac{1.65}{l/w} \tag{7.9}$$

7.3 Model Parameter Calibration

The proposed model of the force-displacement relation of unbonded isolators, referred to as the MPW model, includes the parameters A, α, k_0, β, γ, c, b_1, and b_2. The stiffness k_0 is found from Eq. 7.7. The post-to-yield stiffness ratio α is assumed to be 0.08 based on the bilinear force-displacement relation (Mishra, 2012). The restoring force intercept is identified as 1.65, 3.0, 5.80, and 12.5 kN for STRP-2/1, 2/2, 2/4, and 2/10, respectively, as indicated by Fig. 6.8 in Chapter 6. The parameter b_1 is specified by Eq. 7.9, which is found to be the acceptable approximation of these restoring force intercept values. The parameter b_2 controls the shape of the hysteresis loop due to hardening and roll-over deformation, and a value equal to 0.01 shows the best fitting. It is assumed that $\beta=\gamma$ and these model parameters are calibrated using the linear regression procedure to achieve the best approximation of the force-displacement relation found from the FE analysis result. The regression coefficient R, defined by Eq. 7.10 indicates the contribution rate of the proposed model.

$$R = 1 - \frac{\sum_{i=1}^{N}\left(F_{an,i} - F_{fe,i}\right)^2}{\sum_{i=1}^{N}\left(F_{fe,i} - \bar{F}_{fe}\right)^2} \tag{7.10}$$

where $F_{an,i}$ and $F_{fe,i}$ indicate the restoring force in the model and that from FE analysis, respectively, at the loading step i corresponding to the same shear strain, $\bar{F}_{fe}$ is the average restoring force obtained from the FE analysis, and N is the number of the data. The parameters listed in Table 7.1 are the result of calibration based on the force-displacement relation of the square-shaped STRP-2/1 case obtained from linearly varied cyclic displacement. With the use of these parameters, matching of the proposed model with the FE analysis result was found to be excellent since the value of R was more than 0.98 in the best case. These parameters are employed to analyze unbonded isolators under uni- and bi-directional horizontal displacements.

Table 7.1 Model parameters for unbonded STRP isolator

Parameter	A	α	k_0	β	γ	b_1	b_2	c
value	1.0	0.08	G_eA_0/t_r	0.0009	0.0009	$1.65/(l/w)$	0.01	1.15

7.4 Evaluation of MPW model

7.4.1 Unidirectional Loading Case

Figure 7.2 compares the hysteresis curves for the STRP isolator between the MPW and the FE analysis under linearly varied unidirectional cyclic displacement. Figure 7.3 shows the same comparison under unidirectional components of the bidirectional displacement trajectories given in Fig. 6.1 in Chapter 6. In the plot, Figs. 7.2a-7.2d indicate the hysteretic restoring force in the longitudinal loading cases (displacement, u_x) and Figs. 7.2e-7.2f shows the same in the transverse loading cases (displacement, u_y). Each isolator is subjected to 5.0 MPa vertical compression and horizontal displacement up to 250% shear strain. The model parameters listed in Table 7.1 are used for each isolator model. The comparison of the hysteresis curves indicates that the proposed MPW model for STRP isolators shows an excellent agreement with the FE analysis results. The MPW model well expresses the maximum restoring force at each displacement level and inflation of hysteresis loop inflation. Furthermore, the model also represents the hardening behavior and the roll-over effect in the large displacement range. Tables 7.2 and 7.3 show the values of the contribution rate R for the linear type cyclic unidirectional loading cases and the other four displacement trajectories, respectively. It shows that the contribution rates range between 0.900 and 0.996, indicating good accuracy of the proposed model in reproducibility of restoring force. The restoring force estimated by the proposed model is sufficiently lower than the FE analysis result in the square trajectory (Fig. 7.3b) and the X-component of the hourglass trajectory (Fig. 7.3c). In these cases, each cycle of the

input displacement consists of zero or a constant displacement followed by a linearly varied displacement of an equal period. When the STRP isolator is subjected to zero or constant loads for an extended period, the friction force and the relaxation behavior of the isolator are assumed to be recovered. This is why the force-displacement relationship found from the FE analysis result is higher than that of the MPW model. The MPW model does not consider these factors.

Table 7.2 Contribution rate R for different strip-STRP isolator under unidirectional loading

STRP-	2/1*X*	2/1*Y*	2/2*X*	2/2*Y*	2/4*X*	2/4*Y*	2/10*X*	2/10*Y*
R-value	0.991	0.989	0.989	0.989	0.992	0.996	0.984	0.986

Table 7.3 Contribution rate R for the different trajectory of unidirectional loading

		Square-shaped isolator: 72×72×24				Strip-shaped isolator: 144×72×24			
		Circular	Square	Hourglass	8-shaped	Circular	Square	Hourglass	8-shaped
R-value	*X*-direction	0.969	0.926	0.928	0.954	0.974	0.926	0.936	0.977
	Y-direction	0.960	0.900	0.942	0.954	0.966	0.902	0.948	0.957

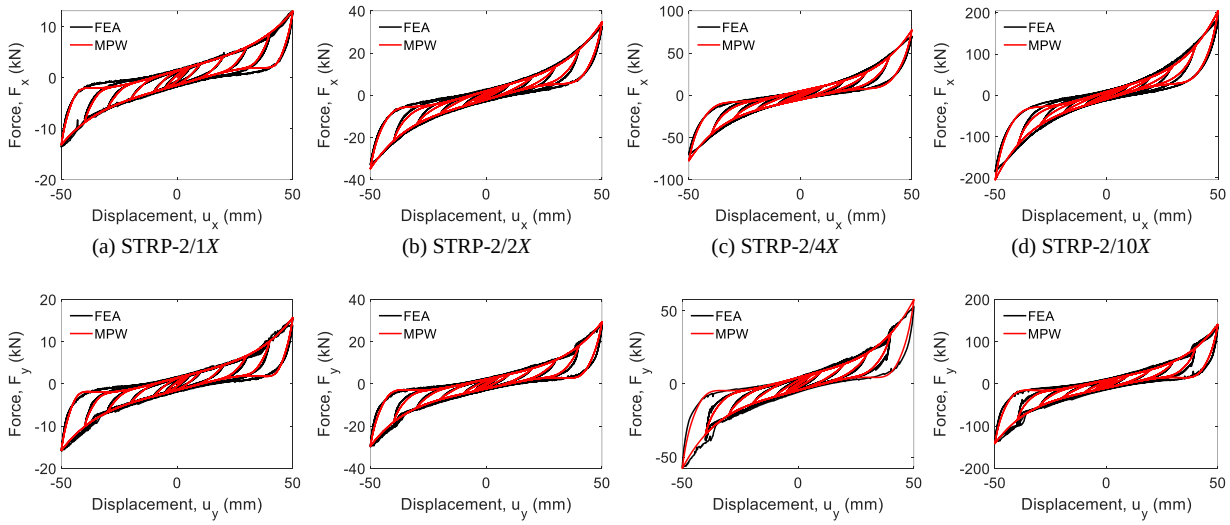

(a) STRP-2/1*X* (b) STRP-2/2*X* (c) STRP-2/4*X* (d) STRP-2/10*X*

(e) STRP-2/1*Y* (f) STRP-2/2*Y* (g) STRP-2/4*Y* (h) STRP-2/10*Y*

Figure 7.2 Hysteresis loop expressed by MPW model for strip-shaped STRP isolators under unidirectional loading.

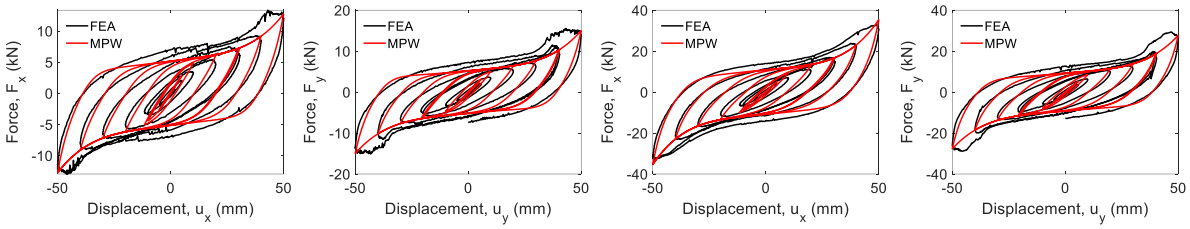

(i) STRP-2/1*X* (ii) STRP-2/1*Y* (iii) STRP-2/2*X* (iv) STRP-2/2*Y*

(a) Circular trajectory

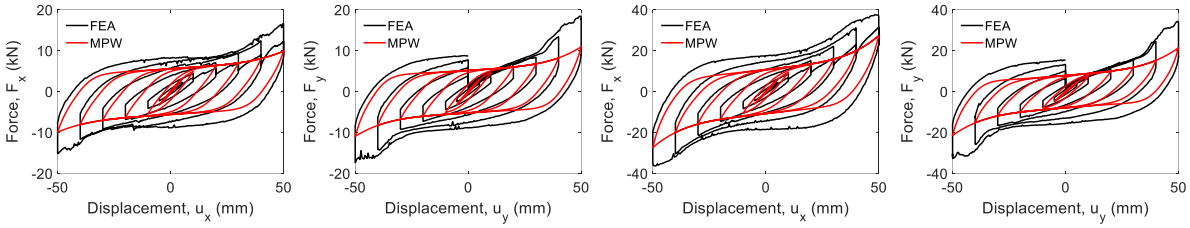

(i) STRP-2/1*X* (ii) STRP-2/1*Y* (iii) STRP-2/2*X* (iv) STRP-2/2*Y*

(b) Square trajectory

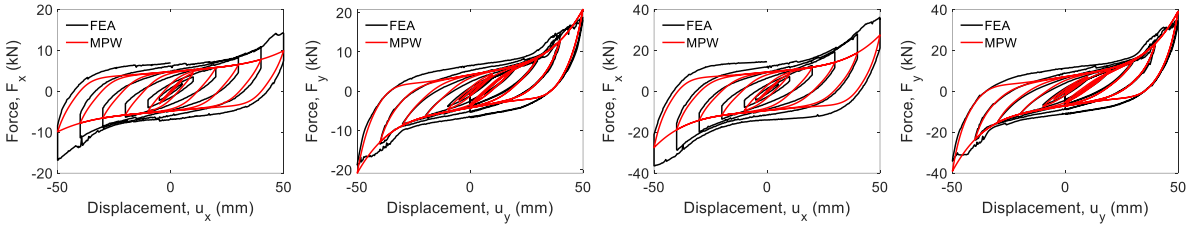

(i) STRP-2/1*X* (ii) STRP-2/1*Y* (iii) STRP-2/2*X* (iv) STRP-2/2*Y*

(c) Hourglass trajectory

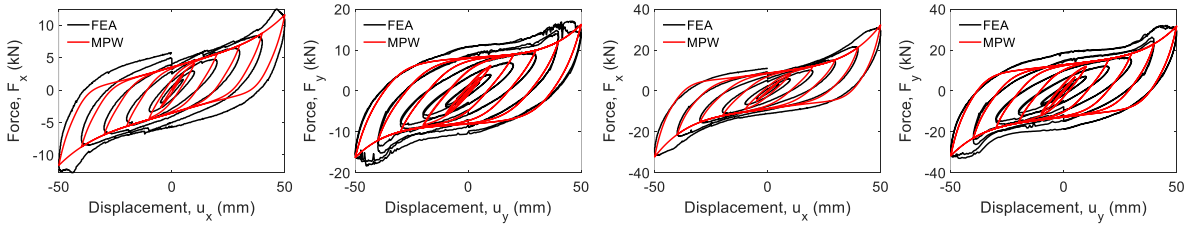

(i) STRP-2/1*X* (ii) STRP-2/1*Y* (iii) STRP-2/2*X* (iv) STRP-2/2*Y*

(d) 8-shaped trajectory

Figure 7.3 Hysteresis loop of square and strip-shaped isolators for different displacement trajectories

7.4.2 Bidirectional Loading Case

Figures 7.4-7.7 show the hysteresis curves for square (STRP-2/1) and strip-shaped (STRP-2/2) isolators subjected to simultaneous actions of *X* and *Y*-components of the bidirectional displacement (u_x and u_y) trajectories. It shows that the proposed MPW has excellent agreement with FE analysis results at each displacement trajectory. Both peak magnitude of restoring force at each level of lateral displacement and the hysteresis loop inflation is well predicted. In the case of 250% shear, the prediction of MPW sometimes disagreed with the FE analysis result because the FE model is highly distorting, particularly under square and hourglass trajectories. The contribution rate *R* for each loading trajectory as listed in Table 7.4 confirms that the MPW model is excellent in reproducing the bidirectional restoring force-displacement relationship of an unbonded isolator. In the circular trajectory case, the contribution rate is around 0.99 for both classes of isolators. For other trajectories, it is 0.96 to 0.98. Therefore, the MPW model with appropriate model parameters is expected as an efficient and effortless procedure in the dynamic analysis and practical design of the unbonded STRP isolator.

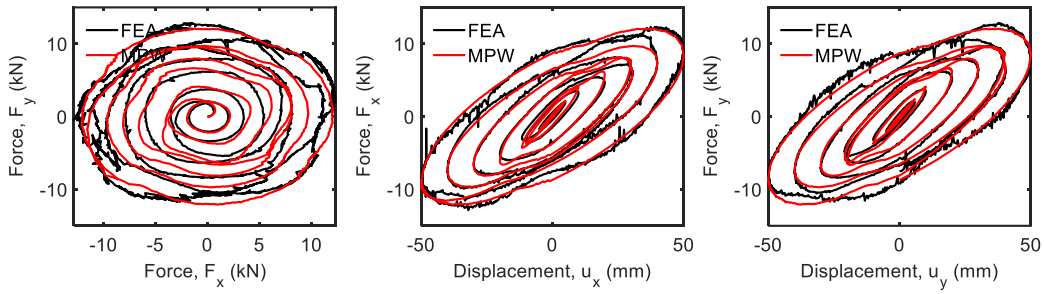

(i) Bidirectional components (ii) *X*-component (iii) *Y*-component

(a) Square-shaped isolator (STRP-2/1)

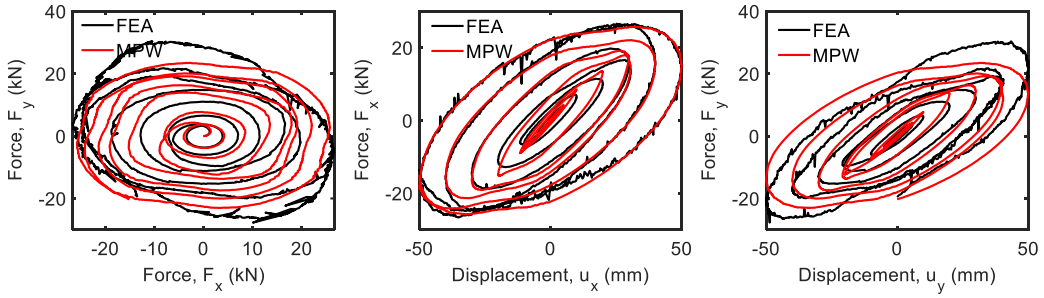

(i) Bidirectional components (ii) *X*-component (iii) *Y*-component

(b) Rectangular-shaped isolator (STRP-2/2)

Figure 7.4 Hysteresis force under the bidirectional circular trajectory

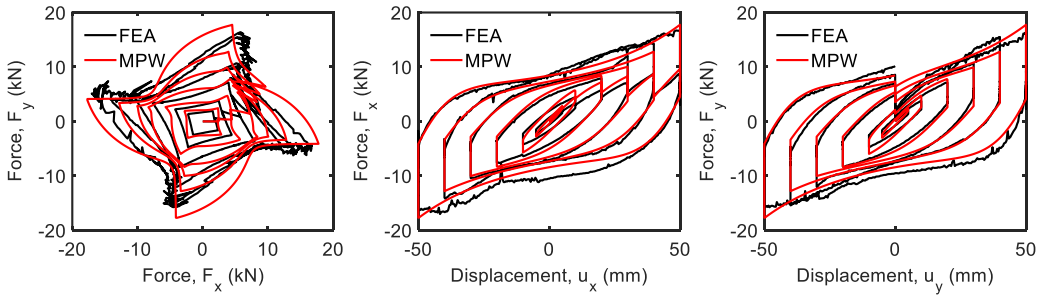

(i) Bidirectional components (ii) *X*-component (iii) *Y*-component

(a) Square-shaped isolator (STRP-2/1)

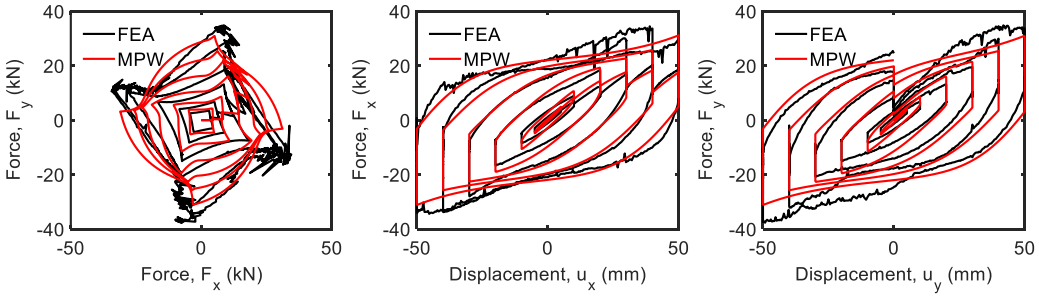

(i) Bidirectional components (ii) *X*-component (iii) *Y*-component

(b) Rectangular-shaped isolator (STRP-2/2)

Figure 7.5 Hysteresis force under the bidirectional square trajectory

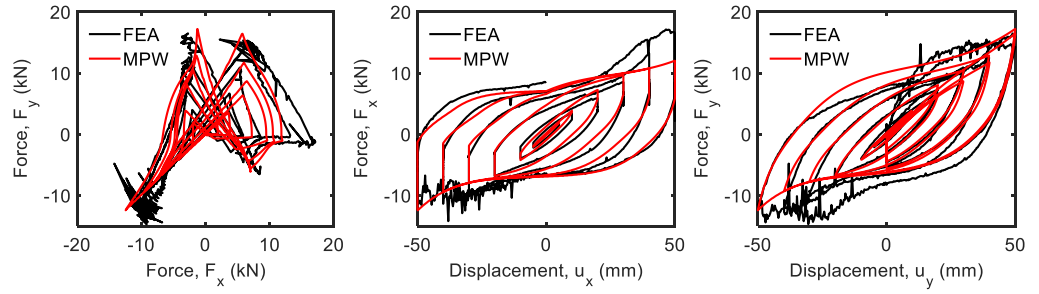

(i) Bidirectional components (ii) *X*-component (iii) *Y*-component

(a) Square-shaped isolator (STRP-2/1)

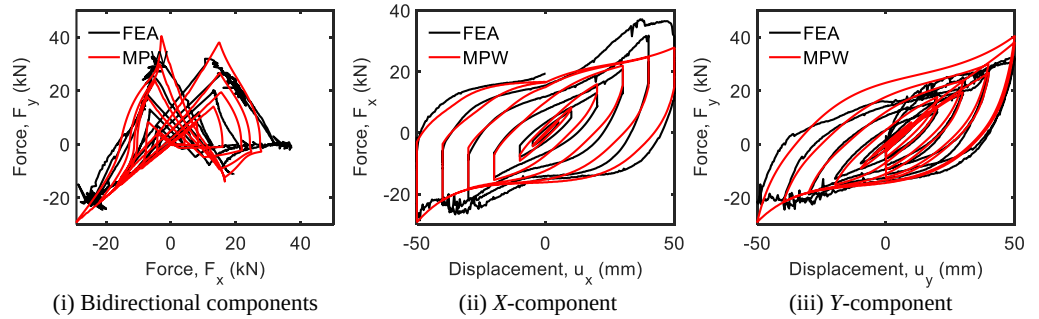

(i) Bidirectional components (ii) *X*-component (iii) *Y*-component

(b) Rectangular-shaped isolator (STRP-2/2)

Figure 7.6 Hysteresis force under bidirectional hourglass trajectory

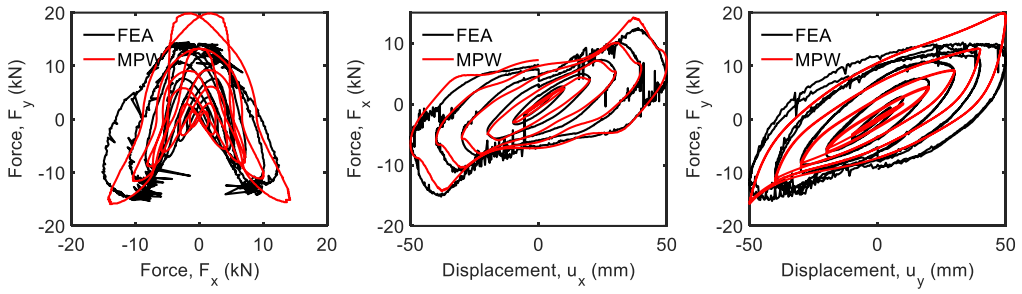

(i) Bidirectional components (ii) *X*-component (iii) *Y*-component

(a) Square-shaped isolator (STRP-2/1)

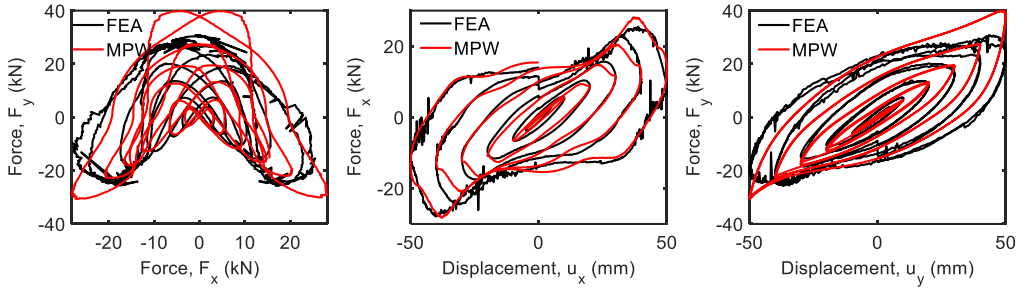

(i) Bidirectional components (ii) *X*-component (iii) *Y*-component

(b) Rectangular-shaped isolator (STRP-2/2)

Figure 7.7 Hysteresis force under the bidirectional 8-shaped trajectory

Table 7.4 Contribution rate R for the different trajectory of bidirectional loading

	Square-shaped isolator: 72×72×24				Strip-shaped isolator: 144×72×24			
R-value	Circular	Square	Hourglass	8-shaped	Circular	Square	Hourglass	8-shaped
	0.993	0.976	0.960	0.975	0.988	0.968	0.960	0.979

7.4.3 Earthquake Loading Case

The hysteresis loop and the time-history of restoring force of the STRP isolator of a size of 72×72×24 mm are computed by the MPW model subjected to the displacement time history of simulated seismic response of an SDOF system. Vertical compression of 5.0 MPa is imposed on the STRP isolator as a gravity load applied at the isolator's top surface. The input displacement time history is obtained from FE analysis of an SDOF system subjected to ground acceleration, assuming a situation of a rigid mass supported by the STRP isolator. Figure 7.8 shows the *X* and *Y* components of the 1940-Imperial Valley and the 1995-Kobe earthquakes. Table 7.5 indicates the scale factor for each acceleration component that is used to keep the deformation of the isolator within 200% shear.

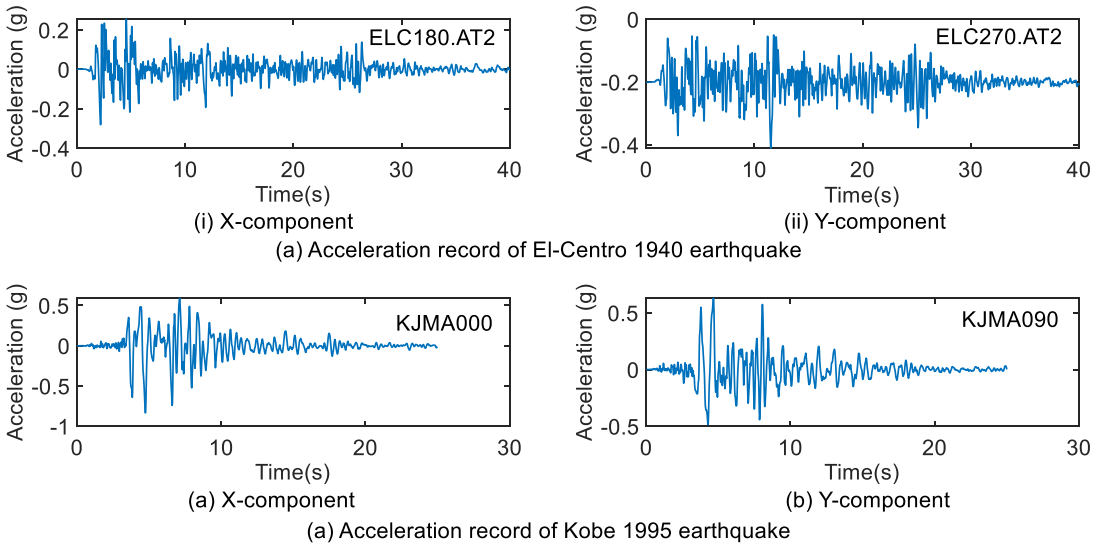

Figure 7.8 Acceleration record of 1940-Imperial Valley and 1995-Kobe earthquakes

Table 7.5 Intensity of input earthquake acceleration

Analysis type	El-Centro earthquake 1940	Kobe 1994 earthquake
Unidirectional	100% of *X*-component	30% of *X*-component
Bidirectional	75% of *X*-component +75% of *Y*-component	20% of *X*-component +20% of *Y*-component

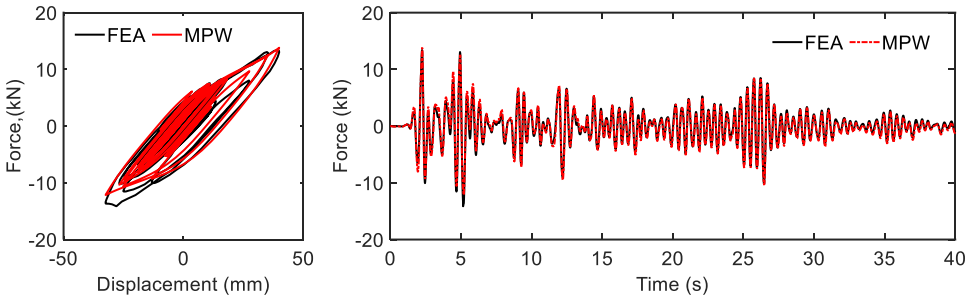

(a) Imperial valley: 100% of ELC180.AT2 acceleration in *X*-direction

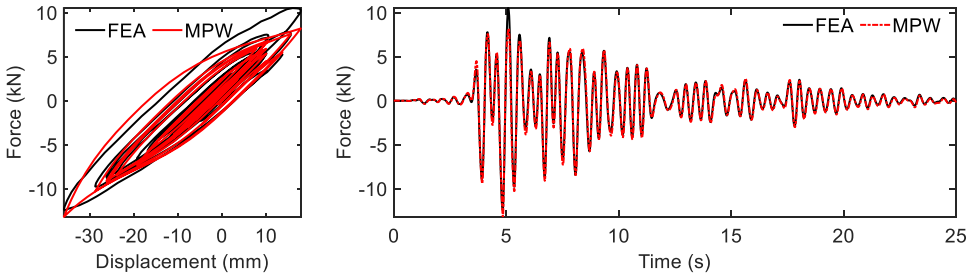

(b) Kobe: 30% of KJMA000 acceleration in *X*-direction

Figure 7.9 Hysteresis loop and restoring under unidirectional earthquake

Figure 7.9 shows the comparison of hysteresis loops and the time history of the restoring force between the FE analysis result and that computed by the MPW mode under unidirectional ground motion. Figures 7.10 and 7.11 show the same comparison of results found from bidirectional analysis. It indicates that the proposed model is also effective in describing the hysteresis behavior of the unbonded STRP isolator under a random loading pattern. The ratio of the difference of the maximum restoring force between the MPW model and FE analysis result is within 15%.

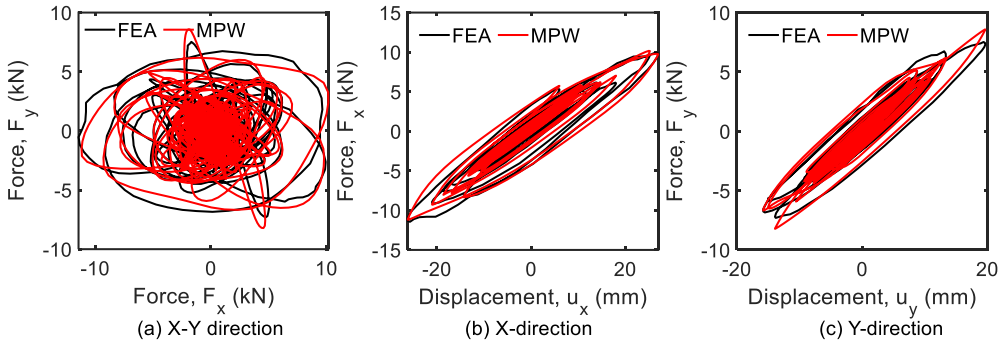

(a) Hysteresis curves under bi-direction component of 1940-Imperial Valley earthquake

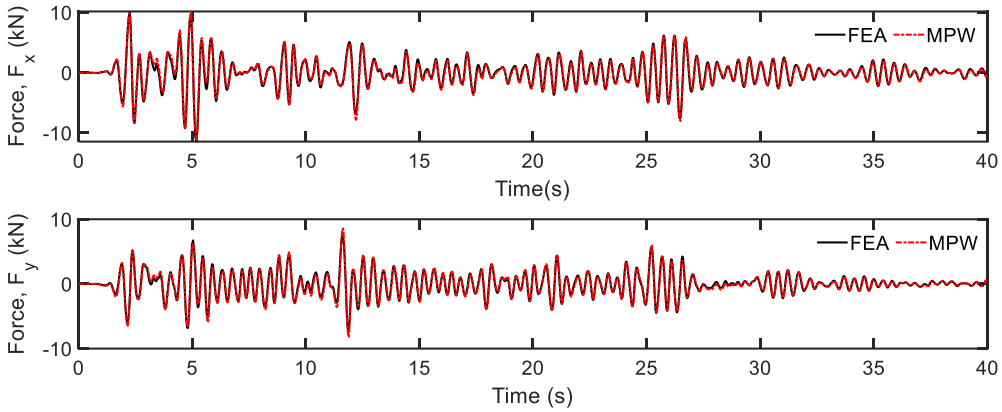

(b) Restoring force-time histories under bi-direction component of 1940-Imperial Valley earthquake

Figure 7.10 Verification of MPW model under bidirectional earthquake: 75% of El-Centro earthquake

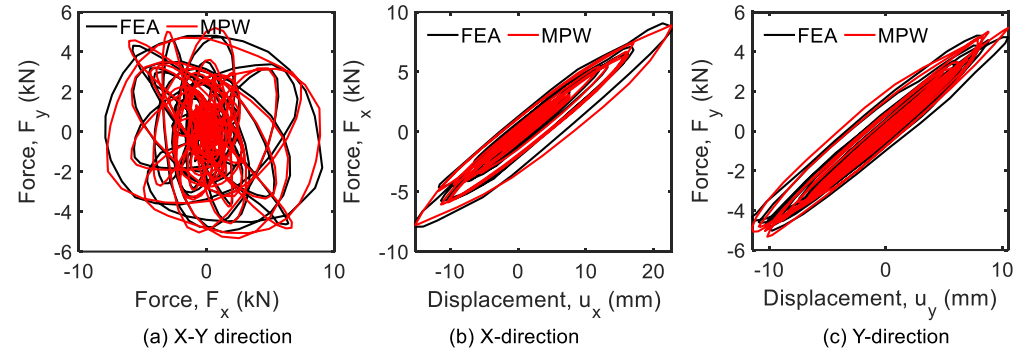

(a) Hysteresis curves under bi-direction component of 1995-Kobe earthquake

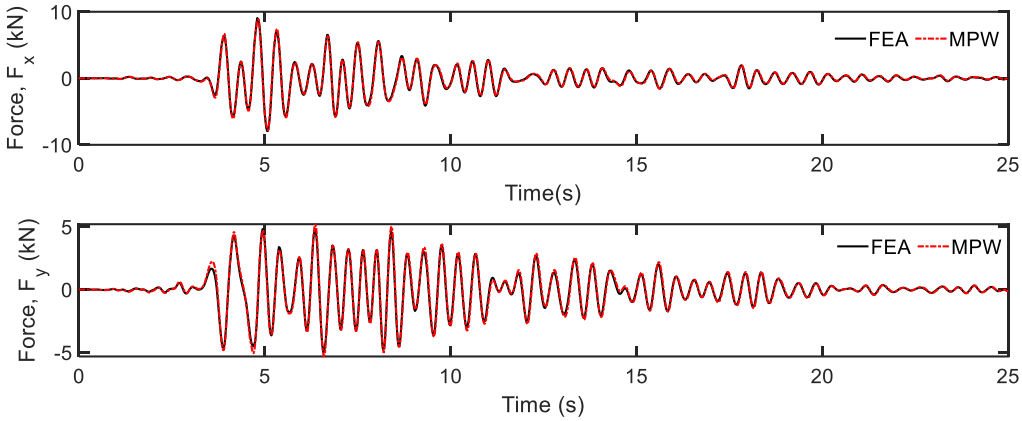

(b) Restoring force-time histories under bi-direction component of 1995-Kobe earthquake

Figure 7.11 Verification of MPW model under bidirectional earthquake: 20% of Kobe earthquake

7.5 Evaluation of a 4-Story Building

7.5.1 FE Modeling of Base Isolated Building

A hypothetical 4-story reinforced concrete building resting on nine square-shaped isolators is considered. It is two-by-two-bay with a total width of 12 m and a height of 12 m, as shown in Fig. 7.12. The column and beam sizes are 500×500 mm and 300×500 mm, respectively, and the slab is 150 mm thick. At the base level, there is no rigid slab. Therefore, isolators are placed at the intersections of beam and column. The unit mass of concrete and that for an infilled wall is 2400 kg/m^3 and 1950 kg/m^3. The mass of the 130 mm thick infill wall (760.5 kg/m) is added to the mass of the beam. The mass of isolators is ignored. The elastic modulus and Poisson's ratio for a 35.0 MPa concrete is 32.1 GPa, 0.20, respectively. Table 7.6 shows the mass and stiffness at the different story levels.

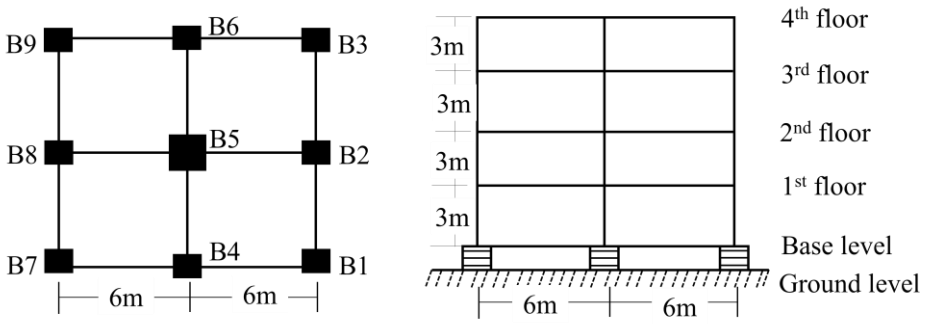

Figure 7.12 Plan and elevation of 4-storied BI building

Table 7.6 Mass and Stiffness properties of STRP base-isolated building

Floor	Base	1st	2nd	3rd	4th
Mass (ton)	69.7	164.4	164.4	164.4	125.1
Stiffness (kN/mm)	9.23	568	568	568	568

Because of axisymmetric mass and stiffness, corner isolators are grouped as *A*-type, periphery-middle isolators as *B*-type, and the central one as *C*-type. Vertical load on each *A*, *B*, and *C*-types isolator is 540.6 kN, 864.1 kN, and 1344 kN, respectively. The geometric properties of STRP isolators listed in Table 7.7 are determined based on 5.0 MPa vertical pressure, target isolation period, and the minimum aspect ratio. A detailed description of designing an STRP isolator is given in Chapter 8. The average static pressure on the isolators group is 3.97 MPa. Shear modulus and effective damping for 3.3~10 MPa pressure and at 100% shear strain are 0.48~0.75 MPa and 12~16%, respectively (Mishra *et* al., 2014). Under sinusoidal loading, the effective damping exceeding 20%. The shear modulus at 100% shear strain and 3.97 MPa compression is about 0.64 MPa. The first mode period is 0.53 s and 1.78 s for fixed-base and base-isolated structures, respectively. The 5% elastic damping is considered for the fixed base structure and 15% for the

Table 7.7 Geometric properties of STRP isolators (mm)

Isolator types	Axial load (kN)	Plan dimension	Height	Aspect ratio	Total rubber thickness, t_r	Rubber layer thickness, t_e	Shape factor, *S*
A	540.6	432×432	144	3.0	120	2.4	45
B	864.1	432×432		3.0			45
C	1344.0	510×510		3.54			53

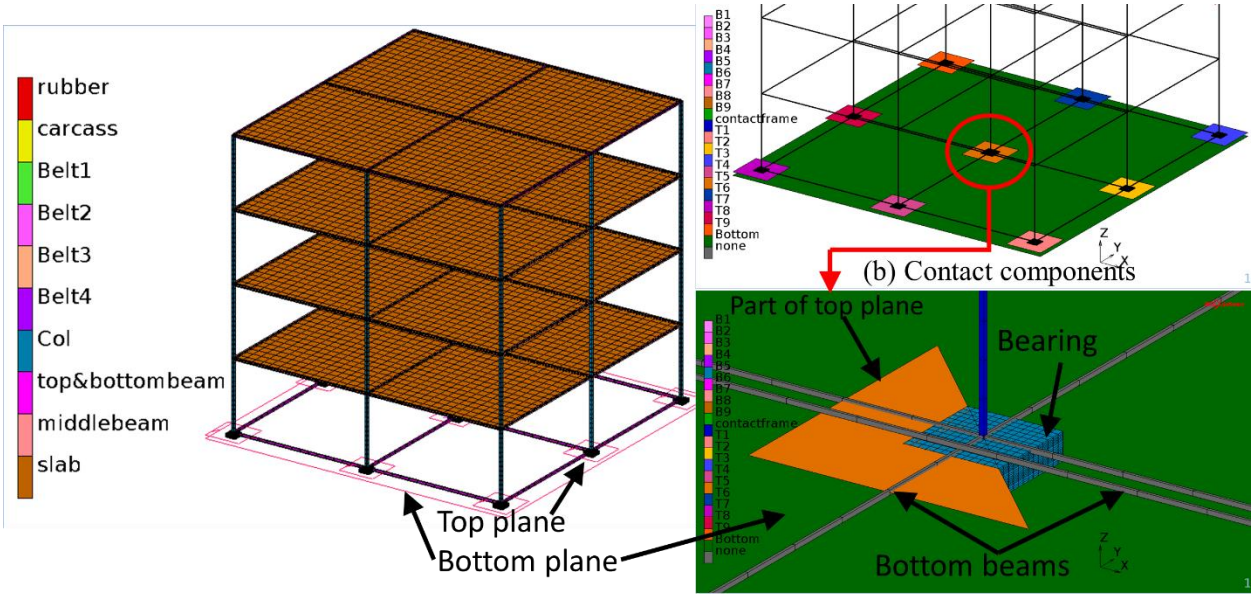

Figure 7.13 Finite element modeling of base-isolated structure

base-isolated structure. The beams and columns are assumed as a linear isotropic elastic-plastic element and the floor slab as a shell element. Figure 7.13 shows the FE model of the STRP base-isolated building. The connection between rigid planes and isolators is the same as described in the previous section. Also, a glued connection is assumed between the top rigid planes and each column's bottom node.

The analytical formulation, including the MPW model for dynamic time-history analysis, is given in Eq. 7.11. The restoring force of the isolation part, [*F*], is replaced by the proposed MPW model in Eq. 7.12.

$$[M]\{\ddot{u}\}+[C]\{\dot{u}\}+[F]=[M]\{a_g\} \tag{7.11}$$

$$[M]\{\ddot{u}\}+[C]\{\dot{u}\}+\{\alpha k_0 u+\left(b_1+b_2|\varepsilon|^4\right)(1-\alpha)k_0[Z]\}=[M]\{a_g\} \tag{7.12}$$

$$[C]=\alpha[M]+\beta[k] \tag{7.13}$$

where [*M*], [*C*], and [*F*] indicate the mass and damping and restoring force matrices, respectively. The $\{\ddot{u}\}$ and $\{\dot{u}\}$ is the acceleration and velocity of the system, and $\{a_g\}$ is the input ground acceleration. Three acceleration records, as shown in Fig. 7.14, are considered as base excitation. The peak ground acceleration (PGA) of the Kobe, Imperial Valley, and Northridge earthquakes is 0.345*g*, 0.47*g*, and 0.569*g*. Newmark-beta integration method with β=1/6 is used. In the analytical approach, the mass's displacement and velocity

are calculated at every timestep, and then the hysteretic component Z and the restoring force are updated for the same. The FE analysis considers only unidirectional ground motion parallel to the carcass steel-cord direction.

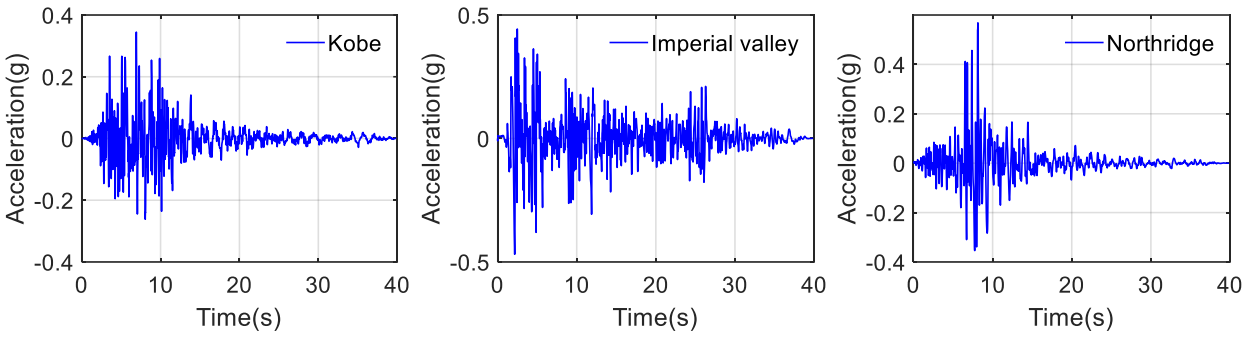

Figure 7.14 Acceleration time history of input earthquakes

7.5.2 Effectiveness of MPW model

Figures 7.15a-7.17a compare hysteresis loops, time-histories for restoring force, and isolator displacement between FE analysis and MPW model. Figures 7.15b-7.17b show the comparison of the MPW model and FE analysis results in terms of top floor displacement and acceleration time histories. The approximation of restoring force and isolator displacement by the MPW model is well agreed with the FF analysis result under the three earthquake inputs. Although the top floor displacement and acceleration time history found from the FE analysis and the MPW model are comparable, the magnitude of the acceleration between the FE analysis and the MPW model display substantial differences. This is because the spring-mass model of the base-isolated building cannot represent the effect of superstructure overturning and its impact on the contact pressure.

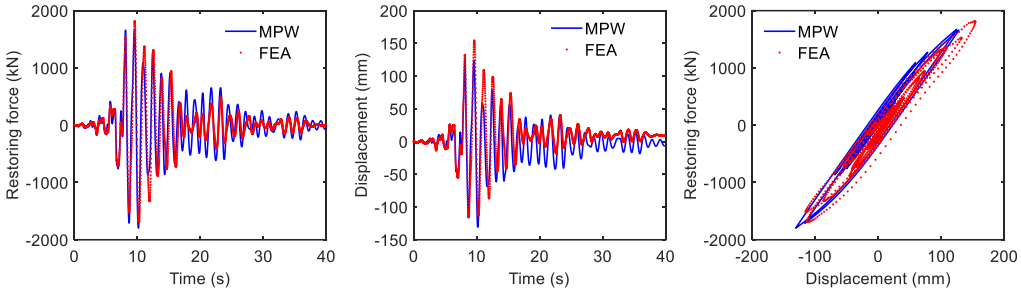

(a) Restoring force and displacement time histories and hysteresis loop

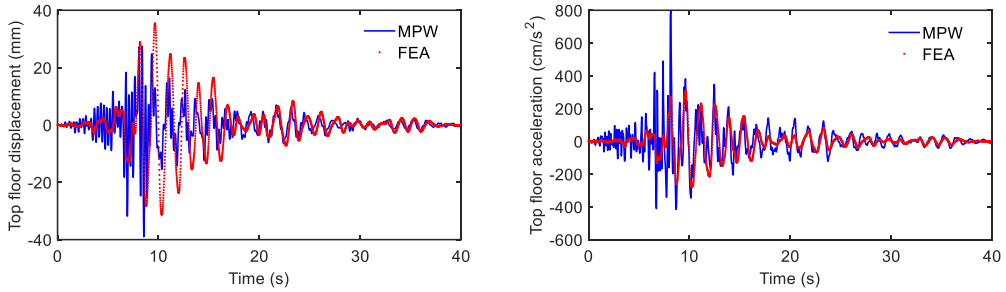

(b) Top floor displacement and acceleration time histories

Figure 7.15 Comparison of MPW model and FE analysis results under Northridge earthquake

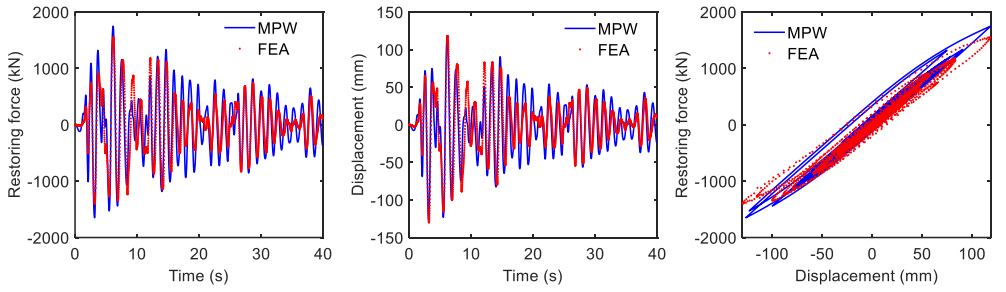

(a) Restoring force and displacement time histories and hysteresis loop

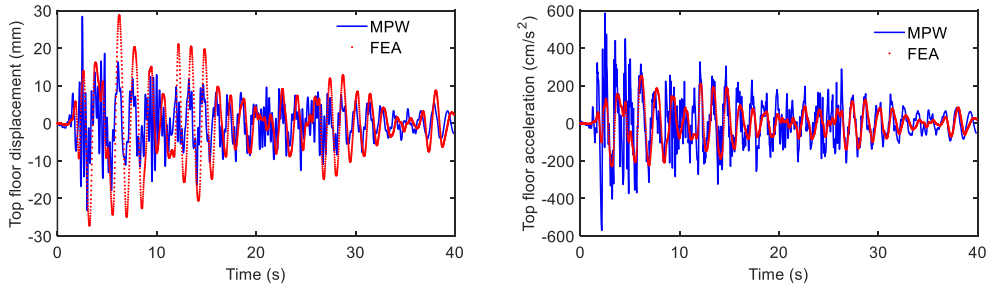

(b) Top floor displacement and acceleration time histories

Figure 7.16 Comparison of MPW model and FE analysis results under Imperial Valley earthquake

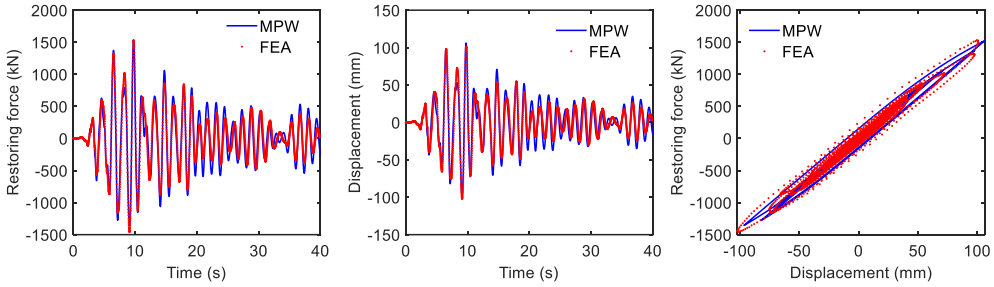

(a) Restoring force and displacement time histories and hysteresis loop

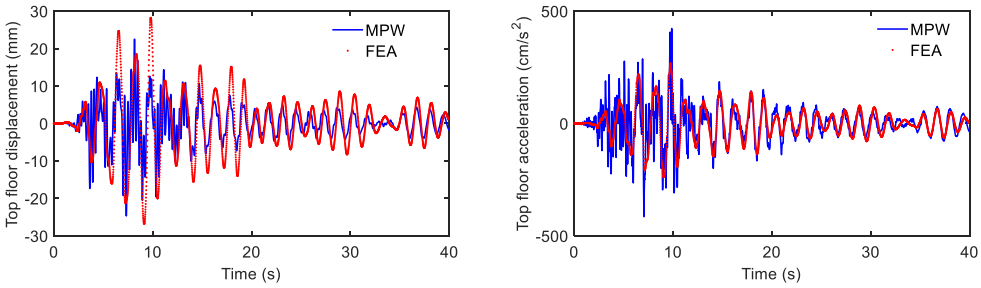

(b) Top floor displacement and acceleration time histories

Figure 7.17 Comparison of MPW model and FE analysis results under Kobe earthquake

Table 7.8 shows the peak of restoring force and the isolator displacement under the three earthquake inputs. The MPW model provides a maximum of 12.9% overestimation of restoring force in Imperial valley and 15.1% underestimation of restoring force in Northridge input. Except for these cases, the difference for both displacement and restoring force between the MPW model and FE analysis is below 4%. Figure 7.18 compares displacement, drift, and peak of floor acceleration to PGA between FE analysis results and the MPW model. The maximum error in story displacement is below 20% and observed at the top floor level. In other floor levels, the displacement difference is about 10%. The story drift is well predicted in all input earthquakes. The difference in the MPW model and FE analysis result varies between 2% to 25%. The ratio of peak floor acceleration to PGA is comparable only at the bottom and top floors level. On other floors, sometimes it is larger than two times of FE analysis results. The model parameters used in the dynamic analysis of the base-isolated building were calibrated based on the force-displacement curve found from the static cyclic load analysis. These parameters do not consider the effect of the superstructure and its overturning. The boundary condition between the isolators and superstructure is the touch connection that can not resist rotation. A spring-mass model consisting of five degrees of freedom used to represent the building is incapable of simulating the overturning of the actual building. In addition, in the actual building, superstructure responses are dependent on the uplifting and touch connection that is not considered in the

spring-mass model. Therefore, it is concluded that approximation of the restoring force and the displacement of isolators in an unbonded base-isolated building by the MPW model is acceptable. However, for a better approximation of superstructure response, it is necessary to include the dynamic load and superstructure effect in the calibration of the model parameters.

Table 7.8 Peak response of the base-isolation system at different earthquake input

Isolator response	Northridge			Imperial Valley			Kobe		
	FEA	MPW	Diff (%)	FEA	MPW	Diff (%)	FEA	MPW	Diff (%)
Restoring force (kN)	1815	1795	1.1	1549	1749	-12.9	1530	1522	0.5
Displacement (mm)	154	130.7	15.1	130	126.5	2.7	102	106.1	-4

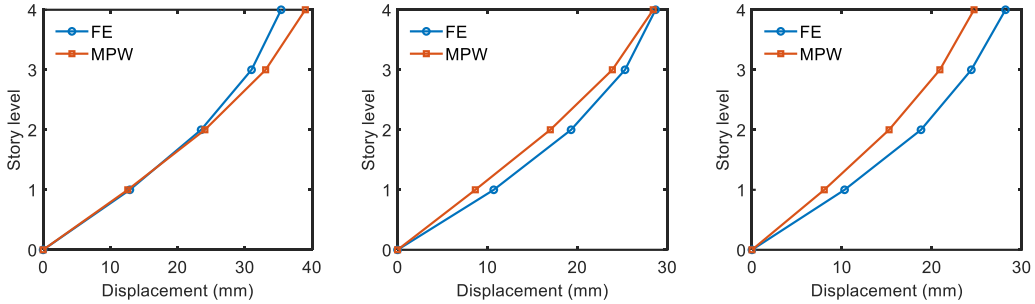

(i) Northridge (ii) Imperial Valley (iii) Kobe

(a) Comparison of story displacement estimated by FE analysis and MPW model

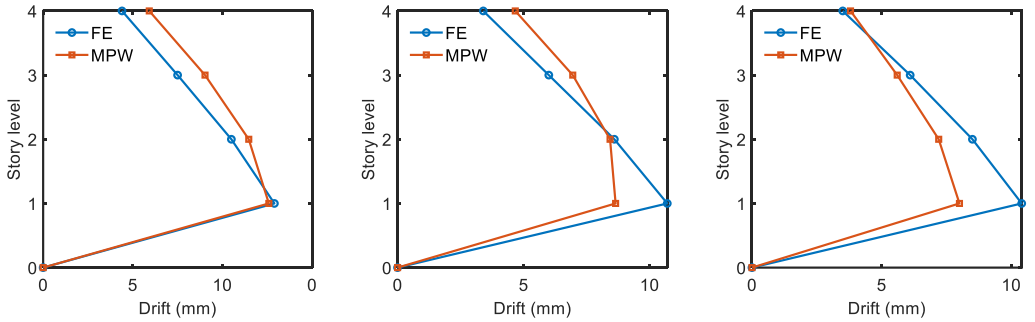

(i) Northridge (ii) Imperial Valley (iii) Kobe

(b) Comparison of story drift estimated by FE analysis and MPW model

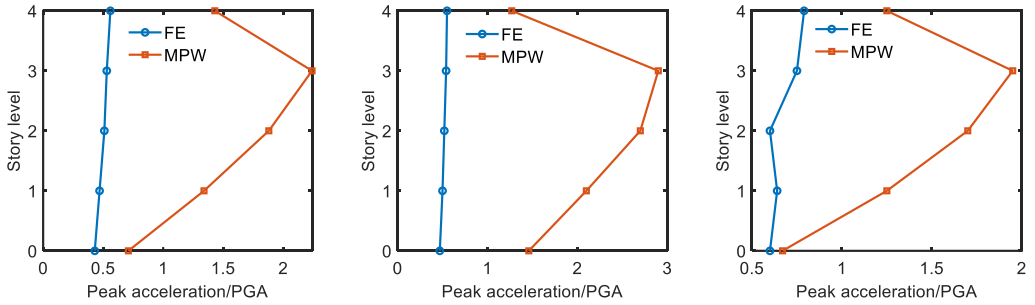

(i) Northridge (ii) Imperial Valley (iii) Kobe

(c) Comparison of peak of story acceleration/PGA estimated by FE analysis and MPW model

Figure 7.18 Comparison of displacement, drift, and acceleration of the building between MPW model and FE analysis result

7.6 Conclusions

This study focused on an analytical model for the hysteresis response of unbonded STRP isolators, including the anisotropy nature of the STRP isolator and the strain dependency of hysteresis force. The model parameters are calibrated using linear regression of restoring force found from FE analysis and the

proposed model. Based on the FE simulation result, it can be concluded that the proposed MPW model is suitable to express the effect of roll-over deformation and the anisotropy in the elastic restoring force component caused by the isolator geometry. Furthermore, the accuracy of the model is successfully shown by comparison with the FE analysis for unidirectional cyclic loading, bidirectional circular displacement trajectories, and random displacement pattern obtained by the simulated seismic response of an SDOF system. Finally, a dynamic analysis of a four-story building by implementing the proposed model shows that the restoring force and displacement of the isolators obtained by the MPW model are acceptable. Furthermore, the peak of displacement and inter-story drift obtained from the MPW model is matched with the FE analysis results. However, the peak of the acceleration and the time history of displacement and acceleration from the MPW model and the FE analysis results show a substantial difference, indicating that the model parameters should be calibrated with the force-displacement relationship of the base-isolated structure due to an earthquake load.

References

AASHTO-LRFD (2014). LRFD Bridge Design Specifications. 7th Ed., Washington, D. C.

Abe M., Yoshida J. and Fujino Y. (2004a). Multiaxial Behaviors of Laminated Rubber Bearings and Their Modeling. II: Modeling. Journal of Structural Engineering, ASCE, 130(8), pp. 1133-1144.

ASCE/SEI 7-10 (2010). Minimum Design Loads for Buildings and Other Structures, ASCE, 1801 Alexander Bell Drive, Reston, Virginia.

Dang J., Igarashi A., and Murakoshi Y. (2016). Development of Hysteretic Model for High-Damping Rubber Bearings Under Bi-Directional and Large Strain Domain Loading, Structural Engineering & Earthquake Engineering, JSCE, 72(1), pp. 250-262 (Japanese).

De Raaf M. G. P., Tait M. J., and Toopchi-Nezhad H. (2011). Stability of Fiber Reinforced Elastomeric Bearings in an Unbonded Application. J. Compos. Mater., 45(18), pp. 1873-1884.

Domaneschi M. (2012). Simulation of Controlled Hysteresis by the Semiactive Bouc Wen Model. Computers & Structures, 106-107, pp. 245-257.

Eurocode 8 (2004). Design of structures for earthquake resistance. BS EN 1998-1:2004.

Grant D. N., Fenves G. L. and Whittaker A. S. (2008). Bidirectional Modelling of High-Damping Rubber Bearings, Journal of Earthquake Engineering, 8:S1, pp. 161-185.

Konstantinidis D., Kelly J. M., and Makris N. (2008). Experimental investigation on the seismic response of bridge bearings. Technical Rep. No. EERC 2008-02, Earthquake Engineering Research Center, Univ. of California, Berkeley, CA.

Manzoori A. and Toopchi-Nezhad H. (2016). Application of an Extended Bouc-Wen Model in Seismic Response Prediction of Unbonded Fiber-Reinforced Isolators, Journal of Earthquake Engineering, 21(1).

Mishra H. K. (2012). Experimental and Analytical Studies on Scrap Tire Rubber Pads for Application to Seismic Isolation of Structures. Ph.D. Thesis, Kyoto University, Japan.

Mishra H. K., Igarashi A., and Matsushima H. (2013a). Finite element analysis and experimental verification of the scrap tire rubber pad isolator. Bulletin Earthquake Engineering, 11(2), pp. 687-707.

Mishra H. K. and Igarashi A. (2013b). Lateral deformation capacity and stability of layer-bonded scrap tire rubber pad isolators under combined compressive and shear loading. Structural Engineering and Mechanics, 48(4), pp. 479-500.

Mishra H. K., Igarashi A., Ji D., and Matsushima H. (2014). Pseudo-Dynamic Testing for Seismic Performance Assessment of Buildings with Seismic Isolation System Using Scrap Tire Rubber Pad Isolators. Journal of Civil Engineering and Architecture, 8(1), pp. 73-88.

Naeim F., and Kelly J. M. (1999). Design of seismic isolated structures, John Wiley & Sons Inc., New York.

Özdemir G. (2010). Response of isolated structures under bi-Directional excitations of near-field ground motions, Ph.D. Thesis, Middle East Technical University, Turkey.

Park Y. J., Wen Y. K., and Ang A. H-S. (1986). Random Vibration of Hysteretic Systems under Bi-Directional Ground Motions," Earthquake Engineering & Structual Dynamics, 14, pp. 543-557.

Peng T. B., Li J. Z., and Fan L. C. (2007). Pilot study on the horizontal shear behaviour of FRP rubber isolators. Asia-Pacific Conference on FRP in Structures (APFIS 2007), pp. 443-449.

Toopchi-Nezhad H. (2014). Horizontal stiffness solutions for unbonded fiber reinforced elastomeric bearings. Structural Engineering and Mechanics, 49(3), pp. 395–410.

Toopchi-Nezhad H., Tait M. J., and Drysdale R. G. (2009). Simplified analysis of a lowrise building seismically isolated with stable unbonded fiber reinforced elastomeric isolators. Can. J. Civ. Eng., 36, pp.1182–1194.

Turer A. and Özden B. (2007). Seismic base isolation using low-cost scrap tire pads (STP). Materials and Structures, 41(5), pp. 891-908.

Sireteanu T., Giuclea M., and Mitu A. M. (2010). Identification of an extended Bouc–Wen model with application to seismic protection through hysteretic devices. J. Eng. Mech., 45, pp. 431–441

Van Engelen N. C., Tait M. J., and Konstantinidis D. (2015). Model of the shear behavior of unbonded fiber-reinforced elastomeric isolators. Journal of Structural Engineering, ASCE, 141 (7), pp. 1-11.

Zhou T., Wu Y., and Li A. (2017). Implementation and Validation of a Numerical Model for Lead-Rubber Seismic Isolation Bearings. Journal of Mechanics, 35(2), 153-165.

Zisan M. B. and Iarashi A. (2020). Lateral Load Performance Evaluation of Unbonded Strip-STRP Base Isolator, 17th World Conference on Earthquake Engineering (17WCEE), September 13th to 18th, 2020, Sendai, Japan.

Zisan M. B. and Iarashi A. (2021). Lateral Load Performance and Seismic Demand of Unbonded STRP Base Isolator, Earthquake Engineering and Engineering Vibration (Accepted).

Chapter 8

Conclusions and Recommendations

This research concentrated on the analytical modeling and finite element simulation for investigating the seismic performance of the unbonded STRP isolator and feasibility in practical implementation. It intended to formulate a force-displacement model and a horizontal stiffness solution to design the STRP isolator for unbonded application. In investigating the lateral load and seismic performance, general features such as the length-to-width ratio, heights, unbonded conditions, and frictions between isolator and structures are considered. The allowable load for the unbonded STRP isolator is expected to be determined based on in-service stress-strain limits and the existing design guidelines. Analytical approaches available in the literature are taken to evaluate the unbonded STRP isolator under the vertical load. The effectiveness of unbonded application and STRP isolator in an actual earthquake condition is intended to investigate using nonlinear time history analysis of a four-story building designed with unbonded STRP isolators. Besides, the effectiveness of unbonded STRP isolator in reducing damage and seismic vulnerability of masonry building is investigated from a practical perspective.

8.1 Significant Findings of the Research

8.1.1 Vertical and Lateral Load Performance for Unidirectional Load

The strip-shaped STRP isolators with different length-to-width ratios and square-shaped isolators with different heights are analyzed to study the lateral load performance and seismic capacity. The isolators are investigated for 5.0 MPa compression and a maximum of 250% shear displacement. In addition, the displacement capacity and isolation periods at DBE and MCE level earthquakes are investigated using the equivalent lateral load procedure of ASCE-SEI 7-10 guidelines. The findings from the FE analysis are summarized as follows:

- The minimum stiffness of the strip-shaped STRP isolator in the transverse and that in the longitudinal directions are 0.65~0.75 and 0.90~1.0 times of the values calculated by the effective shear modulus and the minimum effective damping ratio about 10% within the 100%~150% shear

strain. Stack numbers exceeding three have an insignificant influence on the lateral stiffness of the square-shaped bearing with an aspect ratio of 3.

- STRP isolators are anisotropic, which is highly noticeable for the strip-shape. The influence of the length-to-width ratio on the lateral stiffness is significant in the longitudinal direction providing stiffness 1.15~1.40 times of that in the transverse direction. Besides, as the length-to-width ratio increases from unity to ten, the stiffness increases by 37~58% in the longitudinal direction and decreases by 12% in the transverse direction.

- The effect of the length-to-width ratio on the vertical stiffness is significant for a value below 4.0. Increasing the stack number increases the vertical stiffness of the square-shaped isolator.

- At 250% shear strain, the average reduction of the effective damping ratios is 38% and 33% in the longitudinal and transverse directions, respectively, whereas it is 52% in the square-shaped bearings. The dependence of the damping ratio on the length-to-width ratio exceeding 4.0 or stack numbers exceeding 3 is insignificant.

- At site class C with S1=0.40 and D with S1=0.40 and 0.50 of the ASCE/SEI 7-10 specifications, a 96 mm thick strip-shaped isolator provided an isolation period longer than 1.11s at DBE and MCE levels. The maximum shear strain of the isolators almost satisfies the allowable limit of 150% and 250% at DBE and MCE levels, respectively. The period and displacement capacity in the transverse direction are about 12~15 % and 10~15% larger, respectively, than that of the longitudinal direction. Displacement capacity decreases by 10~15% as the length-to-width ratio increases from unity to 10.

- For a six-stack STRP isolator with aspect ratios of 12 and 3 in the length and width directions, respectively, 72 mm is the minimum height for a period longer than 1.0 s. Thus, the permissible DBE level acceleration is 0.4 g within the allowable displacement limits.

8.1.2 Lateral Load Performance under for Biaxial Loading

The lateral load performance of the unbonded strip-shaped STRP isolators is investigated for circular, square, hourglass, and 8-shaped biaxial displacement trajectories. The same was also investigated for the unidirectional component of each bidirectional displacement path. In all loading cases, vertical compression is 5.0 MPa, and maximum lateral strain is 250%. The key findings are as follows:

- The elastomer strain and restoring force components are coupled in a bidirectional loading. Roll-over deformation and hardening are insignificant in bidirectional loading than that of unidirectional loading.

- The hysteresis behavior of the unbonded isolators depends on the type of the input displacement path, but existing codes do not specify the nature of cyclic displacement. Therefore, an efficient design of an unbonded isolator needs an appropriate selection of input displacement patterns.

- The horizontal stiffness and effective damping ratio in bidirectional loading are higher than that of the unidirectional load. Stiffness increases with shear displacement and can be 1.40 times that of the unidirectional load. In bidirectional loading, the minimum damping ratio is about 10% at 25% shear that raised to nearly 35% at 200% shear displacement, whereas it is 10%~16% for linear and unidirectional displacement.

- The empirical relation between the bidirectional and unidirectional hysteretic response provides that the stiffness for the bidirectional loading test is 0.8~1.25 times that of the unidirectional loading test. The lower response appears for 250% shear displacement. Similarly, effective damping is 1.35 and 0.85 times of that in the unidirectional load.

8.1.3 Analytical Approach for Unbonded STRP Isolator

The vertical stiffness of the unbonded STRP isolators is studied using the pressure solution and pressure approach. An analytical method is proposed for the lateral force-displacement relationship and horizontal stiffness of the unbonded STRP isolator. The hysteresis behavior is presented using a modified version of the Park-Wen model. A brief of the analytical approach is given below:

- The vertical stiffness from the pressure approach is within the ±13% of the FE analysis result. The pressure solution substantially underestimated the vertical stiffness for the strip-shaped STRP isolator.

- The proposed stiffness solution is accurate in predicting the force-displacement relation and horizontal stiffness of the square-shaped STRP isolators. However, the progressive rollover deformation and self-restraining property of STRP with a high length-to-width ratio increase the horizontal stiffness that the proposed solution cannot capture.

- A modified version of the Park-Wen model, including the anisotropic behaviour of the isolator, is proposed for the hysteresis response of the unbonded STRP isolator. The model parameters are calibrated with FE analysis results. The proposed method is appropriate for predicting hysteresis behavior for unidirectional load and different bidirectional displacement orbits: circular, square, hourglass, 8-shaped orbit, as well as the random displacement pattern. A time history analysis of a four-story building by implementing the modified Park-Wen model display consistency with FE analysis result. The modified Park-Wen model is expected to be applicable to dynamic response analysis of unbonded STRP base isolated structures.

8.1.4 Stress-Strain Behavior

The stress and strain in the unbonded STRP isolators with different length-to-width ratios are analyzed for various combinations of compressions, structure-to isolator interface rotations, and lateral displacement. The vertical forces are 2.5, 5.0, 7.5, and 10.0 MPa, including the upper and lower limits in the AASHTO-LRFD specification. The maximum rotation and lateral displacement are 0.05-radian and 250% shear strain, respectively. An examination with existing codes gives the following significant findings.

- STRP isolators show unsymmetrical lateral bulging. The lateral bulging is approximately equal in the two orthogonal directions for a length-to-width ratio between 2.0 and 4.0 and insignificant for a larger value. A progressive rollover deformation initiates at 90% shear displacement and continues until 250% shear. The full-contact occurs at 250% shear instead of 167% observed in FREI.

- The pressure solution can be exercised for elastomer stress considering 16% and 26% underestimation for length-to-width ratios of 1.0 and exceeding 1.0, respectively. Orientation of the steel cords provides stress difference in the FE analysis.

- The aspect ratio 3.0 is suitable against lift-off and instability of an unbonded STRP isolator for combinations of 250% shear displacement, 0.05-radian rotation, and 2.5 MPa compression. An increase in the length-to-width ratio quickens the lift-off initiation, and growth of the compression delays the lift-off rotation.

- Rotation increases the elastomer stress level that is significant at low compression and high length-to-width ratio. Conversely, lateral displacement reduces in-plane compression stress and induces tension more significant for a high length-to-width ratio.

- An unbonded STRP isolator with a length-to-width ratio of 1.0 and an aspect ratio of 3.0 can be performed under any combination of forces within 5.0 MPa compression, 0.05-radian rotation, and 200% shear. The length-to-width ratio of 2.0 complies within 5.0 MPa compression plus rotation and displacement up to 0.02-radian and 100% shear. The elastomer stress-strain relationship disagrees with the design limit for a length-to-width ratio exceeding 2.0, even under 0.01 radian and 2.5 MPa compression. In the absence of rotation, unbonded isolators comply with design limits until 200% shear displacement under 5.0 MPa compression.

- An effective length defined by excluding the tension zone equal to 1.0~1.30 times of the total rubber thickness can be utilized to avoid any occurrence of displacement exceeding 200% shear.

- The maximum elastomer strain for any values of the length-to-width ratio is lower than the design limits.

- Steel cord stress is appreciably insignificant compared with the yield strength. The equivalent thickness of the steel cords is sufficient to meet the design limits.

8.2 Recommendation for Future Research

This research highlighted the lateral load and seismic performance of the STRP isolator and base-isolated buildings using FE element analysis and analytical approach. To advance the STRP isolation for practical application, following further research can be carried out.

- An unbonded STRP isolator is more efficient than that with a bonded one. Since friction is the critical parameter that controls the effectiveness of an unbonded isolator, the shaking table test of an unbonded STRP base-isolated prototype building is essential for accurate prediction.

- An unbonded application of STRP isolators is feasible and effective for protecting structures from the impact of an earthquake. It improves the seismic performance and reduces the damage level of the supporting structures in real earthquake situations. However, problems including

limitation of dislocation associated with the unbonded application of partially bonded STRP isolators, overturning of superstructure and vertical component of earthquakes should be further investigated.

- Further improvement is necessary to include the impact of the length-to-width ratio of a strip-shaped isolator. The anisotropy of the strip-shaped STRP isolators should be considered in the design.

- The tire pad thickness, orientation, and geometric properties of the steel cord vary depending on tire brand and vehicle types. Therefore, it is necessary to investigate the lateral load performance for the STRP isolator made with a different class of automobile tires.

- The durability and environmental degradation of scrap tire pads are a big challenge for practical application and should be considered for further study.